



FEDERAL UNIVERSITY OF PARAÍBA – UFPB (Brazil)

UNIVERSITY OF POTSDAM – UP (Germany)

**COTUTELLE DE THÈSE**

**– PhD THESIS –**

# **GROUNDWATER RECHARGE IN TROPICAL WET REGIONS VIA GIS-BASED METHODS AND COSMIC-RAY NEUTRON SENSING**

*by*

**Luís Romero Barbosa**

PhD thesis defended at Federal University of Paraíba (UFPB) for attaining the double degree in *Doctor of Civil and Environmental Engineering* by UFPB, with emphasis on **Water Resources**, and *Doctor of Engineering (Dr.-Ing.)* by University of Potsdam (UP), with emphasis on **Geocology/Hydrogeology**

This work is licensed under a Creative Commons License:  
Attribution 4.0 International.  
This does not apply to quoted content from other authors.  
To view a copy of this license visit  
<https://creativecommons.org/licenses/by/4.0/>

Published online at the  
Institutional Repository of the University of Potsdam:  
<https://doi.org/10.25932/publishup-46064>  
<https://nbn-resolving.org/urn:nbn:de:kobv:517-opus4-460641>



FEDERAL UNIVERSITY OF PARAÍBA – UFPB (Brazil)

UNIVERSITY OF POTSDAM – UP (Germany)

**COTUTELLE DE THÈSE**

**– PhD THESIS –**

## **GROUNDWATER RECHARGE IN TROPICAL WET REGIONS VIA GIS-BASED METHODS AND COSMIC-RAY NEUTRON SENSING**

PhD thesis submitted to the Examining Board, composed of a German Doctoral Board from the Institute of Environmental Science and Geography at University of Potsdam (UP), and of a Brazilian Doctoral Board from the Postgraduate Program in Civil and Environmental Engineering at Federal University of Paraíba (UFPB), as part of the requisites for attaining the double degree in *Doctor of Civil and Environmental Engineering* by UFPB, with emphasis on **Water Resources**, and *Doctor of Engineering (Dr.-Ing.)* by UP, with emphasis on **Geocology/Hydrogeology**.

**Luís Romero Barbosa**

**Brazilian supervisor: Prof. Cristiano das N. Almeida, Dr.**

**German supervisor: Prof. Sascha E. Oswald, Dr.**

**Catálogo na publicação**  
**Seção de Catalogação e Classificação**

E238g Barbosa, Luís Romero.

Groundwater recharge in tropical wet regions via  
GIS-based methods and Cosmic-Ray Neutron Sensing / Luís  
Romero Barbosa. - João Pessoa, 2020.

209 f. : il.

Orientação: Cristiano das Neves Almeida.

Coorientação: Sascha E Oswald.

Tese (Doutorado) - UFPB/UP/CT/IESG.

1. Recarga de Águas Subterrâneas. 2. Sensoriamento  
Remoto. 3. Detecção de Nêutrons de Raios Cósmicos. 4.  
Propriedades Hidráulicas do Solo. 5. Nordeste do  
Brasil. I. Almeida, Cristiano das Neves. II. Oswald,  
Sascha E. III. Título.

UFPB/BC





FEDERAL UNIVERSITY OF PARAÍBA – UFPB (Brazil) UFPB  
UNIVERSITY OF POTSDAM – UP (Germany)



**COTUTELLE DE THÈSE**

**- PhD THESIS -**

The Examining Board of the PhD thesis

**GROUNDWATER RECHARGE IN TROPICAL WET REGIONS VIA  
GIS-BASED METHODS AND COSMIC-RAY NEUTRON SENSING**

defended by Luís Renato Barbosa on 11/03/2020, for attaining the double degree in: *Doctor of Civil and Environmental Engineering* by UFPB, with emphasis on **Water Resources**, considering the candidate **APPROVED WITH DISTINCTION**; and *Doctor of Engineering (Dr.-Ing)* by UP, with emphasis on **Geocology/Hydrogeology**, considering the candidate **APPROVED**.

Prof. Cristiano das N. Almeida, Dr – UFPB (Brazilian Supervisor)

Prof. Sascha E. Oswald, Dr – UP (German Supervisor)

Prof. Adriano R. da Paz, Dr – UFPB (Brazilian Reviewer)

Prof. Gustavo B. L. Silva, Dr – UFPB (Brazilian Member)

Prof. Axel Bronstert, Dr – UP (German Reviewer)

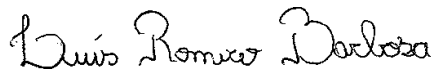
PD Maik Heistermann, Dr – UP (German Member)

## AUTHOR'S DECLARATION

I hereby declare that the academic work embodied in the PhD thesis entitled **“Groundwater recharge in tropical wet regions via GIS-based methods and Cosmic-Ray Neutron Sensing”** is the result of investigations carried out by the author, except where texts and figures were duly quoted and referenced throughout the text.

I also authorize the reproduction and total or partial dissemination of this work, by any conventional or electronic means, for the purposes of study and research, as long as the source be duly quoted and referenced.

No part of this PhD thesis has been concurrently submitted in candidature for any degree at any other institution other than the PhD double degree at the Federal University of Paraíba (UFPB, Brazil) and University of Potsdam (UP, Germany).



---

Luís Romero Barbosa

*To Dr Laércia Karla Diega Paiva Ferreira.*

*For her dignity, her fidelity, her allegiance,  
her wisdom, her humility, her respectfulness,  
her gentleness, her kindness, her patience,  
her strength, her perseverance, her support,  
her joy, her hope, her faith, and her love.*

*Chiefly, for choosing me and fighting for us.*

*I dedicate!*

## MENTION TO יהוה

Romans 8:28-39 (KJV, 1611):

<sup>28</sup> And we know that all things work together for good to them that love God, to them who are the called according to his purpose.

<sup>29</sup> For whom he did foreknow, he also did predestinate to be conformed to the image of his Son, that he might be the firstborn among many brethren.

<sup>30</sup> Moreover whom he did predestinate, them he also called: and whom he called, them he also justified: and whom he justified, them he also glorified.

<sup>31</sup> What shall we then say to these things? If God be for us, who can be against us?

<sup>32</sup> He that spared not his own Son, but delivered him up for us all, how shall he not with him also freely give us all things?

<sup>33</sup> Who shall lay any thing to the charge of God's elect? It is God that justifieth.

<sup>34</sup> Who is he that condemneth? It is Christ that died, yea rather, that is risen again, who is even at the right hand of God, who also maketh intercession for us.

<sup>35</sup> Who shall separate us from the love of Christ? Shall tribulation, or distress, or persecution, or famine, or nakedness, or peril, or sword?

<sup>36</sup> As it is written, for thy sake we are killed all the day long; we are accounted as sheep for the slaughter.

<sup>37</sup> Nay, in all these things we are more than conquerors through him that loved us.

<sup>38</sup> For I am persuaded, that neither death, nor life, nor angels, nor principalities, nor powers, nor things present, nor things to come,

<sup>39</sup> Nor height, nor depth, nor any other creature, shall be able to separate us from the love of God, which is in **Christ Jesus our Lord**.

*Soli Deo Gloria!*

## ACKNOWLEDGEMENTS

This study involved lots of activities regarding data retrieval and processing, as well as personal and spiritual care, thanks to people and financial supports. Hence, this page lends itself to my sincere acknowledgements to:

My almighty, saint, sovereign, and merciful, the **Heavenly Father**; to my lord, saviour, redeemer and intercessor, the **King and Lord Jesus Christ**; and to my comforter, counsellor, supporter and strengthener, the **Holy Spirit of the Truth**. All glory, praise, honour and worship be given to the only **Living God** forever and ever, amen!

My wife, Dr **Laércia Karla Diega Paiva Ferreira**, who virtuously was God's means for my conversion, introducing me the way, the truth and the life, which is the Lord Jesus Christ. Secondly, to all your love and support throughout our marriage years, especially during the eighteen months of my stay in Germany, always upholding on my decisions and being our family's foundation. She is my muse and inspiration!

My family, father **Lúcio Lauro Barbosa**, mother **Fabiana Gonçalves Barbosa**, sisters **Ana Carolina Barbosa** and **Ana Carina Quirino Barbosa**, grandfathers **Antônio Gomes Barbosa** and **Lorival Alfredo Barbosa** (*in memorian*), and grandmothers **Nilda Gonçalves Barbosa** and **Josefa Dorziat Quirino Barbosa** (*in memorian*). For their dignity, integrity, honesty and responsibility in all matters of a righteous conduct, making me a better person and professional. Especially, to my parents **Lúcio Barbosa** and **Fabiana Barbosa** for lovingly enduring me in all moments of either joy or affliction, as well as for wisely teaching me the right way to live. They are my perfect example of God's heart design!

My wife's family, father-in-law **Luiz Carlos de Souza Ferreira**, mother-in-law **Clélia Paiva da Veiga**, sister-in-law **Larissa Adilis Maria Paiva Ferreira**, and grandmother-in-law **Maria de Souza Ferreira**. For lovingly welcoming me in their family's arms, treating me always affectionately as grandson, son and brother, and entrusting me the most valuable treasure of my life, my wife. May God greatly bless this wonderful family!

My brothers and sisters in Jesus Christ from the *Igreja Evangélica Casa de Davi* and *Igreja Lagoinha Berlin* for the friendship, support, affection and love throughout my Christian journey in this world. Especially to my mentor, guide and friend, the Pastor **Emanuel Alves da Silva** (or simply, 'Pastor Mano') and his wife **Rinalda Galdino Alves**, for having patiently and lovingly advising my family throughout all these years. I praise God for our church to be a pillar and ground of the truth!

My supervisors, Prof. Dr **Cristiano das Neves Almeida** (UFPB, Brazil) and Prof. Dr **Sascha Oswald** (UP, Germany), who kindly accepted to oversee this thesis dissertation, working actively throughout the PhD activities. To Prof. Dr **Almeida**, for having me as supervisor during my entire academic career in hydrogeology science, for roughly one decade. To Prof. Dr **Oswald**, for entrusting me the challenge of supervising me as his first cotutelle student, and for dearly welcoming me in Germany.

Members of the examining board, Prof. Dr **Adriano Rolim da Paz** (UFPB), Prof. Dr **Gustavo Lima Barbosa Silva** (UFPB), Prof. Dr **Axel Bronstert** (UP) and PD Dr **Maik Heistermann** (UP) for their availability in accepting to attend at the PhD board, whose thoughtful suggestions contributed undoubtedly to improve the quality of the PhD thesis.

My research colleagues, the members of LARHENA/UFPB, Prof. Dr **Nelson Oswaldo Luna Caicedo**, Prof. Dr **Alain Marie Bernard Passerat de Silans**, Prof. Dr **Victor Hugo Rabelo Coelho**, M.Sc. **Emerson da Silva Freitas**, M.Sc. **Geraldo Moura Ramos Filho**, M.Sc. **André Nóbrega Gadêlha** and M.Sc. **Nicholas Borges de Lira**, and technicians **Edilson Edimar de Souza** and **Rene Neuenschwander**, as well as the members of WMTL/UP, the Dr **Weishi Wang**, M.Sc. **Lena Scheiffle**, and technicians **Peter Bíró** and **Christian Budach**, for their collaborations in the PhD activities and paper publications.

Partner universities and researchers, the Professors and technical-administrative members of the **PPGECAM program** at UFPB and **IESG institute** at UP, as well as the Prof. Dr **Carlos de Oliveira Galvão** at Federal University of Campina Grande (UFCG), Prof. Dr **Suzana Maria Gico Lima Montenegro** at Federal University of Pernambuco (UFPE), Prof. Dr **José Carlos de Araújo** at Federal University of Ceará (UFC) and Prof. Dr **Gabriele Baroni** at University of Bologna (UB), for their educational teaching, academic instruction and scientific knowledge. The universities are also acknowledged for supporting the conference attendance, equipment purchasing and working travel expenses.

My funders: **CAPES foundation**, for the scholarship (Finance Code 001) and financial support allowing for the accomplishment of this *Cotutelle de Thèse* in Germany (grant number: 88887.161412/2017-00); **Cosmic Sense research project** (FOR 2694 from German DFG) for being associated with PhD activities and providing expertise and technical resources; **DAAD service**, for the German preparation course allowing for an easier adaptation to foreign culture; **CNPq council** and **FINEP agency**, for the DTI-B scholarship granted in **BRAMAR research project** (grant number: 557/2013) allowing for provide resources to carry out the sensor acquisitions, fieldwork campaigns, and academic activities; **FAPESQ-PB foundation**, for the efficient service concerning the scholarship formalities.

Barbosa, Luís Romero. **Groundwater recharge in tropical wet regions via GIS-based methods and Cosmic-Ray Neutron Sensing**. PhD thesis: Federal University of Paraíba – UFPB, University of Potsdam – UP, p. 209, 2020.

## ABSTRACT

Studies on the unsustainable use of groundwater resources are still considered incipient since it is frequently a poorly understood and managed, devalued and inadequately protected natural resource. Groundwater Recharge (GWR) is one of the most challenging elements to estimate since it can rarely be measured directly and cannot easily be derived from existing data. To overcome these limitations, many hydro(geo)logists have combined different approaches to estimate large-scale GWR, namely: remote sensing products, such as IMERG product; Water Budget Equation, also in combination with hydrological models, and; Geographic Information System (GIS), using estimation formulas. For intermediary-scale GWR estimation, there exist: Non-invasive Cosmic-Ray Neutron Sensing (CRNS); wireless networks from local soil probes; and soil hydrological models, such as HYDRUS. Accordingly, this PhD thesis aims, on the one hand, to demonstrate a GIS-based model coupling for estimating the GWR distribution on a large scale in tropical wet basins. On the other hand, it aims to use the time series from CRNS and invasive soil moisture probes to inversely calibrate the soil hydraulic properties, and based on this, estimating the intermediary-scale GWR using a soil hydrological model. For such purpose, two tropical wet basins located in a complex sedimentary aquifer in the coastal Northeast region of Brazil were selected. These are the João Pessoa Case Study Area and the Guaraira Experimental Basin. Several satellite products in the first area were used as input to the GIS-based water budget equation model for estimating the water balance components and GWR in 2016 and 2017. In addition, the point-scale measurement and CRNS data were used in the second area to determine the soil hydraulic properties, and to estimate the GWR in the 2017-2018 and 2018-2019 hydrological years. The resulting values of GWR on large- and intermediary-scale were then compared and validated by the estimates obtained by groundwater table fluctuations. The GWR rates for IMERG- and rain-gauge-based scenarios showed similar coefficients between 68% and 89%, similar mean errors between 30% and 34%, and slightly-different bias between -13% and 11%. The results of GWR rates for soil probes and CRNS soil moisture scenarios ranged from -5.87 to -61.81 cm yr<sup>-1</sup>, which corresponds to 5% and 38% of the precipitation. The calculations of the mean GWR rates on large-scale, based on remote sensing data, and on intermediary-scale, based on CRNS data, held similar results for the Podzol soil type, namely 17.87% and 17% of the precipitation. It is then concluded that the proposed methodologies allowed for estimating realistically the GWR over the study areas, which can be a ground-breaking step towards improving the water management and decision-making in the Northeast of Brazil.

**KEYWORDS:** Groundwater Recharge, Remote Sensing, Cosmic-Ray Neutron Sensing, Soil Hydraulic Properties, Northeast of Brazil.

Barbosa, Luís Romero. **Recarga de águas subterrâneas em regiões úmidas tropicais por métodos baseados em SIG e Detecção de Nêutrons de Raios Cósmicos**. Tese de Doutorado: Universidade Federal da Paraíba – UFPB, Universidade de Potsdam – UP, p. 209, 2020.

## RESUMO

Estudos sobre o uso insustentável dos recursos hídricos subterrâneos ainda são considerados incipientes, por se tratar de um recurso natural pouco compreendido e gerenciado, desvalorizado e mal protegido. A Recarga de Água Subterrânea (GWR) é um dos elementos mais desafiadores para estimar, pois raramente pode ser medido diretamente e não pode ser facilmente derivado dos dados existentes. Para superar essas limitações, muitos hidro(geo)logistas têm combinado diferentes abordagens para estimar a GWR em larga escala, a saber: produtos de sensoriamento remoto, como o produto IMERG; Equação do Balanço Hídrico, também em combinação com modelos hidrológicos no solo, e; Sistema de Informação Geográfica (GIS), com o uso de fórmulas de estimativa. Para as estimativas de GWR em escala intermediária, existem: Detecção Não-invasiva de Nêutrons de Raios Cósmicos (CRNS); redes sem fio a partir de sondas locais inseridos no solo; e modelos hidrológicos, como o HYDRUS. Neste contexto, a tese de doutorado visa, por um lado, demonstrar um acoplamento de modelo baseado em GIS para estimar a distribuição da GWR em larga escala em bacias tropicais úmidas. Por outro lado, visa utilizar as séries temporais de CRNS e de umidade do solo de sondas invasivas para calibrar inversamente as propriedades hidráulicas do solo, e com base nisso, estimar a GWR em escala intermediária usando um modelo hidrológico do solo. Para tanto, foram selecionadas duas bacias hidrográficas úmidas tropicais, localizadas em um aquífero sedimentar complexo na região costeira do Nordeste do Brasil. Estas são a Área de Estudo de Caso de João Pessoa e a Bacia Experimental do Guaraíra. Vários produtos de satélite foram usados na primeira área como entrada no modelo de balanço hídrico baseado em GIS para estimar os componentes do balanço hídrico e a GWR em 2016 e 2017. Além disso, as medições em escala pontual e os dados de CRNS foram usados na segunda área para determinar as propriedades hidráulicas do solo, e estimar GWR nos anos hidrológicos 2017-2018 e 2018-2019. Os valores resultantes de GWR em escala larga e intermediária foram então comparadas e validadas pelas estimativas obtidas pelas flutuações do lençol freático. As taxas de GWR para os cenários baseados no IMERG e em medidores de precipitação mostraram correlações semelhantes entre 68% e 89, erros médios semelhantes entre 30% e 34%, e viés ligeiramente diferentes entre -13% e 11%. Os resultados das taxas de GWR para os cenários de umidade do solo para sensores inseridos no solo e CRNS variaram de -5,87 a -61,81 cm ano<sup>-1</sup>, o que corresponde a 5% e 38% da precipitação. Os cálculos das taxas médias de GWR em grande escala, com base em dados de sensoriamento remoto, e em média escala, com base em dados de CRNS, apresentaram resultados semelhantes para o tipo de solo Espodossolo, a saber 17,87% e 17% da precipitação. Conclui-se então que as metodologias propostas permitiram estimar realisticamente a GWR nas áreas de estudo, o que pode ser um passo inovador no tocante ao aprimoramento do gerenciamento e tomada de decisão da água no Nordeste do Brasil.

**PALAVRAS-CHAVE:** Recarga de Águas Subterrâneas, Sensoriamento Remoto, Detecção de Nêutrons de Raios Cósmicos, Propriedades Hidráulicas do Solo, Nordeste do Brasil.



## ZUSAMMENFASSUNG

Studien über die nicht nachhaltige Nutzung von Grundwasserressourcen gelten nach wie vor als am Anfang, da es sich oft um eine schlecht verstandene und unkontrolliert genutzte, geringgeschätzte und unzureichend geschützte natürliche Ressource handelt. Die Grundwasserneubildung (GWR) ist eines der am schwierigsten abzuschätzenden Einflussgrößen, da sie selten direkt gemessen werden kann und nicht einfach aus vorhandenen Daten abzuleiten ist. Um diese Einschränkungen zu überwinden, haben viele Hydro(geo)logen verschiedene Ansätze kombiniert, um die GWR in großem Maßstab zu ermitteln, darunter sind: Fernerkundungsprodukte, wie das IMERG-Produkt; Wasserbilanz-Abschätzungen, auch in Kombination mit hydrologischen Modellen und; Geographische Informationssysteme (GIS) unter Nutzung von Abschätzungsformeln. Für die Ermittlung von GWR auf mittleren Flächenskalen existieren: Nicht-invasive Messung der Albedoneutronen an der Landoberfläche (CRNS); Drahtlosnetzwerke von lokalen Bodensonden, und bodenhydrologische Modelle, wie bspw. HYDRUS. In diesem Kontext zielt die Doktorarbeit zum einen darauf ab, eine GIS-basiert Modellkopplung zur Schätzung der GWR-Verteilung im großen Maßstab in tropisch-feuchte Einzugsgebiete aufzuzeigen. Zum anderen verwendet sie CRNS- und invasive Bodenfeuchtesonden-Zeitreihen zur inversen Kalibrierung der hydraulischen Bodeneigenschaften und darauf aufbauend zur Schätzung der GWR im mittleren Maßstab über ein bodenhydrologisches Modell. Zu diesem Zweck wurden zwei tropisch-feuchte Einzugsgebiete ausgewählt, die sich in einem komplexen Sedimentgrundwasserleiter der Küstenregion des Nordosten-Brasilien befinden. Dies sind das João Pessoa-Fallstudiengebiet und das Guaraíra-Flusseinzugsgebiet. Mehrere Satellitenprodukte wurden im ersten Gebiet als Eingangsdaten für das GIS-basierte Wasserbilanz-Modell zur Schätzung der Wasserhaushaltskomponenten und der GWR in den Jahren 2016 und 2017 verwendet. Daneben wurden im zweiten Gebiet die Punktmessungen- und CRNS-Daten verwendet, um über ein bodenhydrologisches HYDRUS-1D-Modell die hydraulischen Bodeneigenschaften zu ermitteln und die GWR in den hydrologischen Jahren 2017-2018 und 2018-2019 abzuschätzen. Die resultierenden GWR-Werte im großen und mittleren Maßstab wurden dann mit den gemessenen Schwankungen der Grundwasserstände verglichen und daran überprüft. Die GWR-Raten aus IMERG- und Niederschlagsmessern-basierten Szenarien zeigten ähnliche Korrelationen zwischen 68% und 89%, mittlere Fehler zwischen 30% und 34%, und leicht unterschiedliche Abweichungen zwischen -13% und 11%. Die berechneten GWR-Raten für Bodensonden- und CRNS-Bodenfeuchtwerte lagen im Bereich von 58,7 bis 618,1 mm im Jahr, was 5% bzw. 38% der Niederschlagsmengen entspricht. Die Berechnung der mittleren GWR-Raten auf großer Landschaftsskala, basierend auf Fernerkundungsdaten, und auf mittlerer Skala, basierend auf CRNS-Daten, ergaben für den Bodentyp Podsol ähnliche Ergebnisse, nämlich 17,87% bzw. 17% der Niederschläge. Daraus wurde der Schluss gezogen, dass die vorgeschlagenen Methoden eine realistische Schätzung der GWR in den Untersuchungsgebieten ermöglichen, was ein wegweisender Schritt zur Verbesserung des Wassermanagements und Nutzungsentscheidungen im Nordosten Brasiliens sein kann.

**SCHLÜSSELWÖRTER:** Grundwasserneubildung, Fernerkundungsprodukte, Neutronen aus kosmischer Höhenstrahlung, hydraulische Bodeneigenschaften, Nordostbrasilien.

## TABLE OF CONTENTS

<b>ACKNOWLEDGEMENTS</b> .....	<b>I</b>
<b>ABSTRACT</b> .....	<b>III</b>
<b>RESUMO</b> .....	<b>IV</b>
<b>ZUSAMMENFASSUNG</b> .....	<b>V</b>
<b>LIST OF TABLES</b> .....	<b>VIII</b>
<b>LIST OF FIGURES</b> .....	<b>IX</b>
<b>LIST OF SUPPLEMENTARY FIGURES</b> .....	<b>XV</b>
<b>LIST OF ABBREVIATIONS AND SYMBOLS</b> .....	<b>XVI</b>
<b>1 INTRODUCTION</b> .....	<b>1</b>
<b>2 LITERATURE REVIEW</b> .....	<b>5</b>
2.1 CONTEXTUALIZATION OF THE LOCAL HYDROGEOLOGICAL SCENARIO.....	5
2.2 REMOTE SENSING PRODUCTS FOR ESTIMATING THE WATER BALANCE COMPONENTS.....	8
2.2.1 <i>Fundamental concepts of the remote sensing</i> .....	8
2.2.2 <i>Global Precipitation Measurement mission and Integrated Multi-satellitE Retrievals for Global Precipitation Measurement algorithm</i> .....	11
2.2.3 <i>Moderate Resolution Imaging Spectroradiometer sensors and Global Evapotranspiration Project algorithm</i> .....	13
2.2.4 <i>Surface runoff by Natural Resources Conservation Service–Curve Number method</i> .....	16
2.2.5 <i>MapBiomass land use/cover project</i> .....	17
2.2.6 <i>Soil Moisture Active Passive mission</i> .....	19
2.2.7 <i>Global Land Data Assimilation Systems</i> .....	21
2.2.8 <i>Groundwater Recharge rate retrieved via water budget equation</i> .....	23
2.3 SOIL MOISTURE ASSIMILATION BASED ON COSMIC-RAY NEUTRON SENSING .....	25
2.3.1 <i>Theory of the Cosmic-Ray Neutron Sensing</i> .....	25
2.3.2 <i>Applications of the Cosmic-Ray Neutron Sensing</i> .....	30
2.4 VADOSE ZONE MODELLING .....	34
2.4.1 <i>Inverse modelling of the soil hydraulic properties via HYDRUS-1D model</i> .....	34
2.4.2 <i>Water flux modelling via HYDRUS-1D model</i> .....	36
2.5 UNCERTAINTY AND VALIDATION OF THE WATER BALANCE COMPONENTS .....	38
<b>3 HYPOTHESES AND AIMS</b> .....	<b>40</b>
3.1 MAIN HYPOTHESES.....	40
3.2 OVERARCHING AIM .....	40
3.3 SPECIFIC AIMS .....	40
<b>4 MATERIALS AND METHODS</b> .....	<b>41</b>
4.1 STUDY AREAS .....	41
4.2 SOURCES OF THE GROUND-BASED DATA.....	42
4.3 SATELLITE-BASED METHODS IMPLEMENTED IN A GEOGRAPHIC INFORMATION SYSTEM ENVIRONMENT .....	48
4.3.1 <i>Integrated Multi-satellite Retrievals for Global Precipitation Measurement and ground-based datasets</i> .....	49
4.3.1.1 <i>IMERG pixel resampling and bias correction</i> .....	50
4.3.1.2 <i>Rain gauge data correction and interpolation</i> .....	51
4.3.2 <i>Mu’s algorithm and Penman-Monteith equation for actual evapotranspiration estimation</i> .....	52
4.3.2.1 <i>Canopy conductance and vegetation cover fraction</i> .....	54

4.3.2.2	Net radiation and albedo .....	56
4.3.2.3	Plant transpiration and soil evaporation.....	58
4.3.3	<i>Surface runoff by Natural Resources Conservation Service–Curve Number method</i> .....	59
4.3.3.1	Hydrologic Soil Groups .....	62
4.3.3.2	Curve Number values and Antecedent Runoff Conditions.....	64
4.3.4	<i>Soil water storage changes from soil moisture imagery</i> .....	67
4.3.5	<i>GIS-based water budget equation</i> .....	68
4.4	VALIDATION OF THE GIS-BASED WATER BALANCE COMPONENTS .....	70
4.4.1	<i>Performance indexes for goodness-of-fit analysis</i> .....	70
4.4.2	<i>Verification of the daily actual evapotranspiration</i> .....	71
4.4.3	<i>Verification of the monthly surface runoff</i> .....	72
4.4.4	<i>Test of the satellite-based soil moisture</i> .....	74
4.4.5	<i>Validation of the annual Groundwater Recharge</i> .....	74
4.5	CALIBRATION OF THE COSMIC-RAY NEUTRON SENSING.....	76
4.5.1	<i>Soil sampling, footprints and weighting functions</i> .....	77
4.5.2	<i>Neutron intensity calibration and correction factors</i> .....	80
4.5.3	<i>Variably-saturated water flux modelling via HYDRUS-1D model</i> .....	82
4.5.3.1	Local environmental constraints for the groundwater flux modelling.....	82
4.5.3.2	Soil hydraulic property model .....	83
4.5.3.3	Neutron operator COSMIC and inverse modelling .....	84
4.5.3.4	Root water uptake model .....	86
4.5.3.5	Vegetation growth, interception and evapotranspiration partition.....	87
4.5.3.6	Boundary conditions .....	89
4.5.3.7	Water budget equation in HYDRUS-1D .....	90
4.6	VALIDATION OF THE HYDRUS-1D-COSMIC RESULTS.....	91
4.6.1	<i>Validation of the CRNS-based neutron intensity</i> .....	91
4.6.2	<i>Validation of the hydraulic conductivity</i> .....	92
4.6.3	<i>Validation of the simulated soil moisture profile</i> .....	93
4.6.4	<i>Validation of the daily Groundwater Recharge rate</i> .....	94
<b>5</b>	<b>RESULTS.....</b>	<b>95</b>
5.1	DISTRIBUTED GROUNDWATER RECHARGE ESTIMATED BY AN ENHANCED GIS-BASED WATER BALANCE MODEL .....	95
5.1.1	<i>Precipitation analysis</i> .....	95
5.1.2	<i>Evapotranspiration and soil water storage change analyses</i> .....	97
5.1.3	<i>Surface runoff analysis</i> .....	103
5.1.4	<i>Groundwater Recharge rate analysis</i> .....	107
5.2	INTERMEDIARY-SCALE GROUNDWATER RECHARGE MODELLING COUPLED TO SOIL HYDRAULIC PROPERTY INVERSE MODELLING.....	113
5.2.1	<i>Cosmic-Ray Neutron Sensing curve calibration</i> .....	113
5.2.2	<i>Modelling input data and parameters</i> .....	117
5.2.3	<i>Inverse modelling of the soil hydraulic properties</i> .....	120
5.2.4	<i>Soil moisture simulation and validation</i> .....	123
5.2.5	<i>Root Water Uptake and cumulative fluxes</i> .....	126
5.2.6	<i>Groundwater Recharge and cumulative water fluxes</i> .....	128
<b>6</b>	<b>DISCUSSION.....</b>	<b>133</b>
6.1	DISTRIBUTED GROUNDWATER RECHARGE ESTIMATED BY AN ENHANCED GIS-BASED WATER BALANCE MODEL .....	133
6.2	INTERMEDIARY-SCALE GROUNDWATER RECHARGE MODELLING COUPLED TO SOIL HYDRAULIC PROPERTY INVERSE MODELLING.....	137
<b>7</b>	<b>CONCLUSION AND OUTLOOK.....</b>	<b>140</b>
	<b>REFERENCES .....</b>	<b>142</b>
	<b>APPENDIXES .....</b>	<b>166</b>

## LIST OF TABLES

Table 1 – The hydrogen pools influencing the CRNS signal and its dynamics. Source: Andreasen et al. (2017b).....	31
Table 2 – Summary of measured data by monitoring station over JPA CSA and GEB. ....	47
Table 3 – Summary of remote sensing data by satellite products in 2016 and 2017. ....	48
Table 4 – Parameterization of stomatal opening and closing control in MOD16 algorithm. Tminopen: minimum air temperature of stomatal opening; Tminclose: minimum air temperature of stomatal closing; VPDclose: vapour pressure deficit of stomatal closing; VPDopen: vapour pressure deficit of stomatal opening; CL: mean potential stomatal conductance per unit leaf area. Source: based on Mu et al. (2007, 2011) and Running et al. (2017). EBF: Evergreen Broadleaved Forest.....	55
Table 5 – Hydrologic Soil Groups (HSG) defined for the NRCS–CN method. Source: NRCS (1986). ....	62
Table 6 – Classification of Hydrologic Soil Groups (HSG) for Brazilian soils. Source: Sartori (2010). ....	63
Table 7 – Runoff curve numbers for agricultural lands. CN: Curve Number; HSG: Hydrologic Soil Group; HSC: Hydrologic Surface Condition. Source: NRCS (2004). ....	65
Table 8 – List of the performance indexes used in the evaluation and comparison. S: satellite precipitation estimate; G: gauge observed precipitation; $\sigma_G$ : standard deviations of gauge precipitation; $\sigma_S$ : standard deviations of satellite precipitation; $\bar{\cdot}$ : mean of a dataset; $\Sigma$ : sum of a dataset. ....	71
Table 9 – Groundwater recharge obtained by WTF method in 2016 and 2017 over JPA CSA. id: index of measurement location; lon/lat: longitude/latitude at decimal degree in WGS84 datum; $S_y$ : soil specific yield; $\Delta H$ : potential groundwater level rise; P: precipitation averaged around 500 m from the well.....	109
Table 10 – Soil moisture and bulk density weighting-averaged after the gravimetric experiment at three soil sampling depths carried out on October 1st, 2018. $\rho_{bd}$ : bulk density; Id: index of measurement location; r: radial distance; $D_{86}$ : penetration depth; $W_f$ : horizontal weighs; $W_d$ : vertical weighs; $mean_w$ : weighted-mean; $mean_a$ : arithmetic-mean. ....	114
Table 11 – Genuchten-Mualem parameters calibrated at TDR and CRNS sites through inverse modelling from soil moisture datasets. *Considered air-entry of -2 cm (Ries et al., 2015; Šimůnek, 2018). $\theta_r$ : residual soil moisture content; $\theta_s$ : saturated soil moisture content; $\alpha$ : air-entry pressure factor; n: pore size distribution measure; $K_s$ : saturated hydraulic conductivity; l: pore tortuosity and connectivity parameter.....	122

## LIST OF FIGURES

Figure 1 – Representations of the (a) location of Paraíba-Pernambuco sedimentary basin, (b) typical geological mapping, (c) stratigraphic units in geologic time scale, and (d) tectono-sedimentary Quaternary cross-section. Sources: modified from Rossetti et al. (2011) and Andrades Filho (2014). .....	7
Figure 2 – Representation of the (a) Podzol and Acrisol soil types over Brazil, (b) typical soil profiles, and (c) main land uses. Available on: <a href="http://www.agencia.cnptia.embrapa.br">http://www.agencia.cnptia.embrapa.br</a> . .....	8
Figure 3 – Remote sensing conceptual diagram. Source: modified from Shaw and Burke (2003). .....	9
Figure 4 – Electromagnetic radiation spectrum. Source: Modified from <a href="https://www.mpoweruk.com/radio.htm">https://www.mpoweruk.com/radio.htm</a> , according to Scarinci and Marineli (2014)...	9
Figure 5 – Standard solar spectrum. Source: modified from ASTM (2003). .....	10
Figure 6 – Comparison among the generalized spectral signatures of some Earth surface materials. Source: modified from the file available on: <a href="http://www.rsac1.co.uk/images/base2.jpg">http://www.rsac1.co.uk/images/base2.jpg</a> . .....	11
Figure 7 – Half-hourly precipitation obtained by GPM IMERG satellite product on 0.1° spatial resolution over the Earth. Source: <a href="https://pmm.nasa.gov/">https://pmm.nasa.gov/</a> . .....	12
Figure 8 – Annual actual evapotranspiration obtained by MOD16 global evapotranspiration product on 250-m spatial resolution over the Earth. Source: adapted from Mu, Zhao and Running (2011). .....	15
Figure 9 – Annual mean surface runoff (1998-2016) simulated on 0.5° spatial resolution derived from TRMM data through the NRCS–CN method over the Earth. Source: adjusted from Hong et al. (2007). .....	16
Figure 10 – Annual land use/cover obtained by MapBiomas collection 3.1 on 30-m spatial resolution over Brazil. Source: <a href="http://plataforma.mapbiomas.org/map#coverage">http://plataforma.mapbiomas.org/map#coverage</a> . .....	18
Figure 11 – Root-zone soil moisture increments obtained by SMAP SPL4SMAU satellite mission from April 1st, 2015, to April 1st, 2018, on 9-km spatial resolution. Source: Reichle et al (2018). .....	20
Figure 12 – Three-hourly time averaging map obtained by GLDAS Noah 2.1 on 0.25° spatial resolution over the Earth, on May 1st, 2017 from 00:00 to 12:00, of (a) specific humidity, (b) downward shortwave radiation, (c) air temperature, and (d) air pressure. Source: averaged on <a href="https://giovanni.gsfc.nasa.gov/">https://giovanni.gsfc.nasa.gov/</a> . .....	22
Figure 13 – Long-term (1981-2014) annual groundwater recharge rates obtained by a multi-model inference approach on 0.5° spatial resolution over the Earth. Source: adapted from Mohan et al. (2018). .....	23
Figure 14 – Galactic cosmic rays acceleration process by (a) disturbed magnetic fields in dense shock regions of supernova remnants, depicted by the (b) cosmic-ray energy spectrum with typical energies of 1 GeV, indicating extra-galactic processes beyond the “knee” (or bend). Source: Cronin, Gaisser and Swordy (1997). .....	26
Figure 15 – Energy spectra of detected neutron counts at the soil surface coloured according to initial high-energy neutron deceleration after the atom collisions. Solid line: pure incoming component after subtracting the ground reflected component. Vertical coordinate: neutron counts; dashed line: simulation by Sato and Niita (2006); Grey bars: exemplary measurement by Goldhagen et al. (2002). Source: Köhli et al. (2015). ....	27
Figure 16 – Cascade of high-energy secondary neutron and production of fast neutrons in (a) air and (b) ground. Coordinates are in mass shielding units (distance multiplied by density). Source: adapted from Desilets, Zreda and Ferré (2010) and IAEA (2017)..	28

Figure 17 – Elastic neutron scattering cross sections for Hydrogen (red) and other chemical elements. H: Hydrogen; N: Nitrogen; O: Oxygen; C: Carbon; Al: Aluminum; Si: Silicon. Source: Köhli et al. (2015). .....	28
Figure 18 – Components of the CRNS probe, CRS 1000 model, Hydroinnova Ltd. <sup>3</sup> Helium is used as counter gas. NPM: Neutron Pulse Module. Source: adapted from Schrön et al. (2018). .....	29
Figure 19 – Simulation of (a) neutron intensity detected over distance from the CRNS probe, and of (b) radial weighting function, for dry and wet conditions. $\theta$ : soil moisture; h: absolute humidity; N: detected neutron; r: radial distance; $W_r$ : radial weighting function; $R_{63}/R_{86}$ : footprint radii for 63% and 86% cumulative neutron counts. Source: Köhli et al. (2015). .....	30
Figure 20 – Range of applications of CRNS probes and related activities in the <i>Cosmic Sense</i> research project. Source: <a href="https://www.uni-potsdam.de/de/cosmicsense/about/structure-of-cosmic-sense.html">https://www.uni-potsdam.de/de/cosmicsense/about/structure-of-cosmic-sense.html</a> .....	32
Figure 21 – Illustration of (a) equally-detected neutron contribution regions for different climates, and (b) comparative triple-quantile-radii soil sampling schemes based on COSMOS scheme (yellow) and on the revised weighting function for dry and wet condition. COSMOS: COsmic-ray Soil Moisture Observing System. Source: Schrön et al. (2018). .....	33
Figure 22 – CRNS probes operated within the COSMOS network initiative (blue dots), with the cutoff rigidity and the attenuation length isolines in 2010 for incoming primary cosmic rays in red. Northern Brazil has a cut off rigidity similar to China, Northern Australia or Southern Africa, though being close to the equator. Source: Andreasen et al. (2017a). .....	33
Figure 23 – Three main physical processes as considered in the COSMIC model for simulating the aboveground fast neutron intensity. Source: Shuttleworth et al. (2013). .....	36
Figure 24 – Soil discretization available for (a) an one-dimensional domain in HYDRUS-1D, as well as for (b) two-dimensional and (c) three-dimensional domains in HYDRUS (2D/3D). Source: Šimůnek, van Genuchten and Šejna (2016). .....	37
Figure 25 – Location of the (a) Northeast of Brazil, (b) Paraíba state, (c) João Pessoa Case Study Area (JPA CSA), and (d) Guaraira Experimental Basin (GEB) with hydrogeological monitoring network, displaying photos of the (e, f, g, h, i) monitoring sites (1, 2, 3, 4, 5), respectively. ....	41
Figure 26 – Automatically-monitored rain gauges, type tipping bucket on (a) 0.254-mm and (b) 0.2-mm resolutions, as well as type (c) wireless rain gauge, in operation in JPA CSA. ....	43
Figure 27 – The (d) meteorological station in GEB monitoring the air pressure, (a) wind speed, (b) up-/downward longwaves and shortwaves, (c) soil temperature and heat flux, (e) rainfall, (f) air temperature and relative humidity, (g) soil moisture, and (h) groundwater level and temperature. ....	44
Figure 28 – Process of (a) installation, (b) connection and (c) data download of CRNS probe in GEB. ....	45
Figure 29 – Installation of PR2/6 probes in GEB. PR2/6: six-levelled soil moisture profile probe; DL6: data logger for six soil moisture sensors. ....	45
Figure 30 – Automatically-monitored (a) Amazonas and (b) tubular wells in operation in JPA CSA. Ampeq: water depth diver by Ampeq company; CTD: diver of conductivity, temperature and depth. ....	46
Figure 31 – Measurements of (a) bathymetry and (b) discharge in stream gauges of GEB for runoff estimation. Source: (Barbosa, 2015). .....	48

Figure 32 – Flowchart of the logic behind the application of hydro(geo)logical and meteorological methods for estimating the water balance components. LAI: Leaf Area Index; EVI: Enhanced Vegetation Index. ....	49
Figure 33 – Flowchart describing the procedures for the IMERG pixel resampling and bias correction, and rain gauge (or simply Gauge) data correction and interpolation. ....	50
Figure 34 – Flowchart of the logic behind the MOD16 global evapotranspiration algorithm for calculating daily actual evapotranspiration. LAI: Leaf Area Index; EVI: Enhanced Vegetation Index. Source: modified from Mu et al (2007). ....	54
Figure 35 – Flowchart of the logic behind the NRCS–CN method algorithm for calculating the daily surface runoff. ARC-I, ARC-II and ARC-III: dry, average and wet Antecedent Runoff Condition. ....	61
Figure 36 – Conceptual model of water budget equation by remote sensing in João Pessoa Case Study Area (JPA CSA); P: Precipitation; E: Actual Evapotranspiration; Q: Surface Runoff; $\Delta S$ : Soil Water Storage changes; R: Groundwater Recharge; Blue arrows: disregarded water balance components. ....	68
Figure 37 – Two soil water balance scenarios, (a) precipitation higher than zero, and (b) precipitation equal to zero, for reasoning about the water budget equation through the root-zone Control Volume (CV). $h_{cv}$ : Height of CV equal to 1 m; CS: Control Surface; P: Precipitation; E: Actual Evapotranspiration; Q: Surface Runoff; $\Delta S$ : Soil Water Storage changes; R: Groundwater Recharge; C: Capillarity Rise; ....	70
Figure 38 – An illustration of the baseflow separation through the straight-line method, where the dashed line connects the onset and ending point of the runoff. Source: adapted from Boscha et al. (2017). ....	73
Figure 39 – Total groundwater rise ( $\Delta H$ ) obtained by summing the actual groundwater rise ( $\Delta h_{peak}$ ) and potential groundwater decline ( $\Delta h_{rec}$ ) for averaging on groundwater recharge rates in unconfined aquifers through the WTF method. Source: modified from Jie et al. (2011). ....	75
Figure 40 – Flowchart describing the stepwise procedures of data simulation and validation for estimating the percolation water fluxes and groundwater recharge through the HYDRUS-1D-COSMIC model. ....	76
Figure 41 – Soil core sampling scheme for CRNS probe calibration through the gravimetric method. ....	77
Figure 42 – Flowchart describing the procedure for site-specific CRNS calibration based on soil core samples, organic matter and lattice water equivalents and accounting for standard neutron intensity corrections. $N_0$ : dry neutron intensity parameter in CRNS calibration equation. ....	78
Figure 43 – Fast neutron source volume element yielded in z-depth soil plane reaching the measurement point P, which is attenuated by an exponential factor with length constants $L_3$ and $L_4$ . Source: Shuttleworth et al. (2013). ....	85
Figure 44 – Two fixed-interval methods based on the WTF method for groundwater recharge estimation, namely: (a) RISE method, and; Master Recession Curve (MRC) method. Source: Nimmo, Horowitz and Mitchell (2015). ....	94
Figure 45 – Bias correction by the linear-scaling method based on monthly mean correction factors applied on IMERG V05B daily precipitation data for correcting the (e) monthly and annual precipitation in (a, c) 2016 and (b, d) 2017 over JPA CSA. ....	96
Figure 46 – Annual distributed precipitation obtained by (a, d) Inverse Distance Weighting (IDW) interpolation through the rain gauge network, and by (b, e) bilinear interpolation and bias correction through IMERG imagery, as well as (c, f) monthly percentile (10%, 25%, 50%, 75%, 90%) variability in 2016 and 2017. Points: mean. ....	97

Figure 47 – Meteorological variables obtained by GLDAS-2.1 Noah L4 reanalysis data in 2016 and 2017: (a) relative humidity, (b) incoming short-wave radiation, (c) air temperature, and (d) barometric air pressure. Solid line: mean; Dashed line: mean $\pm$ standard deviation.....	98
Figure 48 – Land use/cover classification by MapBiomas collection 3.1 over JPA CSA in (a) 2016 and (b) 2017. ....	99
Figure 49 – Annual distributed (a, b) actual evapotranspiration ( $E_t$ ) obtained by adapted MODIS algorithm (Gusmão, 2017; Mu et al., 2007; Mu, Zhao and Running, 2011; Teixeira et al., 2014, 2013) from MapBiomas land use/cover with map composition for cloud cleaning, and (d, e) soil water storage changes ( $\Delta S$ ) in 1-m root zone obtained by bilinear interpolation, as well as (c, f) monthly percentile (10%, 25%, 50%, 75%, 90%) variability in 2016 and 2017. Points: mean. ....	100
Figure 50 – Verification of daily actual evapotranspiration simulated by adapted MOD16 algorithm (Gusmão, 2017; Mu et al., 2007; Mu, Zhao and Running, 2011; Teixeira et al., 2014, 2013) averaged on 500-m footprint of A320 INMET meteorological station, against the ground-based reference evapotranspiration calculated by Penman-Monteith equation (Allen et al., 1998). ....	101
Figure 51 – Comparison between the daily mean actual evapotranspiration over the JPA CSA simulated by the adapted MOD16 algorithm (Gusmão, 2017; Mu et al., 2007; Mu, Zhao and Running, 2011; Teixeira et al., 2014, 2013) with the ground-based reference evapotranspiration calculated by Penman-Monteith equation from A320 INMET meteorological station data (Allen et al., 1998).....	102
Figure 52 – General soil moisture calibration curve of the TDR probes installed in GEB. Source: data from de Lira (2015). ....	102
Figure 53 – Comparison between the soil moisture time series assimilated by SMAP mission and ground-based measurements. Shaded interval: mean $\pm$ standard deviation.....	103
Figure 54 – Soil types and Hydrological Soil Groups (HSG) of JPA CSA. WRB: World Reference Base for soil resources.....	104
Figure 55 – Distributed Curve Number (CN) estimation under the moderately-wet Antecedent Runoff Condition (ARC) in 2016 and 2017 over JPA CSA. ....	105
Figure 56 – Annual distributed surface runoff obtained by Natural Resources Conservation Service – Curve Number (NCRS-CN) method from soil type mapping, MapBiomas land use/cover, and (a, c) ground-based precipitation and (b, d) satellite-based IMERG imagery, as well as (e, f) monthly percentile (10%, 25%, 50%, 75%, 90%) variability. Points: mean. ....	106
Figure 57 – Verification of the surface runoff in 2017 by comparing the daily water level positive differences of (a) the runoff estimates obtained by baseflow separation method at stream gauge 503 (b), to the daily mean surface runoff estimates obtained by NRCS–CN method from Gauge-based and IMERG*-based precipitation data, averaged on the gauge 503 catchment. ....	107
Figure 58 – Potential groundwater level rise ( $\Delta H$ ) obtained in 2016 and 2017 at 23 manually-monitored wells spread over JPA CSA. W: Well identification. ....	108
Figure 59 – Annual distributed Groundwater Recharge (R) obtained by water budget equation and WTF method, using (a, b) ground-based, interpolated precipitation and (c, d) bias-corrected IMERG imagery, as well as (e, f) monthly percentile (10%, 25%, 50%, 75%, 90%) variability. Coloured circles: WTF-based recharge; Points: mean. ....	110
Figure 60 – Validation of annual groundwater recharge rates at (a, b, e) absolute and (c, d, f) relative scales, for ground-based and remotely-sensed precipitation through WTF method, respectively.....	111



Figure 61 – Relative groundwater recharge rates averaged on JPA CSA in 2016 and 2017 by (a, b, e) land use/cover and (b, d, f) soil type, for Gauge and IMERG* scenarios. Mean plot: mean $\pm$ standard deviation.....	112
Figure 62 – Distribution of the (a) mean vertically-weighted soil moisture for the (b) CRNS probe calibration through the gravimetric experiment carried out on October 1st, 2018. ....	114
Figure 63 – Soil moisture profiles monitored by the three PR2/6 soil profile probes from July 18th, 2018 to June 06th, 2019. ....	115
Figure 64 – Data analysis and experiment results about (a) energy spectra of detected neutron counts and (b) soil organic and lattice water equivalent, for the parametrization of the (c) CRNS calibration curve and (d) COSMIC neutron operator. ....	116
Figure 65 – Soil moisture time series based on (a) 1-h CRNS dataset smoothed by 24-h moving average (b) compared to 10-cm PR2 dataset. P: rainfall; $E_{t_0}$ : reference evapotranspiration; GWL: Groundwater Level. ....	117
Figure 66 – Data analysis and experiment results of the initial model conditions about (a) soil moisture, (b) normalized water uptake distribution, (c) soil particle distribution curves, and (d) soil textures along the soil profile. $b(x)$ : normalized water uptake. .	118
Figure 67 – Time series of the (a) monthly Leaf Area Index (LAI) obtained by geoprocessing the MODIS reflectance imagery over GEB, and the (b) daily potential evaporation ( $E_p$ ) and transpiration ( $T_p$ ) estimated by Penman-Monteith equation. ....	119
Figure 68 – Soil moisture time series based on 1-h TDR dataset at depth of -5, -20 and -40 cm. $E_{t_0}$ : reference evapotranspiration; GWL: Groundwater Level. ....	120
Figure 69 – Neutron intensity simulated by (a) COSMIC neutron operator, after the calibration by using the (b) CRNS dataset through the HYDRUS-1D model. ....	121
Figure 70 – Soil hydraulic properties obtained through inverse modelling from TDR and CRNS datasets, namely (a) retention curves, and (b) hydraulic conductivity curves, compared to Silva (2009) results over GEB. $h$ : soil matric potential; $K$ : hydraulic conductivity. ....	122
Figure 71 – Slug tests carried out to determine the (a) adjusted water level time series for estimating the (b) hydraulic conductivity over GEB. GEB: Guaraira experimental basin. Dashed line in (a): static water level; Solid line: mean; Dashed line in (b): mean $\pm$ standard deviation. ....	123
Figure 72 – Soil moisture time series simulated by HYDRUS-1D using the soil hydraulic properties curves plotted against the TDR datasets at the depths of (a, b) -5 cm, (c, d) -20 cm, and (e, f) -40 cm. ....	124
Figure 73 – Soil moisture time series simulated by HYDRUS-1D, by using the soil hydraulic properties curves obtained by CRNS data, plotted against the PR2 profile probe data at the depths of (a, b) -2 cm, (c, d) -15 cm, (e, f) -25 cm, (g, h) -35 cm, (i, j) -55 cm, and (k, l) -95 cm. *Calculated at -2 cm due to air-entry of -2 cm and soil organic matter. ....	126
Figure 74 – Two salinity events over GEB occurred in (a) 2018 and (b) 2019, according to DPIRD (2019). P: rainfall; T; water temperature; GWL: Groundwater Level; EC: Electrical Conductivity. ....	127
Figure 75 – Time series of (a) root zone pressure head and (b) actual root water uptake ( $RWU_a$ ), at TDR and CRNS sites. P: rainfall. ....	128
Figure 76 – Cumulative outward (positive) and inward (negative) water fluxes at (a) CRNS and (b) TDR sites in 2017-2018 and 2018-2019 hydrological years. P: rainfall; $T_p$ : potential transpiration; $RWU_p$ : Potential Root Water Uptake; $RWU_a$ : Actual Root Water Uptake; $E_p$ : potential evaporation; $E_a$ : actual evaporation; $S_p$ : potential surface flux; $S_a$ : actual surface flux; Inf: infiltration. ....	129

Figure 77 – Cumulative groundwater recharge (R) and percolation water flux and at -20, -30, -40, -60 and -100 cm soil depths at (a) CRNS and (b) TDR sites in 2017-2018 and 2018-2019 hydrological years. P: Rainfall..... 130

Figure 78 – Master Recession Curves (MRC) obtained by linear regression equation along the longer available groundwater recession period at (a) CRNS and (b) TDR sites.  $\Delta h_{rec}$ : potential groundwater decline;  $\Delta t$ : daily time interval; C: constant relative to the time of recharge event occurrence..... 131

Figure 79 – Validation of groundwater recharge rates simulated by HYDRUS-1D through the comparison between the cumulative negative water fluxes obtained by WTF method, for specific yield ( $S_y$ ) equal to 0.10, 0.16 and 0.24, at (a, b) CRNS and (c, d) TDR sites in 2017-2018 and 2018-2019 years, respectively..... 132

## LIST OF SUPPLEMENTARY FIGURES

Supplementary Figure 1 – Monthly distributed precipitation obtained by Inverse Distance Weighting interpolation through the rain gauge network in 2016.....	166
Supplementary Figure 2 – Monthly distributed precipitation obtained by bilinear interpolation and bias correction through IMERG imagery in 2016.....	166
Supplementary Figure 3 – Monthly distributed precipitation obtained by Inverse Distance Weighting interpolation through the rain gauge network in 2017.....	167
Supplementary Figure 4 – Monthly distributed precipitation obtained by bilinear interpolation and bias correction through IMERG imagery in 2017.....	167
Supplementary Figure 5 – Monthly distributed evapotranspiration obtained by MODIS algorithm from MapBiomas land use/cover with cloud cleaning map composition in 2016.....	168
Supplementary Figure 6 – Monthly distributed evapotranspiration obtained by MODIS algorithm from MapBiomas land use/cover with cloud cleaning map composition in 2017.....	168
Supplementary Figure 7 – Monthly distributed soil water storage changes in 1-m root zone obtained by bilinear interpolation in 2016.....	169
Supplementary Figure 8 – Monthly distributed soil water storage changes in 1-m root zone obtained by bilinear interpolation in 2017.....	169
Supplementary Figure 9 – Monthly distributed surface runoff obtained by NCRS-CN method from ground-based, interpolated precipitation in 2016.....	170
Supplementary Figure 10 – Monthly distributed surface runoff obtained by NCRS-CN method from bias-corrected IMERG imagery in 2016.....	170
Supplementary Figure 11 – Monthly distributed surface runoff obtained by NCRS-CN method from ground-based, interpolated precipitation in 2017.....	171
Supplementary Figure 12 – Monthly distributed surface runoff obtained by NCRS-CN method from bias-corrected IMERG imagery in 2017.....	171
Supplementary Figure 13 – Monthly distributed groundwater recharge rates obtained by water budget equation from ground-based, interpolated precipitation in 2016.....	172
Supplementary Figure 14 – Monthly distributed groundwater recharge rates obtained by water budget equation from bias-corrected IMERG imagery in 2016.....	172
Supplementary Figure 15 – Monthly distributed groundwater recharge rates obtained by water budget equation from ground-based, interpolated precipitation in 2017.....	173
Supplementary Figure 16 – Monthly distributed groundwater recharge rates obtained by water budget equation from bias-corrected IMERG imagery in 2017.....	173
Supplementary Figure 17 – Annual distributed relative groundwater recharge rates obtained by water budget equation and WTF method, using ground-based, interpolated precipitation in (a) 2016 and (c) 2017, and using the bias-corrected IMERG imagery in (b) 2016 and (d) 2017.....	174
Supplementary Figure 18 – Delimitation of the 503 stream gauge catchment within the Guaraíra Experimental Basin (GEB).....	174
Supplementary Figure 19 – Time series of the weather variables used for hydrogeological modelling in HYDRUS-1D, namely (a) daily mean global (Rs) and net radiation (Rn), and (b) relative humidity (RH), air temperature (T) and wind speed (U2). .....	175

## LIST OF ABBREVIATIONS AND SYMBOLS

$\langle \rangle$	– Mean of a dataset
$\int$	– Integral sign
$\infty$	– Infinite sign
1D	– One-dimensional
2D	– Two-dimensional
3D	– Three-dimensional
$\alpha$	– Surface albedo   Bulk-density-dependent parameter of COSMIC operator   Factor inversely related to air entry pressure in HYDRUS-1D
$\beta$	– Angle between the flow direction and the vertical axis in HYDRUS-1D
$\delta$	– Solar declination angle
$\gamma$	– Psychrometric constant
$\varepsilon$	– Ratio molecular weight between water vapour ( $M_w$ ) and dry air ( $M_a$ )
$\varepsilon_a$	– Atmospheric emissivity
$\varepsilon_s$	– Surface emissivity
$\theta$	– Soil moisture
$\theta'$	– Soil moisture from the PR2/6 recalibration curve
$\theta_i   \theta_{i+1}$	– Soil moisture at the corner nodes of the soil discretisation elements   Soil moisture in water budget equation at the current and next day (same as $S_i   S_{i+1}$ )
$\theta_{ij}$	– Soil moisture by gravimetric method at each point 'i' and depth 'j'
$\theta_k$	– Weighted average soil moisture
$\theta_{\text{mineral}}$	– Soil moisture from the PR2/6 generalised polynomial mineral soil curve
$\theta_r$	– Residual soil moisture content
$\theta_s$	– Saturated soil moisture content
$\theta(z)$	– Soil moisture profile along the vertical coordinate
$\lambda$	– Latent heat flux density of vaporisation   Initial abstraction ratio
$\lambda E$	– Latent heat flux from the surface
$\lambda E_{\text{soil}}$	– Soil evaporation in MOD16 algorithm
$\lambda E_{\text{transp}}$	– Plant transpiration in MOD16 algorithm
$\lambda E_{\text{soilpot}}$	– Potential soil evaporation in MOD16 algorithm
$\pi$	– Natural constant equal to $\sim 3.1415$
$\rho$	– Air density
$\rho_{\text{bd}}$	– Soil bulk density
$\rho_s(z)$	– Local bulk density of dry soil per unit area at depth 'z'
$\rho_w(z)$	– Total soil water density including lattice water per unit area at depth 'z'
$\sigma$	– Constant of Stefan-Boltzmann
$\sigma_\theta$	– CRNS-based soil moisture error propagation
$\sigma_G$	– Standard deviations of gauge precipitation
$\sigma_S$	– Standard deviations of satellite precipitation

$\tau_{sw24}$	– Average daily atmospheric transmissivity
$\varphi$	– Latitude of the reference point of the meteorological station
$\omega_s$	– Hourly angle of sunrise
$\Delta$	– Median of matched-pairs differences   Slope vapour pressure curve
$\Delta e$	– Measurements of vapour pressure difference
$\Delta h_{peak}$	– Actual groundwater rise
$\Delta h_{rec}$	– Potential groundwater decline
$\Delta t$	– Time interval
$\Delta x_i$	– Size of the element between nodes
$\Delta H$	– Potential groundwater table rise
$\Delta T$	– Measurements of the temperature difference
$\Delta S$	– Soil water storage changes
$\Sigma$	– Sum of a dataset
$\Phi(q)$	– Least-squares objective function to optimize a set of SHP parameters (q)
a	– Regression coefficient between longwave incoming radiation and $\tau_{sw24}$   Parameter of CN empirical equation
$a_0'$	– Slope parameter of the PR2/6 recalibration curve
$a_1'$	– Offset parameters of the PR2/6 recalibration curve
A	– April   August   Available energy in Penman-Monteith equation
$A_{soil}$	– Total net incoming radiation (A or $R_n$ ) partitioned to the soil
$A_c$	– Total net incoming radiation (A or $R_n$ ) partitioned to the canopy and soil
Ampeq	– Water depth diver datalogger by Ampeq company
AnnAGNPS	– Distributed parameter, physically based, continuous simulation model
Al	– Aluminium
AESA	– Executive Agency for Water Management of the Paraíba state
AGRMET	– Air Force Weather Agency's AGRicultural METeorology
ARC	– Antecedent Runoff Condition
ARC-I	– Dry Antecedent Runoff Condition
ARC-II	– Moderate Antecedent Runoff Condition
ARC-III	– Wet Antecedent Runoff Condition
APAC	– Pernambuco State Water and Climate Agency
AQTESOLV	– AQuifer TEst SOLVer
ASF	– Alaska Satellite Facility
b	– Parameter of Curve Number (CN) empirical equation
$b(x)$	– Normalized water uptake distribution
BEER	– Experimental and Representative Basins of Semiarid Hydrology
BRAMAR	– BRAZilian Managed Aquifer Recharge
cph	– Neutron Count Per Hour (counts $h^{-1}$ )
C	– Carbon   Capillarity rise
$C_j$	– Vector line with 'm' (columns) total number of rain gauges

$C_p$	– Specific heat capacity of air in constant pressure
Ca	– Calcium
$C_c$	– Stomatal conductance at canopy surface level
$C_L$	– Mean potential stomatal conductance per leaf unit area
$C_s$	– Stomatal conductance at leaf level
$C(q)$	– Parameter covariance matrix
$C(q_{ij}^*)$	– Parameter covariance matrix of the $q^*$ diagonal elements
CC	– Correlation Coefficient
CEH	– Centre for Ecology and Hydrology
CLM	– Common Land Model
CMA-ES	– Global optimizer Covariance Matrix Adaptation-Evolution Strategy
CMB	– Chloride Mass Balance
CMRSET	– CSIRO MODIS Reflectance-based Scaling EvapoTranspiration
CN	– Curve Number
$CN_I$	– Curve Number at dry condition
$CN_{II}$	– Curve Number at moderate condition
$CN_{III}$	– Curve Number at wet condition
CAPES	– Brazilian Coordination for Improvement of Higher Education Personnel
CNPq	– Brazilian National Council for Scientific and Technological Development
$CO_2$	– Carbon dioxide molecule
COSMIC	– COsmic-ray Soil Moisture Interaction Code
COSMOS	– Cosmic-ray Soil Moisture Observing System
CR	– Pasture/Crop Residue cover
CRNS	– Cosmic-Ray Neutron Sensing
CS	– Control Surface
CS616	– Water content reflectometer model of Campbell Scientific company
CSA	– Case Study Area
CSIRO	– Commonwealth Scientific and Industrial Research Organisation
CT	– Center of Technology
CTD	– Diver datalogger of Conductivity, Temperature and Depth
CV	– Coefficient of Variation   Control Volume
d	– Soil sampling depth
$d_{k,x}^p$	– Geodesic distance from point ‘x’ to station ‘k’, for ‘p’ power parameter
$d_r$	– Square relative distance between the Earth and Sun   Distance at ‘r’ radius in the $R_{86}$ weighting function
$d_s$	– Sequential day of the year
$d\phi$	– Angle of soil volume element in the horizontal plane
$d\theta$	– Angle of soil volume element in the vertical plane
dz	– Thickness of soil volume element
D	– December

$D_{86}$	– Penetration depth at which 86% of the neutrons are detected by CRNS
Dr	– Doctorate title in Brazil
DAAC	– Distributed Active Archive Center for biogeochemical dynamics
DAAD	– German Academic Exchange Service
DEM	– Digital Elevation Model
DFG	– German Science Foundation
DL6	– Data Logger for 6 soil moisture sensors of Delta-T
DOY	– Days Of Year
DPR	– Dual-frequency Precipitation Radar
DS	– Dormant Season
DTI-B	– Scholarship of Technological and Industrial Development, category B
$e_a$	– Actual water vapour pressure
$e_s$	– Saturated water vapour pressure
E	– Maximum potential rate of infiltration or evapotranspiration
$E   E_i$	– Actual evapotranspiration
$E_a$	– Actual evaporation
$E_p$	– Potential evaporation
$E_t_r$	– Actual evapotranspiration
$E_t_o$	– Reference evapotranspiration
$E_t_p$	– Potential evapotranspiration
EASE	– Equal-Area Scalable Earth grid
EBF	– Evergreen Broadleaf Forest
EC	– Electrical Conductivity
EU-HYDI	– EUropean HYdropedological Data Inventory
EVI	– Enhanced Vegetation Index
EVI2	– Enhanced Vegetation Index (without blue band)
$EVI2_{max}$	– EVI signal from dense green vegetation
$EVI2_{min}$	– EVI signal from bare soil
$f_m$	– Incoming cosmic radiation correction factor
$f_p$	– Air pressure correction factor
$f_v$	– Water vapour correction factor
F	– February
$F_i$	– Parameters ( $F_1, \dots, F_8$ ) of $W_r$ weighting function dependent on $\theta_{ij}$ and $h_a$
$F_C$	– Surface Cover Fraction (same as SCF)
Fe	– Iron
FeO:	– Iron (II) oxide
FAO	– Food and Agriculture Organization of the United Nations
FAPESQ-PB	– Paraíba State Research Foundation
FAS	– USDA Foreign Agricultural Services
FINEP	– Brazilian Innovation Agency

FOR	– German research unit
g	– Gravitational acceleration
G	– Soil heat flux   Gauge observed precipitation
$G_s$	– Solar constant
Gauge	– Ground-based precipitation data source
GDAS	– Global Data Assimilation System
GEB	– Guaraíra Experimental Basin
GIS	– Geographic Information System
GLDAS	– Global Land Data Assimilation Systems
GMAO	– Global Modelling and Assimilation Office
GMI	– Global Precipitation Measurement Microwave Imager
GPCP	– Global Precipitation Climatology Project
GPM	– Global Precipitation Measurement
GRACE	– Gravity Recovery And Climate Experiment
GS	– Growing Season
GSFC	– Goddard Space Flight Center
GWC	– Gravimetric Water Content
GWL	– Groundwater Level
GWR	– Groundwater Recharge (same as R)
$h_0$	– Absolute air humidity in an arbitrary baseline reference time   Dynamic water level in the well at time 0
$h_{50}$	– Soil water potential whose root water extraction rate is reduced by 50%
$h_a$   $h$	– Absolute/specific humidity   Pressure head or soil matric potential
$h_r$	– Mean relative humidity
$h_{r,max}$	– Maximum relative humidity
$h_{r,min}$	– Minimum relative humidity
$h_t$	– Dynamic water level in the well at time t
$h_A$	– Minimum permitted pressure head
$h_{CV}$	– Height of CV (from soil surface down to the bottom of the root zone)
$h_s$	– Maximum thickness of the surface water layer
H	– Sensible heat flux from the surface   Hydrogen
$H_0$	– Null hypothesis
$H_1$	– Alternative hypothesis
$H_2O$	– Water molecule
$H_a$	– Altitude
$H_{veg}$	– Vegetation height
He	– Helium
HSG	– Hydrological Soil Group
HSC	– Hydrologic Surface Condition
HYBRAS	– HYdrophysical database for BRAzilian Soils



HRSL	–	USDA Hydrology and Remote Sensing Laboratory
HYDRUS	–	Software for simulating water flow and solute transport
HYPRES	–	HYdraulic PRoperties of European Soils
HYSOGs250m	–	Globally-gridded HSG dataset
i	–	Interception constant
I	–	Interception depth
I <sub>a</sub>	–	Initial abstraction
Id	–	Index of measurement location
Inf	–	Infiltration
IAEA	–	International Atomic Energy Agency
IBESA	–	Implementation of Semiarid Experimental Basins
IDW	–	Inverse Distance Weighting interpolation method
IESG	–	Institute of Environmental Science and Geography
IMERG	–	Integrated Multi-satellitE Retrievals for Global Precipitation Measurement (GPM)
IMERG*	–	IMERG data corrected by Linear Scaling (LS) bias correction
INMET	–	Brazilian National Institute of Meteorology
INPE	–	Brazilian National Institute for Space Research
IUSS	–	International Union of Soil Sciences
J	–	January   June   July
JAXA	–	Japanese Aerospace Agency
JPA	–	João Pessoa
JPL	–	Jet Propulsion Laboratory
k	–	Light extinction coefficient
K	–	Hydraulic conductivity   Potassium
K <sub>s</sub>	–	Saturated hydraulic conductivity
KGE	–	Kling-Gupta Efficiency coefficient
KJV	–	King James Version
l	–	Lumped parameter that accounts for soil pore tortuosity and connectivity
lat	–	Latitude at decimal degree in WGS84 datum
lon	–	Latitude at decimal degree in WGS84 datum
L	–	Adjust factor of SAVI calculation   Mass attenuation length for high-energy neutrons   Length of soil profile discretization
L <sup>0</sup>	–	Mean precipitation of ‘m’ (columns) total number of rain gauges
L <sub>1</sub>   L <sub>2</sub>   L <sub>4</sub>	–	Site-independent, time-constant parameters of COSMIC operator
L <sub>3</sub>	–	Bulk-density-dependent, time-constant parameter of COSMIC operator
L <sub>i</sub>	–	Column vector or regional vector with ‘n’ (lines) total number of years
L <sub>c</sub>	–	Filter section length of the well
L <sub>r</sub>	–	Root zone total depth
L <sub>w</sub>	–	Saturated thickness of the well
L4	–	Level 4 of SMAP satellite product   Level 4 of GLDAS Noah product

LAI	– Leaf Area Index
LARHENA	– Laboratory of Water Resources and Environmental Engineering
LIS	– Land Information System
LSM	– Land Surface Models
LW	– Lattice Water equivalent
$m_{105}$	– Soil mass weighting after the drying at 105°C
$m_{400}$	– Soil mass weighting of 10-g dry soil sample after the burning at 400°C
$m_{1000}$	– Soil mass weighting of 10-g dry soil sample after the burning at 1000°C
$m_s(z)$	– Integrated mass of dry soil per unit area at depth ‘z’
$m_w(z)$	– Integrated mass of water per unit area at depth ‘z’
$m(T_{\min})$	– Potential stomatal conductance for minimum air temperatures
$m(\text{VPD})$	– Potential stomatal conductance for Vapour Pressure Deficits
$\text{mean}_a$	– Arithmetic-mean
$\text{mean}_w$	– Weighted-mean
M	– March   May   Molecular weight of water
M.Sc.	– Master of Science
$M_0$	– Neutron intensity in an arbitrary baseline reference time
$M_a$	– Molecular weight of dry air
$M_i$	– Incoming monitored neutron intensity at the time step of measurement
$M_w$	– Molecular weight of water vapour
MapBiomass	– Research project in Brazilian land use/cover on high spatial resolution
MA	– Brazilian Ministry of Agriculture
MABC	– Ministry of Agriculture of British Columbia
MCD43A2/A3	– MODIS surface albedo product
MODFLOW	– Modular three-dimensional finite-difference groundwater flow model
MOD16	– MODIS Global Evapotranspiration Project
MOD09Q1	– MODIS reflectance product on-board Terra satellite
MODIS	– MOderate-Resolution Imaging Spectroradiometer
MRC	– Master Recession Curve
MYD09Q1	– MODIS reflectance product on-board Aqua satellite
n	– Measure of pore size distribution
N	– November   Nitrogen   CRNS-measured neutron intensity
$N^?$	– Corrected neutron intensity
$N_0$	– Dry neutron intensity
$N_c$	– High-energy neutrons at the soil surface
$N_{\text{COSMIC}}$	– Aboveground neutron intensity simulated by COSMIC operator
NASA	– National Aeronautics and Space Administration of USA
NCEP	– National Centers for Environmental Prediction
NPM	– Neutron Pulse Module
NOAA	– National Oceanic and Atmospheric Administration

NRCS	– Natural Resources Conservation Service
NSIDC	– National Snow and Ice Data Center
O	– October   Oxygen
O <sub>2</sub>	– Oxygen molecule
O <sub>3</sub>	– Ozone molecule
p	– Probability value   Empirical coefficient (=2 to IDW; =3 to RWU)
P	– Precipitation   rainfall
P <sub>0</sub>	– Arbitrary baseline reference pressure
P <sub>5d</sub>	– 5-days-antecedent cumulative precipitation
P <sub>atm</sub>	– Mean barometric air (atmospheric) pressure
P <sub>d<sup>s</sup></sub>	– Original satellite precipitation on the dth day of the mth month
P <sub>d<sup>s'</sup></sub>	– Bias-corrected satellite precipitation on the dth day of the mth month
P <sub>i</sub>	– Barometric air (atmospheric) pressure at the time step of measurement   Precipitation depth in water balance equation
$\hat{P}_{i,j}$	– Original precipitation of a rain gauge ‘j’ in a year ‘i’ on regional vector
P <sub>i,j</sub>	– Synthetic precipitation of a rain gauge ‘j’ in a year ‘i’ on regional vector   Precipitation values at four nearest pixels on original spatial resolution
P <sub>m<sup>o</sup></sub>	– Observed accumulated precipitation in the mth month per grid box
P <sub>m<sup>s</sup></sub>	– Satellite accumulated precipitation in the mth month per grid box
P <sub>x</sub>	– Interpolated precipitation at a point ‘x’ in IDW interpolation method
P <sub>x,y</sub>	– Predicted value of precipitation at the new point (x, y)
PhD	– Doctor of Philosophy
PBIAS	– Percent bias
PD	– Post-Doctoral fellowship
PDF	– Probability Density Function
PEST	– Parameter ESTimation software
POE	– Probability Of Exceedance
PPGECAM	– Postgraduate Program in Civil and Environmental Engineering of UFPB
PR2/6   PR2	– Six-levelled soil moisture profile probe
q	– Vector of the parameters of the soil hydraulic properties to be optimized by CMA-ES
q*	– Final parameter set of q, obtained by the square root of C(q <sub>ij</sub> *)
q <sub>0</sub>	– Net infiltration rate
q <sub>i</sub>	– Nodal water flux
q <sub>ij</sub>	– Diagonal elements of C(q)
Q   Q <sub>i</sub>	– Surface runoff
r	– Radial distance
r <sub>1</sub>	– Spectral reflectance of band 1 (red) of MOD09Q1-MYD09Q1 products
r <sub>2</sub>	– Spectral reflectance of band 2 (near-infrared) of MOD09Q1-MYD09Q1
r <sub>a</sub>	– Aerodynamic resistance
r <sub>c</sub>	– Convective heat transfer resistance   Piezometer radius

$r_i(q)$	– Residuals of the ‘q’ vector to be optimized by CMA-ES
$r_r$	– Radiative heat transfer resistance
$r_s$	– Surface resistance
$r_{tot}$	– Aerodynamic resistance to the vapour transport
$r_{tot,c}$	– Adjustment parameter of total aerodynamic drag
$r_v$	– Vapour transport resistance
$r_w$	– Well perforation radius
rad	– Downward short-wave radiation
R   $R_i$	– Universal gas constant   Groundwater Recharge (same as GWR)
$R^2$	– Coefficient of determination
$R_{63}$	– Footprint radius for 63% cumulative neutron counts
$R_{86}$	– Footprint radius for 86% cumulative neutron counts
$R_e$	– Effective radial distance over which the hydraulic gradient is dissipated
$R_h$   RH	– Relative humidity
$R_n$	– Net radiation
$R_s$	– Global radiation
$R_{s\downarrow}$	– Downward shortwave incoming radiation
$R_{s\downarrow A}$	– Downward shortwave incoming radiation on top of the atmosphere
$R_{WTF}$	– Groundwater Recharge estimated by WTF method
Rosetta	– Software for estimating soil hydraulic properties by hierarchical pedotransfer functions
RISE	– Method of GWR estimation based on a fixed-interval
RMSE	– Root Mean Square Error
RRMSE	– Relative Root Mean Square Error
RS	– Remote sensing
RWU	– Root Water Uptake
$RWU_a$	– Actual Root Water Uptake
$RWU_p$	– Potential Root Water Uptake
s	– Slope of curve relating saturated water vapour pressure to temperature
S	– September   Maximum potential retention
$S_a$	– Actual surface flux
$S_i$   $S_{i+1}$	– Soil moisture in water balance equation at the current and next day (same as $\theta_i$   $\theta_{i+1}$ )
$S_p$	– Potential surface flux
$S_t$	– Sink term in Richards’ equation
$S_y$	– Aquifer specific yield
Si	– Silicon
$SiO_2$	– Silicon dioxide
SiBCS	– Brazilian System of Soil Classification
SAVI	– Soil Adjusted Vegetation Index
SCF	– Surface Cover Fraction (same as $F_C$ )
SCS	– Soil Conservation Service

SD	– Standard Deviation
SDS	– Science Data System
SEBAL	– Surface Energy Balance Algorithm for Land
SEEG/OC	– Greenhouse Gas Emission and Removal System/Climate Observatory
SMAP	– Soil Moisture Active and Passive
SMOS	– Soil Moisture Ocean Salinity
SOSMA	– SOS Atlantic Forest foundation
SOW	– Soil Organic matter Water equivalent
SPL4SMAU	– SMAP level-4 surface (root zone soil moisture analysis update product)
SR	– Agriculture cultivated in Straight Rows
SRTM	– Shuttle Radar Topography Mission
SUDENE	– Development Superintendency of the Northeast of Brazil
SWDI	– Soil Water Deficit Index
SWAT	– Soil and Water Assessment Tool
SWIG	– Soil Water Infiltration Global database
t	– Time
T	– Mean air temperature   Water temperature
$T_a$	– Actual transpiration
$T_{max}$	– Maximum temperature
$T_{min}$	– Minimum temperature
$T_{min_{close}}$	– Minimum air temperature of stomatal closing
$T_{min_{open}}$	– Minimum air temperature of stomatal opening
$T_p$	– Potential transpiration
$T_s$	– Soil temperature
TDR	– Time-Domain Reflectometry
TERENO	– TERrestrial ENvironmental Observatories
TMPA	– TRMM Multi-satellite Precipitation Analysis
TRMM	– Tropical Rainfall Measuring Mission
$u_2$	– Wind speed at 2-m height of measurement
$u_z$	– Wind speed at 'z' height of measurement
UB	– University of Bologna
UFC	– Federal University of Ceará
UFCG	– Federal University of Campina Grande
UFPB	– Federal University of Paraíba
UFPE	– Federal University of Pernambuco
UK	– United Kingdom
UNSODA	– UNsaturated SOil hydraulic DATabase
UP	– University of Potsdam
USA	– United States of America
USGS	– United States Geological Survey

USDA	– United States Department of Agriculture
UTC	– Coordinated Universal Time
V	– Actual volume of water   Variable of PR2/6 measurement in millivoltage
$V_j   V_{j-1}$	– Water volumes in a soil region at the current and previous time levels
VBA	– Visual Basic for Application
VIC	– Variable Infiltration Capacity
VPD	– Vapour Pressure Deficit
$VPD_{close}$	– Vapour Pressure Deficit of stomatal closing
$VPD_{open}$	– Vapour Pressure Deficit of stomatal opening
VWC	– Volumetric Water Content
$w_k$	– Weigh between the interpolated point ‘x’ and kth nearby rain gauges
W	– Well identification
$W_d$	– Vertical weighting function
$W_{ij}$	– Weights for each point ‘i’ and depth ‘j’
$W_k$	– Vertical ( $W_d$ ) or horizontal ( $W_r$ ) weighting functions
$W_r$	– Radial weighting function
WMTL	– Water and Mass Transport in Landscapes
WRB	– World Reference Base for soil resources
WTF	– Water Table Fluctuation method
x	– Simplified variable in COSMIC operator to speed up calculations   Vertical coordinate from soil bottom in HYDRUS-1D
y	– Function of ‘x’ variable in COSMIC operator to speed up calculations
z	– Vertical coordinate along the soil profile in COSMIC operator   Vertical coordinate along the soil profile in $\Delta S$ calculation

# 1 INTRODUCTION

Studies over the groundwater resources unsustainable use, albeit recently documented at global and regional scales, are still considered incipient when compared to surface water assessments (Gleeson et al., 2012), even though groundwater represents the most extensive unfrozen freshwater source on Earth (Aeschbach-Hertig and Gleeson, 2012). Nevertheless, due to its strong dependence on local features and insufficient access to it, groundwater is still considered a poorly understood and managed, devalued and inadequately protected natural resource (Foster et al., 2013).

The low cost and high availability of groundwater are advantages which attract people for using this water resource worldwide (Maliva, 2014), either for agricultural, industrial or human consumption purposes. However, changes in natural drainage patterns and groundwater exploitation may have negative consequences, such as dramatic volume-stored reduction (Chaudhuri and Ale, 2014), coastal aquifers marine-intrusion risk (Cary et al., 2015), soil subsidence risk (Pardo et al., 2013), and groundwater contamination (Chatton et al., 2016). Additionally, the excessive use of groundwater resources may impair the water cycle running and weaken the aquifer-rivers hydraulic connections (Zou et al., 2015), with severe consequences to the humanity and environment. Hence, for sustainable aquifer use, it is necessary to better know the groundwater reservoir hydraulic properties and recharge processes.

Among the water balance components, the Groundwater Recharge (GWR) contribution is one of the most challenging components to estimate, since it can rarely be measured directly (Crosbie et al., 2015) and cannot be easily derived from hydraulic head data due to the inherent uncertainty of hydraulic conductivities. Furthermore, it is a potentially random variable in space, whose observed data regularly represents local characteristics. Thus, the local-scale recharge data conversion into distributed regional information has become one of the leading challenges in hydrological research (Brunner et al., 2007).

In recent years, innovative technologies and data processing tools, such as remote sensing and Geographic Information Systems (GIS), have played a key role for providing global-, regional-, and large-scale distributed information for the water resource management. Nevertheless, precisely for groundwater research, these techniques have substantially contributed to recharge zones delimitation (Agarwal and Garg, 2016; Rahman

et al., 2013) and aquifer vulnerability assessment (Ertürk et al., 2017; Valle Junior et al., 2015).

For GWR estimation, remote sensing has not been able to progress similarly since the current satellite imagery data can detect just spatial processes and patterns related to near-surface resources. On account of these limitations, all possibilities for achieving those goals are based on indirect methods (Lucas et al., 2015). Thus, the recharge inferences ought to be generated from satellite products able to translate large-scale detection patterns of further water balance parameters, required for groundwater modelling (Brunner et al., 2007), such as precipitation (Prakash et al., 2016), soil moisture (López López et al., 2016), evapotranspiration (Mahmoud; Alazba, 2016) and surface runoff (Mahmoud, 2014).

Recent studies have merged satellite and terrestrial measurements to estimate large-scale GWR from water budget equations worldwide (Coelho et al., 2017; Gokmen et al., 2013; Münch et al., 2013; Szilágyi, Kovács and Józsa, 2012). Despite the similarities of their methodologies, all these studies used different remote sensing products in the water budget equations. However, recent studies have assessed GWR based on the difference between precipitation and evapotranspiration, ignoring changes in runoff and soil moisture (Crosbie et al., 2015), even though some soil moisture remote sensing products are already available, such as SMAP (Soil Moisture Active and Passive) mission (Entekhabi et al., 2010). Furthermore, the emergence of meteorological retrospective analysis (or reanalysis) data has provided a novel source of grid-box near-surface meteorological data useful for better estimating the water balance components (Ji, Senay and Verdin, 2015).

The use of remote sensing data for GWR estimation through a simple water budget equation, however, is frequently constrained on large-scale due to the lack of consideration of soil water storage changes, which could lead to unrealistic estimations if provided on intermediary scale. Its account is particularly important for understanding the GWR in complex sedimentary coastal basins, whose unsaturated vadose zone width may vary from thin to thick soil layers. This is the case of mostly the metropolitan cities of Northeast of Brazil, which are occasionally featured by sandy soils with high hydraulic conductivity and shallow groundwater table, subjected to heavy rainy seasons and very hot dry seasons (Araújo Filho et al., 2000; Cabral da Silva et al., 2000a). Those characteristics require a proper survey of the soil hydraulic properties when intending to estimate the GWR, which not always reflect the field-scale features when directly-measured at point scale.

Inverse modelling then emerges as an underlying tool to obtain information about a physical entity from its direct or indirect measurements (Tarantola, 2005). In soil science,



inverse modelling may allow for calibrating the parameters of pedotransfer functions from internal measuring conditions, namely soil moisture or soil water storage, by setting the boundary conditions, such as meteorological variables and groundwater level, and eventually the parameters of rooting growth and Root Water Uptake (RWU) (Šimůnek, van Genuchten and Šejna, 2016). These models contain the pedotransfer functions, which consist of van Genuchten-Mualem parameters that, when calibrated, may allow for obtaining soil hydraulic properties, which are essential to simulate the vertical water percolation rates at different depths and the GWR rate as the percolation rate at the bottom boundary.

The calibration of the soil hydraulic properties by inverse modelling, however, requires the use of soil moisture time series that often lack a high data quality (Vereecken et al., 2016), although there exists a wide range of invasive point-scale measurement sensors available, such as Time-Domain Reflectometry (TDR) probes (Graeff et al., 2010). To fill this gap, Cosmic-Ray Neutron Detection (CRNS) probes may be a promising solution as they can continuously measure the average soil moisture over hundreds of meters and deep to tens of centimetres (Brocca et al., 2017; Köhli et al., 2015; Rivera Villarreyes, Baroni and Oswald, 2014). Recently, Brunetti et al. (2019) externally coupled in the hydrogeological model HYDRUS-1D, the forward neutron operator COsmic-ray Soil Moisture Interaction Code (COSMIC) (Shuttleworth et al., 2013), allowing for inputting the neutron intensity time series assimilated by CRNS. The application of inverse modelling on CRNS data in HYDRUS-1D-COSMIC coupled model allows for averaging on soil hydraulic properties, better representing the soil characteristics in a simulation of intermediary-scale GWR.

Although several achievements on the use of remote sensing and vadose zone modelling in the simulation of hydrogeological response have been accomplished, the lack of validation of the water balance components estimates has put in check the reliability of the results. On the other hand, there is a high availability of methods that could be used to analyse the uncertainties and to validate the results of those techniques (Uusitalo et al., 2015), among which the data-based approaches are frequently used in the hydrogeological sciences (van Steenbergen, Ronsyn and Willems, 2012). For validating the resulting values of GWR, the following ones stand out: the Water Table Fluctuation (WTF) method (Cai and Offerdinger, 2016; Chung et al., 2016); and tracer techniques, such as Chloride Mass Balance (CMB) method (Crosbie et al., 2018; Hornero et al., 2016). Nonetheless, these techniques still have been few used to validate the water balance components in order to improve their estimates and better understand their effects over the GWR.

Therefore, this PhD thesis evaluated the estimations of water balance components from different techniques and methods, with certain modifications, validating their estimates with those from ground-based methods, and providing comparative discussions of results. For such purpose, different data sources, namely: remote sensing, reanalysis data, CRNS, and unsaturated vadose zone modelling; were employed, so that GWR estimates on different spatial resolutions could embrace the specificities of complex sedimentary coastal basins in Atlantic Forest biome of Brazil.

## 2 LITERATURE REVIEW

The literature review was subdivided in five major items, addressing all subjects of the methodology in the following order: contextualization of hydrological scenario; remote sensing products for estimating the water balance components; soil moisture assimilation based on CRNS method; vadose zone modelling, and; uncertainty and validation of water balance components.

### 2.1 Contextualization of the local hydrogeological scenario

In countryside areas of metropolitan cities of the Northeast of Brazil, the crop production has increased thanks to a growing expansion of energy and ethanol production stemmed from the city growth and the excessively-used road system, respectively (Filoso et al., 2015; Montenegro and Ragab, 2010). These capital cities are mainly located on complex sedimentary aquifers subjected to heavy rainy seasons mostly concentrated in winter, followed by very hot, dry seasons (Cabral da Silva et al., 2000a). They eventually are featured by sandy soils, high hydraulic conductivity and shallow groundwater levels, which confers a low soil crop capacity requiring a high employ of fertilizers (Araújo Filho et al., 2000).

The low nutrient fixation and high leaching in potential agricultural areas, however, have prevented a faster crop expansion, which allowed for crucial conservation of natural vegetation covers, but made them valuable sand extraction sources for the civil construction industry (Araújo Filho et al., 2000). These natural areas are responsible for the sustainable maintenance, regulation and control of water cycle, leading to the recycle of contaminants coming from agricultural fertilizer (Mateo-Sagasta, Zadeh and Turrall, 2017). Their excessively low natural fertility soils are subjected to waterlogging during the rainy season, leading to high water drainage through lateral flow (Araújo Filho et al., 2000). Accordingly, other hydrological processes are triggered: perennial creek runoff with short travel time (Barbosa, 2015), very high to extreme contamination risk (Linhares et al., 2014), heterogeneous sediment yields (Silva, 2009), and stream sediment load because of erosion susceptibility partly due to anthropological action (da Silva and Almeida, 2017).

Due to the critical hydrogeological scenario of the aforementioned areas, a few Brazilian research projects, such as IBESA (Implementation of Semiarid Experimental Basins) and BEER (Experimental and Representative Basins), and an international project,

named BRAMAR (BRAzil Managed Aquifer Recharge), have settled and maintained some representative and experimental basins in Northeast of Brazil (IBESA, 2004; Tsuyuguchi et al., 2018). Such research projects aim to provide insights on water resources management strategies in the region, by gaining knowledge about the relationships among the hydrological processes. In the same region, the Guaraíra Experimental Basin (GEB) was installed and, more recently, the João Pessoa Case Study Area (JPA CSA) was then conceived, both under the tropical wet climate condition.

The JPA CSA is located in the Alhandra sub-basin, within the Paraíba-Pernambuco sedimentary basin. They are mainly formed by the following sequence of stratigraphic units: Precambrian basement, Beberibe, Itamaracá, Gramame, Maria Farinha and Barreiras Formations, and Post-Barreiras sediments (Figure 1); whose origins were summarized by Andrade Filho (2014) as follows. The sedimentary fill of the JPA CSA began in the Coniacian-Santonian epochs, after the opening of the Atlantic Ocean (Matos, 1992). Throughout these epochs and the Campanian one, Beberibe unit was formed by the sandstones and conglomerates consisting of medium to coarse grains in fluvial and lacustrine environments (Beurlen, 1967). During the Campanian-Maastrichtian epochs, the Itamaracá unit was formed by a mixing of carbonates, calciferous sandstones and shales on the estuaries and lagoons in shelf environments (Barbosa et al., 2003). Then, all over the Maastrichtian-Paleogene epochs, a transgression between a generalized and less expressive deposition of carbonate rocks in shallow shelf environment were recorded, which were called Gramame and Maria Farinha units, respectively (Barbosa et al., 2003; Mabesoone, 1994). Between the Itamaracá and the Gramame units, a phosphatic horizon can be eventually found (Furrier, de Araújo and de Meneses, 2006).

In the first half of Miocene epoch, the Barreiras unit formed by sandstones interbedded with conglomerates and mudstones was deposited in fluvial and estuarine environments (Araújo et al., 2006; Morais et al., 2006; Rossetti et al., 2012). Overlying this unit were formed the Late Pleistocene and Holocene Post-Barreiras Sediments (Rossetti et al., 2011), the former was composed mostly of seismites consisting of sandstones, mudstones, conglomerates and breccias that display soft sediment deformation (Rossetti et al., 2012), and the latter was constituted solely of friable massive sands. Between the Barreiras and Post-Barreiras units, as well as between the Maria Farinha and Barreiras units, there were developed the lateritic paleosol unconformity (Rossetti et al., 2012).

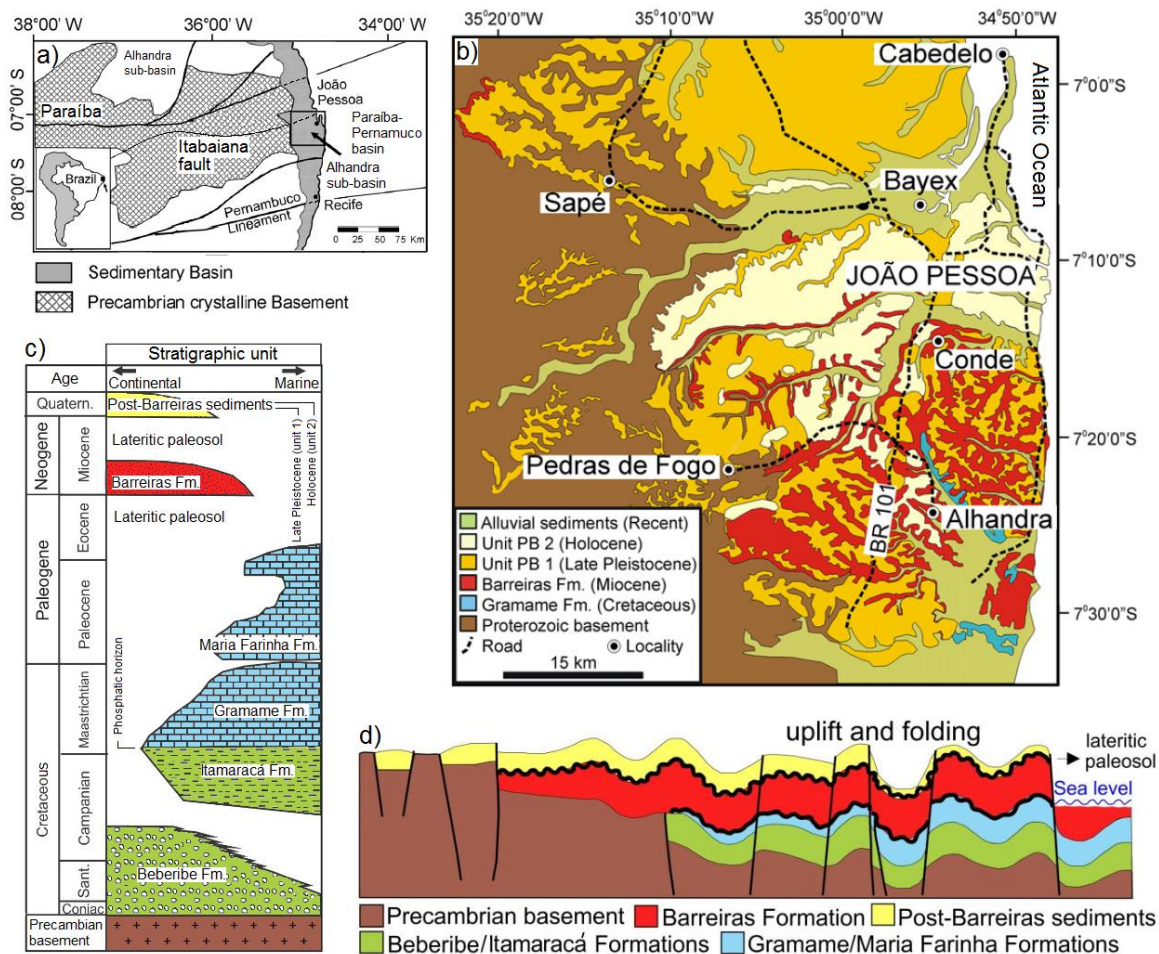


Figure 1 – Representations of the (a) location of Paraíba-Pernambuco sedimentary basin, (b) typical geological mapping, (c) stratigraphic units in geologic time scale, and (d) tectono-sedimentary Quaternary cross-section. Sources: modified from Rossetti et al. (2011) and Andrade Filho (2014).

In this context, the JPA CSA is mostly composed of Haplic Acrisols, Fluvisols and Carbic Podzols, according to World Reference Base (WRB) for soil resource (IUSS Working Group WRB, 2015), or by *Argissolos Vermelho-Amarelo*, *Neossolos Flúvicos* and *Espodossolos Humilúvicos* according to Brazilian System of Soil Classification (SiBCS) (dos Santos et al., 2018). In turn, GEB also encompasses both Haplic Acrisols and Carbic Podzols, mainly the latter, which is characterised by the: arenic, organic, moderated horizon A (98.41%); eluvial, albic horizon E; illuvial, spodic horizon B, followed by duripan horizon (Araújo Filho et al., 2000; Cabral da Silva et al., 2000a; de Lira, 2015) (Figure 2). On one hand, the horizons A and E have thickness usually ranging from 8 to 90 cm and 60 to 90 cm, respectively, and together they can exceed 2 m in some cases; holding many small pores and loose consistency for wet and dry conditions, and non-plastic and non-sticky consistency for wet condition (Araújo Filho et al., 2000). On the other hand, the horizon B is often cemented

and compact, constituting the duripan, which is rich in concretions or iron oxides, with silt and clay contents that can exceed 10% (Araújo Filho et al., 2000).

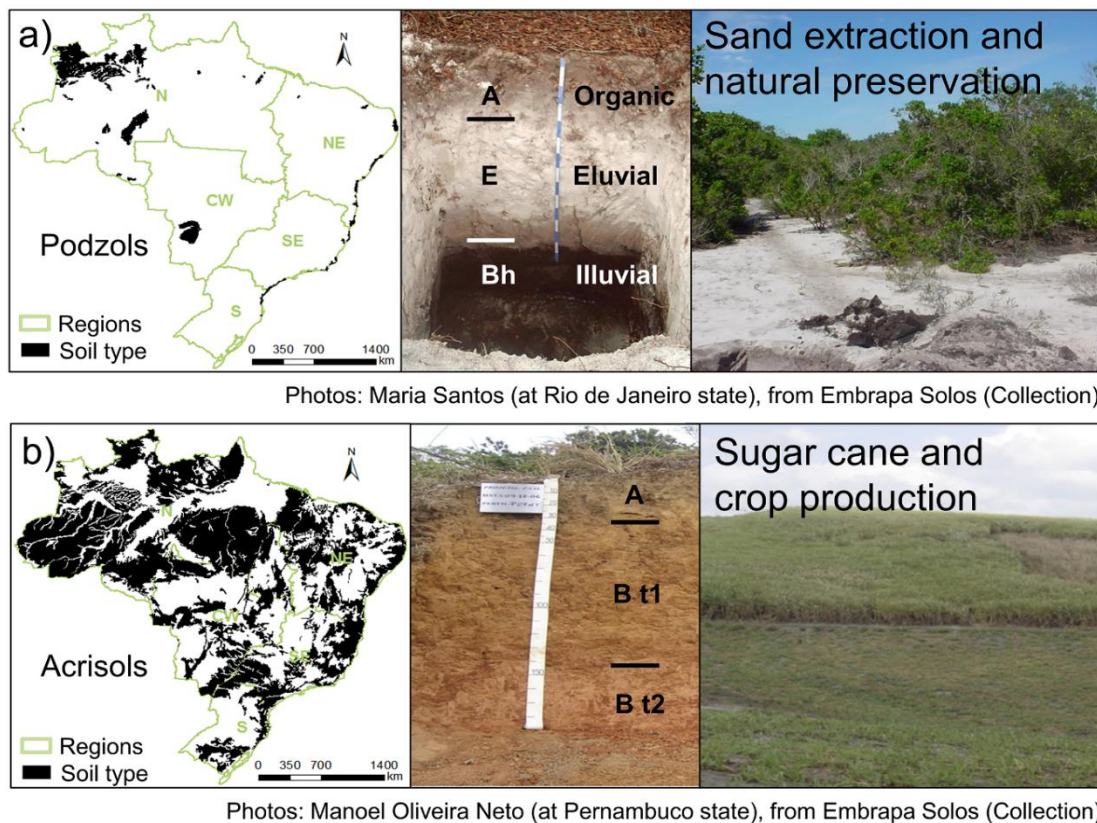


Figure 2 – Representation of the (a) Podzol and Acrisol soil types over Brazil, (b) typical soil profiles, and (c) main land uses. Available on: <http://www.agencia.cnptia.embrapa.br>.

## 2.2 Remote sensing products for estimating the water balance components

### 2.2.1 Fundamental concepts of the remote sensing

Remote sensing techniques are based on the acquisition or measurement of object information or phenomenon properties through a recording device without physical contact (Braga, 2014). As such, remote sensing can provide a synoptic and multi-temporal view of large areas over Earth surface, which turn the acquisition by on-board sensors in artificial satellites (at orbital level), a vastly used approach in environmental studies (Florenzano, 2007) (Figure 3). Amongst the application are the agriculture (Bastiaanssen, 2000), water resources (Tong et al., 2014), land use and vegetation cover (Coelho et al., 2014) and climatology (Zeng et al., 2013). In addition, the remote sensing allows for identifying the Earth surface changes stemming from natural and/or anthropic phenomena (Gusmão et al., 2012).



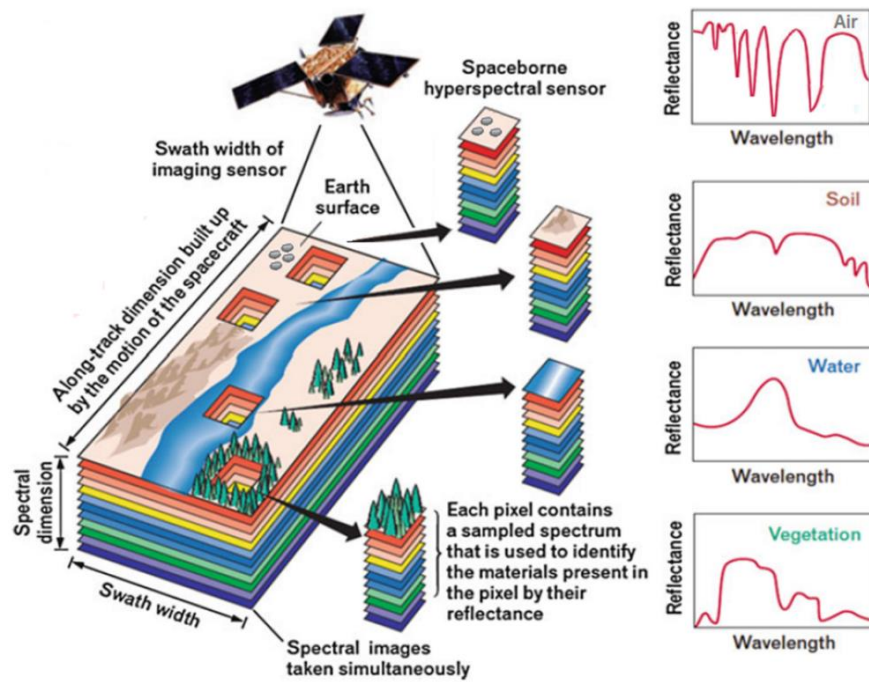


Figure 3 – Remote sensing conceptual diagram. Source: modified from Shaw and Burke (2003).

The information trade-off between the Earth surface objects and the on-board satellite sensors are transmitted at the light speed through the electromagnetic radiation, which originates mainly from the Sun and propagates in all directions through the electromagnetic waves (Aggarwal, 2004). Such electromagnetic radiation can be ordered through its wavelength or frequency, forming the spectrum regions that together bring forth the electromagnetic spectrum, in which the most used regions comprehend the bands between the micro-waves ( $10^0$  m) and the visible ( $4 \times 10^{-7}$  m) spectrum (Scarinci and Marineli, 2014) (Figure 4).

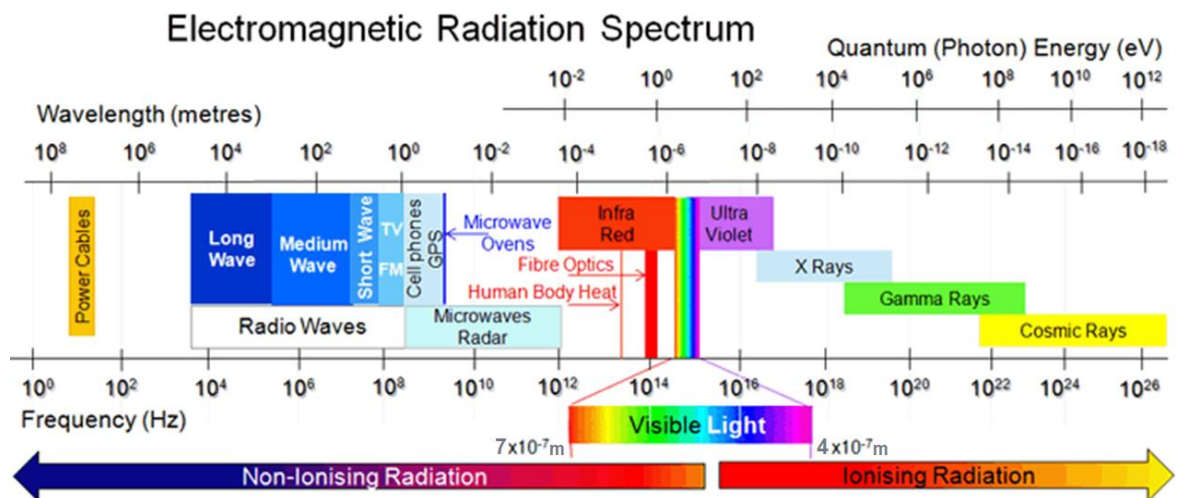


Figure 4 – Electromagnetic radiation spectrum. Source: Modified from <https://www.mpoweruk.com/radio.htm>, according to Scarinci and Marineli (2014).

The electromagnetic radiation arrives at the Earth surface with less intensity, as it is subjected to atmospheric component effects (Figure 5). Amongst these components, there exist the H<sub>2</sub>O, O<sub>2</sub>, O<sub>3</sub>, CO<sub>2</sub> and other gases, which are responsible for the main radiation absorption bands (Lillesand, Kiefer and Chipman, 2004). Nevertheless, some spectral bands are less affected by those atmospheric components, such as the visible band, allowing for a better transmission of the solar electromagnetic radiation, which in turn makes the remote sensing of the Earth surface possible.

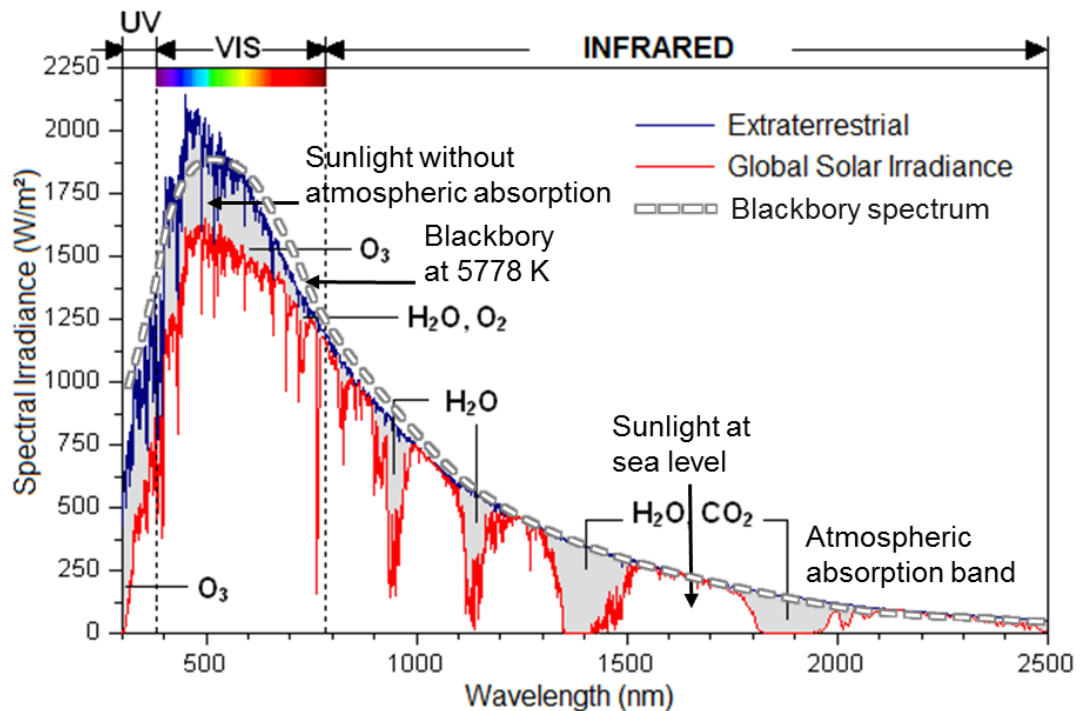


Figure 5 – Standard solar spectrum. Source: modified from ASTM (2003).

Upon reaching the Earth surface, the electromagnetic radiation can be partially transmitted, reflected or absorbed, of which only the two latter can be captured by the sensors and transformed into electrical signals. The absorbed portion used by remote sensing is that reemitted by the target through the thermal processes and/or dissipated as heat (Weng, 2010). The physical, chemical and biological properties of the imaged targets, as well as their surface irregularities, affect the reflected, absorbed and transmitted solar radiation, which characterizes the spectral signature of different resources (Figure 6).



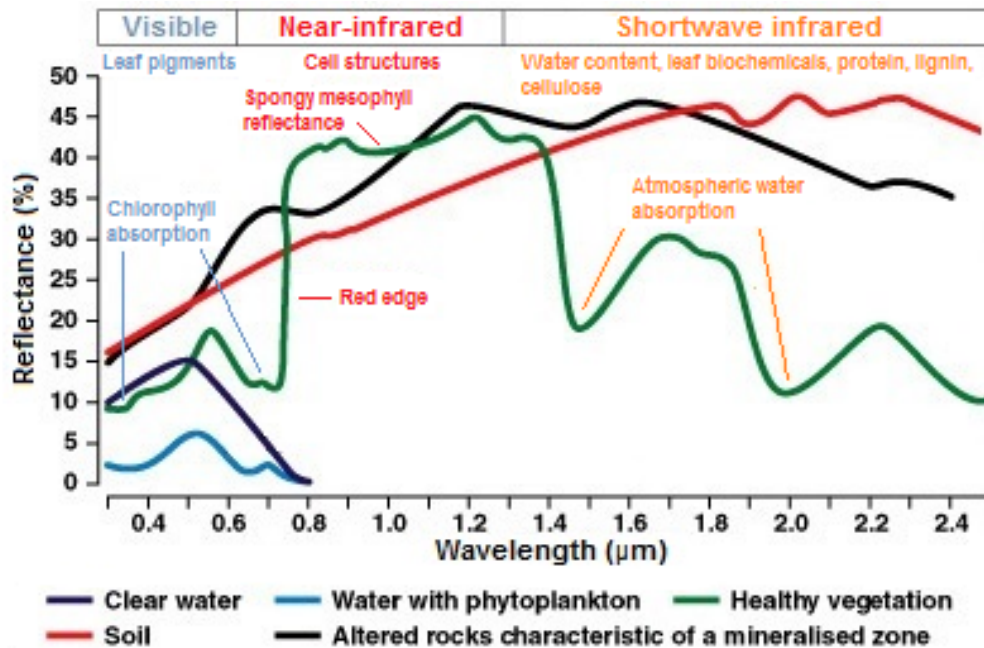


Figure 6 – Comparison among the generalized spectral signatures of some Earth surface materials. Source: modified from the file available on: <http://www.rsac1.co.uk/images/base2.jpg>.

Earth surface and atmospheric characteristics detected and recorded by the on-board satellite sensors depend on their resolutions, which vary according to their use purposes. There exist four basic sensing capabilities of the sensors: spatial, temporal, radiometric and spectral resolutions (Jensen, 2009). Spatial or geometric resolution refers to the instantaneous field of view, namely the spatial details represented by the smallest surface area, which the sensor is capable of individualizing. Temporal resolution is the time of satellite passage in the same place, namely the frequency that a sensor returns to a previously imaged location. Radiometric resolution is the electromagnetic radiation reflected and/or emitted by terrestrial surface targets, represented by binary digits or bits, required to store the maximum value of each pixel. Spectral resolution is the size and number of wavelength ranges or bands that a sensor can record, namely the sensor ability to distinguish different objects on the surface.

### 2.2.2 Global Precipitation Measurement mission and Integrated Multi-satellite Retrievals for Global Precipitation Measurement algorithm

Global Precipitation Measurement (GPM) mission is an international network of satellites project undertaken by the National Aeronautics and Space Administration of USA (NASA) and the Japanese Aerospace Agency (JAXA), which provide the next-generation of

global observations of rain and snow (Huffman, Bolvin and Nelkin, 2017). According to Huffman, Bolvin and Nelkin (2017), the GPM mission was designed to provide climatological and precipitation monitoring on near-real-time, and aims to improve the: (1) precipitation estimates; (2) knowledge about precipitation mechanisms, water cycle variability and fresh water availability; (3) climate modeling and forecasting; (4) weather forecasting and four-dimensional climate reanalysis; (5) hydrological forecasting and modeling.

The GPM Core Observatory launched in February 28th, 2014, accounts for GPM Microwave Imager (GMI), a microwave sensor with multichannel-tapered scanning with frequency of channels ranging from 10 GHz to 183 GHz, and a Dual-frequency Precipitation Radar (DPR) with: Ku-band at 13.6 GHz, and Ka-band at 35.5 GHz (Li et al., 2015). Thus, GPM provides rainfall and snow global information through the Integrated Multi-satellitE Retrievals for GPM (IMERG) products (consisting of eight satellites) on 0.1° (spatial) and 30-min (temporal) resolutions, with a 65° to North and South orbital slope (Hou et al., 2014; Liu et al., 2017; Skofronick-Jackson et al., 2017) (Figure 7).

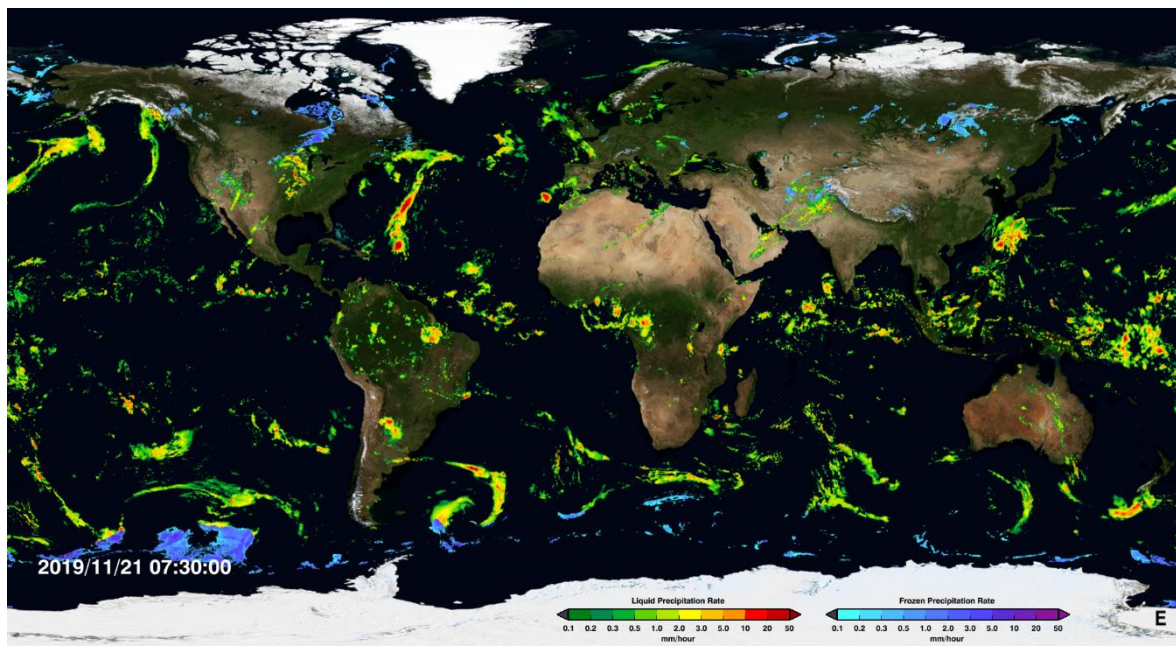


Figure 7 – Half-hourly precipitation obtained by GPM IMERG satellite product on 0.1° spatial resolution over the Earth. Source: <https://pmm.nasa.gov/>.

According to Huffman, Bolvin and Nelkin (2017), the GPM improved the main features of its precursor Tropical Rainfall Measuring Mission (TRMM), namely: (1) measurement of microphysical properties and vertical structure information using active remote sensing techniques over a wide spectral range; (2) measurement of snow and light

rain rates through high-frequency passive microwave radiometry; (3) algorithm improvements on passive microwave recovery over the Earth; and (4) better precipitation measurements at medium and high latitudes during colder seasons.

The IMERG algorithm embodies infrared and microwave estimates from GPM constellation, ground-based observations, and other ancillary data (Huffman, Bolvin and Nelkin, 2017). Several products are provided by NASA Goddard Space Flight Center (GSFC), available on <https://pmm.nasa.gov/data-access/downloads/gpm>. To date, six IMERG versions (from V01 to V06) are available in three different products, namely: Early Run, Late Run, and Final Run. The two first products provide proper data at near-real-time for time-sensitive applications, whose data are accessible between 4 and 12 h after the assimilation. On the other hand, the latter product improves the satellite estimations by ground-based data from the Global Precipitation Climatology Centre (GPCC) appropriate for hydrological modelling purposes, whose data are accessible around 3.5 months after the assimilation (Tang et al., 2016).

Wang et al. (2018) compared the IMERG V03, V04 and V05 Early, Late and Final Run products to different satellite-based and ground-based data over the Earth. They found that V04 and V03 Final Runs show comparable performance, while V05 Final Run generally outperforms both V04 and V03, holding the best performance. Over Brazil, Gadêlha et al. (2019) found that the IMERG V05 Late Run captures effectively the precipitation spatial patterns, with a slight overestimating behaviour compared to ground-based rainfall data. Conversely, they also found a relevant underestimation of the IMERG data throughout the coastal zone of the Northeast of Brazil, likely due to the inability of the passive microwave and infrared sensors in detecting warm-rain processes over land. Recently, the IMERG V06 was also released, but the version V06A presented failures and the V06B did not outperform the prior IMERG V05B (Anjum et al., 2019).

### **2.2.3 Moderate Resolution Imaging Spectroradiometer sensors and Global Evapotranspiration Project algorithm**

The MODerate Resolution Imaging Spectroradiometer (MODIS) is a scientific instrument launched in Earth orbit by NASA GSFC, which is composed by sensors on-board the Terra (since 1999) and Aqua (since 2002) satellites, which transmit data of 36 spectral bands, available on <https://modis.gsfc.nasa.gov/data/>. Amongst those, the visible and medium infrared (0.405 to 2.155  $\mu\text{m}$ ) regions are proposed to terrestrial, oceanic and

atmospheric applications, while the thermal portion of the electromagnetic spectrum (3,660 to 14,385  $\mu\text{m}$ ) can be used by further fields of investigations on natural sciences (Justice et al., 2002). MODIS sensor also holds wide spatial, radiometric and temporal resolutions, featuring from 250 m (red and near-infrared ranges) to 1 km (thermal infrared range) grid cells, mapping the surface every 8-day, and releasing information on monthly and annual resolutions (Velpuri et al., 2013).

The main features of MODIS sensor are: (1) the high geometric quality of imagery; (2) the almost daily imaging frequency over the entire terrestrial globe; (3) the sophisticated procedure for atmospheric imagery correction (Arai and Freitas, 2007; Caballero, 2012), (4) a wide range of products related to biophysical vegetation parameters, and (5) the free availability of imagery (Latorre et al., 2007). With regards to the available MODIS products, Anderson et al. (2003) listed the most notable ones, namely: (1) MOD09, which collects the surface spectral reflectance; (2) MOD11, which provides the surface temperature and emissivity; (3) MOD13, which contains the spatiotemporal data of Earth surface vegetation cover; and (4) MOD44, which identifies the global changes resulting from extreme natural events and human activities.

The MODIS Global Evapotranspiration Project (MOD16) emerged from the MODIS measurements (Mu et al., 2007), providing exceptional information about vegetation and surface energy on the regional and global scale (Justice et al., 2002). The original MOD16 evapotranspiration algorithm (Mu et al., 2007) based on the Penman-Monteith equation (Allen et al., 1998) covered the entire 109.03 Million  $\text{km}^2$  global vegetated land areas, masking out water bodies, urban/built-up areas and barren lands. This algorithm uses as inputs the MODIS products: leaf area index (LAI), Enhanced Vegetation Index (EVI), albedo, and land cover; as well as the daily meteorological data from NASA Global Modeling and Assimilation Office (GMAO) reanalysis dataset (Mu et al., 2007; Mu, Zhao and Running, 2011).

Improvements were latter provided by Mu, Zhao and Running (2011) in the original MOD16 algorithm (Figure 8), namely: (1) simplification of the calculation of the vegetation cover fraction; (2) separation between dry and wet canopy surfaces; (3) enhanced estimates of stomatal conductance and aerodynamic drag; (4) adding the heat flux calculation in the soil; (5) creation of saturated and moist surfaces from a single prior soil surface, and; (6) evapotranspiration calculation as sum of daily and night evapotranspiration components. On the other hand, an important source of errors in MOD16 estimates may stems from land use, as shown by Ruhoff et al. (2013).

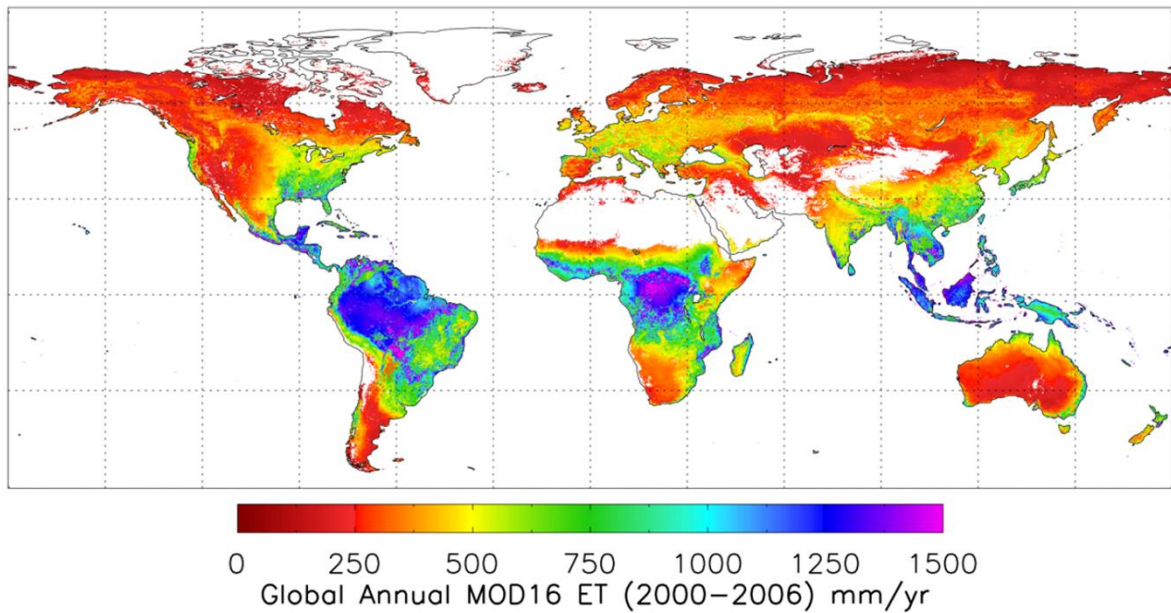


Figure 8 – Annual actual evapotranspiration obtained by MOD16 global evapotranspiration product on 250-m spatial resolution over the Earth. Source: adapted from Mu, Zhao and Running (2011).

Estimates of MOD16 evapotranspiration between the original and modified algorithm stood on 416 to 431 mm yr<sup>-1</sup>, respectively, with a mean annual estimate of 1,180.16 mm yr<sup>-1</sup> over evergreen broadleaf forests (Mu, Zhao and Running, 2011). A multi-decadal trend analysis of MOD16 evapotranspiration revealed a significant positive tendency driven mainly by Leaf Area Index (LAI) increase, dominated by greening, whose estimates compared to 95 eddy-covariance flux towers yielded a good agreement, indicated by R<sup>2</sup> and PBIAS equal to 77% and -6% (Zhang et al., 2016). The choice of forcing input data may produce a mean uncertainty on monthly evapotranspiration corresponding to ~20% of global mean one, with net radiation driving the majority difference (Badgley et al., 2015). Further comparisons for different uses and soil cover reported errors of up to 13% on the annual scale (Loarie et al., 2011). In Northeast of Brazil, the reliability of MOD16 products was also confirmed, once the monthly MOD16 data produced a value of R<sup>2</sup> equal to 82% (Miranda et al., 2017). Recently, in the same region, the MOD16 evapotranspiration product showed a better performance throughout all seasons, with BIAS, RMSE and R<sup>2</sup> equal to -0.08 mm d<sup>-1</sup>, 0.61 mm d<sup>-1</sup> and 80%, in relation to eddy-covariance measurements, whose mean energy balance closure achieved 84%, considerably high for the region (dos Santos et al., 2020). In such region, the land degradation together with precipitation are the main drivers on evapotranspiration anomalies, holding the former a high potential impact on the hydrological cycle, which feedbacks the land degradation cycle (Mariano et al., 2018).



## 2.2.4 Surface runoff by Natural Resources Conservation Service–Curve Number method

The Natural Resources Conservation Service–Curve Number (NRCS–CN) method (NRCS, 1986), originally called Soil Conservation Service (SCS) method (SCS, 1972), is a popular, ubiquitous, and enduring method of runoff estimation originally based on rainfall event that requires a single parameter per ungauged catchments (Hawkins et al., 2009). Although originally created for rural areas of the United States of America (USA), it has been gained credibility and is now employed over different areas worldwide (Nagarajan and Basil, 2014).

According to Ponce and Hawkins (1996), the grounds of NRCS–CN popularity comes from its clear advantage in simply, conveniently and responsively identify catchment properties, namely: land use/cover, soil type, surface condition, and Antecedent Runoff Condition (ARC). Furthermore, NRCS–CN methodology is the only well-established method that provides readily-grasped and properly-documented environmental inputs, making it widely accepted throughout the world (Abdulkareem et al., 2019).

After the introduction of Geographic Information Systems (GIS) in the 1990s, the NRCS–CN method could easily employ remote sensing products to estimate distributed surface runoff for several hydrological applications. Sinha et al. (2019) applied NRCS–CN to compute the urbanization impact on distributed surface runoff over 44 years. Kayet et al. (2018) employed NRCS–CN to assess the annual soil erosion in 15 catchments related to distributed surface runoff. Coelho et al. (2017) estimated the GWR distribution in the semiarid zone of Brazil by inputting distributed NRCS–CN surface runoff in the water budget equation. However, Hong et al. (2007) were the first who simulated global surface runoff using TRMM satellite-based rainfall estimation (Figure 9).

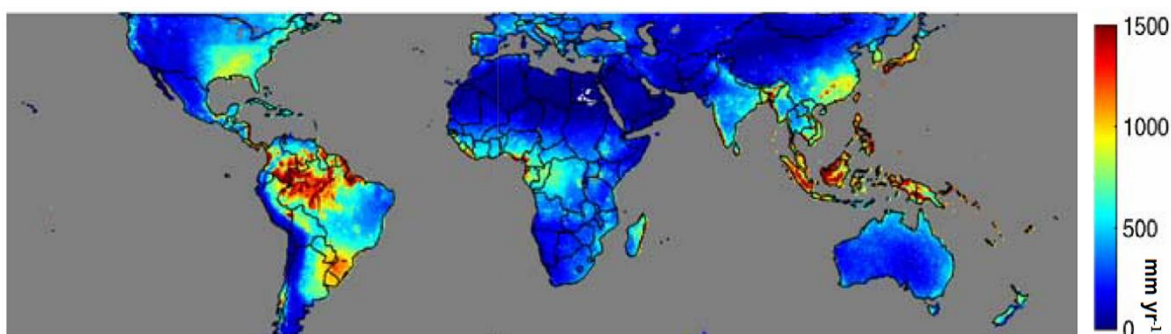


Figure 9 – Annual mean surface runoff (1998-2016) simulated on 0.5° spatial resolution derived from TRMM data through the NRCS–CN method over the Earth. Source: adjusted from Hong et al. (2007).

Although the NRCS–CN method is successfully used in hydrology, some limitations have been eventually claimed in literature. Amongst the limitations of NRCS–CN, the most important are: fixed initial abstraction ratio equal to 0.20; instability of CN parameters to ARC values, and; the weak physical basis for infiltration (Ajmal et al., 2015; Ajmal, Kim and 2015; Cho and Engel, 2018). In addition, using NRCS–CN to estimate continuous long-term runoff time series and its use in large-sized watersheds are not recommended by some authors (Efstratiadis et al., 2014; Ponce and Hawkins, 1996). Thus, NRCS–CN hybrid methods have attempting to improve the estimates of long-term, spatially-distributed surface runoff (Cho and Engel, 2018).

Despite the limitations, NRCS–CN holds a high and distinct potential to estimate distributed surface runoff in relation to other methods (Muthu and Santhi, 2015). By comparing three different methods, Meresa (2019) found that NRCS–CN outperforms the others by showing median bias close to zero in 10 catchments, being suitable to predict runoff with reasonable accuracy and calculate distributed surface runoff. The good performance of NRCS–CN method stems from its flexibility in combining climatic and physiographic characteristics in the Curve Number (CN) parameter (Nagarajan and Poongothai, 2012).

### **2.2.5 MapBiomass land use/cover project**

Land use/cover is commonly obtained by remote sensing data, which may vary in spatial and temporal resolution. Satellite-based land use/cover with 30-m grid-box is a good solution for large watersheds, providing up to 80% reality compliance (Kwoczyńska et al., 2014; Lunetta et al., 2006). On the other hand, land use/cover time series has been systematically updated leading to a quick outdated of existing databases (Siejka et al., 2017; Walega and Salata, 2019). Nevertheless, depending on the characteristics of the classification algorithm, changes in land use/cover overtime may be improperly undetected (Lu et al., 2012).

The MapBiomass project is an initiative of the Greenhouse Gas Emission and Removal System/Climate Observatory (SEEG/OC), composed of a collaborative network and launched in 2015, which that provides annual national-level land use and land cover transitions in all biomes of the Brazilian territory with a 30-m spatial resolution on annual basis (Figure 10), available on <http://mapbiomas.org>. The collection 1.0, 2.0 and 2.1 were released in April 2016, April 2017, and January 2018, respectively, applying a simplified

legend in the former and providing enhancements after the random forest using. Then, the collections 3.0 and 3.1 were released in August 2018 and in April 2019, respectively, providing data from 1985 to 2017 based on a pixel-per-pixel automatic classification using the entire archive of Landsat observations. More recently the collection 4.0 and 4.1 were released, but little information about its accuracy has been published since then.



Figure 10 – Annual land use/cover obtained by MapBiomias collection 3.1 on 30-m spatial resolution over Brazil. Source: <http://plataforma.mapbiomas.org/map#coverage>.

As a relatively new project at national-scale, the MapBiomias data are recently getting more attention and supporting Brazil-based studies in many areas (Garrett et al., 2018; Mariano et al., 2018; Mccord, Tonini and Liu, 2018; Tyukavina et al., 2017; Wang et al., 2019d), but just a few have used them to estimate evapotranspiration and runoff (Cavalcante et al., 2019; Lima and Ribeiro, 2018; Silva, Manzione and Teixeira, 2018). Wang et al. (2019c) showed the MapBiomias capacity in allowing for the identification of forest degradation and secondary-growth vegetation. In the Northeast of Brazil, land use changed minimally during the 2000–2016 period with greater agricultural expansion in the southwestern zone (Dias et al., 2016; Noojipady et al., 2017). In the Brazilian shoreline zone, the mangrove area from 1985 to 1998 showed an upward trend in detriment to a lesser trend recorded from 1999 to 2018; however, ~75% of the Brazilian mangroves remained unchanged for two decades or more (Diniz et al., 2019).



## 2.2.6 Soil Moisture Active Passive mission

Soil Moisture Active Passive (SMAP) is a NASA GSFC mission in cooperation with Foreign Agricultural Services (FAS) and Hydrology and Remote Sensing Laboratory (HRSL), both from United States Department of Agriculture (USDA). SMAP monitors the global near-surface soil moisture since April 2015, mapping the globe between 85.044°N and S in 2–3 days, depending on location (Entekhabi et al., 2010). SMAP was designed to record co-located L-band active radar and passive radiometer measurements at a constant incidence angle of 40°, in order to provide global measurements of surface soil moisture and soil freeze/thaw state (Leon, Khalsa and Leslie, 2015; Montzka et al., 2017). Although the on-board radar failed after 3 months, the radiometer continues to work, producing brightness temperatures and derived products on a 36 km fixed Earth grid.

SMAP holds four levels of products comprehended by Level 1 passive microwave products and Level 2-4 passive microwave and radar products (Entekhabi et al., 2014). The National Snow and Ice Data Center (NSIDC, <https://nsidc.org/>) and Alaska Satellite Facility (ASF, <http://asf.alaska.edu>) are responsible for the storage, distribution, and support of the SMAP data supplied by SMAP Science Data System at Jet Propulsion Laboratory (SDS/JPL, Level 1-3), and GMAO at NASA GSFC (Level 4).

SMAP Level 4 (L4) product provides global near-surface (0-5 cm) and root-zone (0-100 cm) soil moisture from brightness temperature data from an L-band (1.4 GHz) microwave radiometer. The brightness temperature scaling parameters are based on eight years of Soil Moisture Ocean Salinity (SMOS) observations and three years of SMAP observations. The current baseline Single Channel Algorithm (Jackson, 1993) and a dielectric mixing model converts horizontally polarized brightness temperatures to soil moisture.

The L4 root-zone product assimilates the near-surface (5 cm) retrieved by passive radiometer into the catchment land surface model, providing the SMAP L4 Surface and Root Zone Soil Moisture Analysis Update (SPL4SMAU) product (Reichle et al., 2017). SPL4SMAU product is gridded using an Earth-fixed, global, cylindrical, 9-km, Equal-Area Scalable Earth Grid, Version 2.0 (EASE-Grid 2.0) projection (Brodzick et al., 2012). SPL4SMAU product provides root-zone soil moisture data at 3-hour temporal resolution, corrected by satellite- and ground-based precipitation estimates (Liu et al., 2011). The soil water storage in the root zone can also be calculated easily by averaging the soil moisture increments (Reichle et al., 2018) (Figure 11).

It is worthwhile to mention that another option available to assimilate the soil water storage change is the GRACE (Gravity Recovery And Climate Experiment) mission. The GRACE mission is composed of two twin satellites – GRACE-A and GRACE-B – whose aim is to map the terrestrial gravitational field, with a 30-day time scale and a spectral range from 400 km to 40,000 km (Tapley et al., 2004). Data are available at three levels: Level-1A, Level-1B, and Level-2, of which the latter produces uncertainties, on a global scale, less than 9.4 mm (Ferreira et al., 2016); available on <http://www.csr.utexas.edu/grace>. Moreover, these uncertainties take into account: (1) errors of subtracting residuals from long-term trends, annual and semi-annual signs, and (2) errors introduced in the data filtering process.

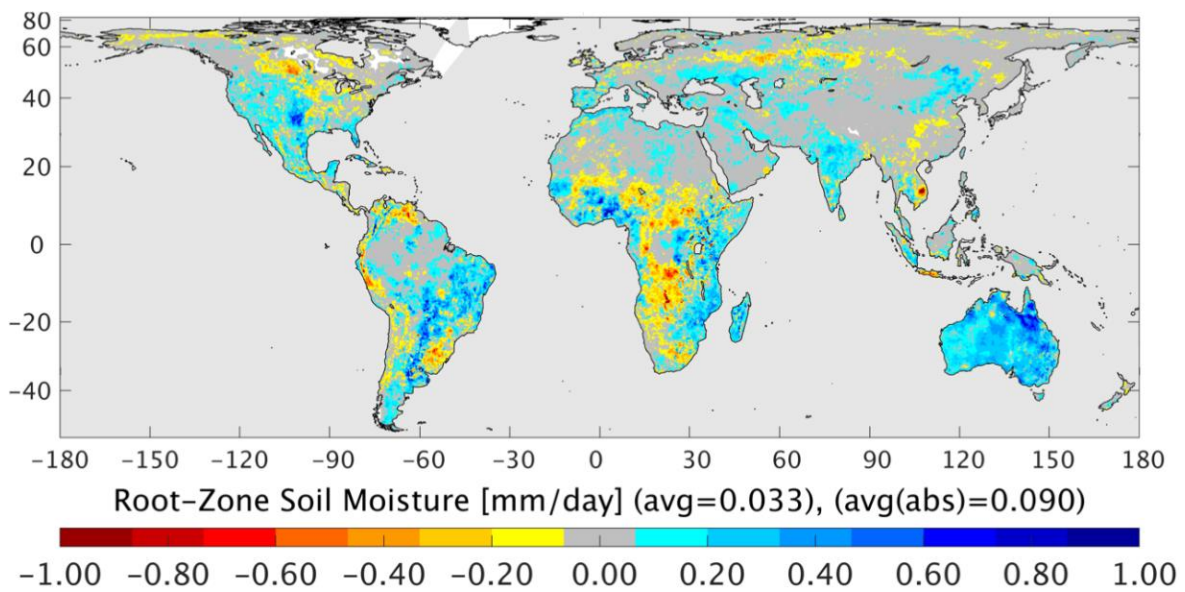


Figure 11 – Root-zone soil moisture increments obtained by SMAP SPL4SMAU satellite mission from April 1st, 2015, to April 1st, 2018, on 9-km spatial resolution. Source: Reichle et al (2018).

Regarding the SMAP surface soil moisture products, the data performances of the first eleven months were assessed through 34 core validation sites spread throughout the Earth (Colliander et al., 2017). The results indicate that the SMAP radiometer-based soil moisture data product meets its expected unbiased root mean square error of soil moisture equal to  $0.04 \text{ m}^3 \text{ m}^{-3}$ . Furthermore, six different soil moisture satellites products, including SMAP, were validated on intermediary field scale using CRNS probes on five continents (Montzka et al., 2017). Amongst the satellites, the use of SMAP data was recommended since it showed relatively low bias, an adequate dynamic range as identified by the triple-collocation error covariance, and the highest signal-to-noise ratio.

### 2.2.7 Global Land Data Assimilation Systems

The Global Land Data Assimilation Systems (GLDAS) is a global, high-resolution, offline (uncoupled to the atmosphere) terrestrial modelling system developed in 2001 by NASA/GSFC and the National Oceanic and Atmospheric Administration (NOAA)/National Centers for Environmental Prediction (NCEP) (Rodell et al., 2004). GLDAS project combines satellite- and ground-based data to constrain the modelled Land Surface Models (LSMs) to produce optimal fields of land surface states and fluxes on near-real-time (Rodell et al., 2004). According to Bi et al. (2016), GLDAS mainly uses the following LSMs: Noah (Chen et al., 1996), Common Land Model (CLM) (Dai et al., 2003), Mosaic (Koster, Suarez and 1996), and Variable Infiltration Capacity (VIC) (Liang et al., 1994).

The GLDAS version 2 (hereafter, GLDAS-2) that replaced the GLDAS version 1 (hereafter, GLDAS-1) hold two components: one forced entirely with the Princeton meteorological forcing data (hereafter, GLDAS-2.0), and the other forced with a combination of model and observation-based forcing datasets (hereafter, GLDAS-2.1) (Rodell et al., 2004). The reanalysis data are available on <https://disc.gsfc.nasa.gov/>, from 1979 to present (GLDAS-1.0), 1948 to 2010 (GLDAS-2.0), and from 2000 to present (GLDAS-2.1). The spatiotemporal resolutions of the products vary from 3 hours to monthly, and from 1° (CLM, Noah, Mosaic and VIC) to 0.25° (Noah), depending on the concerning version. Moreover, the newly GLDAS-2.1 NOAH 0.25°, 3-hourly dataset simulated with the Noah Model 3.3 in Land Information System (LIS) Version 7, contains 36 land surface fields.

The main difference between the previously-mentioned versions lies on their forcing data. Overall, GLDAS products include meteorological forcing data (precipitation, near-surface air temperature, specific humidity, wind speed, downward shortwave/longwave radiations, and surface pressure) (Figure 12), land surface states (sub-surface runoff and soil moisture), and flux data (sensible heat flux and evaporation) (Wang et al., 2016). Lv et al. (2018) lists the following main differences between GLDAS-1 and GLDAS-2.1: the GPCP (Global Precipitation Climatology Project) and GDAS (Global Data Assimilation System) precipitation combination; the AGRMET (Air Force Weather Agency's Agricultural Meteorology) and GDAS radiation corrections; the use of MODIS-based land surface parameters; the Noah model version upgrade; and, a soil moisture initialization enhancement over desert.

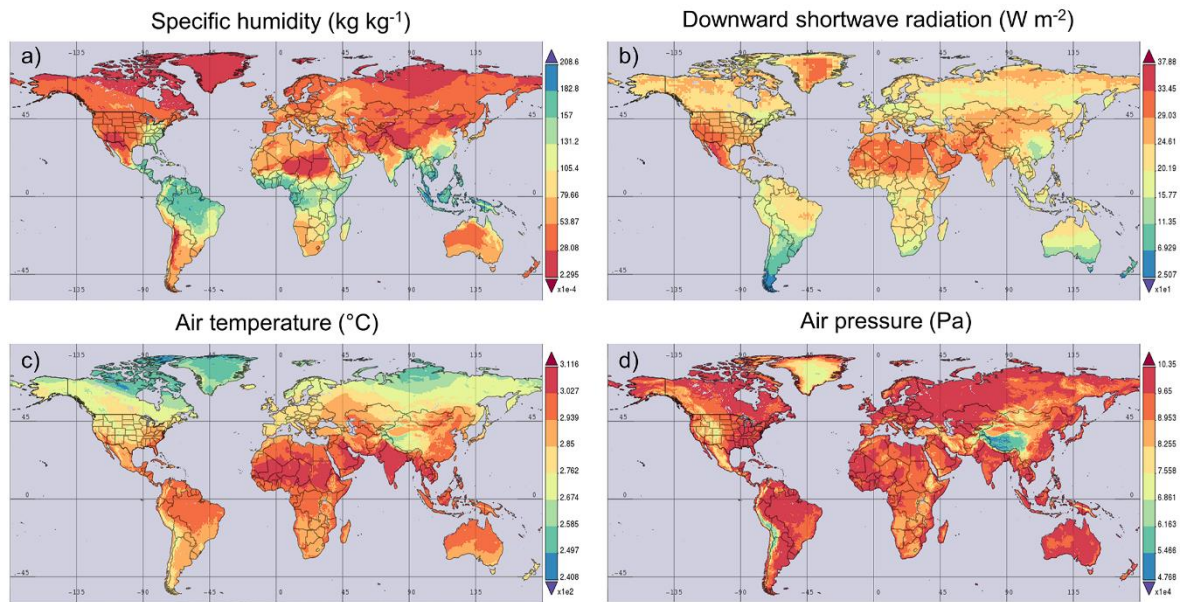


Figure 12 – Three-hourly time averaging map obtained by GLDAS Noah 2.1 on 0.25° spatial resolution over the Earth, on May 1st, 2017 from 00:00 to 12:00, of (a) specific humidity, (b) downward shortwave radiation, (c) air temperature, and (d) air pressure. Source: averaged on <https://giovanni.gsfc.nasa.gov/>.

By evaluation GLDAS-1.0 and GLDAS-2.0, Wang et al. (2016) showed that GLDAS-1.0 may present serious discontinuity issues in its forcing data, with large precipitation and temperature errors, while the GLDAS-2.0 holds a better temporal continuity, reduced biases, but larger mean absolute errors. According to them, using GLDAS-2.0 to simulate water balance components, such as runoff and evapotranspiration, provides more accurate estimates than GLDAS-1.0, even though both versions were not very capable of capturing the seasonal variation in monthly soil water storage.

Zhang et al. (2019) built a coupled diagnostic biophysical model for estimating global evapotranspiration by inputting GLDAS-2.1 forcing data, whose results compared to 95 widely-distributed flux towers indicates a robust model performance. Furthermore, Baik, Liaqat and Choi (2018) found that GLDAS-2.1 product outperformed the evapotranspiration estimates among different satellite- and reanalysis-based products, mainly over cropland areas and in tropical regions. In Brazil, de Oliveira et al. (2016a) integrated successfully MODIS images with GLDAS 2.0 products to retrieve distributed net radiation in Amazon biome, eliminating the need for ground-based measurements. Lima and Ribeiro (2018) found that using GLDAS-2.1 forcing data for evaluating the daily evapotranspiration in Atlantic Forest biome of Brazil, may allow for capturing in detail the evapotranspiration spatial distribution without using ground-based data.

## 2.2.8 Groundwater Recharge rate retrieved via water budget equation

The groundwater recharge rates (GWR rates), frequently understood as the vertical water percolation rate below the root zone in the unsaturated zone, is a valuable underground information but hugely challenging to be measured directly due to its boundary conditions and sensitivity to climate forcing (Mathias, Sorensen and Butler, 2017). This requires alternative means of indirect estimation, for example, by using soil moisture and groundwater level data (Crosbie et al., 2015; Mathias, Sorensen and Butler, 2017; Naylor et al., 2016; Rivera Villarreyes, Baroni and Oswald, 2014). Additionally, in underdeveloped and developing countries, this information frequently is only poorly estimated on point-scale, in small-density hydrogeological networks, and often with limited data access and only as short time series, which may compromise the modelling feasibility and reliability (Ottoni et al., 2018). To date, solely Mohan et al. (2018) managed to globally estimate the GWR rates, which was done through a multi-model inference approach (Figure 13), using 715 estimates retrieved for a period of 34 years. They were obtained by the following methods: WTF, tracers, water budget equation, lysimeter, modelling, and baseflow

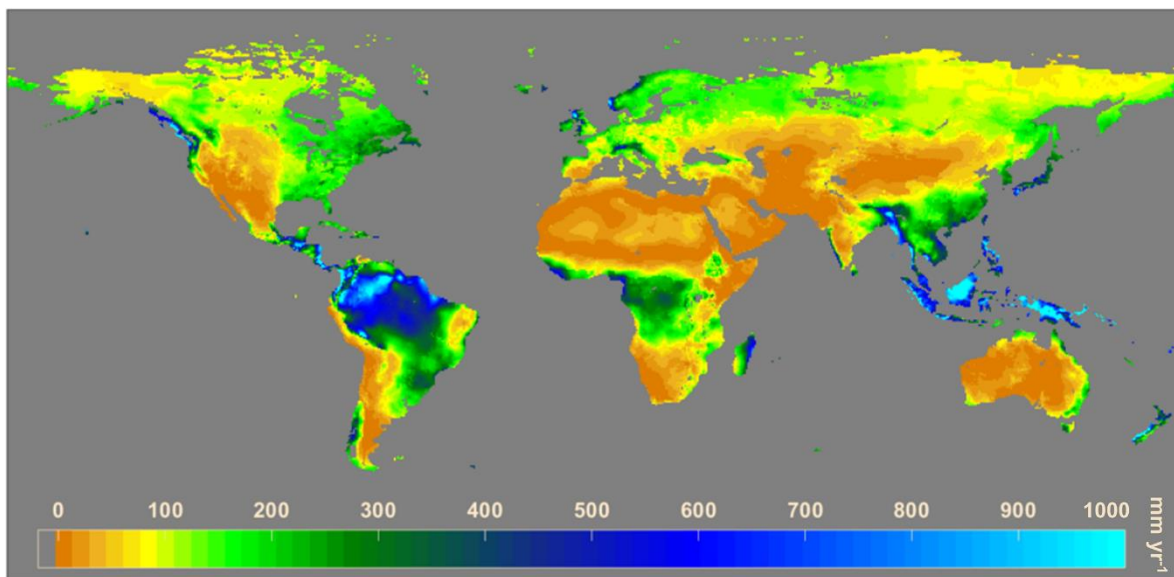


Figure 13 – Long-term (1981-2014) annual groundwater recharge rates obtained by a multi-model inference approach on 0.5° spatial resolution over the Earth. Source: adapted from Mohan et al. (2018).

Although the GWR spatial distribution may be considerably variable, most of the existing methods are based on observed data that characterise the hydrological features only on a local scale (Coelho et al., 2017). Such circumstance is not be a problem in regions where the monitored network is very dense; however, this is not the usual scenario in most regions



throughout the Earth. Therefore, the hydrological challenge in respect to this is to estimate distributed information about GWR (Brunner et al., 2007).

Some methods using orbital remote sensing data are now in discussion, and most of these approaches are based on the application of the simplified water budget equation using precipitation and evapotranspiration data as input on a grid-box basis, ignoring changes in soil moisture and surface runoff (Crosbie et al., 2015; Gokmen et al., 2013; Khalaf and Donoghue, 2012; Lucas et al., 2015; Münch et al., 2013; Szilagyi et al., 2011; Szilágyi, Kovács and Józsa, 2012; Yin et al., 2011). More recently, in order to improve the GWR estimates, a few studies have attempted to add other water balance components in the water budget equation using remote sensing approaches, such as interception by vegetation, irrigation, surface runoff, and soil water storage (Coelho et al., 2017; Kahsay et al., 2019; Kubicz et al., 2019; Subramanian and Abraham, 2019; Mushtaha, van Camp and Walraevens, 2019; Usman, Liedl and Kavousi, 2015).

Most of the previous studies have used distinct remote sensing products to calculate the water balance components in order to estimate the GWR through the water budget equation. For example, Khalaf and Donoghue (2012) used data derived from TMPA (TRMM Multi-satellite Precipitation Analysis) product and SEBAL (Surface Energy Balance Algorithm for Land) algorithm, whereas the study conducted by Crosbie et al. (2015) used the Bureau of Meteorology gridded data and the CMRSET (CISRO MODIS Reflectance-based Scaling Evapotranspiration) algorithm, to calculate precipitation and evapotranspiration, respectively, and to estimate the GWR as their difference. Nevertheless, the spatial resolution of some satellite products, such as the TMPA, were recently outperformed by using satellite constellation and improving the algorithms, whereas other methods, such as the SEBAL method, depends on ground-based data availability; which can limit their uses in poorly-monitored, tropical wet representative basins.

More importantly, most of the aforementioned studies were conducted in regions under semiarid or continental climates where precipitation tends to be scarce or moderate in amount, respectively. As a result, the performance of these approaches could be checked in regions under clear-sky conditions, but not comprehensively under cloud-sky conditions (as typical for tropical wet basins), and that is why the quality of estimates of satellite-based water balance components turns out to be substantially affected (Luo et al., 2015).

Therefore, those situations reveal an important lack of knowledge by using remote sensing products for GWR estimation in tropical wet basins, which calls for the development of an enhanced GIS-based model that copes with their particular characteristics.

## **2.3 Soil moisture assimilation based on Cosmic-Ray Neutron Sensing**

Soil moisture plays a vital role in the water cycle, influencing climate and weather conditions (Wu and Dickinson, 2004), as well as determining surface runoff after precipitation events, and controlling the GWR. Despite the importance of soil moisture, there is still a lack of high-quality soil moisture data (Vereecken et al., 2016), even though a wide range of invasive, point-based measurement sensors are available, such as TDR probes (Graeff et al., 2010). There still are other techniques that can deliver large-area soil moisture estimates using remote sensing products, such as SMAP mission (Entekhabi et al., 2010). In addition, soil water storage estimates obtained from GRACE satellite data may provide a satisfactory representation of soil water storage changes for large areas (de Oliveira et al., 2014). Nevertheless, these satellite techniques – with exception of GRACE – assimilate soil moisture data just in near-surface layers and with low spatial resolution.

For overcoming this limitation, the CRNS method (Zreda et al., 2008) is one of the most promising techniques concerning soil moisture monitoring in the rooted zone at field scale (Brocca et al., 2017; Schrön et al., 2017). CRNS probes can continuously measure mean soil moisture over several hectares and down to about half a meter depth (Köhli et al., 2015; Zreda et al., 2012). The CRNS method is one of the few candidates to close the inconvenient scale gap between ground-based point data and remote sensing products (Bogena et al., 2015; Robinson et al., 2008), making it attractive for studies at experimental basins.

### **2.3.1 Theory of the Cosmic-Ray Neutron Sensing**

Primary cosmic-ray particles consist mainly of high-energetic protons and helium nuclei derived permanently from supernovae, throughout the Milky Way (galactic cosmic rays) and eventually from the Sun (solar cosmic rays) (Vink et al., 2006; Blasi, 2014). They are also derived secondarily from extragalactic origins, where long-living jets and outflows from active galactic centers can contribute to post-acceleration of cosmic-rays (Dorfi and Breitschwerdt, 2012). The main acceleration processes of thermal cosmic-rays are the multiple diffusive shocks occurring in supernovae remnants (Blandford and Ostriker, 1978; Malkov and Drury, 2001; Hillas, 2005), whose strong magnetic gradient forces make them spin and accelerate until enough energy is reached to leave the structure, peaking at about 1 GeV and quickly decreasing logarithmically (Cronin, Gaisser and Swordy, 1997; Schrön, 2016) (Figure 14). However, once in the heliosphere, the galactic cosmic ray particles are

strongly influenced by the solar magnetosphere, where the solar activity index prevails upon the cosmic-ray intensity (Forbush, 1954; Schlickeiser, 2002). By reaching the Earth magnetosphere, the solar cosmic ray particles are partially or even nearly completely deflected when below an energy-dependent cut-off rigidity (Forbush, 1954; Köhli et al., 2015). As a result, the typical incoming radiation energies are diminished to several hundreds of MeV per nucleon (Nesterenok, 2013).

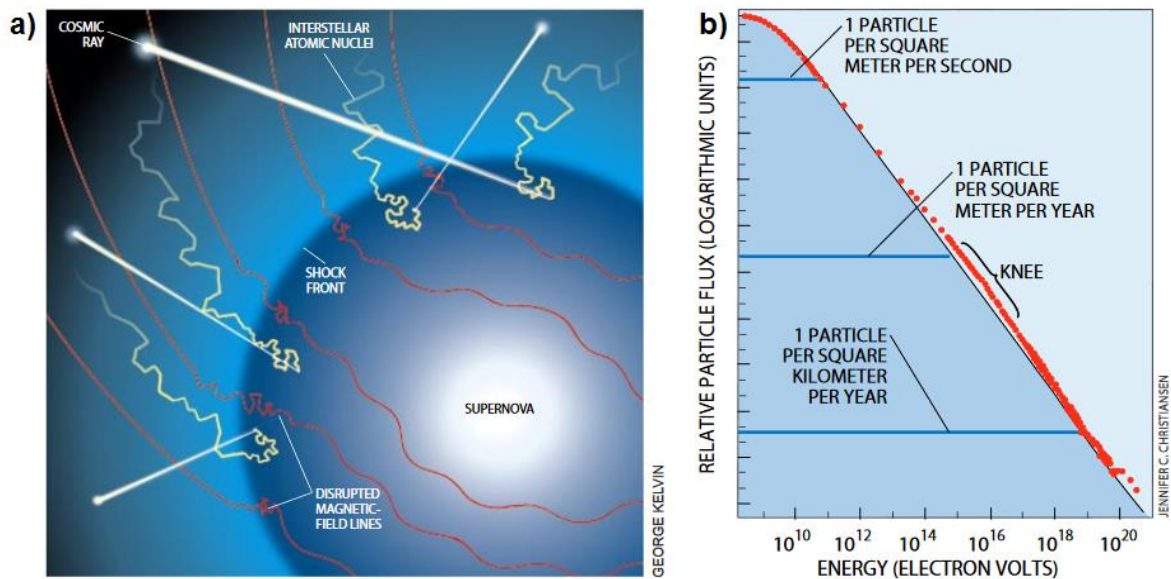


Figure 14 – Galactic cosmic rays acceleration process by (a) disturbed magnetic fields in dense shock regions of supernova remnants, depicted by the (b) cosmic-ray energy spectrum with typical energies of 1 GeV, indicating extra-galactic processes beyond the “knee” (or bend). Source: Cronin, Gaisser and Swordy (1997).

Secondary cosmic-ray particles originate from the electromagnetic and nuclear interactions of primary cosmic rays that penetrate the outer part of the Earth atmosphere. The primary cosmic rays then collide with atomic nuclei, mainly nitrogen and oxygen (Letaw and Normand, 1991), losing energy by ionization interactions, exploding particle nuclei, and producing cascades of protons, neutrons and other subatomic particles, such as mesons, pions, and alpha particles (IAEA, 2017; Lal and Peters, 1967; Villarreyes, 2013). Secondary neutrons are high-energy neutrons (energy up to 10 MeV), which multiply at number but decelerate in energy as a chain reaction when they move down towards Earth surface. As a result, eventually, they no longer propagate effectively being absorbed or moderated in an exponential radiation attenuation that depends on the atmospheric column and its composition (Phillips, Stone and Fabryka-Martin, 2001). According to Krane (1988), they are following classified into energy level classes (Figure 15), namely: (1) thermal



neutrons ( $\sim 0.025$  eV); (2) epithermal/fast neutrons ( $\sim 1$  eV -  $\sim 100$  keV) (3) fast evaporation neutrons ( $\sim 100$  keV – 10 MeV).

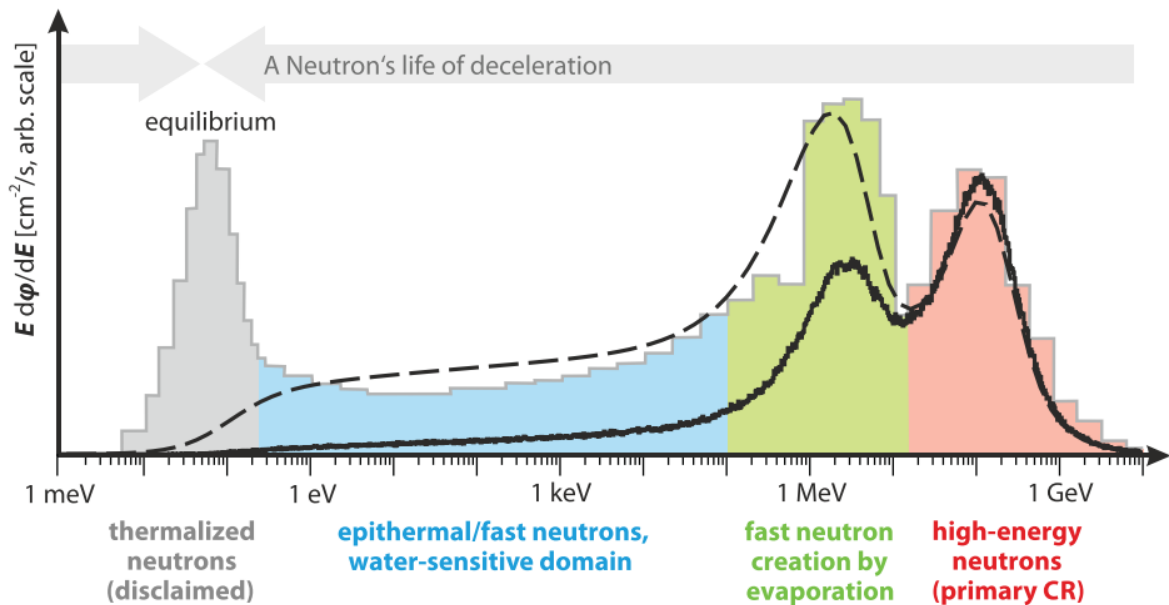


Figure 15 – Energy spectra of detected neutron counts at the soil surface coloured according to initial high-energy neutron deceleration after the atom collisions. Solid line: pure incoming component after subtracting the ground reflected component. Vertical coordinate: neutron counts; dashed line: simulation by Sato and Niita (2006); Grey bars: exemplary measurement by Goldhagen et al. (2002). Source: Köhli et al. (2015).

Fast evaporation, cosmogenic neutrons originate from interactions of high-energy neutrons or protons with nuclei in the atmosphere and first few meters of the Earth crust after penetrating the soil porous media, in a nuclear evaporation process (Desilets and Zreda, 2013) (Figure 16). When a secondary cascade particle collides with terrestrial nuclei (H, N, O, C, Al and Si), those simply heat up rather than immediately bursting into fragments but then cool off rapidly by releasing (evaporating) fast neutrons in random directions (IAEA, 2017). After several collisions, the unbound neutrons lose most of the energy and eventually are captured by terrestrial nuclei, ceasing to contribute to the environmental radiation. This process occurs below the  $\sim 1$ -MeV peak, whose strong absorption is due to distinct resonances of non-hydrogen atoms (Köhli et al., 2015).

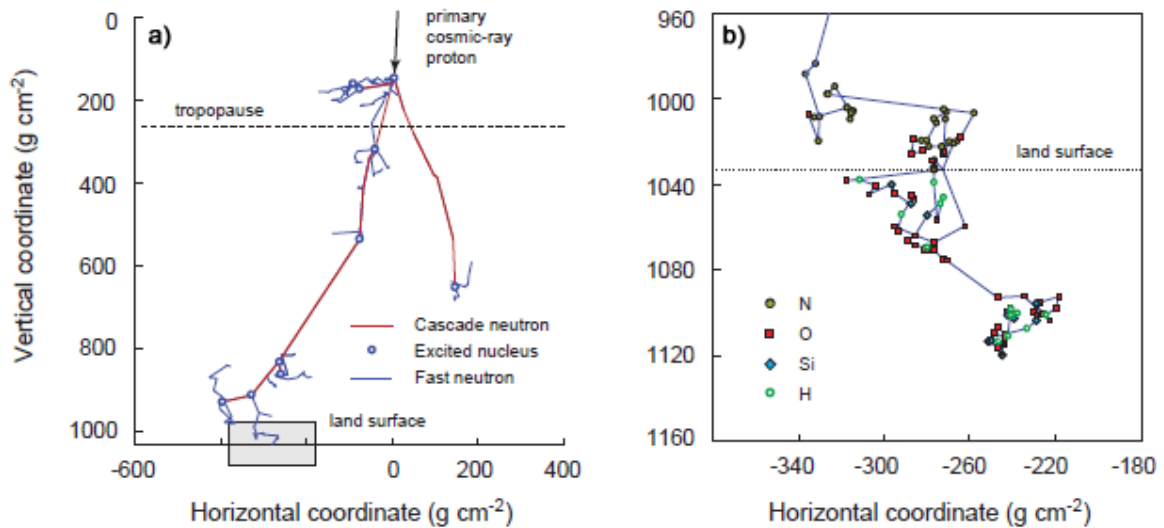


Figure 16 – Cascade of high-energy secondary neutron and production of fast neutrons in (a) air and (b) ground. Coordinates are in mass shielding units (distance multiplied by density). Source: adapted from Desilets, Zreda and Ferré (2010) and IAEA (2017).

Epithermal/fast neutrons mostly originate from elastic collisions moderated mainly by hydrogen atoms above soil surface due to relatively large elastic scattering cross-section (Sears, 1992) (Figure 17). Because neutrons and the hydrogen atoms have similar mass, a number of collisions is needed to moderate epithermal/fast neutrons, so that it can be directly correlated to their intensity. These characteristics confer to hydrogen a very high capacity to slow down epithermal/fast neutrons, leading the sub-MeV region to be a very sensitive band to water and organic molecules, because they contain hydrogen (Köhli et al., 2015). From the different types of natural neutrons, those at the fast energy level present the better estimation of soil moisture (Zreda et al., 2008).

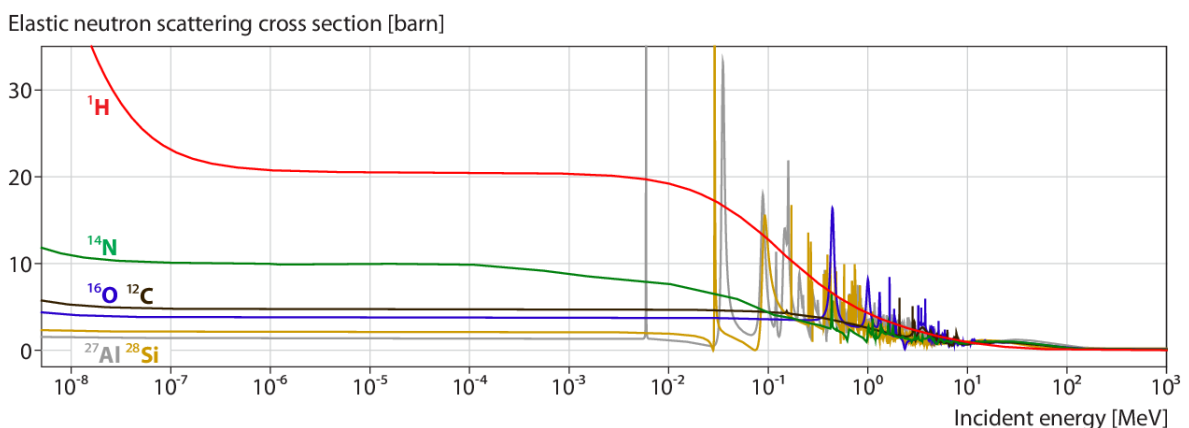


Figure 17 – Elastic neutron scattering cross sections for Hydrogen (red) and other chemical elements. H: Hydrogen; N: Nitrogen; O: Oxygen; C: Carbon; Al: Aluminum; Si: Silicon. Source: Köhli et al. (2015).

Thermal neutrons originate from progressive elastic collisions with hydrogen and other light nuclei, which remove them from the system since they are slowed to thermal equilibrium being prone to be captured by the nearby nuclei (Heidbüchel, Güntner and Blume, 2016; Köhli et al., 2015). Absorbing elements are mainly Fe, Ca, K and some trace elements, on top of them being scattered by hydrogen, the thermal neutron intensity is sensible to soil chemistry but less to soil water changes (IAEA, 2017; Zreda et al., 2008). Thus, the CRNS probes can register the neutron intensity by two channels (Figure 18): (1) a moderated counter, which responds to neutrons in epithermal to fast (soil moisture) regions, avoiding non-hydrogen-atoms dependency on soil chemical composition; and (2) a bare counter, which responds to neutrons in thermal (soil chemistry) regions, but also may be used to correct and calibrate the moderated counter signal.

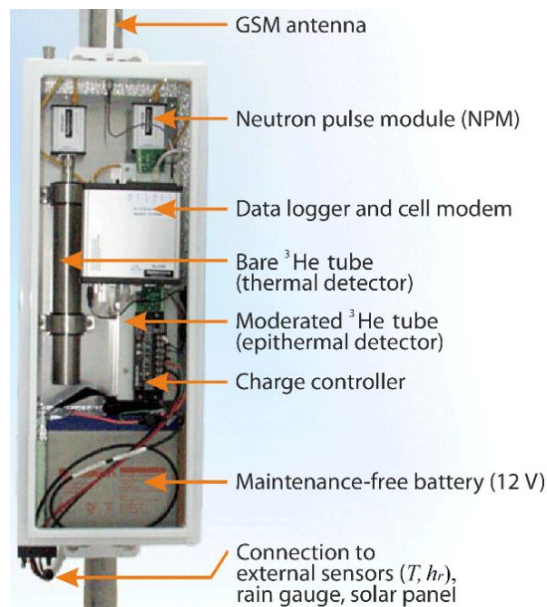


Figure 18 – Components of the CRNS probe, CRS 1000 model, Hydroinnova Ltd. <sup>3</sup>Helium is used as counter gas. NPM: Neutron Pulse Module. Source: adapted from Schrön et al. (2018).

Since the number of hydrogen atoms in soil rises with increasing soil moisture, these soils with high water content re-emit fewer epithermal/fast neutrons than soils with low water content. This leads to fewer fast neutrons being detected aboveground by the CRNS probe, which is generally installed at 1 to 2 m above the soil surface (Heidbüchel, Güntner and Blume, 2016). In addition, water vapour, oxygen, and nitrogen are particularly responsible for the neutron deceleration in air, so that the range a neutron can travel before thermalization is expected to diminish with decreasing altitude and increasing air humidity (Köhli et al., 2015). Additionally, dense soils, organic matter, and soil moisture are expected to reduce the penetration depth into soil (Köhli et al., 2015).

### 2.3.2 Applications of the Cosmic-Ray Neutron Sensing

The first study using cosmogenic neutrons for soil moisture measurement was conducted by Kodama, Kudo and Kosuge (1985) by burying a neutron probe at 40-cm depth into the soil, but this covered a short soil area of less than 1-m radius. Zreda et al. (2008, 2012) found a much higher areal sensitivity to soil moisture of several hectares when a CRNS probe was installed aboveground and defined the footprint to be the area around the sensor where 86% of detected neutrons originate from (Desilets and Zreda, 2013). According to Köhli et al. (2015), the footprint radius ranges from 130 to 240 m depending on air humidity, soil moisture, and vegetation (Figure 19). In addition, the penetration depth depended on moisture and ranged from 15 to 83 cm decreasing exponentially downwards from the sensor. Thereby, CRNS method can fill the gap between the conventional point-scale (electromagnetic sensors) and large-scale measurement (satellite sensing) methods (Bogena et al., 2015).

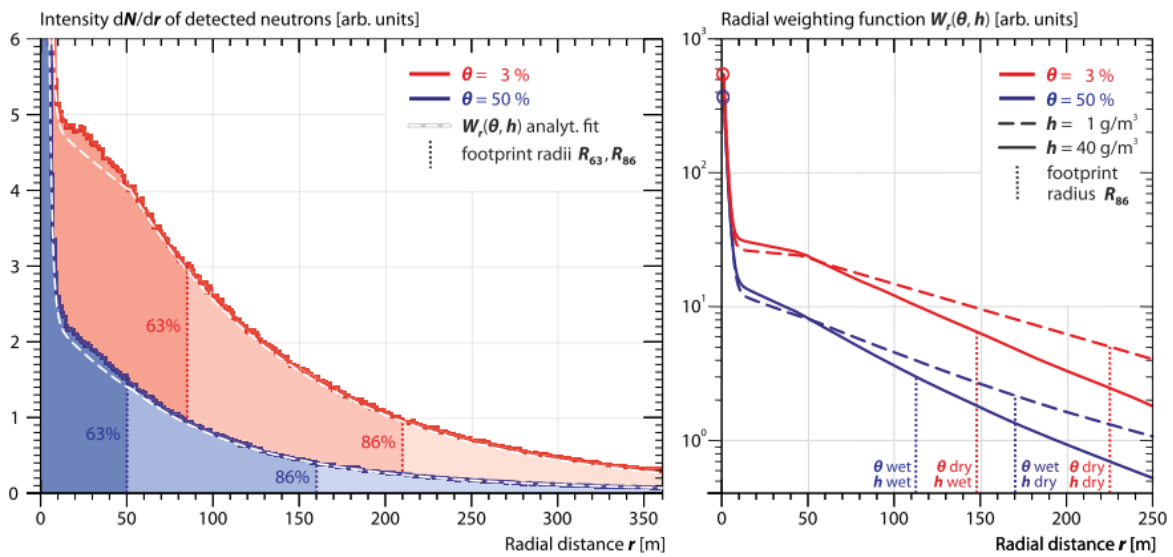


Figure 19 – Simulation of (a) neutron intensity detected over distance from the CRNS probe, and of (b) radial weighting function, for dry and wet conditions.  $\theta$ : soil moisture;  $h$ : absolute humidity;  $N$ : detected neutron;  $r$ : radial distance;  $W_r$ : radial weighting function;  $R_{63}/R_{86}$ : footprint radii for 63% and 86% cumulative neutron counts. Source: Köhli et al. (2015).

Background cosmic radiation holds an inverse relationship between cosmic-ray neutrons intensity and all closer hydrogen content pools (Desilets, Zreda and Ferré, 2010; Hendrick and Edge, 1966), affecting the CRNS signal statically, quasi-statically and dynamically (Andreasen et al., 2017a) (Table 1). The hydrogen pools affecting CRNS signals are: (1) subsurface water (Andreasen et al., 2017b), such as soil moisture and lattice

water; (2) open water (Köhli et al., 2015), such as sea, lake, river and puddles; (3) vegetation biomass (Franz et al., 2013a) such as stems, leaves, roots, fruits and also soil organic matter; (4) canopy water interception (Baroni and Oswald, 2015), anthropogenic infrastructure (Schrön et al., 2017), such as buildings, tanks and roads; (5) snow cover (Rivera Villarreyes, Baroni and Oswald, 2011; Schattan et al., 2017), and (6) atmospheric humidity (Köhli et al., 2015).

Table 1 – The hydrogen pools influencing the CRNS signal and its dynamics. Source: Andreasen et al. (2017b).

Medium	Static (yearly)	Quasi-static (sub-yearly)	Dynamic (daily)
Soil moisture			×
Tree roots		×	
Soil organic matter		×	
Water in soil minerals	×		
Vegetation (cellulose, water)		×	×
Snow		×	×
Puddles			×
Open water (river, sea, lake)		×	
Canopy-intercepted water			×
Buildings/roads	×		
Atmospheric water vapour			×

New perspectives of promising methods for separating the different hydrogen pool signals have been developed and tested aiming for further hydrological applications (Andreasen et al., 2016). The recently-started *Cosmic Sense* research project in Germany (<https://www.uni-potsdam.de/cosmicsense/>) aims at bridging existing gaps between scales and disciplines, applying CRNS method together with remote sensing, hydrological and land-surface models, to infer also GWR and atmospheric fluxes (Figure 20). The non-invasive character still confers to CRNS technique the roving capacity for regional soil moisture estimates (Chrisman and Zreda, 2013; Dong et al., 2014). The neutron ratio between thermal neutron and fast neutron intensity contains also information on other hydrogen pools such as vegetation dynamic, canopy interception, and snow (Jakobi et al., 2018). Thus, the singular potential of CRNS method requires a greater investigation for averaging soil moisture, which includes calibration functions for soil moisture estimation, correction factors, and footprint analyses (Andreasen et al., 2017a).

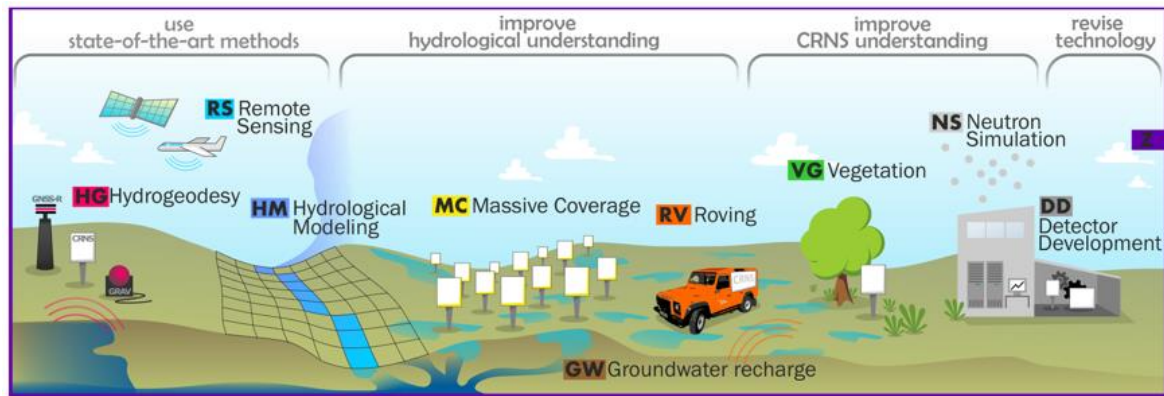


Figure 20 – Range of applications of CRNS probes and related activities in the *Cosmic Sense* research project. Source: <https://www.uni-potsdam.de/de/cosmicsense/about/structure-of-cosmic-sense.html>

The performance of the CRNS method can be improved by calibrating it from the theory described by Desilets, Zreda and Ferré (2010) based on one-field-dependent and three-semi-physical parameters. The integrative character of CRNS signal to wetting and drying cycles shows a good agreement between neutron intensity and gravimetric soil moisture observations when averaged by horizontal and vertical weighting (Franz et al., 2012a, 2013b; Köhli et al., 2015). As a result, only one calibration campaign would *a priori* be enough to calibrate the field-dependent parameter while the semi-physical ones would hold fixed values (Desilets, Zreda and Ferré, 2010). Conversely, some studies have proposed and tested at least two calibration campaigns at dry and wet conditions for either better calibrate the CRNS probes or recalibrate the fixed parameters (Heidbüchel; Güntner; Blume, 2016; Iwema et al., 2015; Rivera Villarreyes, Baroni and Oswald, 2013). Zreda et al. (2008) proposed a widely-applied soil sampling scheme composed by three concentric circles around the CRNS probes at 25, 75, and 200 m radii, intersected by six straight lines equally spaced for 60° from azimuth reference. Moreover, Schrön et al. (2017) proposed a revised formulation of the spatial sensitivity function, so-called the weighting function, for improving CRNS calibration, which takes into account for dry, humid and wet conditions on its footprint (Figure 21).

According to Andreasen et al. (2017a), important networks of CRNS probes have been installed worldwide, mainly on the Northern Earth hemisphere and almost none close to the equator (Figure 22), accounting for 194 stationary stations making the data openly available, namely: (1) COsmic-ray Soil Moisture Observing System (COSMOS) network (Zreda et al., 2012); (2) the United Kingdom COSMOS-UK network (Evans et al., 2016); (3) the Australian CosmOz network (Hawdon, Mcjannet and Wallace, 2014); and, (4) parts



of the Terrestrial Environmental Observatories (TERENO) network in Germany (Baatz et al., 2014).

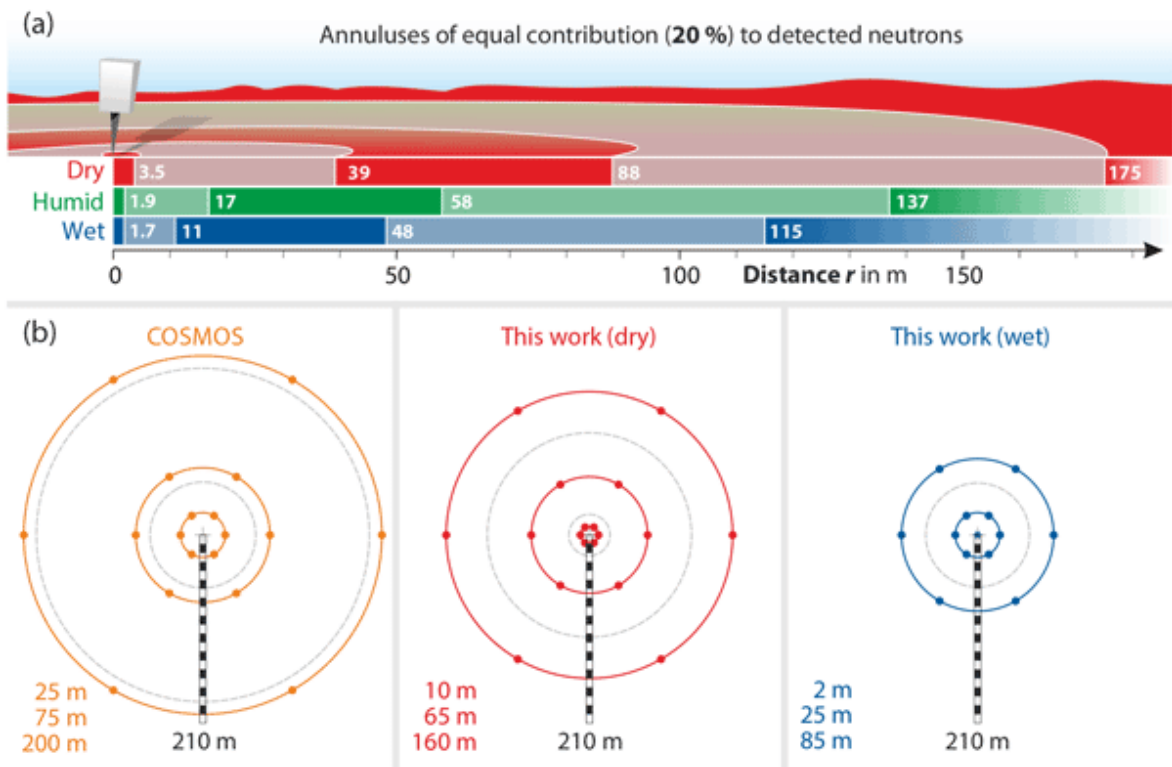


Figure 21 – Illustration of (a) equally-detected neutron contribution regions for different climates, and (b) comparative triple-quantile-radii soil sampling schemes based on COSMOS scheme (yellow) and on the revised weighting function for dry and wet condition. COSMOS: Cosmic-ray Soil Moisture Observing System. Source: Schrön et al. (2018).

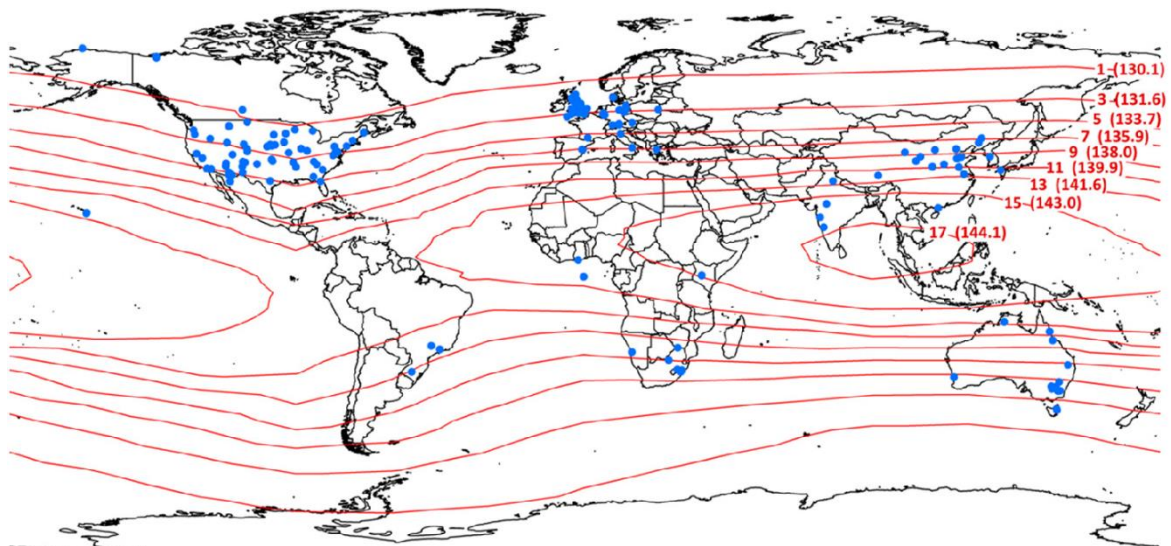


Figure 22 – CRNS probes operated within the COSMOS network initiative (blue dots), with the cutoff rigidity and the attenuation length isolines in 2010 for incoming primary cosmic rays in red. Northern Brazil has a cut off rigidity similar to China, Northern Australia or Southern Africa, though being close to the equator. Source: Andreasen et al. (2017a).

## 2.4 Vadose zone modelling

### 2.4.1 Inverse modelling of the soil hydraulic properties via HYDRUS-1D model

Understanding how near-surface soil moisture is affected by land surface net water flux (i.e., infiltration minus evapotranspiration) allows for a more comprehensive modelling of GWR (Sadeghi et al., 2018), whose simulations depend fundamentally on soil hydraulic properties which should be known. Some existing vadose zone models, such as HYDRUS-1D, solve the governing flow equations for partially-saturated porous media by simulating water flux via Richards' nonlinear partial differential equation (Šimůnek, van Genuchten and Šejna, 2008). These models can hold pedotransfer functions, which yield soil hydraulic properties, such as the van Genuchten-Mualem (shape and normalization) parameters and unsaturated hydraulic conductivity. After calibrating the soil hydraulic properties (retention curve and hydraulic conductivity curve), the models should be even better suited to calculate vertical water percolations (Wessolek, Duijnisveld and Trinks, 2008).

According to Vogeler et al. (2019), many hydraulic databases have compiled soil hydro-physical data for different soil types and textures allowing for modelling applications, namely: the Unsaturated SOil hydraulic DATabase (UNSODA) (Nemes et al., 2001); the EUROpean HYdropedological Data Inventory (EU-HYDI) (Weynants et al., 2013); the Soil Water Infiltration Global (SWIG) database (Rahmati et al., 2018); Rosetta (Schaap, Leij and van Genuchten, 2001); and HYdraulic PROPERTIES of European Soils (HYPRES) (Wosten et al., 1999). In Brazil, Ottoni et al. (2018) recently established a dedicated Hydrophysical Database for Brazilian Soils (HYBRAS) suitable for the development of pedotransfer functions. However, these databases not always reflect the local characteristics of each study area, thus requiring another approach.

Inverse modelling seems to be a suitable solution as it may optimize the parameter calibration of the soil hydraulic properties from direct or indirect measurements of physical entities (Šimůnek, van Genuchten and Šejna, 2016; Tarantola, 2005). Nevertheless, for a well-posed inverse problem, three conditions should be satisfied: existence, uniqueness, and stability of the solutions (Maclaren and Nicholson, 2019). For such purpose, it is important that the model uses an inverse approach capable of quantifying and evaluating the prediction uncertainty, particularly for complex systems, where the observations are limited, models reflect imperfectly the processes, and unknown parameters and observable variables have nonlinear and non-unique relationships (Sun et al., 2013).



Graham et al. (2018) compared four different methods of parameterisation of the soil hydraulic properties and found that inverse parameter estimation based on field soil moisture data yielded the best prediction of drainage by the HYDRUS-1D model. Vogeler et al. (2019) found the good performance of inverse modelling on determining the soil hydraulic conductivity in slowly permeable subsoil horizons, such as fragipan and duripan. And, Børgesen et al. (2006) claim that under near-saturated condition, such as shallow groundwater table, the relationship between hydraulic conductivity and soil moisture is very important when simulating water movement in the unsaturated zone. Thereby, under all these local environmental constraints (which actually are the conditions at GEB), the HYDRUS-1D is able to calibrate the soil hydraulic properties by inverse modelling.

Brunetti et al. (2019) externally coupled the forward neutron operator COSMIC (COsmic-ray Soil Moisture Interaction Code) (Shuttleworth et al., 2013) into HYDRUS-1D, allowing for directly using CRNS neutron intensities for calibrating the parameters of the soil hydraulic properties. According to Shuttleworth et al. (2013), COSMIC is a simple, physically-based and analytic operator capable to represent the following main processes (Figure 23): (1) exponential reduction of high energy neutron flux towards deeper soil layers, (2) fast neutron generation from high energy neutrons at different depths, and (3) additional depth-dependent reduction of lower energy neutrons before they are detected at the surface. The code then counts the resulting fast neutrons that enter a defined detector volume above the ground, which is perfectly compatible with CRNS method (Shuttleworth et al., 2013; Brunetti et al., 2019). COSMIC requires several site-independent and site-specific time-constant parameters, among which the latter ones may be inferred from dry bulk density, total lattice water content, and empirical equations (Baatz et al., 2014). The use of CRNS data and COSMIC coupled externally with HYDRUS-1D allows for obtaining the soil hydraulic properties on intermediary-scale by inverse modelling, which should better represent the soil characteristics for water flux modelling purposes.

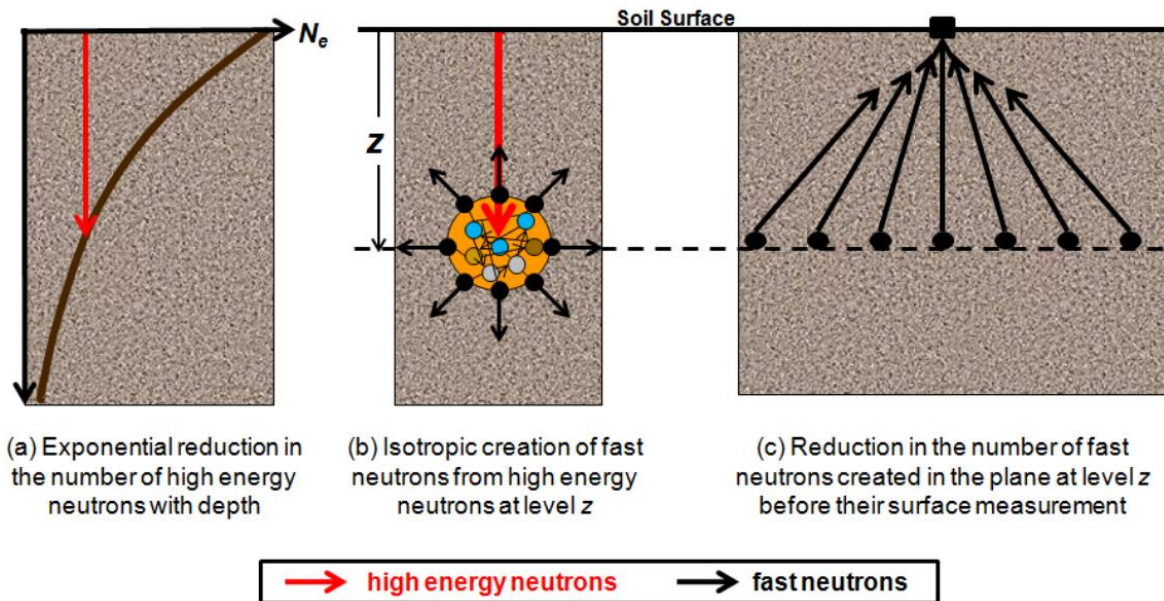


Figure 23 – Three main physical processes as considered in the COSMIC model for simulating the aboveground fast neutron intensity. Source: Shuttleworth et al. (2013).

#### 2.4.2 Water flux modelling via HYDRUS-1D model

HYDRUS-1D and HYDRUS (2D/3D) models have a user-friendly, interactive interface based on graphics for information pre-processing, soil profile discretisation, and graphical outcome representation (Šimůnek and van Genuchten, 2008; Šimůnek, van Genuchten and Šejna, 2008) (Figure 24). HYDRUS is a model recognized for its many applications implemented in the finite element method for one-, two- and three-dimensional simulations (Šimůnek, van Genuchten and Šejna, 2016). The HYDRUS programs are applicable for modelling the water and solute transport in saturated and variably-saturated systems, and they are also widely used to assess the transport and fate of several chemicals on top of conservative transport, especially in the vadose zone between the soil surface and groundwater table (Šimůnek et al., 2013a). The popularity of the HYDRUS models is in part due to the implementation of a large number of processes in their codes, their flexibility in allowing its application to a broad range of agricultural, industrial and environmental problems, the possibility to consider inverse (parameter estimation) problems, and their ease of use (Šimůnek et al., 2013a; Šimůnek, van Genuchten and Šejna, 2016).

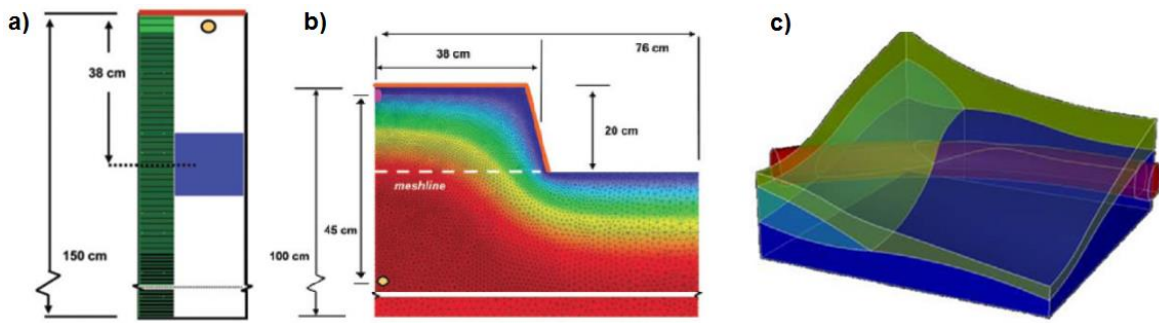


Figure 24 – Soil discretization available for (a) an one-dimensional domain in HYDRUS-1D, as well as for (b) two-dimensional and (c) three-dimensional domains in HYDRUS (2D/3D). Source: Šimůnek, van Genuchten and Šejna (2016).

Recent developments on HYDRUS-1D have also allowed for considering different processes from the vadose zone in hydrological modelling, among which the following are highlighted: Root Water Uptake (RWU), soil heat transport and variable bottom boundary condition (Šimůnek, van Genuchten and Šejna, 2016). RWU is controlled by the root density distribution that is influenced by the average vegetation rooting (Hoffman and van Genuchten, 1983; Van Genuchten, 1987). The average rooting in typical native vegetation in Northeast of Brazil reached ~70 cm (Pinheiro, Costa and de Araújo, 2013), which affects the soil moisture profiles and, in turn, the vertical water percolation (MABC, 2015; Narasimhan, 2009). The soil heat flux of HYDRUS-1D encompasses molecular heat conduction and convective heat transport by liquid water flux and water vapour flux (Iden et al., 2019; Šimůnek et al., 2013b), requiring the calibration of specific parameters (Chung and Horton, 1987).

For simulating the vertical water percolation and GWR under a shallow groundwater table condition the way setting the lower boundary condition, however, may be more important than properly adjusting the soil hydraulic properties (Wang et al., 2009). Variations on boundary conditions in pure phase (non-aqueous) and interlayered one-dimensional profiles may cause significant deviations in water fluxes, soil moisture and hydraulic conductivities (Leão and Gentry, 2011). As such, the water percolation time-lag between infiltration and GWR was found to be related to depths to groundwater table (Lu et al., 2011). In addition, the capillarity rise from the groundwater table may have strong effects on plant transpiration (Han et al., 2015). Evapotranspiration and GWR are then controlled by the lower boundary condition under shallow groundwater systems (Doble and Crosbie, 2016). All those conclusions were drawn from HYDRUS-1D simulations, showing its capacity on estimating the water percolation and GWR in field conditions similar to GEB.

## 2.5 Uncertainty and validation of the water balance components

Uncertainty is the lack of exact knowledge that, irrespective of what is the cause of this model deficiency, may stem from natural variability, inherent randomness, systematic error, subjective judgement, model characteristics and measurement error (Refsgaard et al., 2007; Regan, Colyvan and Burgman, 2002). The best way to evaluate the uncertainty depends on the model selection and from the quantity and quality of data available to the modeller (Uusitalo et al., 2015). In hydro-meteorological sciences, the atmospheric processes have chaotic characteristics which yield uncertainties in hydrological variables, whose instability in the initial condition determination influences the modelling results of meteorological variables (Gusev et al., 2016). While the primary source of uncertainties on hydro(geo)logical response may arise from errors in the satellite-based precipitation data, the uncertainties on water balance components are mainly due to the inconsistent monitoring of hydro-meteorological data (de Oliveira et al., 2014; Sheffield et al., 2009). Hence, although the remote sensing is a useful tool able to yield good regional estimates, the use of consistent ground-based measurements is still indispensable for validating the water balance components, whose monitoring requires high costs and suffer with data transparency and accessibility (Sheffield, Wood and Roderick, 2012; Voss et al., 2013).

Several methods have been used to analyse uncertainties and validate the outputs of deterministic models, among which are expert judgement, analysis of model sensitivity, analysis of spatiotemporal variability, and statistical methods (Uusitalo et al., 2015). Within the hydro-meteorological fields, the data-based approaches are frequently used for validation due to data availability, which allows for a statistical assessment upon the model outputs (Steenbergen, Ronsyn and Willems, 2012). For validating the water balance components, several ground-based techniques have been used for analysing the uncertainties of those model-based and remote sensing estimates. For example, for the actual evapotranspiration, there exist the Bowen ratio-energy balance and lysimeter approaches (Escarabajal-Henarejos et al., 2015), as well as the large aperture scintillometers and the eddy covariance systems (Liu et al., 2013). Moreover, for the GWR, there exist several ground-based methods available, among which stands out the tracer techniques, such as the Chloride Mass Balance (CMB) method (Crosbie et al., 2018; Hornero et al., 2016), and the WTF method (Healy and Cook, 2002; Cai and Ofterdinger, 2016; Chung et al., 2016). Still for GWR, a comparative study applying multiple methods revealed that the uncertainties of estimates depend on several aspects, namely: spatiotemporal scales; inherent uncertainty of the method, and; what

recharge represents (actual, potential, minimum recharge or change in aquifer storage) (Walker et al., 2019).

The WTF is frequently used to validate the GWR estimates due to the small variety of monitoring data required for. There exist three commonly-used WTF methods: graphical method, RISE method, and Master Recession Curve (MRC) method (Nimmo, Horowitz and Mitchell, 2015). The graphical method calculates the GWR on hydrologic episode scale, from the difference between the water table peak and the extrapolated recession curve, depending strongly on expert judgement (Scanlon, Healy and Cook, 2002). The RISE method calculates the GWR on fixed-time intervals, when the differences between the water table at the end and beginning of the interval is positive, lacking on recession curve correction (Delin et al., 2007). The MRC method also calculates GWR on fixed-time intervals, but the recharge episode is defined as a period during which the recharge exceeds its steady-state condition due to a substantial water-input event (Nimmo, Horowitz and Mitchell, 2015). Recently, a modified WTF method was also proposed to characterize the regional groundwater discharge patterns in stressed aquifers resulting from intensive agricultural pumping (Yang et al., 2018).

### 3 HYPOTHESES AND AIMS

#### 3.1 Main hypotheses

The hypotheses that oriented the activities of this PhD thesis are following described:

- Large-scale groundwater recharge may be estimated via water budget equation in tropical wet regions under cloudy-sky condition using the distributed information of water balance components obtained solely by satellite products and reanalysis data;
- Intermediary-scale groundwater recharge may be estimated via a soil hydrological model after the inverse modelling of the parameters of soil hydraulic properties from soil moisture datasets based on Cosmic-Ray Neutron Sensing and invasive probes.

#### 3.2 Overarching aim

This PhD thesis aims, on the one hand, to demonstrate a GIS-based model coupling for estimating the groundwater recharge distribution in a large tropical wet region, by using remote sensing satellite products and reanalysis data rather than ground-based monitoring data. On the other hand, it also aims to use the soil moisture time series from Cosmic-Ray Neutron Sensing and invasive probes to inversely calibrate the soil hydraulic properties, and based on this, estimating the intermediary-scale GWR using a soil hydrological model.

#### 3.3 Specific aims

The specific aims for accomplishing the overarching aim are listed below:

- Establish the necessary improvements on hydrological methods for modelling the tropical wet regions with cloudy-sky condition and complex sedimentary aquifer;
- Assess the spatiotemporal distribution of the water balance components obtained solely by satellite products and reanalysis data through geoprocessing in GIS;
- Determine the soil hydraulic properties via inverse modelling from soil moisture datasets based on Cosmic-Ray Neutron Sensing and invasive probes;
- Compare the groundwater recharge rates simulated on large- and intermediary-scale via water budget equation approaches in the Podzol soil type;
- Verify the goodness-of-fit of the water balance components and groundwater recharge estimates via ground-based methods and monitoring data.

## 4 MATERIALS AND METHODS

The methodology was subdivided according to the overarching and specific aims previously set up. However, information about the study areas and ground-based data sources are addressed upfront.

### 4.1 Study areas

This study was carried out in the João Pessoa Case Study Area (JPA CSA), metropolitan capital of the Paraíba state within the Northeast of Brazil, implemented at the end of 2014 by the BRAMAR project (Figure 25a,b,c). JPA CSA embraces a total area of 1,032 km<sup>2</sup>, between 7°09'22.55"–7°24'31.82"S and 34°50'21.36"–35°13'15.03"W, and comprehending the Gramame river basin (589.1 km<sup>2</sup>) and the right-bank downstream part of Paraíba river basin (442.9 km<sup>2</sup>), located within the Paraíba-Pernambuco sedimentary coastal aquifer. It is located in the Atlantic Forest biome and holds a tropical wet climate with dry summer (As) (Alvares et al., 2013; Köppen, 1936), with land use/cover traces of the semiarid transition zone.

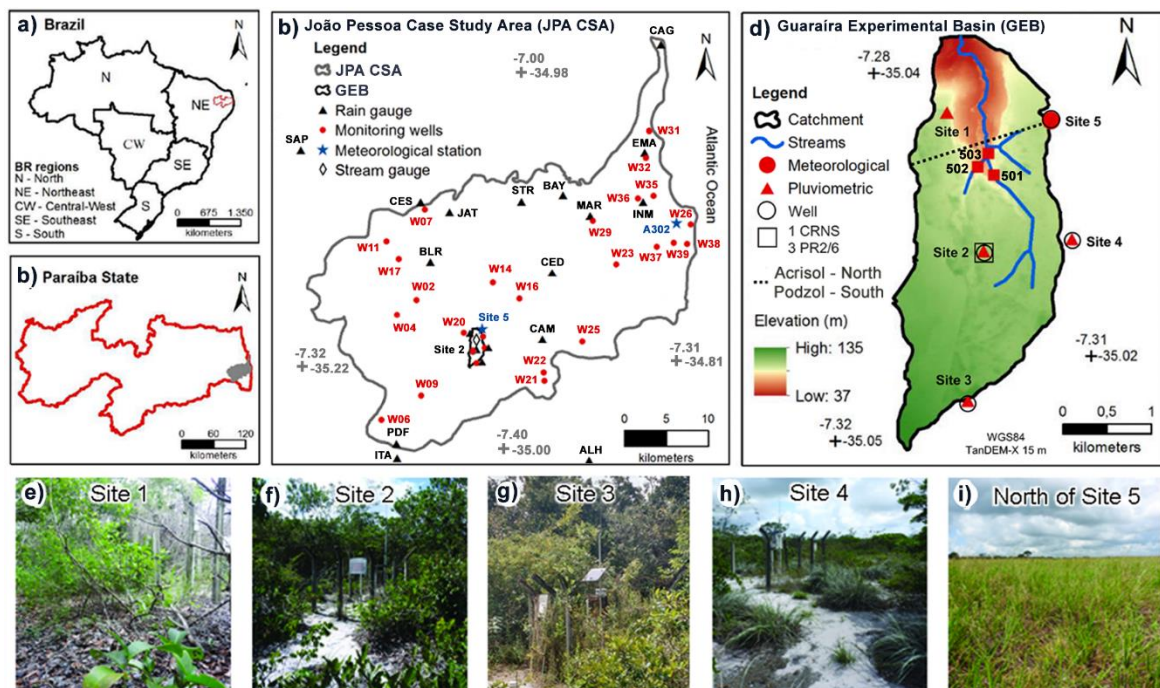


Figure 25 – Location of the (a) Northeast of Brazil, (b) Paraíba state, (c) João Pessoa Case Study Area (JPA CSA), and (d) Guaraiá Experimental Basin (GEB) with hydrogeological monitoring network, displaying photos of the (e, f, g, h, i) monitoring sites (1, 2, 3, 4, 5), respectively.



In JPA CSA, the precipitation is formed mainly by shallow convective clouds, registering the mean annual depth equal to ~1,700 mm, of which ~70% occurs throughout the rainy season that comprises five months (March to July) during the autumn and winter seasons (Barbosa et al., 2018). The mean air temperature ranges from 23.7 (July) and 28.2°C (January), and the mean relative humidity ranges from 67% (September) to 87% (July). The original native vegetation in JPA CSA comprises 147.78 km<sup>2</sup> (13.89% of area), less than sugarcane (347.45 km<sup>2</sup>, 32.66%) and area of high urban density (162.55 km<sup>2</sup>, 15.28%), but higher than grassland (108.63 km<sup>2</sup>, 10.21%), the remaining land uses are described by Fernandes (2017). It also features a mean evaporation rate equal to 1,300 mm yr<sup>-1</sup> obtained by class-A pan around grassland, and mean potential evapotranspiration rate over João Pessoa city reaching ~1,500 mm yr<sup>-1</sup> (Almeida et al., 2017; Cabral da Silva et al., 2000a).

The Guaraíra Experimental Basin (GEB) is a small-scale watershed that was implemented in 2003 by IBESA project within the JPA CSA (Figure 25d) It covers an area of 5.84 km<sup>2</sup>, between in 7°16'34.94"–7°19'10.85"S and 35°01'17.79"–35°02'26.95"W, whose eastern border holds off ~25 km from the shoreline, at upstream of Gramame-Mamuaba dam (volume of 56.94 hm<sup>3</sup>), which supplies freshwater to more than 70% inhabitants of João Pessoa city (AESAs, 2010). The elevation in GEB ranges from 37 to 135 m, featuring a mean slope equal to 1.8%. It consists of Quaternary-age sediments originating from the regional basement erosion, whose soil texture consists of sand (70%), sandy loam (26%) and sandy clay loam (4%) (Santos, Silva and da Silva, 2012). The vegetation cover is composed by secondary-growth vegetation (Capoeira xeric-shrubland vegetation) (67%), Atlantic Forest remnants (4%) and grassland (1%), while the anthropic land use consists mostly of sugarcane crops (27%), with small pineapple crops (1%), and few unpaved roads (IBESA, 2004; Santos, Silva and da Silva, 2012) (Figure 25e to i).

The aforementioned study areas may be seen as partly representative of other shallow aquifers with similar hydrogeological and climate characteristics in the Northeast of Brazil. Nevertheless, these areas have been investigated by few studies related to groundwater yet, especially regarding the application of new technologies for GWR estimation.

## **4.2 Sources of the ground-based data**

The data required for this study are periodically collected by team members of the Laboratory of Water Resources and Environmental Engineering (LARHENA) at UFPB. Currently, the GEB is equipped with 5 rain gauges with automatic precipitation records (see



item 4.1), installed during the IBESA project. The JPA CSA was also equipped with 15 rain gauges with manual and automatic precipitation measurements mainly monitored by AESA (Executive Agency for Water Management of the Paraíba State), INMET (Brazilian National Institute of Meteorology) and APAC (Pernambuco State Water and Climate Agency), as well as by the *Usina Olho D'Água* company. In addition, other manual and automatic rain gauges were being operated by other institutions or were installed by BRAMAR project, but their data either was missing data or not comprehended the period of study, and then, were not mentioned in this study. Figure 26 shows the different types of automatic rain gauges monitored by LARHENA team in JPA CSA.

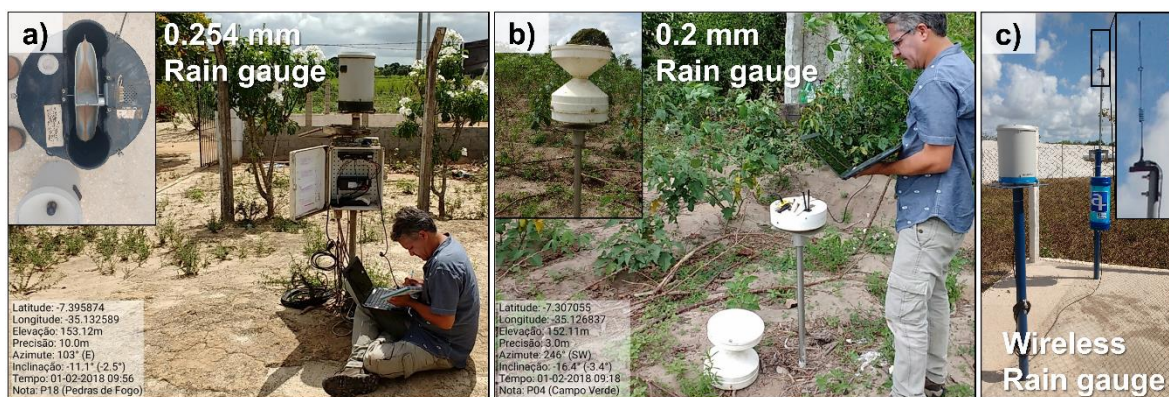


Figure 26 – Automatically-monitored rain gauges, type tipping bucket on (a) 0.254-mm and (b) 0.2-mm resolutions, as well as type (c) wireless rain gauge, in operation in JPA CSA.

Within the boundaries of the GEB, a meteorological station acquired and installed by BRAMAR project, as shown in Figure 27. It registers information of air pressure, precipitation at 6.3 m, wind speed at 6.3 m, air temperature and relative humidity at 6.3 and 5.3 m, upward/downward longwave and shortwave radiation at 5.3 m, soil heat flux at -8 cm, soil temperature at -2, -4 and -6 cm, soil moisture at -5, -20, -40, and also between -2.5 and -7.5 cm, and groundwater level and temperature in a shallow well (~2 meters depth). The soil moisture was monitored by three TDR probes horizontally-inserted at site 5 to build the near-surface soil moisture profile, but also by three TDR probes vertically-inserted at site 2, 3 and 4 in GEB to roughly average soil moisture in GEB (see sites in Figure 25). Another thermo-hygrometer was temporarily installed at 4.3 m for calculating the actual evapotranspiration in different heights, but it was prone to errors already after four months of operation. Furthermore, in the vicinity of the shoreline, the A320 meteorological station monitored by INMET was used for checking some results obtained in this study. It measured air pressure, temperature and relative humidity, precipitation, wind speed and direction, and

global radiation; whose data were suitable to calculate the reference evapotranspiration (see item 4.4.2).

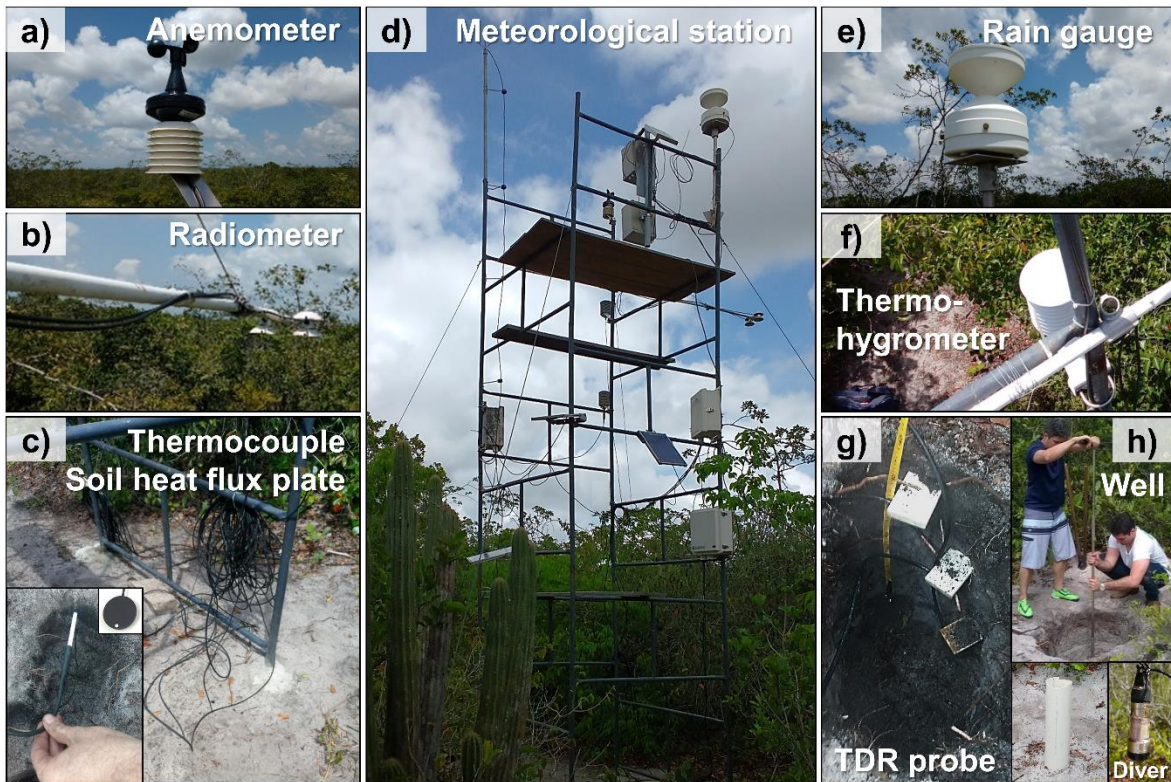


Figure 27 – The (d) meteorological station in GEB monitoring the air pressure, (a) wind speed, (b) up-/downward longwaves and shortwaves, (c) soil temperature and heat flux, (e) rainfall, (f) air temperature and relative humidity, (g) soil moisture, and (h) groundwater level and temperature.

The CRNS probe, a CRS 1000 model from Hydroinnova Ltd., belonging to Institute of Environmental Science and Geography (IESG) at University of Potsdam (UP), was temporally imported and installed in the middle of GEB, at site 2 (see Figure 25d). The CRNS monitored the aboveground neutron flux associated to soil moisture on intermediary field scale from July 18th, 2018, to June 26th, 2019 (Figure 28). For such purpose, the CRNS probe had to be calibrated by collecting soil core samples at different depths and distances from the probe, so that the weighted mean soil moisture could be obtained. Moreover, three soil moisture profile probes, model PR2/6 Delta-T, from IESG were also temporally imported and installed at 17.5 m (DL6-2), 65.6 m (DL6-4) and 153.2 m (DL6-1) distance from CRNS probe, for monitoring the soil moisture at -5, -15, -25, -35, -55, and -95 cm (Figure 29). They have a range up to  $0.4 \text{ m}^3 \text{ m}^{-3}$  soil moisture and  $40^\circ\text{C}$  temperature (DELTA-T, 2016). Thus, the variability of the soil moisture profile could be investigated and the CRNS soil moisture measurements could be validated, once the three profile probes have the same period of operation as the CRNS probe.



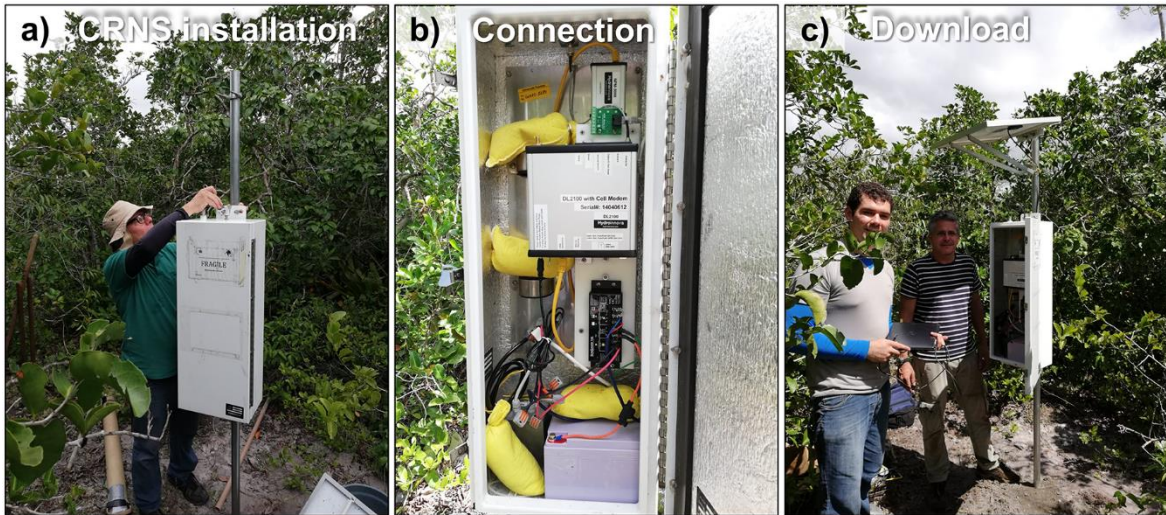


Figure 28 – Process of (a) installation, (b) connection and (c) data download of CRNS probe in GEB.

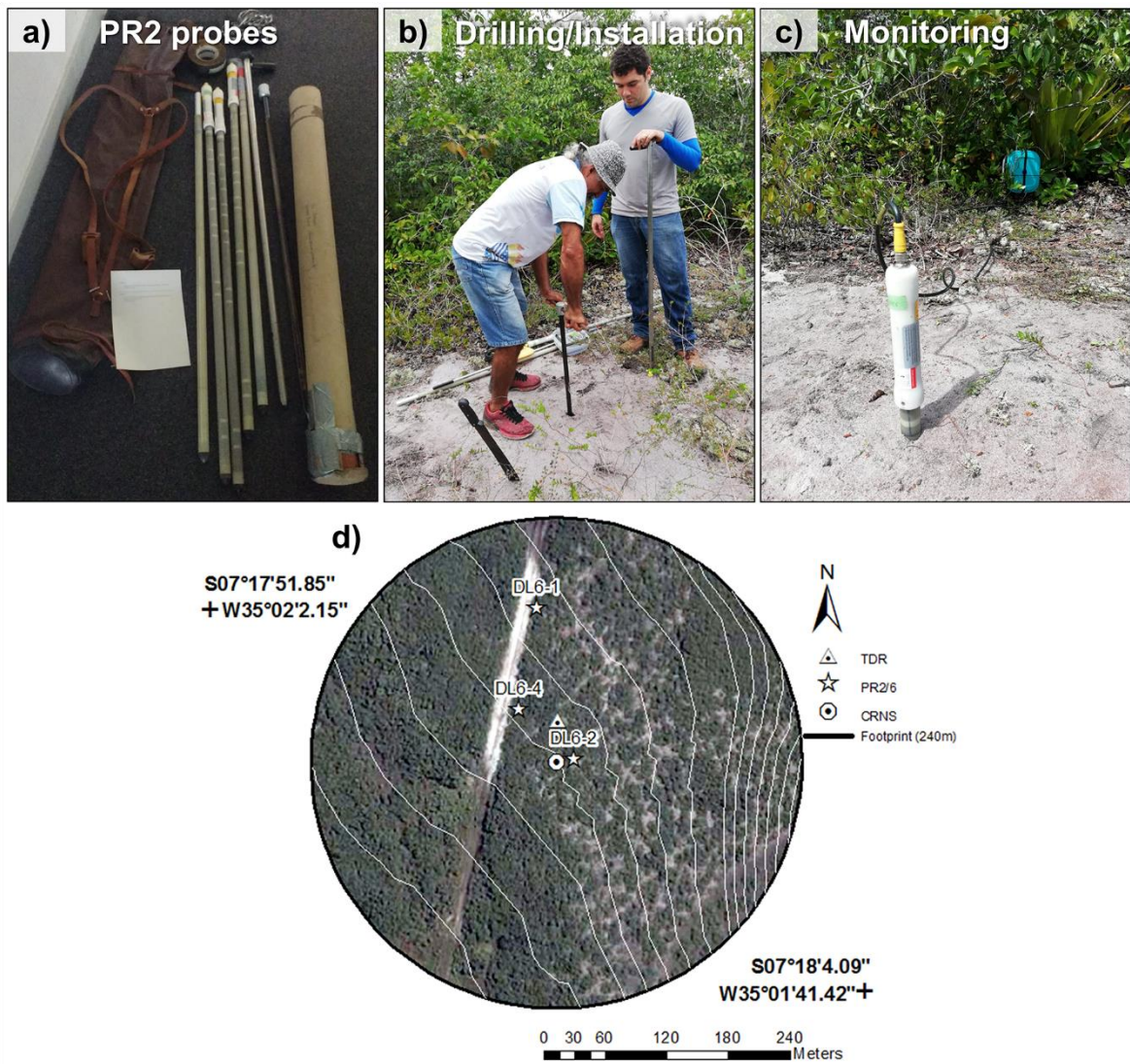


Figure 29 – Installation of PR2/6 probes in GEB. PR2/6: six-levelled soil moisture profile probe; DL6: data logger for six soil moisture sensors.



Concerning the groundwater, four monitoring wells were drilled manually from 2015 to 2017 by the LARHENA team in the shallow unconfined aquifer of GEB, which includes monthly manual and sub-hourly automatic measurements of the groundwater levels. Furthermore, the JPA CSA holds a groundwater monitoring network created at the end of 2015 by the BRAMAR project, from which 23 wells either built by inhabitants of rural area, so-called Amazon (large) wells, or built by specialized companies, so-called tubular (narrow) wells (Figure 30). Pressure transducers and monitoring divers were installed in some wells to automatically collect data every 15 minutes of groundwater depth, temperature and/or conductivity (this latter at site 2 as well, Figure 25d), as well as to check if the manual monitoring of the groundwater depth were suitable for being further used to validate the modelling results. The network consisted of other wells that were disregarded in this study, mainly because of unusual behaviour in the time series due to water pumping into housing supply, but also because of some negligible recharge values stemmed likely from the inappropriate well construction.

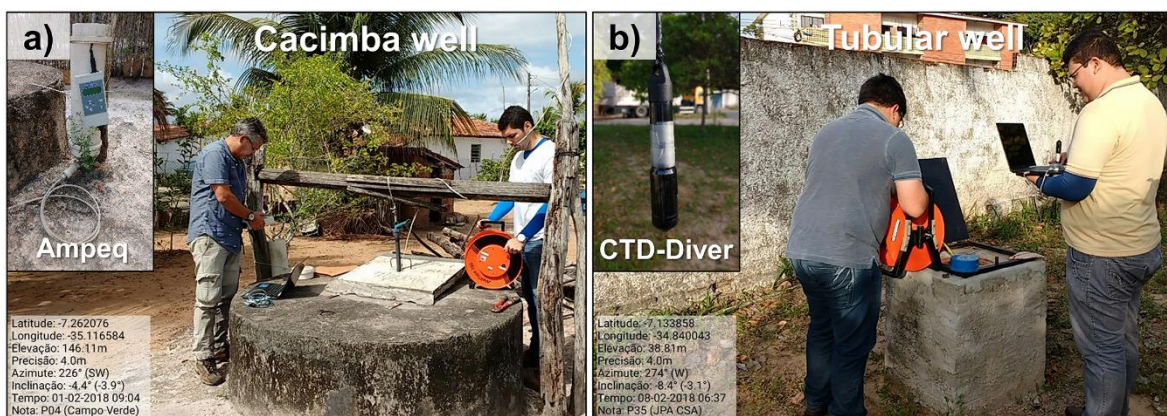


Figure 30 – Automatically-monitored (a) Amazonas and (b) tubular wells in operation in JPA CSA. Ampeq: water depth diver by Ampeq company; CTD: diver of conductivity, temperature and depth.

The water level and runoff data were also obtained automatically at one (at downstream) out of the three stream gauges within the GEB, both located in nearby streams (dark diamond in Figure 25c, and red squares in Figure 25d). Similar water depth divers used for groundwater monitoring were installed into wells at banks of the streams, and their data loggers were placed inside the polyvinyl chloride shelters fixed in tough tree trunks. The rating curves in their cross-sections were built in 2014 through bathymetry and discharge measurements, allowing for yielding the runoff time series (Figure 31). Furthermore, a few other stream gauges were installed throughout the JPA CSA by BRAMAR project, but their rating curves were not built, preventing their use for the purposes of this study.

The source of the measured data previously described are summarized in Table 2.

Table 2 – Summary of measured data by monitoring station over JPA CSA and GEB.

Station	Identification	Measured data	Period	Time step	Source
Rain gauges (JPA CSA)	ALH, BAY, BLR, CAG, EMA, CAM, CES, ITA, JAT, CED, INM, MAR, PDF, STR, SAP	Rainfall	2016 - 2017	Manual: 24 hours Automatic: 1 min	<i>Usina Olho D'Água</i> , AESA, APAC, INMET
Monitoring wells (JPA CSA)	W02, W04, W06, W07, W09, W11, W14, W16, W17, W20, W21, W22, W23, W25, W26, W29, W31, W32, W35, W36, W37, W38, W39	Groundwater level	2015 - 2017	Manual: ~45 days Automatic: 15 min	UFPB: Tubular wells Inhabitants: Cacimba wells
Meteo- rological station (JPA CSA)	A302	Rainfall, Wind speed, Wind direction, Global radiation Air pressure, Air temperature, Air relative humidity	2016 - 2017	1 hour	INMET
Rain gauges (GEB)	Site 1 (no well) Site 2 (used in JPA) Site 3 Site 4	Rainfall, Soil moisture, Groundwater level,	2016 - 2019	Rainfall: 1 min Soil moisture: 1 hour Groundwater level: 15 min	UFPB
Salinity monitoring (GEB)	Site 2	Electrical conductivity, Groundwater level, Groundwater temperature	2018 - 2019	15 min	UFPB
CRNS gauge (GEB)	Site 2	Neutron intensity, Soil moisture profile	2018 - 2019	1 hour	UP
Stream gauges (GEB)	501 502 503	Water level, Discharge	2017	15 min	UFPB
Meteo- rological station (GEB)	Site 5	Rainfall, Wind speed, Up-/downward long-/ shortwave radiation, Air pressure, Air temperature, Air relative humidity, Soil heat flux, Soil temperature, Soil moisture, Groundwater level, Groundwater temperature	2017 - 2019	Majority: 10 min Air pressure: 15 min Groundwater level: 15 min Groundwater temperature: 15 min	UFPB



Figure 31 – Measurements of (a) bathymetry and (b) discharge in stream gauges of GEB for runoff estimation. Source: (Barbosa, 2015).

### 4.3 Satellite-based methods implemented in a Geographic Information System environment

A set of satellite-based approaches and methods were used for determining the water balance components, and then, the water budget equation was applied for estimating the GWR below the root zone. In this study, they include the following products: GPM IMERG product; SMAP product; MODIS products; MapBiomass land use/cover data, and; GLDAS reanalysis data. Their main characteristics were summarized in Table 3. Those data were implemented in a GIS environment using a spatial model platform to optimise the image processing according to Figure 32, as it is a time-consuming and hard-tasking activity. Some routines were also programmed externally in Visual Basic for Application (VBA) to facilitate the data pre-processing. In the following items, the algorithms of every water balance component shall be thoroughly detailed.

Table 3 – Summary of remote sensing data by satellite products in 2016 and 2017.

Satellite product	Remote sensing data	Spatial resolution	Time step	Source
GPM IMERG V05B	Precipitation	0.1° (~11.1 km)	30 min	NASA/GSFC
SMAP SPL4SMAU	Soil moisture in root zone (1-m depth)	9 km	3 hours	NSIDC, ASF
MOD09Q1 V006 and MYD09Q1 V006	Spectral reflectances: band 1 (red) and band 2 (near-infrared)	250 m	8 days	NASA/GSFC
MapBiomass collection 3.1	Land use and cover	30 m	Annual	MapBiomass
GLDAS-2.1 Noah L4	Downward shortwave radiation, Air pressure, Air temperature, Air specific humidity	0.25° (~27.7 km)	3 hours	NASA/GSFC

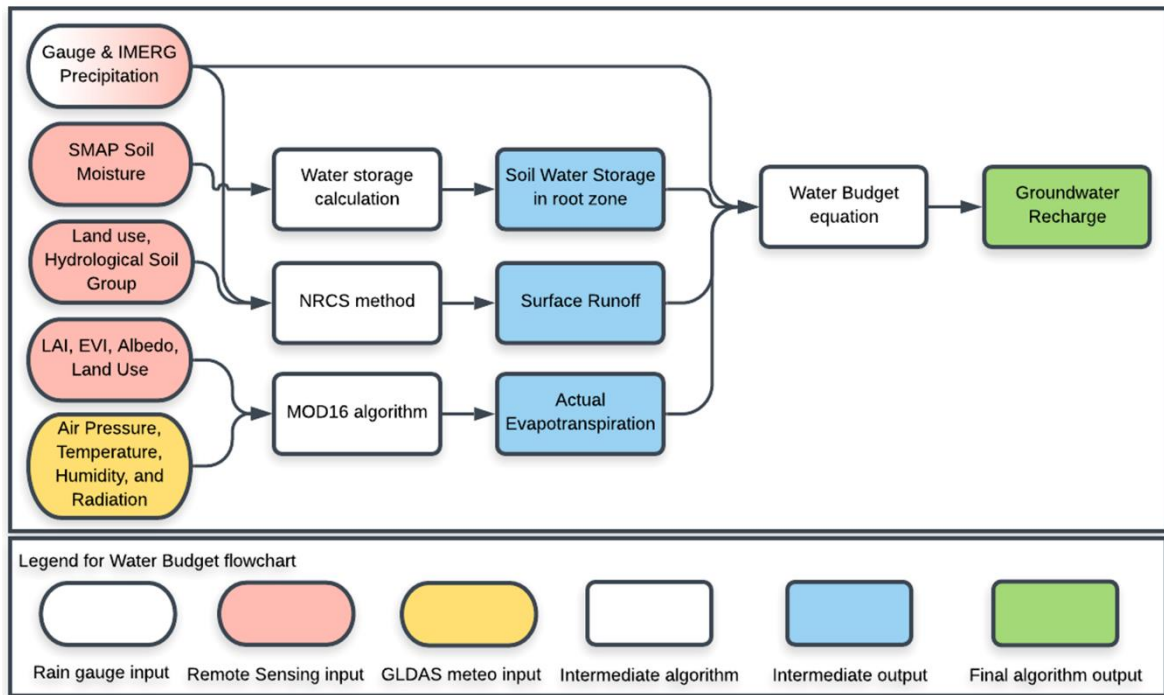


Figure 32 – Flowchart of the logic behind the application of hydro(geo)logical and meteorological methods for estimating the water balance components. LAI: Leaf Area Index; EVI: Enhanced Vegetation Index.

#### 4.3.1 Integrated Multi-satellite Retrievals for Global Precipitation Measurement and ground-based datasets

The main input in the water budget equation is the precipitation, which in this study was based on ground-based and satellite-based information obtained by the rain gauge network and IMERG Final Run V05B product, respectively. Only the precipitation data from the manual rain gauge network were employed in this study because the automatic time series were unable to encompass the entire 2016-2017 period of analysis. The selected IMERG data was the multi-satellite precipitation estimate with gauge calibration, so-called Final Run product (in  $\text{mm h}^{-1}$ ), identified by ‘precipitationCal’ in the data file; which is recommended for general use by Huffman, Bolvin and Nelkin (2017). Both datasets were used to assess the performance of remote sensing precipitation data in estimating the GWR with regards to a reference scenario of ground-based precipitation data.

Firstly, the measurement time-steps of both data sources had to be aggregated and, then, converted to the same temporal resolution. Since the ground-based data are collected every day at 9:00 a.m. (at local time), the 30-min IMERG data unit were converted from  $\text{mm h}^{-1}$  to  $\text{mm 30-min}^{-1}$  dividing by 2, and then accumulated from 09:00 a.m. to the subsequent 24 hours, i.e. from 12:00 to 12:00 of another day at UTC-0 datum. Then, the ground-based



(or simply Gauge) and IMERG datasets were subjected to some procedures to prepare them for use in the water budget equation, including the following activities: data correction, pixel resampling and data interpolation (Figure 33).

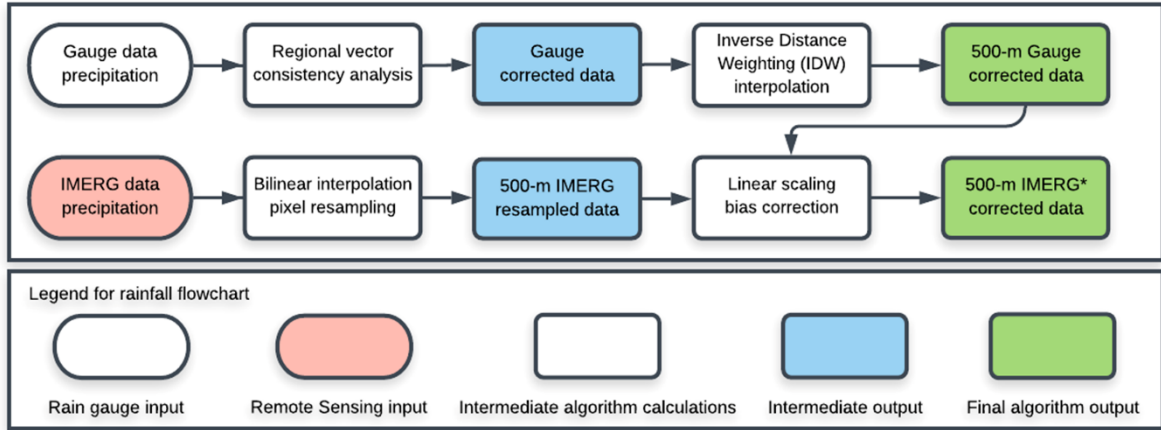


Figure 33 – Flowchart describing the procedures for the IMERG pixel resampling and bias correction, and rain gauge (or simply Gauge) data correction and interpolation.

#### 4.3.1.1 IMERG pixel resampling and bias correction

The IMERG precipitation was then resampled from  $0.1^\circ$  squared cell size ( $\sim 11.1$  km) to  $0.045^\circ$  ( $\sim 0.5$  km) spatial resolution by bilinear resampling because it is a uniform disaggregating method. Due to its simplicity, this method is used as a benchmark to explore potential enhancements of other downscale approaches, as it is able to minimize footprint impact of a coarse resolution providing a smooth interpolation (Ulloa et al., 2017; Zhang et al., 2019). The bilinear interpolation performs well when leading with continuous data, such as precipitation (Yang, 2015). Thus, it calculates the predicted value based on a weighted distance average of the four nearest pixels by Equation (1):

$$P_{x,y} = \frac{1}{(x_2 - x_1)(y_2 - y_1)} [x_2 - x \quad x - x_1] \begin{bmatrix} P_{1,1} & P_{1,2} \\ P_{2,1} & P_{2,2} \end{bmatrix} \begin{bmatrix} y_2 - y \\ y - y_1 \end{bmatrix} \quad (1)$$

where  $P_{x,y}$  is the predicted value of precipitation, in mm, at the new point  $(x, y)$ , and  $P_{i,j}$  are the precipitation values, in mm, at the four nearest pixels on the original spatial resolution.

For the bias correction of the IMERG data, the linear-scaling (LS) approach was used based on a monthly correction factor (Teutschbein and Seibert, 2012), calculated as the ratio between the monthly mean data for ground and IMERG and applied to daily precipitation data. Rather than perform a grid-box correction (i.e. pixel-per-pixel), the IMERG estimates



over JPA CSA were corrected by one correction factor per month, to preserve the original IMERG precipitation gradient but correcting the shift (i.e. bias) between IMERG and gauge observation (Gadelha et al., 2019). The LS bias correction is calculated by Equation (2):

$$P_d^{s'} = P_d^s \frac{P_m^o}{P_m^s} \quad (2)$$

where  $P_d^s$  and  $P_d^{s'}$  (mm) denote, respectively, the original and bias-corrected satellite precipitation on the  $d$ th day of the  $m$ th month, and  $P_m^o$  and  $P_m^s$  (mm) denote, respectively, the observed and satellite accumulated precipitation in the  $m$ th month per grid box (latitude, longitude).

#### 4.3.1.2 Rain gauge data correction and interpolation

The consistency analysis and data correction of 16 rain gauges – only one from GEB due to high density – was carried out by the regional vector method (Hiez, 1977), frequently used as benchmark (de Oliveira et al., 2010), which consists of determining the chronological, synthetic precipitation time series stemmed from the maximum likelihood between the data contained in a set of rain gauges regionally grouped, as shown in Equations (3) to (6):

$$L_i^o = \frac{1}{m} \sum_{j=1}^m P_{i,j} \quad , \quad \text{for } i = 1 \text{ to } n \quad (3)$$

$$C_j = \frac{\sum_{i=1}^n L_i^o P_{i,j}}{\sum_{i=1}^n (L_i^o)^2} \quad , \quad \text{for } j = i \text{ to } m \quad (4)$$

$$L_i = \frac{\sum_{j=1}^m C_j P_{i,j}}{\sum_{j=1}^m (C_j)^2} \quad , \quad \text{for } i = i \text{ to } n \quad (5)$$

$$\hat{P}_{i,j} = L_i C_j \quad , \quad (P_{i,j} - \hat{P}_{i,j})^2 \rightarrow 0 \quad (6)$$

where  $\hat{P}_{i,j}$  and  $P_{i,j}$  (mm) are, respectively, the original and synthetic precipitation of a rain gauge ‘ $j$ ’ in a year ‘ $i$ ’,  $L_i$  is the column vector or regional vector with ‘ $n$ ’ lines,  $C_j$  is the vector line with ‘ $m$ ’ columns,  $n$  is the total number of years, ‘ $m$ ’ is the total number of rain gauges,  $e L^o$  is the mean precipitation of all ‘ $m$ ’ rain gauges.

The ground-based map was then obtained by interpolating the datasets using the Inverse Distance Weighting (IDW) method, as it provides good results over Brazil (Xavier, King and Scanlon, 2016). In the IDW method, the interpolated precipitation depth  $P_x$  at a point 'x' is based upon a weight ( $w_k$ ) that is inversely proportional to the distance between this point and the data from the  $k$ th nearby rain gauges, as shown in Equation (7):

$$P_x = \frac{\sum_{i=1}^k w_k X_k}{\sum_{i=1}^k w_k}, \quad \text{for } i = 1 \text{ to } k, \quad w_k = \frac{1}{d_{k,x}^p} \quad (7)$$

where  $d_{k,x}^p$  is the geodesic distance between the station 'k' and a specified point 'x', and 'p' is the power parameter (= 2, from Ly, Charles and Degré, 2011). Due to the rainfall gradient from shoreline towards inward (Cabral da Silva et al., 2000b) and the small number of rain gauges available, the 12 nearest rain gauges were considered for the interpolation, smoothing the interpolated values instead of changing them abruptly if fewer gauges were considered.

#### 4.3.2 Mu's algorithm and Penman-Monteith equation for actual evapotranspiration estimation

The main limitation for obtaining satellite-based groundwater estimates over large regions under intense cloud coverage is related to the determination of the daily actual evapotranspiration component. For this purpose, this study used the algorithm based on the Penman-Monteith equation (Allen et al., 1998) calculated by Equation (8), the same applied by (Mu et al., 2007) to generate the 1-km MOD16 evapotranspiration product, with recent enhancements in the spatial resolution and in the calculation of vegetation indexes, vegetation cover fraction, net radiation and surface albedo (Gusmão, 2017; Mu, Zhao and Running, 2011; Running et al., 2017; Teixeira et al., 2014, 2013).

$$\lambda E = \lambda E_{\text{transp}} + \lambda E_{\text{soil}} = \frac{\Delta A + \rho C_p (e_s - e_a) / r_a}{\Delta + \gamma (1 + \frac{r_s}{r_a})} \quad (8)$$

where  $\lambda E$  is the latent heat flux density ( $\text{W m}^{-2}$ ) and represents the sum of plant transpiration ( $\lambda E_{\text{transp}}$ ) and soil evaporation ( $\lambda E_{\text{soil}}$ ), i.e. the evapotranspiration during the same time interval of precipitation (i.e. from 12:00 to 12:00 at UTC-0 datum),  $\lambda$  is latent heat flux density of vaporization ( $=2.45 \times 10^6 \text{ J kg}^{-1}$ ),  $A$  is the available energy ( $\text{W m}^{-2}$ ),  $\rho$  is the air density ( $=1.2 \text{ kg m}^{-3}$ ),  $C_p$  is the specific heat capacity of air in constant pressure ( $=1005$

$\text{J kg}^{-1} \text{ } ^\circ\text{C}^{-1}$ , from Gusmão, 2017),  $e_s$  is the saturated water vapour pressure (kPa) calculated by Equation (9),  $e_a$  is the actual water vapour pressure (kPa) calculated by Equation (10),  $r_a$  is the aerodynamic resistance ( $\text{s m}^{-1}$ ),  $r_s$  is the surface resistance ( $\text{s m}^{-1}$ ),  $\Delta$  is the slope of the curve relating saturated water vapour pressure to temperature ( $\text{kPa } ^\circ\text{C}^{-1}$ ) calculated by Equation (11), and  $\gamma$  is the psychrometric constant ( $\text{kPa } ^\circ\text{C}^{-1}$ ) calculated by Equation (12). According to Allen et al (1998), the aforementioned equations are:

$$e_s = \langle e_s(T_{\max}), e_s(T_{\min}) \rangle = 0.6108e^{\left(\frac{17.27T}{T+237.3}\right)} \quad (9)$$

$$e_a = \langle e_a(h_{r,\max}), e_a(h_{r,\min}) \rangle = e_s \frac{h_r}{100} \quad (10)$$

$$\Delta = \frac{4098e_s}{(T + 237.3)^2} \quad (11)$$

$$\gamma = \left(\frac{C_p P_{\text{atm}}}{\varepsilon \lambda}\right) = 0.665 \cdot 10^{-3} P_{\text{atm}} \quad (12)$$

where  $T$ ,  $T_{\max}$  and  $T_{\min}$  are the mean, maximum and minimum daily temperatures, respectively,  $h_r$ ,  $h_{r,\max}$  and  $h_{r,\min}$  are the mean, maximum and minimum daily relative humidity, respectively,  $P_{\text{atm}}$  is the mean daily atmospheric pressure (kPa),  $\varepsilon$  is the ratio molecular weight between water vapour ( $M_w$ ) and dry air ( $M_a$ ) ( $= 0.622$ ). The  $P_{\text{atm}}$  can be calculated by as a function of the air temperature ( $T$ ,  $^\circ\text{C}$ ) and altitude ( $H_a$ ) by Equation (13) in relation to the sea-level standard condition of barometric pressure ( $P_{\text{atm}} = 101.3 \text{ kPa}$ ).

$$P_{\text{atm}} = 101.3 \left(\frac{T}{T + 0.0065H_a}\right)^{5.26} \quad (13)$$

The algorithm proposed by Mu et al. (2007) uses MODIS product collections to obtain the Leaf Area Index (LAI), Enhanced Vegetation Index (EVI), and surface albedo ( $\alpha$ ). The meteorological data of four pixels from GLDAS Noah L4 v2.1 reanalysis data with 3-hourly and  $0.25^\circ$  resolutions were also retrieved and averaged in JPA CSA, namely: incoming short-wave radiation, air temperature, air pressure, and specific air humidity (quite similar in concept to absolute humidity) from which the relative humidity was averaged (see Equation (67), in item 4.5.1). In addition, the 30-m annual Landsat-based land use/cover maps by MapBiomas Project collection 3.1 were reclassified to match the biophysical parameters proposed by Running et al. (2017) and then used. These datasets were then used to estimate plant transpiration and soil evaporation, in order to determine the actual

evapotranspiration, as depicted in the schematic flowchart shown in Figure 34. The evaporation from water bodies, such as reservoirs, are disregarded in these methods, as shall be explained in the following items.

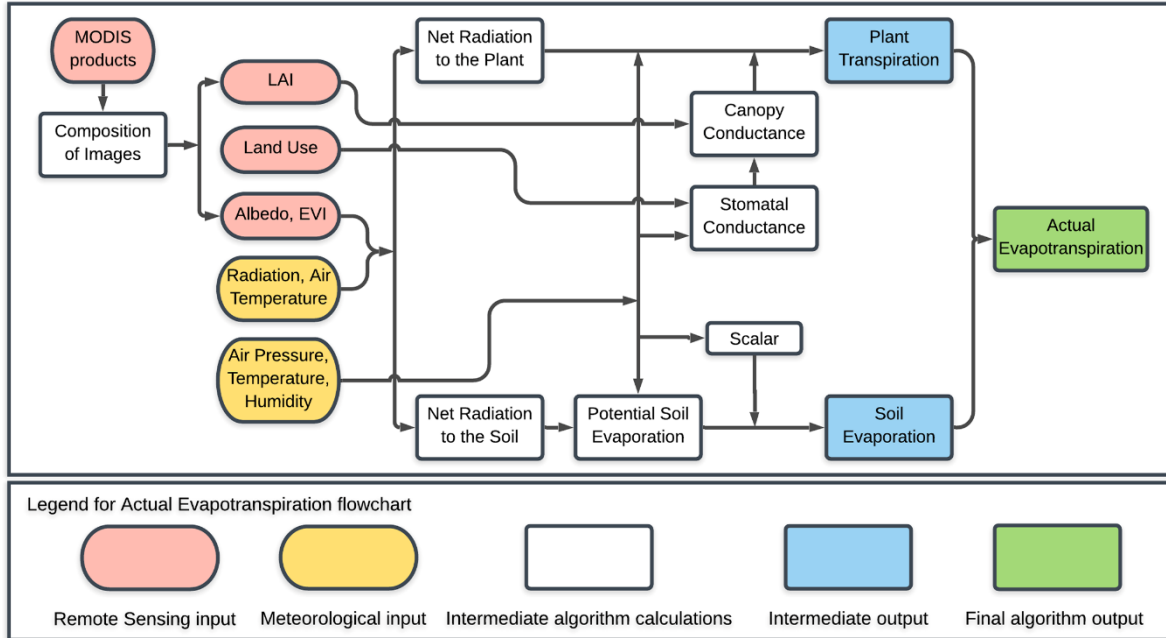


Figure 34 – Flowchart of the logic behind the MOD16 global evapotranspiration algorithm for calculating daily actual evapotranspiration. LAI: Leaf Area Index; EVI: Enhanced Vegetation Index. Source: modified from Mu et al (2007).

#### 4.3.2.1 Canopy conductance and vegetation cover fraction

The original Mu's algorithm uses the Leaf Area Index (LAI) to scale stomatal conductance ( $C_S$ , leaf level) up to canopy conductance ( $C_C$ , surface level) (Landsberg and Gower, 1997) by Equations (14) and (15).  $C_S$  is mainly expressed as a function of minimum air temperature ( $T_{min}$ ) and Vapour Pressure Deficit (VPD), as follows (Oren et al., 1999; Xu and Baldocchi, 2003):

$$C_S = C_L * m(T_{min}) * m(VPD) \quad (14)$$

$$C_C = C_S * LAI \quad (15)$$

where  $C_L$  ( $m s^{-1}$ ) denotes the mean potential stomatal conductance per leaf unit area ( $m s^{-1}$ ),  $f_{wet}$  denotes the water cover fraction, and  $m(T_{min})$  and  $m(VPD)$  are limiting factors of potential stomatal conductance for minimum air temperatures ( $^{\circ}C$ ) and vapour pressure deficits (Pa), respectively, high enough to reduce canopy conductance. The  $m(T_{min})$  and  $m(VPD)$  are obtained by Equations (16) and (17):

$$m(T_{\min}) = \begin{cases} 1.0, & T_{\min} \geq T_{\min_{\text{open}}} \\ \frac{T_{\min} - T_{\min_{\text{close}}}}{T_{\min_{\text{open}}} - T_{\min_{\text{close}}}}, & T_{\min_{\text{close}}} < T_{\min} < T_{\min_{\text{open}}} \\ 0.1, & T_{\min} \leq T_{\min_{\text{close}}} \end{cases} \quad (16)$$

$$m(\text{VPD}) = \begin{cases} 1.0, & \text{VPD} \leq \text{VPD}_{\text{open}} \\ \frac{\text{VPD}_{\text{close}} - \text{VPD}}{\text{VPD}_{\text{close}} - \text{VPD}_{\text{open}}}, & \text{VPD}_{\text{open}} < \text{VPD} < \text{VPD}_{\text{close}} \\ 0.1, & \text{VPD} \geq \text{VPD}_{\text{close}} \end{cases} \quad (17)$$

where ‘open’ indicates no inhibition for transpiration and ‘close’ indicates almost complete inhibition (closure of stomata). The values of  $T_{\min_{\text{open}}}$ ,  $T_{\min_{\text{close}}}$ ,  $\text{VPD}_{\text{close}}$ ,  $\text{VPD}_{\text{open}}$  and  $C_L$  are summarized in Table 4:

Table 4 – Parameterization of stomatal opening and closing control in MOD16 algorithm.  $T_{\min_{\text{open}}}$ : minimum air temperature of stomatal opening;  $T_{\min_{\text{close}}}$ : minimum air temperature of stomatal closing;  $\text{VPD}_{\text{close}}$ : vapour pressure deficit of stomatal closing;  $\text{VPD}_{\text{open}}$ : vapour pressure deficit of stomatal opening;  $C_L$ : mean potential stomatal conductance per unit leaf area. Source: based on Mu et al. (2007, 2011) and Running et al. (2017). EBF: Evergreen Broadleaved Forest.

Parameter	Water	Forest (EBF)	Mosaic/Pasture	Urban	Bare soil
$T_{\min_{\text{open}}} (\text{°C})$	8.31	9.09	12.02	12.02	12.02
$T_{\min_{\text{close}}} (\text{°C})$	-8	-8	-8	-8	-8
$\text{VPD}_{\text{close}} (\text{Pa})$	2900	4000	4200	4200	4200
$\text{VPD}_{\text{open}} (\text{Pa})$	650	1000	650	650	650
$C_L (\text{m s}^{-1})$	0.0000	0.0024	0.0055	0.0055	0.0055

The cloud cover in the tropical coastal areas of Brazil are frequently high, which can lead to incorrect evapotranspiration estimates (Running et al., 2017). Thus, the algorithm uses an empirical equation set forth by Bastiaanssen et al. (1998) and Allen et al. (2007) to compute LAI using both 8-days MOD09Q1 (Terra Satellite) and MYD09Q1 (Aqua Satellite) reflectance products. Thus, LAI is calculated by the Soil Adjusted Vegetation Index (SAVI) proposed by Huete (1988), as shown in Equations (18) and (19):

$$\text{SAVI} = \frac{(1 + L)(r_2 - r_1)}{(L + r_2 + r_1)} \quad (18)$$

$$\text{LAI} = -\frac{\ln\left(\frac{0.69 - \text{SAVI}}{0.59}\right)}{0.91} \quad (19)$$

where  $r_1$  and  $r_2$  are the spectral reflectances of the bands 1 (red) and 2 (near-infrared) of the MOD09Q1 and MYD09Q1 reflectance products, and  $L$  is an adjust factor considered in this study equal to 0.1, the same used by Silva et al. (2015).

The algorithm also uses the surface cover fraction ( $F_C$ , varying from 0 to 1) information for partitioning the net radiation between canopy and soil surface. Similarly to Jiang et al. (2008), this study calculated the  $F_C$  by using the 2-band (red and infrared) Enhanced Vegetation Index (EVI2, without a blue band) to reduce pixel size as shown in Equations (20) and (21), differently from Mu et al. (2007) who used the Enhanced Vegetation Index (EVI). This approach provides satisfactory results mainly when atmospheric effects are insignificant and data quality is good (Bolton and Friedl, 2013; Rocha and Shaver, 2009).

$$EVI2 = 2.5 \frac{r_2 - r_1}{r_2 + 2.4r_1 + 1.0} \quad (20)$$

$$F_C = \frac{EVI2 - EVI2_{\min}}{EVI2_{\max} - EVI2_{\min}} \quad (21)$$

where  $EVI2_{\min}$  is the signal from bare soil ( $LAI \rightarrow 0$ ) and  $EVI2_{\max}$  is the signal from dense green vegetation ( $LAI \rightarrow \infty$ ) during the study period, generally set as invariant constants varying between 0.05 and 0.95, respectively. LAI maximum values were limited up to  $6 \text{ m}^2 \text{ m}^{-2}$ , similar to Gusmão (2017). Similar to the SAVI procedures, the EVI2 was also considered a fixed input parameter throughout the month using 8-days MOD09Q1-MYD09Q1 reflectance products.

To minimize cloud-sky condition, monthly compositions of 8-day LAI and EVI2 maps were then performed by simply overlapping the map pixels influenced by clouds for pixels of another map in the same month, whose values indicated clear sky condition, assuming, therefore, that these variables are monthly parameters (de Oliveira et al., 2016a).

#### 4.3.2.2 Net radiation and albedo

The available energy ( $A$ , in Equation (8)) is usually determined by calculating the daily net radiation of the land surface ( $R_n$ ) (Cleugh et al., 2007; Mu et al., 2007), as shown in Equation (22):

$$R_n = (1 - \alpha) R_{S\downarrow} + \sigma (\varepsilon_a - \varepsilon_s)(273.15 + T)^4 \quad (22)$$

where  $\alpha$  corresponds to the surface albedo,  $R_{S\downarrow}$  is the downward shortwave incoming radiation,  $\sigma$  is the constant of Stefan-Boltzmann ( $= 5.67 \cdot 10^{-8} \text{ W m}^{-2} \text{ K}^{-4}$ ),  $\varepsilon_a$  is the atmospheric emissivity,  $\varepsilon_s$  is the surface emissivity, and  $T$  represents the mean daily air temperature in  $^{\circ}\text{C}$ .

However, in this study the  $R_n$  was calculated using the equation proposed by de Bruin (1987), which has been often employed in the literature (Bastiaanssen et al., 1998; Gusmão, 2017; Santos et al., 2015), as shown in Equation (23):

$$R_n = (1 - \alpha) R_{S\downarrow} + a\tau_{sw24} \quad (23)$$

Where  $\alpha$  corresponds to the surface albedo,  $R_{S\downarrow}$  is the downward shortwave incoming radiation obtained from 3-hours GLDAS Noah L4 v2.1 reanalysis data, 'a' is the regression coefficient between the daily longwave incoming radiation and daily atmospheric transmissivity ( $= \sim -75.5$ , from Gusmão, 2017) and  $\tau_{sw24}$  is the average daily atmospheric transmissivity calculated by Equation (24):

$$\tau_{sw24} = \frac{R_{S\downarrow}}{R_{S\downarrow A}} \quad (24)$$

where  $R_{S\downarrow}$  is the downward shortwave incoming radiation, and  $R_{S\downarrow A}$  is the downward shortwave incoming radiation on top of the atmosphere that is calculated by Equation (25):

$$R_{S\downarrow A} = \frac{24(60)}{\pi} G_s d_r [\omega_s \sin(\varphi) \sin(\delta) + \cos(\varphi) \cos(\delta) \sin(\omega_s)] \quad (25)$$

where  $G_s$  is the solar constant ( $= 0.0820 \text{ MJ m}^{-2} \text{ min}^{-1}$ ),  $d_r$  is the square relative distance between the Earth and Sun (rad),  $\omega_s$  is the hourly angle of sunrise (rad),  $\delta$  is the solar declination angle (rad), and  $\varphi$  is the latitude of meteorological station ( $= -7.25\pi/180$  rad). The values of  $d_r$ ,  $\delta$  and  $\omega_s$  were obtained, respectively, from the Equations (26) to (28):

$$d_r = 1 + 0.033 \cos\left(\frac{2\pi}{365} d_s\right) \quad (26)$$

$$\delta = 0.409 \sin\left(\frac{2\pi}{365} d_s - 1.39\right) \quad (27)$$

$$\omega_s = \cos^{-1}[-\tan(\varphi) \tan(\delta)] \quad (28)$$

where  $d_s$  is the sequential day of the year.

The surface albedo ( $\alpha$ ) is provided in the original algorithm from the 8-day composite MCD43A2/A3 product with 500 m spatial, which may also be contaminated by cloud cover

and dramatically increase the albedo signal (Running et al., 2017). However, this study considered again the two MOD09Q1-MYD09Q1 bands product to calculate the surface albedo using the Equation (29) calibrated by (Teixeira et al., 2014, 2013), with good results found by Gusmão (2017).

$$\alpha = 0.08 - 0.41r_1 + 0.14r_2 \quad (29)$$

where  $r_1$  and  $r_2$  are the spectral reflectances of the bands 1 (red) and 2 (near-infrared) of the MOD09Q1 and MYD09Q1 products. Similar to SAVI and EVI2, the monthly composition of surface albedo was also considered in this step to reduce the influence of clouds on actual evapotranspiration estimates.

#### 4.3.2.3 Plant transpiration and soil evaporation

For the determination of plant transpiration and soil evaporation, the available energy (A) represented by net radiation (Rn) had to be firstly linearly partitioned between the canopy ( $A_C$ ) and the soil surface ( $A_{soil}$ ), to what the vegetation cover fraction ( $F_C$ ) was used, as shown in Equations (30) and (31):

$$A_C = F_C A \quad (30)$$

$$A_{soil} = (1 - F_C) A \quad (31)$$

where  $A_C$  and  $A_{soil}$  are the total net incoming radiation (A ou Rn) partitioned to the canopy and soil, respectively. In this study, soil heat flux (G) was assigned as zero in this study due to its small magnitude compared to Rn on daily scale, similarly to Gusmão (2017).

The plant transpiration and potential soil evaporation were determined by the Penman-Monteith equation (see Equation (8)) using the  $A_C$  and  $A_{soil}$  parcels, as shown in Equations (32) and (33):

$$\lambda E_{transp} = \frac{\Delta A_C + \rho C_p (e_s - e_a) / r_a}{\Delta + \gamma (1 + \frac{r_s}{r_a})} \quad (32)$$

$$\lambda E_{soil_{pot}} = \frac{\Delta A_{soil} + \rho C_p (e_s - e_a) / r_a}{\Delta + \gamma (1 + \frac{r_{tot}}{r_a})} \quad (33)$$

where  $r_{tot}$  denotes the aerodynamic resistance to the vapor transport ( $s \ m^{-1}$ ), represented by the sum of the surface resistance ( $r_s$ ,  $s \ m^{-1}$ ) – equal to the inverse of canopy



conductance ( $C_c$ , see item 4.3.2.1) (Mu et al., 2007) – and the vapor transport resistance ( $r_v$ ,  $s\ m^{-1}$ ), namely  $r_{tot} = r_s + r_v$  (van de Griend and Owe, 1994). The  $r_{tot}$  can be straightforwardly calculated by Equations (34) and (35), for the standard atmospheric conditions of air temperature ( $T = 20^\circ C$ ) and barometric pressure ( $P_{atm} = 101.3\ kPa$ ).

$$r_{cor} = \frac{1.0}{\frac{101.3}{P_{atm}} \left( \frac{273.15 + T}{293.15} \right)^{1.75}} \quad (34)$$

$$r_{tot} = r_{tot,c} r_{cor} \quad (35)$$

where  $r_{tot,c}$  ( $= 107\ s\ m^{-1}$ ) is an adjustment parameter that refers to total aerodynamic drag (Mu et al., 2007). The  $r_a$  is calculated as a function of convective heat transfer resistance ( $r_c$ ,  $s\ m^{-1}$ ) and radiative heat transfer resistance ( $r_r$ ,  $s\ m^{-1}$ ), as shown in Equations (36) and (37). In addition,  $r_c$  is calculated in the same way as  $r_{tot}$ , because it is assumed to be equal to the resistance of the boundary layer (Thornton, 1998).

$$r_r = \frac{\rho_a C_p}{4.0 \sigma T^3} \quad (36)$$

$$r_a = \frac{r_c r_r}{r_c + r_r} \quad (37)$$

The actual soil evaporation of the soil ( $\lambda E_{soil}$ ) is then calculated based on the interactions between the surface and the atmosphere from VPD and relative humidity ( $h_r, \%$ ) (Mu et al., 2007), as shown in Equation (38):

$$\lambda E_{soil} = \lambda E_{soil,pot} \left( \frac{h_r}{100} \right)^{(e_s - e_a)/100} \quad (38)$$

### 4.3.3 Surface runoff by Natural Resources Conservation Service–Curve Number method

The Natural Resources Conservation Service–Curve Number (NRCS–CN) method (NRCS, 1986), originally called Soil Conservation Service (SCS) method (SCS, 1972), is an approach based on empirical formulas, which converts basic descriptive data into numeric values to estimate the excess precipitation that was not intercepted, stored in depressions, and/or lost through infiltration into the soil (Ajmal et al., 2015; Ajmal and Kim, 2015). Apart from descriptive data, NRCS–CN also requires information about precipitation depth and an

empirical parameter, which allow for simulating surface runoff at a given point (e.g. surface site or cross-section), without modelling the flow direction over time (Matei, 2012).

The NRCS–CN is based on the water budget equation and on two fundamental hypotheses (NRCS, 2004). The first hypothesis states that the ratio between the actual soil water storage ( $F$ , mm) and potential maximum soil water storage ( $S$ , mm) both after runoff begins, is equivalent to the ratio between the actual runoff ( $Q$ , mm) and potential maximum runoff ( $P$ , mm) (if no initial abstraction occurs), as shown in Equation (39):

$$\frac{F}{S} = \frac{Q}{P} \quad (39)$$

Nevertheless, for most applications the rainfall is abstracted. Thereby, the second hypothesis is that the initial abstraction ( $I_a$ ) is a fraction of the  $S$ , as shown in Equation (40). There exist three main abstractions: interception (precipitation minus throughfall, stem flow and water drip); depression storage (topographic undulations); and infiltration into the soil.

$$I_a = \lambda S \quad (40)$$

Thus, the total precipitation must exceed the initial abstraction before any runoff is triggered, leading to available potential maximum runoff ( $P - I_a$ ) and available actual soil water storage ( $P - I_a - Q$ ), so that Equation (39) is substituted by Equation (41):

$$\frac{P - I_a - Q}{S} = \frac{Q}{P - I_a} \quad (41)$$

Rearranging the Equation (41), surface runoff ( $Q$ ) can be expressed by Equation (42):

$$Q = \begin{cases} \frac{(P + I_a)^2}{(P - I_a + S)} & , \quad \text{if } P \geq I_a = \lambda S \\ 0 & , \quad \text{if } P = 0 \end{cases} \quad (42)$$

Since the NRCS–CN method comes up with rainfall-runoff relationships based on  $S$ , a need for its average estimation under distinct land use/cover conditions shows up. For such purpose, the NRCS–CN proposed the dimensionless empirical parameter Curve Number (CN), which reflects, in just one value, the soil impervious nuance intimately related to  $S$  component. Thereby, after assessing different scenarios, an inverse relationship between CN and  $S$  was found and expressed by Equation (43):

$$CN = \frac{25400}{254 + S}, \quad \text{for } 0 \leq CN \leq 100 \quad (43)$$

The  $I_a$  is conventionally assigned equal to 0.20 of  $S$  (NRCS, 1986; SCS, 1972) due to unavailability of a complete database of CN calibrated values. Conversely, Lal et al. (2016) and Lal, Mishra and Kumar (2019) reviewed the initial abstraction ratios for 63 watersheds worldwide with different land covers, finding  $\lambda$  equal to 0.03 as best value for runoff simulation, and proposing an equation to convert the original CN values. Thus, this study applied the Equations (44) and (45) proposed by the aforementioned authors.

$$Q = \begin{cases} \frac{(P - 0.03S)^2}{(P + 0.97S)} & , \quad \text{if } P \geq I_a = 0.03S \\ 0 & , \quad \text{if } P = 0 \end{cases} \quad (44)$$

$$S = \frac{25400}{CN_{II,\lambda=0.03}} - 254 \quad (45)$$

The surface runoff was calculated by the NRCS–CN method using the Gauge and IMERG-bias-corrected precipitation data. They were summed from 09:00 to 09:00, and then, the resulting surface runoff was summed to annual and monthly basis. This artifice was carried out because obtaining the annual or monthly runoff straightforwardly from the annual or monthly rainfall would be a violation of the event-based Hortonian principle (Awadallah, Farahat and Haggag, 2017). It is assumed that adapting the NRCS–CN temporal basis from event-based to daily resolution would result in inexpressive uncertainties for monthly and annual runoff estimates; which was similarly used by several studies in literature (Mushtaha, van Camp and Walraevens, 2019; Freitas et al., 2019; Subramanian and Abraham, 2019). Lastly, Figure 35 depicts the NRCS algorithm for obtaining the daily surface runoff.

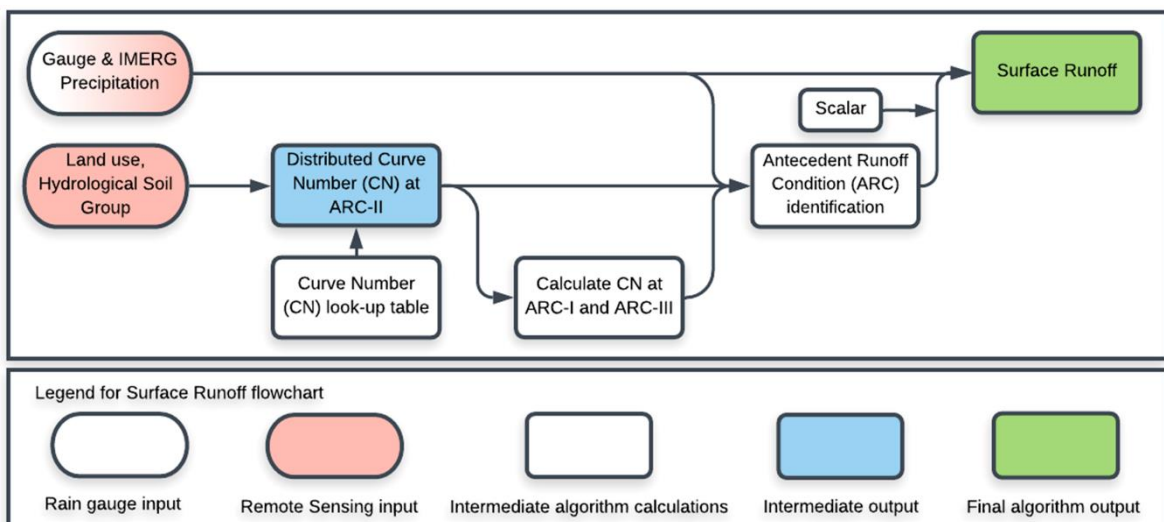


Figure 35 – Flowchart of the logic behind the NRCS–CN method algorithm for calculating the daily surface runoff. ARC-I, ARC-II and ARC-III: dry, average and wet Antecedent Runoff Condition.

### 4.3.3.1 Hydrologic Soil Groups

Due to the extremely variable aspect of soil types, a new classification reflecting the influence of soil properties over the surface runoff was required by the NCRS method. Thereby, SCS (1972) and NRCS (1986) assumed that soil profiles with similar characteristics respond similarly to long-term rainfall and high intensity. Such soils were grouped in four Hydrologic Soil Groups (HSG) based on their water infiltration and transmission capacities, i.e. A, B, C and D, as described in Table 5. If the soil is placed in group D because of a shallow groundwater table, it may be assigned to a dual hydrologic group (i.e. A/D, B/D, or C/D), first letter representing the soil's group if drained, and the D the natural condition.

Table 5 – Hydrologic Soil Groups (HSG) defined for the NRCS–CN method. Source: NRCS (1986).

HSG	Soil characteristics	Infiltration rate
A	Soils with high infiltration rate, high water transmission rate and low runoff potential, when completely wet. It comprises deep, well-drained sands and gravelly sands.	$> 7.62 \text{ mm h}^{-1}$
B	Soils with moderate infiltration rate, moderate water transmission rate and moderate runoff potential, when completely wet. It comprises moderately to deep, well-drained soils featuring moderately fine to moderately coarse textures.	$3.81 \text{ to } 7.62 \text{ mm h}^{-1}$
C	Soils with slow infiltration rate, slow water transmission rate and high runoff potential, when completely wet. It comprises fine-textured soils holding layers that impede the downward water movement.	$1.27 \text{ to } 3.81 \text{ mm h}^{-1}$
D	Soils with a very slow infiltration rate, very slow water transmission rate and very high runoff potential, when completely wet. It comprises high shrink-swell clays, featuring a claypan near-surface impervious layer and a shallow water table.	$< 1.27 \text{ mm h}^{-1}$

Some modifications on the hydrologic group of soils types have been proposed due to relatively subjective aspect of the HSG classification, as claimed by Langan and Lammers (1991). For instance, Berhanu, Melesse and Seleshi (2013) provided a spatial geodatabase of HSGs for the Ethiopian soils types identifying and mapping the hydrological zones, and Cordeiro et al. (2018) derived the agriculturally relevant soils types to HSGs in Canada for using in runoff simulation. In 2018, the Distributed Active Archive Center for

biogeochemical dynamics (DAAC) provides a globally-gridded HSG dataset (HYSOGs250m) a 250-m projected resolution, derived from soil texture classes and depth to bedrock on (Ross et al., 2018).

Because some inconsistencies on HSG classification may stem from using foreign and global parameters, some studies have suggested new criteria for classifying Brazilian soil types (Lombardi Neto et al., 1989; Sartori et al., 2005). Sartori (2010) proposed 19 criteria for HSG soil classification based on survey of 58 soil profile and hydrodynamic data in Brazil, as described in Table 6. In this study, this soil classification method was applied to the soil types of the coastal sedimentary aquifer in Paraíba state to obtain the HSG in JPA CSA.

Table 6 – Classification of Hydrologic Soil Groups (HSG) for Brazilian soils. Source: Sartori (2010).

Depth to the water table	----- Restrictive layer -----		Further soil characteristics	HSG
	Hard	Moderate		
> 100 cm	> 100 cm	> 100 cm	Sandy texture throughout the well-drained hydromorphic soil profile.	A
			Sandy or medium texture (< 20% clay) down to restrictive layer.	A
			Medium to very clayey texture, with low colloidal activity and high FeO content and/or acric properties.	A
> 100 cm	-	50 and 100 cm	Sandy or medium texture down to moderate restrictive layer and clay with low colloidal activity.	B
			Medium to very clayey texture, with low colloidal activity and high FeO content and/or acric properties	B
			Sandy or medium texture down to moderate restrictive layer and clay with high colloidal activity.	C
> 100 cm	-	≤ 50 cm	Sandy to very sandy texture with abrupt clayey change and low colloidal clay activity.	C
			Medium, clayey or very clayey texture down to moderate restrictive layer and low clay colloidal activity.	C
			Sandy to very clayey texture with abrupt change and high clay colloidal activity.	D

> 100 cm	-	Absent	Clayey/clayey or clayey/very clayey texture, with low colloidal activity and a textural ratio less than 1.5.	B
			Medium/medium, medium/clayey or clayey/very clayey texture, with low colloidal clay activity.	B
			Clayey/very clayey texture, with low colloidal activity, low/medium FeO content and non-acric.	B
			Incipient B horizon, with morphological characteristics similar to the subsurface ferralsol horizon.	B
			Medium/medium, medium/clayey or clayey/very clayey texture, with high colloidal clay activity.	C
			Medium/clayey, clayey/clayey or clayey/very clayey texture and vertic horizon.	D
> 100 cm	50 and 100 cm	-	Sandy to very clayey texture, with low clay colloidal activity; or medium with high clay activity.	C
			Medium texture ( $\geq 20\%$ clay), clayey or very clayey, with high colloidal clay activity.	D
> 100 cm	-	-	-	D
$\leq 100$ cm	-	-	-	D

#### 4.3.3.2 Curve Number values and Antecedent Runoff Conditions

The combinations among HSG and land use/cover, soil treatment and hydrological surface condition yield a hydrological soil-cover complex (NRCS, 2002; SCS, 1972). Land use classes comprise all types of vegetation, crop residues, exposed soil, water and impermeable surfaces. Land treatment is applied mainly to agricultural lands, with distinctions between mechanical practices (contouring and terracing) and management practices (grazing control and crop rotation). Hydrological surface condition is commonly stated as poor, fair or good.

Each hydrological complex holds a mean CN value that reflects its potential surface runoff, calculated or assigned by interpolation from rainfall-runoff events observed in

American watersheds. All the hydrological complexes and their respective mean values of the CN are arranged in three tables available in the NRCS (2004), divided according to their characteristics in agriculture lands, urban areas and arid/semiarid rangelands. Therefore, the CN (Curve Number) is a dimensionless index ranging from 0 (no runoff,  $S = \infty$ ) to 100 (all precipitation becomes runoff,  $S = 0$ ).

In this study, all possible CN values were selected from NRCS (2004) tables, and then spatially assigned to hydrological soil-cover complexes in a GIS platform. A Look-Up table was build and used for geoprocessing the combination of HSG (assigned by soil type characteristics in Table 7) and land use/cover by MapBiomass collection 3.1 (NRCS, 1986).

Table 7 – Runoff curve numbers for agricultural lands. CN: Curve Number; HSG: Hydrologic Soil Group; HSC: Hydrologic Surface Condition. Source: NRCS (2004).

----- Cover description -----			----- CN for HSG -----			
Cover type	Treatment	HSC	A	B	C	D
Fallow	Bare soil	-	77	86	91	94
Forest*	-	Good	30	55	70	77
Pasture**	-	Good	39	61	74	80
Urban area***	-	-	77	85	90	92
Mosaic****	SR + CR	Good	67	78	85	89

\*Woods are protected from grazing, and litter and brush adequately cover the soil.  
 \*\*Pasture/grassland having the ground covered higher than 75%, and lightly or only occasionally grazed.  
 \*\*\*Townhouses by average lot size lower than 1/8 acres (506 m<sup>2</sup>) with 65% average impervious area.  
 \*\*\*\*Mosaic of agriculture cultivated in straight rows (SR) with pasture/crop residue (CR) cover.

The runoff potentiality before the surface runoff event is also taken into account in the SCS–CN method by the Antecedent Runoff Condition (ARC) index. Three ARC are then considered, namely: ARC-I, which denotes the dry soils able to be ploughed and cultivated; ARC-II, which denotes the moderately-wet soils, mostly due to flood occurrence; ARC-III, which denotes the practically-saturated soils, due to antecedent rainy events. As stated by Hawkins et al. (2010), the ARC-II is the benchmark condition for obtaining the listed CN values (Table 7), whereas the dry (ARC-I) and wet (ARC-III) conditions are obtained by empirical equations for defined application ranges.

Plenty of empirical equation for ARC-I and ARC-III calculation are available in literature (Ajmal et al., 2015; Ajmal and Kim, 2015; Arnold et al., 1990; Chow, Maidment and Mays, 1988; Hawkins, Hjelmfelt and Zevenbergen, 1985; Lal et al., 2016; Lal, Mishra

and Kumar, 2019; Mishra et al., 2008; Sobhani, 1975; Woodward et al., 2003). Most of these equations may be obtained by fitting the parameters of the Equation (46) – minimizing the sum of squared residuals – using rainfall-runoff datasets monitored or published in literature. Lal, Mishra and Kumar (2019) performed comparative analyses of different, well-known methods and three proposed methods, using data from 63 watersheds spread in almost all continents. The better performance was found by fitting Equations (44) and (45), from which they  $CN_I$  and  $CN_{III}$  ( $\lambda=0.03$ ) with Probability Of Exceedance (POE) equal to 12% and 88%.

$$CN = \frac{CN_{II}}{a - bCN_{II}}, \quad \text{where } b = \frac{(1 - a)}{100} \quad (46)$$

In this study, the  $CN_I$  and  $CN_{III}$  values were determined under ARC-I and ARC-III conditions, respectively, by Equations (47) and (48) (Lal, Mishra and Kumar, 2019). For selecting the proper condition, the 5-days-antecedent cumulative precipitations ( $P_{5d}$ , mm) were spatially-calculated from ground-based and IMERG product. To this end, similarly to Ajmal et al. (2015), Ajmal and Kim (2015) and Lal, Mishra and Kumar (2019), intervals were considered for distinguishing the ARC, and the  $P_{5d}$  values were calculated for determining them. For the Growing Season (GS, from March to July) and Dormant Season (DS, from August to February), the ARC intervals were the following: for ARC-I, if  $P_{5d} < 35.56$  mm (GS) or  $P_{5d} < 12.7$  mm (DS); for ARC-II, if  $35.56 \leq P_{5d} \leq 53.34$  mm (GS) or  $12.70 \leq P_{5d} \leq 27.94$  mm (DS); and, for ARC-III, if  $P_{5d} > 53.34$  mm (GS) or  $P_{5d} > 27.94$  mm (DS) (Chow, Maidment and Mays, 1988; SCS, 1972). While the urban area and bare soil were considered only in DS condition, the forest was considered only in GS condition.

$$CN_{I,\lambda=0.03} = \frac{CN_{II,\lambda=0.03}}{2.42081 - 0.01421CN_{II,\lambda=0.03}} \quad (47)$$

$$CN_{III,\lambda=0.03} = \frac{CN_{II,\lambda=0.03}}{0.42405 + 0.00576CN_{II,\lambda=0.03}} \quad (48)$$

As shown in Equations (47) and (48), the  $CN_{II}$  values must be obtained for  $\lambda$  equal to 0.03 instead of the conventional  $\lambda$  equal to 0.20 before estimating the surface runoff. Lal, Mishra and Kumar (2019) found that in 61 out of 63 watersheds throughout the world, the  $\lambda$  was lower than 0.20, among which roughly 50% featured  $\lambda$  lower than 0.05. In Southern Brazil, da Costa et al. (2019) found that 67% of the rainfall events held  $\lambda$  lower than 0.06, whereas only 12% held  $\lambda$  higher than 0.20. Thus, for converting CNs from  $\lambda$  equal to 0.2 ( $CN_{II,\lambda=0.20}$ ) to  $\lambda$  equal to 0.03 ( $CN_{II,\lambda=0.03}$ ), the Equation (49) was used (Lal et al., 2016).



$$CN_{II,\lambda=0.03} = \frac{25400}{\left[ 254 + 0.654 \left( \frac{25400}{CN_{II,\lambda=0.20}} - 254 \right)^{1.248} \right]} \quad (49)$$

#### 4.3.4 Soil water storage changes from soil moisture imagery

Soil water storage capacity is defined, in soil science, as the total amount of water stored in soil within the plant root zone (MABC, 2015). This stored water can either be returned to the atmosphere by plant transpiration and evaporation or be conducted to lower levels and groundwater (Saxton and Rawls, 2006). Soil water storage depends importantly on the soil structure and texture, as well as on organic content and crop rooting depth, which affects the percolation flux and root water uptake (MABC, 2015; Narasimhan, 2009), leading to different soil moisture profiles.

According to Clothier and Green (2005), the change in the soil water storage,  $\Delta S$ , can be calculated by the change in the soil moisture content profile,  $\theta(z)$ , from one day to another,  $\Delta t$ , integrated from the surface down to the base of root zone,  $h_{CV}$ , by Equation (50):

$$\Delta S = \int_0^{h_{CV}} \Delta \theta(z) dz \quad (50)$$

A vertically-averaged soil moisture (in %) was retrieved from SMAP SPL4SMAU product, which assimilates one integrated value per pixel down to 1 m at every 3 hours. Thus, 1 m was considered as the average rooting depth and, therefore, as the bottom boundary of the Control Volume (i.e., the  $h_{CV}$ ), for applying the water budget equation. The  $\Delta S$  may be either positive or negative when the average soil moisture of the next day ( $\theta_{i+1}$ , or simply  $S_{i+1}$ ) is higher and lower than the current day ( $\theta_i$ , or simply  $S_i$ ), respectively, through  $S_{i+1} - S_i$  in Equation (51). Similarly, Long, Longuevergne and Scanlon (2014) found the water budget equation closure by calculating the soil water storage changes from land surface models and from remote sensing data.

$$\Delta S = \frac{(S_{i+1} - S_i) \cdot h_{CV}}{\Delta t} = \frac{(S_{i+1} - S_i) \cdot 1000 \text{ mm}}{1 \text{ day}}, \quad \text{for } S_{i+1} \text{ and } S_i \text{ given in \%} \quad (51)$$

Since the JPA CSA is located near to the equator, the soil moisture was retrieved at 6:00 a.m. and 6:00 p.m. (at the local solar time), when SMAP satellite crosses the hemispheres. Conversely, since the satellite takes 2 to 3 days to map the whole globe, some images over the JPA CSA were unmapped on a couple of days of the year. Thus, similarly

to Souza, Neto and Souza (2018), the daily soil moisture data was computed in three ways: (1) if both orbits were completed on the same day, the two values were averaged; (2) if only one orbit had a valid value, this value was considered for that day; and (3) if no valid value was obtained in either orbit, the soil moisture calculated on the previous day was repeated. Lastly, the images were then resampled from 9-km to 500-m resolution by using bilinear interpolation (see Equation (1), in item 4.3.1.1).

#### 4.3.5 GIS-based water budget equation

Water budget equation was employed on monthly and annual resolutions to obtain the GWR below the 1-m root zone, which is commonly understood, for the sake of modelling purposes, as the water effective infiltration parcel that crosses vertically the root-zone control volume. Four categories of variables were considered in the water budget equation according to JPA CSA conceptual model proposed in Figure 36, namely: (1) Main input: precipitation; (2) Output parcels: actual evapotranspiration and surface runoff; (3) Input-output variable: soil water storage changes in the root zone, and; (4) Outcome, either positive for GWR rates, or equal to zero for capillarity rise occurrence (Melo and Wendland, 2017).

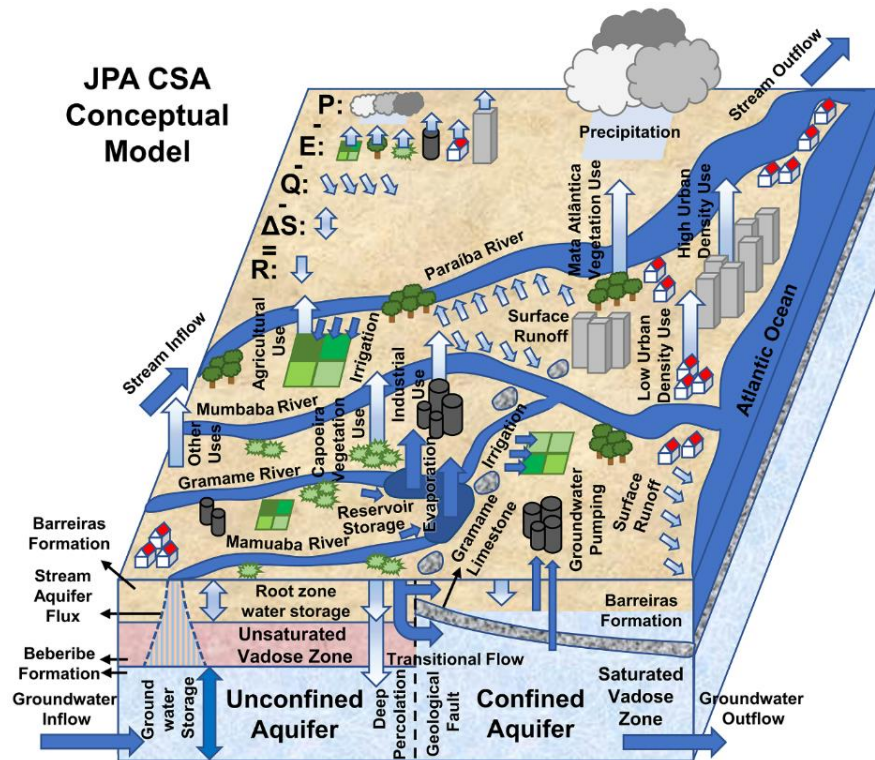


Figure 36 – Conceptual model of water budget equation by remote sensing in João Pessoa Case Study Area (JPA CSA); P: Precipitation; E: Actual Evapotranspiration; Q: Surface Runoff;  $\Delta S$ : Soil Water Storage changes; R: Groundwater Recharge; Blue arrows: disregarded water balance components.

The data scarcity or unavailability with regards to irrigation, pumping and interception parcels, makes unfeasible their accounting in the water budget equation. Moreover, the complexity of unconfined-confined aquifer connections and the diversity of soil type and geological formations revealed the insufficient soil knowledge for more complex modelling, so that the horizontal inflow effects were disregarded. Such assumption of no lateral flow has been similarly adopted on different spatial resolutions in the literature (Liu et al., 2016; Long et al., 2015; Lv et al., 2017; Wan et al., 2015), which seems plausible due to monthly and annual resolution of calculation. Therefore, for the sake of simplicity and applicability, the application of the water budget equation was performed in the near-surface root zone using the pixel area as the hydrological response unit. The water budget equation then represented the soil water balance in the root zone, as formulated in Equation (52):

$$S_{i+1} = S_i + P_i - E_i - Q_i - R_i, \quad \text{in mm} \quad (52)$$

where ‘i’ denotes the present day, ‘i+1’ denotes the next day, and the other symbols are related to the water balance components, namely: ‘P’ is precipitation; ‘E’ is actual evapotranspiration; ‘Q’ is surface runoff; ‘S’ is average root-zone soil moisture, and; ‘R’ is groundwater recharge (same as GWR).

The groundwater recharge, or simply ‘R’, is then the expected outcome of the water budget equation and stands for the downward soil water movements. As such, by isolating the ‘R’, the Equation (53) is formulated:

$$\begin{cases} R = P - E - Q - 1000 \cdot \Delta S, & \text{if } P - E - Q - 1000 \cdot \Delta S > 0 \\ R = 0 & , \text{ if } P - E - Q - 1000 \cdot \Delta S < 0' \end{cases} \quad \text{where } \Delta S = (S_{i+1} - S_i) \quad (53)$$

for S given in %

Once the water budget equation is formulated, some important scenarios can be highlighted, which are depicted in Figure 37 as follows. On one hand, if there exists precipitation (Figure 37a), two situations are possible: (1) the input (P, or P and  $\Delta S$ ) are higher than the losses (E and Q, or E, Q and  $\Delta S$ ), in this case there exists recharge, or; (2) the input are lower than the losses, in this case the capillarity rise ‘C’ occurs rather than recharge (i.e. R equal to zero, similar to Melo and Wendland, 2017). It is noteworthy to mention that  $\Delta S$  can be input or loss component, namely: (1) if  $S_{i+1}$  is higher than  $S_i$ , the  $\Delta S$  is a loss component holding a negative sign in Equation (53) (i.e.,  $-1000 \cdot \Delta S$ ), or; (2) if  $S_{i+1}$  lower than  $S_i$ , the  $\Delta S$  become an input component holding a positive sign in equation in Equation (53) (i.e.,  $+1000 \cdot \Delta S$ ).

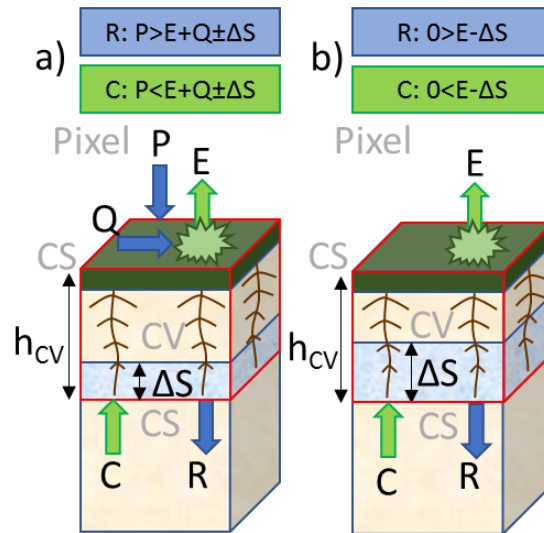


Figure 37 – Two soil water balance scenarios, (a) precipitation higher than zero, and (b) precipitation equal to zero, for reasoning about the water budget equation through the root-zone Control Volume (CV).  $h_{cv}$ : Height of CV equal to 1 m; CS: Control Surface; P: Precipitation; E: Actual Evapotranspiration; Q: Surface Runoff;  $\Delta S$ : Soil Water Storage changes; R: Groundwater Recharge; C: Capillarity Rise;

On the other hand, if there exists no precipitation but the  $S_i$  is lower than  $S_{i-1}$  (Figure 37b), then there may still be R, and two more situations are possible: (1) if  $\Delta S$  is higher than 'E', the water stored flows downward, or; (2) if  $\Delta S$  is lower than 'E', the water stored is lost by 'C'.

#### 4.4 Validation of the GIS-based water balance components

##### 4.4.1 Performance indexes for goodness-of-fit analysis

Five statistic metrics were selected to evaluate comprehensively the goodness-of-fit of the results of this study (Table 8). Only relative values of the metrics were adopted so that a comparative discussion of the results in relation to literature outcomes could be performed. On one hand, the first category of metrics includes the correlation coefficient (CC, Equation (54)) the coefficient of determination ( $R^2$ , Equation (55)) and the Kling-Gupta Efficiency coefficient (KGE, Equation (56)), describing the agreement between simulated and observed estimates. On the other hand, the second category of metrics includes the percent bias (PBIAS, Equation (57)) and the relative root mean square error (RRMSE, Equation (58)), which are used to describe the bias and error between simulated and observed estimates, respectively. The equations and perfect values of those metrics are listed in Table 8.

Table 8 – List of the performance indexes used in the evaluation and comparison. S: satellite precipitation estimate; G: gauge observed precipitation;  $\sigma_G$ : standard deviations of gauge precipitation;  $\sigma_S$ : standard deviations of satellite precipitation;  $\langle \rangle$ : mean of a dataset;  $\Sigma$  : sum of a dataset.

Equation	Statistic metrics	Formulation	Perfect value
(54)	Correlation Coefficient (CC)	$CC = \frac{\langle (S - \langle S \rangle)(G - \langle G \rangle) \rangle}{\sigma_S \sigma_G} \times 100\%$	100%
(55)	Coefficient of Determination ( $R^2$ )	$R^2 = CC^2$	100%
(56)	Kling-Gupta Efficiency coefficient (KGE)	$KGE = 1 - \left[ (CC(S, G) - 1)^2 + \left( \frac{\sigma_S}{\sigma_G} - 1 \right)^2 + \left( \frac{\langle S \rangle}{\langle G \rangle} - 1 \right)^2 \right]^{\frac{1}{2}} \times 100\%$	100%
(57)	Percent Bias (PBIAS)	$PBIAS = \frac{\Sigma(S - G)}{\Sigma G} \times 100\%$	0%
(58)	Relative Root Mean Square Error (RRMSE)	$RRMSE = \frac{((S - G)^2)^{1/2}}{\langle G \rangle} \times 100\%$	0%

The CC, PBIAS and RRMSE metrics were used to assess the goodness-of-fit of the bias-corrected precipitation and the GWR estimates. For the verification of runoff surface and soil moisture satellite product, the CC metric was applied. And, the KGE and  $R^2$  metrics were used for validating the CRNS data and HYDRUS-1D-COSMIC results.

#### 4.4.2 Verification of the daily actual evapotranspiration

The GIS-based actual evapotranspiration data could not be validated provided by Bowen ratio energy balance method (Bowen, 1926), because the meteorological data in GEB were available from September/2017, covering only the four last months of 2016-2017 analysis period. As such, similar to what was done by de Oliveira et al. (2018), the actual evapotranspiration was compared to the reference evapotranspiration ( $E_{to}$ ,  $\text{mm h}^{-1}$ ), the latter being calculated using the Penman-Monteith equation (Allen et al., 1998) in Equation (59):

$$Et_o = \frac{0.408\Delta(Rn - G) + \gamma[37/(T + 273)]u_2(e_s - e_a)}{\Delta + \gamma(1 + 0.34u_2)} \quad (59)$$

where  $Rn$  is the net radiation at the crop surface ( $\text{MJ m}^{-2} \text{ day}^{-1}$ ),  $G$  indicates the soil heat flux density ( $\text{MJ m}^{-2} \text{ day}^{-1}$ ),  $u_2$  is the mean hourly wind speed at 2 m height ( $\text{m s}^{-1}$ ),  $e_s$  defines the saturation vapour pressure at air temperature  $T$  height (kPa, see Equation (9)) and  $e_a$  indicates the actual vapour pressure (kPa, see Equation (10)),  $\Delta$  represents the slope vapour pressure curve ( $\text{kPa}^\circ\text{C}^{-1}$ , see Equation (11)),  $\gamma$  is the psychrometric constant ( $\text{kPa}^\circ\text{C}^{-1}$ , see Equation (12)), and  $T$  is the mean air temperature at 2 m height ( $^\circ\text{C}$ ).

Since the wind speed data is measured at 6.3 m (see item 4.2), differently of the 2-m height advocated by Penman-Monteith equation, a logarithmic wind speed profile may be used to convert the data to the standard height of measurements, as shown by Equation (60):

$$u_2 = u_z \frac{4.87}{\ln(67.8z + 5.42)} \quad (60)$$

where  $u_2$  and  $u_z$  are the wind speeds ( $\text{m s}^{-1}$ ) at 2 m and  $z$  height of measurement (m) above the ground surface, respectively. To ensure the integrity of computations, the further weather measurements should similarly be converted to 2-m height (refer to Allen et al., 1998), as they are measured at 5.3-m height (see item 4.2). These operations may all be carried out by hydro(geo)logical models, such as HYDRUS-1D (Šimůnek et al., 2013b).

The verification of daily actual evapotranspiration was carried out against the daily reference evapotranspiration time series rather than potential evapotranspiration. It was performed because the JPA CSA is placed in a tropical wet area rather than a tropical dry semiarid zone, which was the case of Coelho et al. (2017). Such comparison may reveal if the simulated actual evapotranspiration behaves conveniently within the maximum boundary imposed by the reference evapotranspiration. Moreover, it is expected that such comparison may also reveal the influence of the meteorological forcing data over the two evapotranspiration time series.

#### 4.4.3 Verification of the monthly surface runoff

Baseflow is a discharge phenomenon with distinctive and recognisable features and a plausible physical explanation, but very difficult to be precisely defined or reliably separated from other streamflow components (Duncan, 2019). Thus, the most widely used method to differentiate the runoff from baseflow is the graphical straight-line method, which

consists of graphically extending a straight line from hydrograph rising limb onset to an ending point of the hydrograph recession after the discharge peak (Boscha et al., 2017). The runoff is referred to as the discharge volume above the straight line, while the baseflow is the discharge volume below the line (Figure 38). The only dependence on expert judgement, make the straight-line method a valuable tool for validation purposes, even though several updated baseflow separation methods are available (Indarto, Novita and Wahyuningsih, 2016; Yang, Choi and Lim, 2018; Yang et al., 2019b; Zhang et al., 2017).

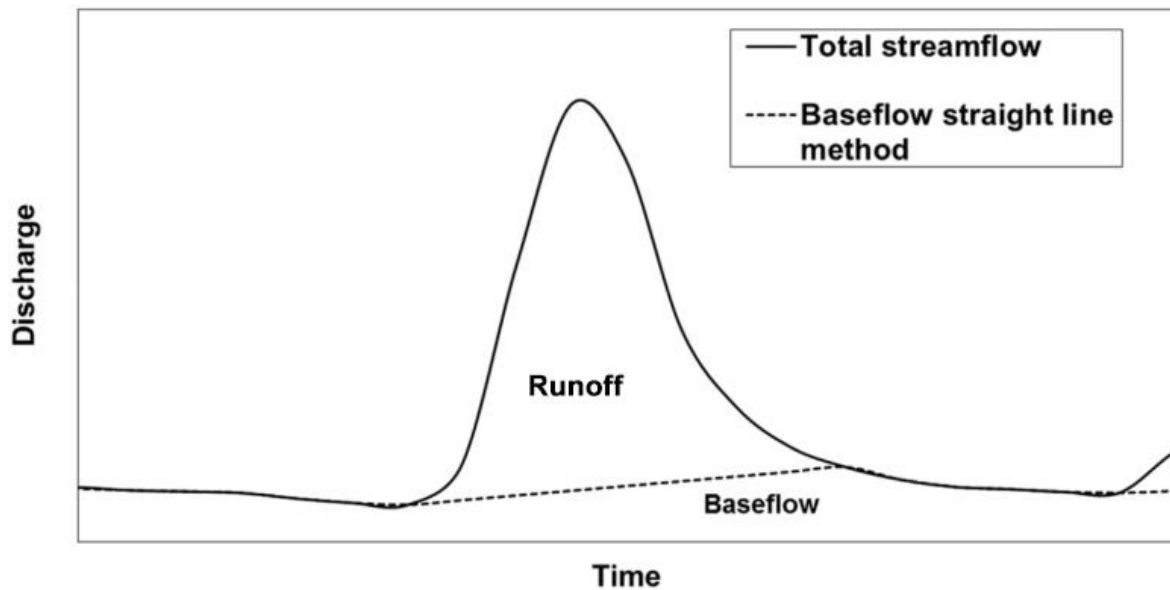


Figure 38 – An illustration of the baseflow separation through the straight-line method, where the dashed line connects the onset and ending point of the runoff. Source: adapted from Boscha et al. (2017).

To date, only three stream gauges installed in GEB hold rating curves ready for yielding the runoff time series (Barbosa, 2015). The stream gauge 503, located slightly at downstream of the confluence of GEB tributaries, was selected for runoff verification because it encompassed the larger catchment. Yet, its water level time series only covered the year 2017 from the 2016-2017 study period. The catchment of gauge 503 was delimited through a GIS software from the Digital Elevation Model (DEM) provided by Shuttle Radar Topography Mission (SRTM) on 30-m spatial resolution (Supplementary Figure 18).

Owing to the small-scale dimension of stream gauge 503, it was assumed that the time travel was lower than one day, so that the 15-min water level measurements were averaged from 09:00 to 09:00, due to ground-based precipitation resolution. Then, the baseflow separation was carried out over the daily discharge time series, in order to obtain the daily average runoff at the stream gauge. The daily water level positive differences

(increments) were compared to daily mean surface runoff values summed on gauge 503 catchment, the later obtained by NRCS–CN method from both ground- and IMERG-based precipitation data. The daily increments obtained from either gauge 503 water level measurements or NRCS–CN estimates (using the Gauge and IMERG data) were then summed to compute the respective monthly water depth stemmed from the surface runoff, and the CC metric was calculated to assess the goodness-of-fit of the results.

#### **4.4.4 Test of the satellite-based soil moisture**

The high spatiotemporal variability of soil moisture hampers for the remote sensing products, such as SMAP products, using *in situ* monitoring networks. The presence of heterogeneous land use/cover should also be taken into account for SMAP validation, using a weighted average approach based on proportions of different coverages (Yee et al., 2016). Such SMAP validation might be even harder-tasking when considered along the 1-m root zone, such as SPL4SMAU product, which was used in this study for averaging on soil water storage changes. On the other hand, some studies have claimed about the good performance of SPL4SMAU root-zone product compared to *in situ* and other satellite (such as GRACE) measurements worldwide, stating its high potential to several applications (Das, Singh and Hazra, 2019; Jia et al., 2019; Zeng et al., 2016). In Northeast of Brazil, the lack of extensive ground-based networks, reported by Barbosa et al. (2019), impairs a comprehensive soil moisture validation, only possible by a few point-scale monitoring probes. Thus, three TDR probes vertically-inserted in GEB (site 2, 3 and 4, see Figure 25d) were used to averaged soil moisture down to 30-cm depth, allowing for testing the overall behaviour of SMAP SPL4SMAU product averaged on GEB after the 500-m pixel resampling. Thus, both soil moisture time series were plotted on daily scale, as well as the CC metric between them was calculated, so that the SMAP ability in responding to rainfall events could be checked.

#### **4.4.5 Validation of the annual Groundwater Recharge**

The Water Table Fluctuation method, so-called WTF method, was carried out using water level variation data in monitoring wells, to validate the GWR estimates obtained by water budget equation through the GIS-based modelling. The WTF method is based on the premise that the elevation of water levels in unconfined aquifers is the result of precipitation that reaches the free surface by infiltration, which characterises the recharge process



(Scanlon, Healy and Cook, 2002). For its application, manual and automatic groundwater level fluctuation data of the 23 wells in JPA CSA were used (see Figure 25c) – not the wells in GEB due to their shallow groundwater depths – because they featured GWR and their measurements were not meaningfully affected by water pumping.

Accordingly, the WTF method requires only the knowledge of the aquifer specific yield ( $S_y$ , dimensionless) and the information about the potential groundwater level rise ( $\Delta H$ , mm yr<sup>-1</sup>) during a particular time ( $\Delta t$ , yr) to estimate the GWR rates ( $R_{WTF}$ , mm yr<sup>-1</sup>) (Equation (61) and Figure 39):

$$R_{WTF} = S_y \frac{\Delta H}{\Delta t} \quad (61)$$

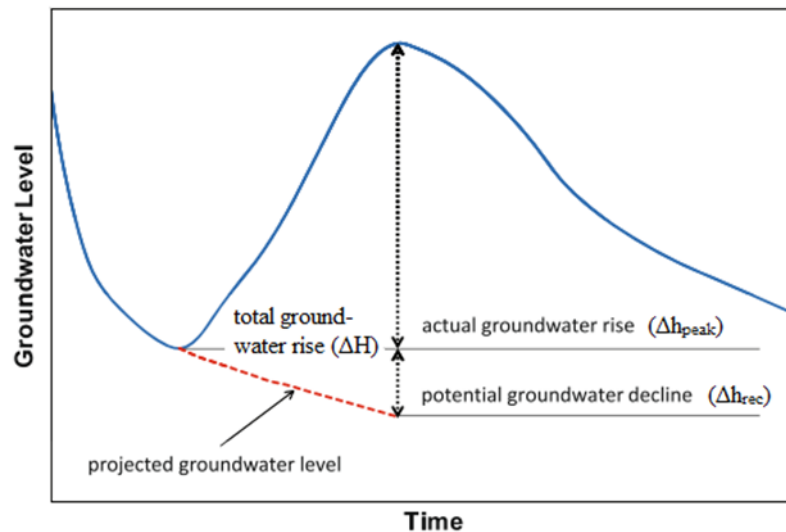


Figure 39 – Total groundwater rise ( $\Delta H$ ) obtained by summing the actual groundwater rise ( $\Delta h_{peak}$ ) and potential groundwater decline ( $\Delta h_{rec}$ ) for averaging on groundwater recharge rates in unconfined aquifers through the WTF method. Source: modified from Jie et al. (2011).

The application of the Equation (61) for each water level elevation results in a recharge process where  $\Delta H$  is set equal to the difference between the peak of the rise and the lowest point of an extrapolated antecedent recession curve at the peak time (Healy and Cook, 2002). The extrapolated recession curve is the line that the water level would have without the elevation level; which was generated in this study by the same potential function adopted by Wendland et al. (2007). Furthermore, the  $S_y$  values of 0.10, 0.16 and 0.24 were simulated through the AQTESOLV v4.5 (AQUIFER TEST SOLVER) software (Duffield, 2007) by Prof. Dr Nelson Caicedo. Such  $S_y$  values are similar to those reported by Vasconcelos, Teixeira and Neto (2010), ranging from 10.36% to 26.26%, in Jandaíra unconfined coastal aquifer in the Northeast of Brazil. Because of its simplicity and the wide availability of water level

hydrographs from the monitoring wells, the WTF method has been used for many years by hydrogeologists (Healy and Cook, 2002).

#### 4.5 Calibration of the Cosmic-Ray Neutron Sensing

For estimating the GWR, the CRNS and TDR probes were installed at site 2 and site 5 in GEB, respectively. The two techniques measure the soil moisture, but on different field scales: CRNS on intermediary-scale and TDR on point-scale. Both information were used to calibrate the parameters of the soil hydraulic properties via inverse modelling, as well as using the COSMIC operator for CRNS data. The soil hydraulic properties are essential for modelling the water flux processes in variably-saturated soils, such as GEB soil. As a result, the percolation water fluxes at different soil depths, and the GWR at the variable boundary bottom, could be estimated using HYDRUS-1D-COSMIC model. The stepwise procedures of data simulation and validation used for estimating the GWR are briefly described in Figure 40, which include: Root Water Uptake (RWU), inward and outward water fluxes, percolation water fluxes, and GWR rates.

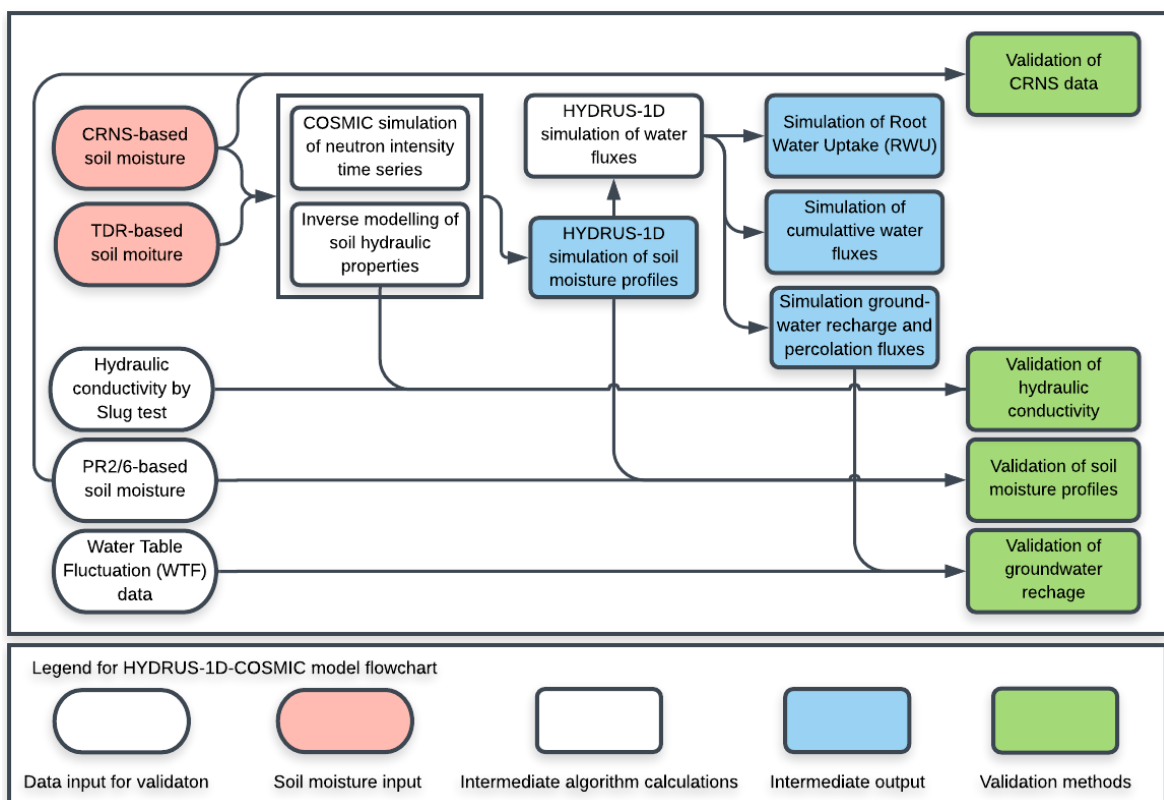


Figure 40 – Flowchart describing the stepwise procedures of data simulation and validation for estimating the percolation water fluxes and groundwater recharge through the HYDRUS-1D-COSMIC model.

#### 4.5.1 Soil sampling, footprints and weighting functions

The calibration scheme of the CRNS was conceived to cover different moisture conditions at 17 locations and 3 depths around the CRNS probe (Figure 41). The field campaign took place on July 20th, 2018, with the soil in a moderate humid condition. A higher number of soil core samples were extracted within ~10 m from the CRNS probe due to its high neutron counting sensitivity inside this radius (Köhli et al., 2015). Due to the presence of a shallow groundwater table in Podzol soil type, the soil was sampled only in three depth intervals: 0-5, 5-10 and 15-20 cm (IAEA, 2017). At laboratory, the soil core samples were immediately weighed before and after drying in an oven at 105°C, so that the Gravimetric Water Content (GWC, in  $\text{g g}^{-1}$ ), Volumetric Water Content (VWC, in  $\text{cm}^3 \text{cm}^{-3}$ ) and soil bulk density ( $\rho_{\text{bd}}$ , in  $\text{g cm}^{-3}$ ) could be calculated.

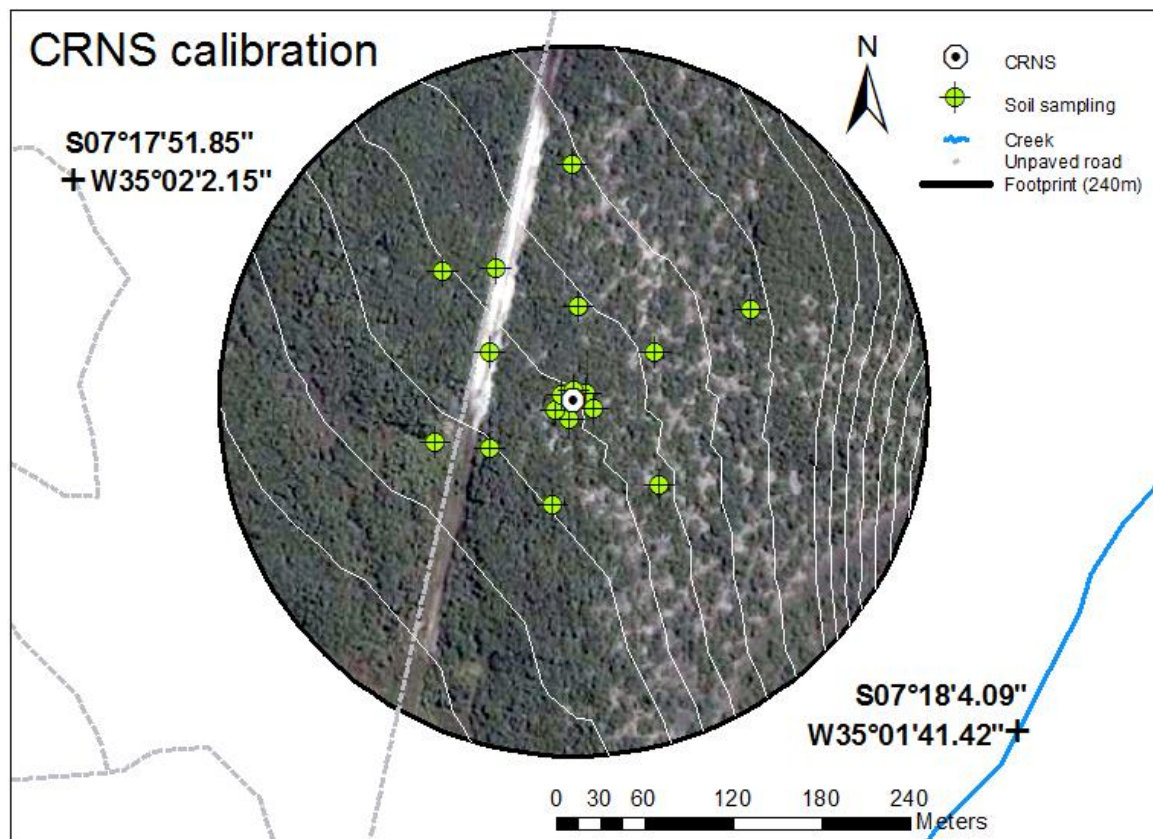


Figure 41 – Soil core sampling scheme for CRNS probe calibration through the gravimetric method.

Once the soil samples are collected, an average value shall be calculated in order to proceed with the CRNS calibration, whose procedures are depicted in Figure 42. Köhli et al. (2015) proposed a weighting method composed by the calculation sequence of VWC vertical, horizontal and final weighted average.

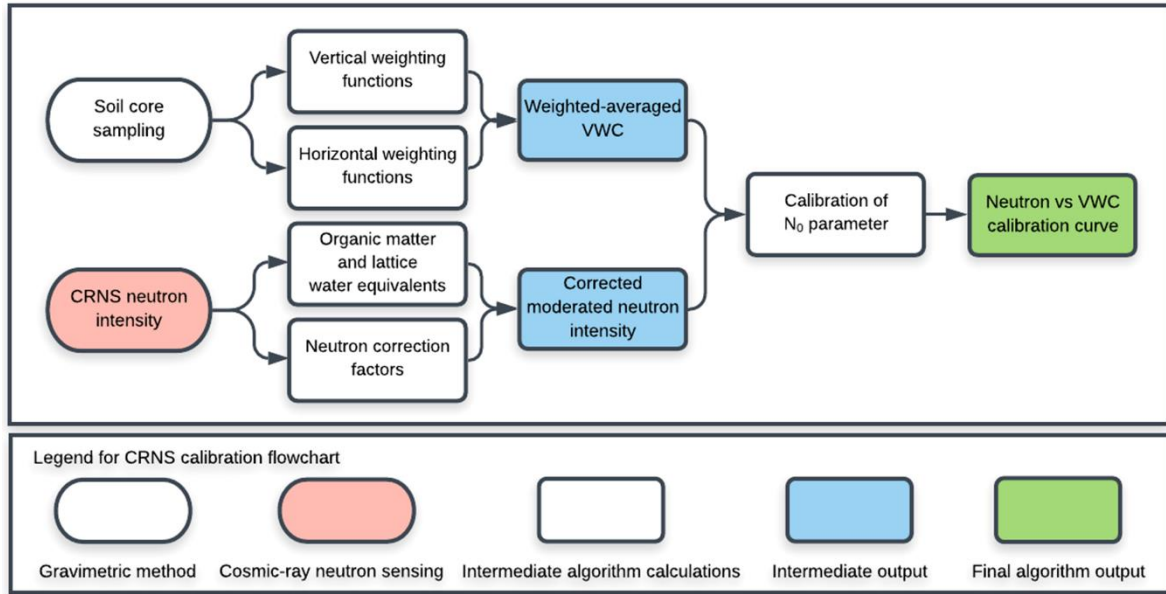


Figure 42 – Flowchart describing the procedure for site-specific CRNS calibration based on soil core samples, organic matter and lattice water equivalents and accounting for standard neutron intensity corrections.  $N_0$ : dry neutron intensity parameter in CRNS calibration equation.

Thus, the vertical weights are calculated in Equation (62):

$$W_d(r, \theta) = e^{-2d/D_{86}} \quad (62)$$

where  $d$  is the depth of soil sampling and  $D_{86}$  the penetration depth. The  $D_{86}$  is given the vertical extent of the soil column from which – in our case during the calibration day – 86% of the neutrons detected by CRNS probe have come from; and it is also called vertical footprint. It is negatively correlated to soil moisture, depends little on soil properties (e.g. bulk density:  $\rho_{bd}$ , in  $\text{g cm}^{-3}$ ), but can be influenced by other hydrogen pools (such as soil organic matter, lattice water and vegetation) (Bogena et al., 2013; Franz et al., 2012b). Thus, according to Köhli et al. (2015), the  $D_{86}$  decreases with distance to the CRNS probe similar to an irregular hemisphere, and can be calculated at a radial distance  $r$  (in m) by Equation (63):

$$D_{86}(\rho_{bd}, r, \theta) = \rho_{bd}^{-1} \left( 8.321 + 0.142(0.967 + e^{-r/100}) \frac{26.42 + \theta}{0.057 + \theta} \right) \quad (63)$$

Moreover, Köhli et al. (2015) also proposed a calculation of the horizontal footprint,  $R_{86}$ , ranging usually from 130 to 240 m depending on absolute air humidity ( $h_a$ , in  $\text{g m}^{-3}$ ), air pressure ( $p$ , in mbar), VWC (or  $\theta$ , in %), and vegetation height ( $H_{veg}$ , m), as shown by Equation (64):

$$R_{86}(h_a, \theta, p, H_{veg}) = \left( \frac{0.5}{0.86 - e^{-p/1013.25}} \right) \cdot (1 - 0.17(1 - e^{-0.41H_{veg}})(1 + e^{-7\theta})) \cdot R_{86}(h_a, \theta) \quad (64)$$

where  $R_{86}(h_a, \theta)$  is a basic size of the horizontal footprint given by  $(0.86 \int_0^\infty W_r dr)$ , which has to be calculated iteratively from horizontal weights,  $W_r$ , which are calculated as a function of radial distance,  $r$ , from the CRNS probe,  $r$ , and field-mean VWC by Equation (65):

$$W_r(h_a, \theta) \approx \begin{cases} F_1 e^{-F_2 r} + F_3 e^{-F_4 r}, & 0.5 \text{ m} < r \leq 50 \text{ m} \\ F_5 e^{-F_6 r} + F_7 e^{-F_8 r}, & 50 \text{ m} < r \leq 600 \text{ m} \end{cases} \quad (65)$$

where  $F_i$  ( $i$  varying from 1 to 8) is individually dependent on field-mean VWC,  $\langle \theta_{ij} \rangle$ , and field-mean absolute air humidity,  $\langle h_a \rangle$ , which can be averaged with equal weights, i.e.  $W_{ij} = 1 \forall i, j$ , for each depth 'j' and point 'i'. Equation (66) summarizes the equations to calculate  $F_i$ :

$$\begin{cases} F_1 \\ F_2 \\ F_3 \\ F_4 \\ F_5 \\ F_6 \\ F_7 \\ F_8 \end{cases} = \begin{cases} 8735(1 + 0.00978h_a)e^{-17.1758\theta} + 11720(1 + 0.003632h_a) - 70450 \\ ((6.8513 \times 10^{-5}h_a - 2.7925 \times 10^{-2})e^{-5.0399\theta/(1+9.2926\theta)} + 2.8544 \times 10^{-2})(1 + 0.002455h_a) \\ 247970(1 + 0.00191h_a)e^{-17.63\theta} + 374655 - 195725\theta \\ 5.4818 \times 10^{-2}e^{-15.921\theta} + 0.6373 - 5.99 \times 10^{-2}\theta + 5.425 \times 10^{-4}h_a \\ 1383702 \left( 0.02 - \frac{1}{0.130(1521\theta + h_a - 0.130)} \right) (0.0156 - \theta)e^{-4.156(\theta - 0.0156)} + 5325(0.7 - 0.00238h_a\theta) \\ 6.031(h_a + 98.5) + 1.0466 \times 10^{-3}\theta \\ (11747(1 - 0.00475h_a)e^{-41.66\theta(1 - 0.00604h_a)} + 4521 - 2534\theta)(2 + 0.01998h_a) \\ ((8.81 \times 10^{-5}h_a - 1.543 \times 10^{-2})e^{-10.06\theta/(1+0.0405h_a+20.24\theta)} + 1.807 \times 10^{-2})(2 + 0.0011h_a) \end{cases} \quad (66)$$

The absolute air humidity is calculated from relative humidity ( $h_r$ , in %) and air temperature ( $T$ , in °C) by Equation (67):

$$h_a = \frac{h_r}{100} \left( \frac{6.112e^{\left(\frac{17.62T}{243.12+T}\right)} 216.68}{T + 273.16} \right) \quad (67)$$

Finally, the VWC final weighted average,  $\langle \theta_k \rangle$ , is calculated by Equation (68):

$$\langle \theta_k \rangle = \frac{\sum_i W_k \theta_k}{\sum_i W_k} \quad (68)$$

where  $W_k$  refers to vertical ( $W_d$ ) or horizontal ( $W_r$ ) weighting functions, and  $\theta_k$  denotes the VWC values obtained by gravimetric method.

Köhli et al. (2015) recommend to first compute the vertical VWC average  $\langle \theta_{ij} \rangle_i$  at each point 'i' with the weighting function  $W_d(r_i, \langle \theta_{ij} \rangle)$  (Equation (62)), and then average horizontally these values with the weighting function  $W_r(h, \langle \theta_{ij} \rangle)$  (Equation (65)). Later, Schrön et al. (2017) published a simpler, approximate formula for calculating the  $W_r$ .

#### 4.5.2 Neutron intensity calibration and correction factors

A theoretical relationship between corrected neutron intensity ( $N'$ , in counts  $h^{-1}$ ) and VWC (or  $\theta$ ) in Equation (69) was proposed by Desilets, Zreda and Ferré (2010) after applying a neutron particle transport model for homogeneous sand ( $SiO_2$ ), which depends on one site-specific calibration parameter, the dry neutron intensity parameter ( $N_0$ , in counts  $h^{-1}$ ). For calculating the  $N_0$ , it shall be isolated in that equation and, then,  $N'$  and  $\theta$  shall be averaged from the CRNS corrected intensity and the VWC weighting-averaged (see item 4.5.1) in the calibration period, respectively.

$$\theta(N', N_0) = \left( \frac{0.0808}{N'/N_0 - 0.372} - 0.115 \right) \rho_{bd} - SOW - LW \quad (69)$$

Similarly to Heidbüchel, Güntner and Blume (2016), the soil organic matter and lattice water equivalents (SOW and LW, respectively) were obtained in this study by weighting soil samples after the drying at  $105^\circ C$ , and the burning of 10 g of each dry sample at  $400^\circ C$  (for 16 h) and  $1000^\circ C$  (for 12 h), successively. The SOW and LW were then calculated in volumetric values by Equation (70) and (71):

$$SOW = 0.556 \frac{m_{105} - m_{400}}{m_{105}} \rho_{bd} \quad (70)$$

$$LW = \frac{m_{400} - m_{1000}}{m_{105}} \rho_{bd} \quad (71)$$

This ground-level neutron intensity is notably affected by air barometric pressure, incoming neutron flux, and atmospheric water vapour (Andreasen et al., 2017a). Thus, some correction models were developed to correct the CRNS intensity to arbitrary reference conditions.

Air pressure is inversely proportional to neutron intensity acting as an atmospheric mass-shielding, which varies with geographic location and meteorological condition (Desilets and Zreda, 2001; Wang et al., 2019b). Thus, the air pressure correction factor for latitude and altitude is shown by Equation (72) (Desilets and Zreda, 2001):

$$f_p = e^{\left( \frac{P_i - P_0}{L} \right)} \quad (72)$$

where  $L$  is the mass attenuation length for high-energy neutrons (Desilets, Zreda and Prabu, 2006), calculated as 138.45 hPa from geomagnetic cut-off rigidity map provided by (Andreasen et al., 2017a).  $P_0$  (in hPa) is an arbitrary baseline reference pressure, usually

averaged for the entire measurement period, equal to 1001.6 hPa in this study.  $P_i$  (in hPa) is the barometric air pressure at the time step of measurement.

Solar activity can strongly influence the neutron intensity either on monthly or on weekly time scales (Desilets and Zreda, 2001). Thus, the incoming cosmic radiation correction factor normalizes the neutron intensity to a single reference solar activity level as shown by Equation (73) (Zreda et al., 2012):

$$f_m = \frac{M_0}{M_i} \quad (73)$$

where  $M_i$  (in counts  $h^{-1}$ ) is the incoming monitored neutron intensity retrieved from the neutron monitor database at the time step of measurement, available on: <http://www.nmdb.eu/nest/>. Data from the Potchefstroom monitor, South Africa, (PTFM), corrected by pressure and efficiency, were used because the nearby monitors either was closed down or had no data available online. In addition,  $M_0$  (in counts  $h^{-1}$ ) is the neutron intensity in an arbitrary baseline reference time, usually averaged for the entire measurement period, equal to 125 counts  $h^{-1}$  in this study.

Atmospheric water vapour content affects the number of hydrogen atoms responsible to moderate the near-ground cosmic-ray neutrons (Köhli et al., 2015; Wang et al., 2019b). Thus, the water vapour correction factor was also developed to correct the CRNS intensity as shown by Equation (74) (Rosolem et al., 2013):

$$f_v = 1 + 0.0054(h_a - h_0) \quad (74)$$

where  $h_a$  (in  $g\ m^{-3}$ ) is the absolute air humidity calculated at each measurement time by Equation (67) (see item 4.5.1), and  $h_0$  (in  $g\ m^{-3}$ ) is the absolute air humidity in an arbitrary baseline reference time, usually averaged over entire measurement period, equal to 18.45  $g\ m^{-3}$  in this study.

Finally, the corrected neutron intensity ( $N'$  in counts  $h^{-1}$ ) can be calculated from the measured neutron intensity ( $N$  in counts  $h^{-1}$ ) of the CRNS probe and the correction factors for air barometric pressure, incoming cosmic radiation, and atmospheric water vapour, as shown in Equation (75):

$$N' = N \cdot f_p \cdot f_m \cdot f_v \quad (75)$$

Regarding the vegetation biomass, it may have an important influence over CRNS time series over forest condition (Heidbüchel, Güntner and Blume, 2016), but it was disregarded in this study due to unavailability of biomass information in GEB. The close



proximity of CRNS probe to leaves and stems induce the assimilation of exceeding thermalized neutrons that may compensate the subtraction effect of the biomass water equivalent term on CRNS calibration, such as obtained by Scheiffele (2015). Furthermore, the correction factor based on soil moisture profiles proposed by Baroni et al. (2018) was not used in this study due to insufficient amount and high sensibility of soil profile probes installed in GEB.

### **4.5.3 Variably-saturated water flux modelling via HYDRUS-1D model**

#### **4.5.3.1 Local environmental constraints for the groundwater flux modelling**

The GEB study area encompasses the main meteorological, geomorphological, geological, pedological and land covering characteristics of coastal sedimentary aquifer systems in coastal Northeast of Brazil (see item 2.1). It is featured by well-defined rainy and dry seasons, complex vegetation mosaic, high solar radiation incidence, shallow groundwater level and sandy soil texture, which together lead to a seasonally-variable soil saturation responsible for the high evapotranspiration rates, perennial stream flows, ephemeral sloped creeks, and ponding occurrences (see item 4.1).

On one hand, the unconfined aquifer might be subject to high evaporation rates likely due to great net radiation during the dry season (Spring and Summer) (see Supplementary Figure 19). On the other hand, the free aquifer might undergo high transpiration rates through the Root Water Uptake (RWU) likely due to shallow groundwater capillarity rise during the rainy season (Fall and Winter) (Wolski and Savenije, 2006). These circumstances imply a strong groundwater dependency on rainfall depth temporal distribution, soil characteristics and vegetation cover that may lead to an accentuated annual variability of vertical percolation fluxes. Such characteristics may roughly mimic a semiarid condition, where well-defined rainy and dry seasons along with thin-flat-shaped sandy soil types, covered by complex variable vegetations, make them susceptible to seasonal saturation events (Ries et al., 2015).

Vadose zone models are a suitable choice for modelling the recharge under shallow groundwater conditions, even though its use is hampered by short time series of a few poorly-monitored hydrological data, which make the multi-dimensional modelling unfeasible due to the data-demanding calibration process (Neto, Chang and van Genuchten, 2013; Šimůnek, van Genuchten and Šejna, 2016). On the other hand, the one-dimensional simplification goes

along with the fact that the CRNS probe does not provide neither a horizontal nor a vertical resolution of soil moisture, but an integral quantification in its entire support volume instead (Baatz et al., 2014; Brunetti et al., 2019; Rivera Villarreyes, Baroni and Oswald, 2014). As such, unidimensional models can cope with these uncertainties simplifying the calibration process, but still providing valuable average information on intermediary scale.

#### 4.5.3.2 Soil hydraulic property model

HYDRUS-1D model was selected to solve the governing flow equations for partially-saturated porous medium, extended from the soil surface down to 1.94 m at CRNS location (site 2) and to 2.15 m at TDR location (site 5). Thus, the water flux was simulated using a modified form of Richards' equation (Šimůnek and van Genuchten, 2008) shown in Equation (76):

$$\frac{\partial \theta}{\partial t} = \frac{\partial}{\partial t} \left[ K(h, x) \left( \frac{\partial h}{\partial x} + \cos \beta \right) \right] - S_t \quad (76)$$

where  $\theta$  is the VWC [ $L^3L^{-3}$ ],  $h$  is the water pressure head [L],  $t$  is time [T],  $x$  is the spatial coordinate [L] (positive upward),  $S_t$  is the sink term [ $L^3L^{-3}T^{-1}$ ],  $\beta$  is the angle between the flow direction and the vertical axis ( $= 0^\circ$  for vertical flow, as in this study), and  $K$  is the unsaturated hydraulic conductivity function [ $LT^{-1}$ ].

HYDRUS-1D implemented the soil hydraulic functions of van Genuchten (1980) which used pore-size distributions of Mualem (1976) to solve Richards' equation by Equations (77) and (78):

$$\theta(h) = \begin{cases} \theta_r = \frac{\theta_s - \theta_r}{[1 + |\alpha h|^n]^{(1-1/n)}} & , \text{ if } h < 0 \\ \theta_s & , \text{ else if } h \geq 0 \end{cases} \quad (77)$$

$$K(h) = K_s \left( \frac{\theta - \theta_r}{\theta_s - \theta_r} \right)^l \left[ 1 - \left( 1 - \left( \frac{\theta - \theta_r}{\theta_s - \theta_r} \right)^{1/(1-1/n)} \right)^{(1-1/n)} \right]^2, \quad \text{if } n > 1 \quad (78)$$

where are six parameters divided into three shape factors and three normalized factors, the latter are:  $\alpha$  [ $L^{-1}$ ], factor inversely related to the air entry pressure,  $n$  [-], measure of pore size distribution, and  $l$  [-], lumped parameter that accounts for pore tortuosity and connectivity; the formers are:  $\theta_r$  [ $L^3 L^{-3}$ ], residual soil moisture,  $\theta_s$  [ $L^3 L^{-3}$ ], saturated soil moisture, and  $K_s$  [ $L T^{-1}$ ], saturated hydraulic conductivity.

For coarser soil textures as in GEB, GWR mostly depends on the shape  $n$  factor, where higher values produce higher GWR; however, this relationship is highly nonlinear (Wang et al., 2009). The air entry of -2 cm was tested, for it seems appropriate in reducing the non-linearity effect of the hydraulic conductivity function close to saturated conditions (Ries et al., 2015; Vogel, van Genuchten and Cislerova, 2001). In addition, for shallow groundwater level as in GEB, the upward soil moisture fluxes are largely controlled by the  $n$  factor as well as by the '1' factor, whose effects still remain underexplored in the literature, which is usually assumed to be equal to 0.5 (Mualem, 1976; Wang et al., 2009; Ventrella et al., 2019).

#### 4.5.3.3 Neutron operator COSMIC and inverse modelling

The inexistence of values of the soil hydraulic properties obtained experimentally in GEB, such as by Richards' chamber equipment, leave the calibration process at the mercy of either literature-reviewed or indirectly-modelling-estimated values. In this study, the one-dimensional inverse modelling were applied to TDR-based soil moisture and CRNS neutron intensity data to calibrate the soil hydraulic properties. For CRNS data, the physically-based neutron operator COSMIC (Shuttleworth et al., 2013), externally coupled with HYDRUS-1D (Brunetti et al., 2019), was used to simulate the aboveground neutron intensity, so-called  $N_{\text{COSMIC}}$ , by Equation (79) and (80):

$$N_{\text{COSMIC}} = N_C \int_0^{\infty} A(z) [\alpha \rho_s(z) + \rho_w(z)] e^{-\left(\frac{m_s(z)}{L_1} + \frac{m_w(z)}{L_2}\right)} \cdot dz \quad (79)$$

$$A(z) = \left(\frac{2}{\pi}\right) \int_0^{\pi/2} e^{-\frac{1}{\cos\theta} \left(\frac{m_s(z)}{L_3} + \frac{m_w(z)}{L_4}\right)} \cdot d\theta = \left(\frac{2}{\pi}\right) \int_0^{\pi/2} e^{-\frac{x}{\cos\theta}} \cdot d\theta = e^y \quad (80)$$

where the pairwise  $\rho_s(z)$  and  $m_s(z)$ , and  $\rho_w(z)$  and  $m_w(z)$ , are respectively the: local bulk density and integrated mass of dry soil per unit area; and total soil water density including lattice water and integrated mass of water per unit area, at the depth  $z$  and from the soil surface (Figure 43).

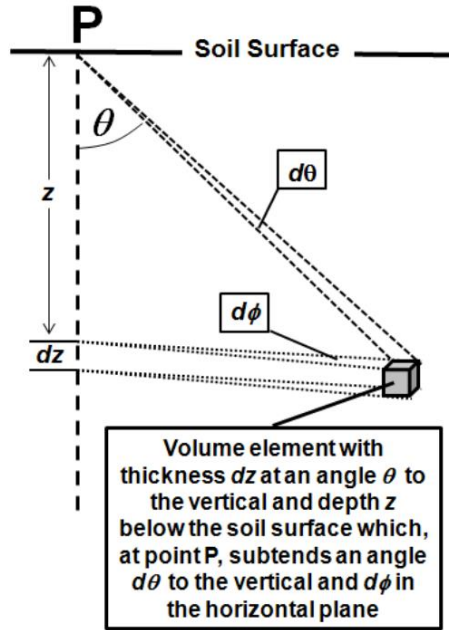


Figure 43 – Fast neutron source volume element yielded in z-depth soil plane reaching the measurement point P, which is attenuated by an exponential factor with length constants  $L_3$  and  $L_4$ . Source: Shuttleworth et al. (2013).

The variables ‘x’ and ‘y’ in Equation (80) were associated to speed up the calculations when using COSMIC in data assimilation applications, using a set of functions defined for different ranges of ‘x’, as shown in Equation (81):

$$\left\{ \begin{array}{l} x \leq 0.05 \\ 0.05 < x \leq 0.1 \\ 0.1 < x \leq 0.5 \\ 0.5 < x \leq 1 \\ 1 < x \leq 5 \\ 5 \leq x \end{array} \right\} = \left\{ \begin{array}{l} y = -347.86105x^3 + 41.642335x^2 - 4.018x - 0.00018 \\ y = -16.240665x^3 + 6.64468x^2 - 2.82003x - 0.01389 \\ y = -0.952455x^3 + 1.44751x^2 - 2.18933x - 0.04034 \\ y = -0.097815x^3 + 0.36907x^2 - 1.72912x - 0.10761 \\ y = -0.004165x^3 + 0.05808x^2 - 1.361482x - 0.25822 \\ y = 0.00061x^2 - 1.04847x - 0.96617 \end{array} \right\} \quad (81)$$

The COSMIC also requires several site-independent and site-specific time-constant parameters. Thus, while the parameters  $L_1 = 162.0 \text{ g cm}^{-2}$ ,  $L_2 = 129.1 \text{ g cm}^{-2}$ ,  $L_4 = 3.16 \text{ g cm}^{-2}$  were all found to be constant for all locations (Shuttleworth et al., 2013), the parameters  $L_3 \text{ (g cm}^{-2}\text{)}$  and  $\alpha \text{ (cm}^{-3} \text{ g}^{-1}\text{)}$  were found to be dependent on bulk density (Equations (82) and (83)), averaged down to 20-m depth in this study (see item 4.5.1). Moreover, two other parameters must be determined: total lattice water equivalent (SOW+LW) [ $\text{L}^3 \text{ L}^{-3}$ ] (see item 4.5.2), and the high-energy neutrons at the soil surface, so-called  $N_C$ . The latter was obtained by the correlation set forth by Baatz et al. (2014) in relation to parameter  $N_0$ , as shown in Equation (84). The fully calibrated COSMIC neutron operator can then be used to inversely determine the soil hydraulic properties, retention curve and soil moisture from the measured neutron intensity.

$$L_3 = -31.65 + 99.29\rho_{bd} \quad (82)$$

$$\alpha = 0.404 - 0.101\rho_{bd} \quad (83)$$

$$N_C = 0.1612N_0 + 7.1956 \quad (84)$$

The convergence of the parameters of the soil hydraulic properties also relies on the input of initial values of the soil hydraulic properties. Thus, the Rosetta Lite v.1.1 module (Schaap, Leij and van Genuchten, 2001), incorporated to HYDRUS-1D (Šimůnek, van Genuchten and Šejna, 2008), was also used to calculate the initial values of the soil hydraulic properties from soil texture and soil hydrophysical data. The vertical soil texture was then obtained through the soil particle distribution experiment from soil samples collected at different depths (-5, -15, -25, -35, -55 and -95 cm), and averaged by sieving (particle size > 0.063 mm) and sedimentation methods (particle size < 0.063 mm).

The global optimizer covariance matrix adaptation-evolution strategy (CMA-ES) (Durner and Iden, 2011; Hansen, Müller and Koumoutsakos, 2003) was used to optimize the values of the soil hydraulic properties through the Parameter ESTimation software (PEST) from Doherty (2004). Inverse modelling used a least-squares objective function described in Equation (85):

$$\Phi(q) = \sum_{i=1}^N \{r_i(q)\}^2 \quad (85)$$

where  $q$  denotes the vector of the parameters of the soil hydraulic properties to be optimized,  $r_i$  are the residuals, and the summation is carried out over the number of observations  $N$ . The uncertainty of each optimized parameter  $q_j$ ,  $j = 1, \dots, m$ , was determined from the diagonal elements ( $q_{jj}$ ) of the parameter covariance matrix  $C(q)$ , evaluated for the final parameter set  $q^*$  (Rivera Villarreyes, Baroni and Oswald, 2014). This result represents an estimate of the standard deviation:  $\sqrt{C(q_{jj}^*)}$ .

#### 4.5.3.4 Root water uptake model

The water taken up by roots is frequently assumed to be controlled by a root density exponential distribution that decreases with soil depth (Yu et al., 2016). Root water uptake is mathematically described by a macroscopic model that represents water extraction as the matric-potential related single sink term  $RWU_a(h)$ , defined by Equation (86) (van

Genuchten, 1987). This equation is a simplification of the one by Feddes, Kowalik and Zaradny (1978), which is recommended to be used when saturated or near-saturated conditions occur for a short period (van Genuchten, 1987).

$$RWU_a(h) = \frac{1}{1 + \left(\frac{h}{h_{50}}\right)^p} RWU_p \quad , \quad \text{where } RWU_p = b(x)T_p \quad (86)$$

where  $RWU_p$  is the potential root water uptake calculated from the potential transpiration rate,  $T_p$  [L], and  $b(x)$  the normalized water uptake distribution [ $L^{-1}$ ],  $h$  is the pressure head [L],  $h_{50}$  represents the soil water potential [L] at which the water extraction rate is reduced by 50% from the potential rate, which can be set as -370 cm for a sand soil, and  $p$  is an empirical coefficient (= 3, van Genuchten and Gupta, 1993). Apropos, Rivera Villarreyes, Baroni and Oswald (2014) found a negligible effect of  $h_{50}$  relative to the parameters of the soil hydraulic properties on inverse modelling. The normalized water uptake distribution function is shown by Equation (87) (Hoffman and van Genuchten, 1983):

$$b(x) = \begin{cases} \frac{1.667}{L_r} & , \quad x > L - 0.2L_r \\ \frac{2.0833}{L_r} \left(1 - \frac{L - x}{L_r}\right) & , \quad x \in (L - L_r; L - 0.2L_r) \\ 0 & , \quad x < L - L_r \end{cases} \quad (87)$$

where  $L_r$  is the total depth of the root zone [L] set constant equal to 0.70 m similar to wet-period rooting depth in Xeric Shrubland vegetation (Pinheiro, Costa and de Araújo, 2013), and  $L$  is the x-coordinate of the soil surface [L] discretised on nodes at each 0.5 cm; knowing that the soil profile bottom is located at  $x = 0$  and the soil surface at  $x = L$ . The  $L$  is set constant equal to 194 cm (389 nodes) at CRNS location (site 2) and to 215 cm (431 cm) at TDR location (site 5), which were found when groundwater completely dried up in the observed wells, which is in agreement with the mean depth down to restrictive layer in the Podzol soil type of the Northeast of Brazil (MA and SUDENE, 1972).

#### 4.5.3.5 Vegetation growth, interception and evapotranspiration partition

The vegetation growth plays important roles in modelling results due to shallow groundwater conditions at GEB. To account for time-dependent plant growth, monthly information about Leaf Area Index (LAI) variation obtained by remote sensing imagery was inputted into the model, as explained in item 4.3.2. On the other hand, since the GEB mostly

features the natural vegetation (see item 4.1), the crop height was set as a constant value equal to 330 cm, determined by arbitrary *in situ* observations. Regarding the intercepted water from rainfall, the plant canopy interception was calculated by an empirical equation using the aforementioned variables and daily precipitation data (Šimůnek et al., 2013b) due to lack of measurements in GEB, as shown in Equation (88):

$$I = i \cdot LAI \left( 1 - \frac{1}{1 + \frac{SCF \cdot P}{i \cdot LAI}} \right) \quad (88)$$

where I is interception depth [L], P is precipitation depth [L], LAI is Leaf Area Index [ $L^2 L^{-2}$ ], which was averaged over GEB from a map composition of bands 1 and 2 of MYD09Q1-MOD09Q1 satellite products (see item 4.3.2), i is the interception constant [ $L T^{-1}$ ], set equal to 0.25 mm d<sup>-1</sup> commonly used for ordinary agricultural crops, and SCF is the Surface Cover Fraction [-] of incidence radiation not intercepted by the canopy, calculated by Equation (89) (Šimůnek et al., 2013b):

$$SCF = e^{-k \cdot LAI} \quad (89)$$

where k is the light extinction coefficient, set equal to 0.463 (Raoufi and Beighley, 2017) due to arboreal-shrub physiognomies of the vegetation, with a generally rounded canopy.

Although this study have considered the reference evapotranpiration (see Equation (59), in item 4.4.2) due to the tropical wet condition of GEB (see item 4.1), the potential evapotranspiration ( $E_{tp}$ ) could also be calculated by the Penman equation (Penman, 1948) modified by Shuttleworth (1993) in Equation (90):

$$E_{tp} = \frac{\Delta R_n + 6.43\gamma(1 + 0.536u_2)(e_s - e_a)}{2.45(\Delta + \gamma)} \quad (90)$$

where  $R_n$  is the net radiation at the crop surface ( $MJ m^{-2} day^{-1}$ ),  $G$  indicates the soil heat flux density ( $MJ m^{-2} day^{-1}$ ),  $u_2$  is the mean hourly wind speed at 2 m height ( $m s^{-1}$ ),  $e_s$  defines the saturation vapour pressure (kPa, see Equation (9)) and  $e_a$  indicates the actual vapour pressure (kPa, see Equation (10)),  $\Delta$  represents the slope vapour pressure curve ( $kPa^\circ C^{-1}$ , see Equation (11), and  $\gamma$  is the psychrometric constant ( $kPa^\circ C^{-1}$ , see Equation (12)).

Then, in this study, the Beer's equation was used to split  $E_{t_0}$  rather than  $E_{tp}$  into potential soil surface evaporation and potential plant transpiration based on LAI/SCF by



Equation (91) and (92), respectively. For a detailed explanation of the partitioning of evapotranspiration, see Sutanto et al. (2012).

$$T_p = Et_o(1 - e^{-k \cdot LAI}) = Et_o SCF \quad (91)$$

$$E_p = Et_o e^{-k \cdot LAI} = Et_o(1 - SCF) \quad (92)$$

Both fluxes shall be reduced to actual values ( $T_a$  and  $E_a$ ) based on a root water uptake model (Feddes, Kowalik and Zaradny, 1978), explained previously, and a surface energy balance model (Camillo and Gurney, 1986). Actual evaporation ( $E_a$ ) in the model is the result of the Richards equation solution for the given boundary conditions, as shall be explained in Equation (93) (see item 4.5.3.6). Some other hydro-phenomenological influences were disregarded on model setting due to the data unavailability, such as temporal variations of rooting depth and root density.

#### 4.5.3.6 Boundary conditions

Set boundary conditions for GWR simulation is always a pivotal initial step for yielding trustworthy outcomes, but in GEB its constrained environmental aspect makes it a prominent modelling step. According to Wang et al. (2009), setting an appropriate lower boundary condition should be more important than selecting values of the soil hydraulic properties (such as the hydraulic conductivity) for simulating the GWR in shallow groundwater condition.

For the upper boundary, it was set the atmospheric condition allowing for a surface layer of water to built up when infiltration capacity is exceeded, due to the occurrence of surface ponding because of the flat landscape at upstream of GEB. The maximum thickness of the surface water layer ( $h_s$ ) before surface runoff be initiate was set as 5 cm, determined by arbitrary *in situ* observations. In the absence of surface ponding, for a flat surface, the boundary condition is obtained by limiting the absolute value of the flux by Equation (93) (Neuman, Feddes and Bresler, 1974):

$$\left| -K \frac{\partial h}{\partial x} - K \right| \leq E \quad , \quad \text{if } h_A \leq h \leq h_s \quad (93)$$

where  $E$  is the maximum potential rate of infiltration or evapotranspiration under the current atmospheric conditions,  $K$  is the hydraulic conductivity,  $h$  is the pressure head at the

soil surface, and  $h_A$  is the minimum permitted pressure head under the prevailing soil conditions. The  $h_A$  was calculated by Equation (94) (Šimůnek et al., 2013b):

$$h_A = -\frac{RT \ln(h_r)}{gM} \quad (94)$$

where  $R$  is the universal gas constant equal to  $8.314 \text{ J mol}^{-1}\text{K}^{-1}$ ,  $T$  is the absolute air temperature (in K),  $h_r$  is the relative humidity (in %),  $g$  is the gravitational acceleration equal to  $9.81 \text{ m s}^{-2}$ , and  $M$  is the molecular weight of water equal to  $0.018015 \text{ kg mol}^{-1}$ .

Another option is to allow for building up a water height on the surface, in case of a surface ponding be expected for a flat surface, as shown in Equation (95) (MIs, 1982):

$$\left(-K \frac{\partial h}{\partial x} - K\right) = q_0(t) - \frac{dh}{dt} \quad , \quad \text{at } x = L \quad (95)$$

The flux  $q_0$  denotes the net infiltration rate, namely the difference between precipitation and evaporation, and  $h(L,t)$  denotes the height of surface water layer (pressure head), which increases due to precipitation, and reduces due to infiltration and evaporation.

The lower boundary was set as a variable pressure head condition, using the groundwater height from the bottom of soil discretization, since the Podzol soil type features a shallow groundwater table stemmed from the presence of a restrictive layer  $\sim 2 \text{ m}$  below the surface (see item 2.1). This condition affects considerably the soil moisture profile which is highly influenced by capillary rise close to groundwater table, affecting, in turn, the downward water flux. The initial condition was assumed to be a soil moisture profile defined from the PR2 probes at the beginning of model processing.

#### 4.5.3.7 Water budget equation in HYDRUS-1D

The GWR rates was calculated on an annual scale, after the accumulation of the daily water flux at the bottom boundary, which was set as variable pressure head, namely the groundwater level. The HYDRUS-1D code may perform the computations of the water budget equation at prescribed times for several and preselected subregions of the flow domain, but this study considered only one homogeneous region consisting of sandy soil texture. The water balance information consists of the actual volume of water,  $V$ , in that region, and the soil water storage changes,  $\Delta S$ , of inflow or outflow to or from the region. These variables  $V$  and  $\Delta S$  are evaluated in HYDRUS-1D through the Equations (96) and (97) (Šimůnek et al., 2013b). The volume difference in a certain time period yields  $\Delta S$ .

$$V = \sum \Delta x_i \frac{\theta_i + \theta_{i+1}}{2} \quad (96)$$

$$\Delta S = \frac{V_j - V_{j-1}}{\Delta t} \quad (97)$$

where  $\theta_i$  and  $\theta_{i+1}$  refers to soil moisture evaluated at the corner nodes of the element,  $\Delta x_i$  is the size of the element between nodes, and  $V_j$  and  $V_{j-1}$  are volumes of water in a soil region (the entire profile) computed at the current and previous time levels, respectively.

The water flux is simulated along the soil profile discretized into N-1 adjoining elements, being N the number of nodes, which was set equal to 194 cm (389 nodes) at CRNS location (site 2) and to 215 cm (431 nodes) at TDR location (site 5) (see item 4.5.3.4). HYDRUS-1D assumes that the vertical coordinate x is directed positive upward, and from Darcy's law, the x-components of the nodal fluxes are computed for each node n according to Equation (98) (Šimůnek et al., 2013b):

$$q_i^{j+1} = \frac{-K_{i+1/2}^{j+1} \left( \frac{h_{i+1}^{j+1} - h_i^{j+1}}{\Delta x_i} + 1 \right) \Delta x_{i-1} - K_{i-1/2}^{j+1} \left( \frac{h_i^{j+1} - h_{i-1}^{j+1}}{\Delta x_{i-1}} + 1 \right) \Delta x_i}{\Delta x_{i-1} + \Delta x_i} \quad (98)$$

where subscripts 'i-1', 'i', and 'i+1' indicate the position in the finite-difference mesh and superscripts 'j+1' represent the current time levels.

Finally, the annual GWR rate (or simply R) was calculated at the bottom boundary by integrating the water flux over time, and then, it was checked through the water budget equation, by applying all previously-mentioned water balance components, namely: rainfall (P), interception (I), actual root water uptake (RWU<sub>a</sub>), actual evaporation (E<sub>a</sub>), surface runoff (Q), and soil water storage changes (ΔS), according to Equation (99):

$$R = P - I - RWU_a - E_a - Q - \Delta S \quad , \quad \text{in cm d}^{-1} \quad (99)$$

## 4.6 Validation of the HYDRUS-1D-COSMIC results

### 4.6.1 Validation of the CRNS-based neutron intensity

The CRNS neutron counts recorded at hourly basis were smoothed with 8-h and 24-h moving windows to diminish the measurement noise, similarly to Bogen et al. (2013). As such, the dry neutron intensity ( $N_0$ , in counts  $h^{-1}$ ) was firstly calibrated for these different moving averages. Then, the corrected neutron intensity ( $N'$  in counts  $h^{-1}$ ) was calculated by

Equation (75) (see item 4.5.2) and summed for these different moving averages. Finally, the soil moisture could be calculated by Equation (69) (see item 4.5.2), together with its standard deviation calculated from error propagation by Equation (100), once the neutron intensity follows Poissonian statistics (IAEA, 2017).

$$\sigma_{\theta} = \frac{0.372N_0\sqrt{N'}}{(N' - 0.115N_0)^2} \quad (100)$$

For validating the CRNS results, soil moisture data were monitored down to 1 m below soil surface from three profile probes, model PR2/6 by Delta-T Devices (see item 4.2). The measurements of the three PR2/6 (or simply PR2) were converted from millivoltage output unit (denoted as V) to VWC (denoted as  $\theta_{\text{mineral}}$ ) using the generalised polynomial mineral soil moisture calibration by Equation (101). The generalised calibration curve was optimised by the manufacturer to cover a wide range of mineral soil types with organic content of ~1% (DELTA-T, 2016), which is the case at GEB. Then, the sensor measurements were smoothed using moving windows, similarly to CRNS situation, and then averaged using the weighting functions (see item 4.5.1) for validating the CRNS time series.

$$\theta_{\text{mineral}} = \frac{(1.125 - 5.53V + 67.17V^2 - 234.42V^3 + 413.56V^4 - 356.68V^5 + 121.53V^6) - 1.6}{8.4} \quad (101)$$

The PR2 recalibration for the GEB soil condition was also carried out by Equation (102) through the gravimetric method, double collecting and oven-drying soil core samples in each depth of measurement. Conversely, the results were not as good as that obtained by the generalised curve, likely due to the insufficient number of field campaign data. Likewise, the PR2 manufacturer recommends the curve recalibration only when soil features stood out of provided specification; whose number field campaign data should also cover all interval of soil moisture variation (DELTA-T, 2016).

$$\theta' = \frac{(1.125 - 5.53V + 67.17V^2 - 234.42V^3 + 413.56V^4 - 356.68V^5 + 121.53V^6) - a'_0}{a'_1} \quad (102)$$

where  $\theta'$  is the soil moisture obtained by PR2/6 recalibration curve, and  $a'_0$  and  $a'_1$  are the slope and offset parameters of the recalibration curve.

#### 4.6.2 Validation of the hydraulic conductivity

Amongst the parameters of the soil hydraulic properties, the hydraulic conductivity is one of those obtained via inverse modelling, and one of the most important as it represents the ability of a medium to transmit water when subjected to a hydraulic gradient. The

hydraulic conductivity in an unconfined aquifer can be simply obtained by water-level displacement data, resulting from the overdamped injection or withdrawal of a slug in a well, the so-called Slug test. Bouwer and Rice (1976) developed an empirical logarithmic relationship describing the water-level response in an unconfined aquifer, which represents the vertical distance between the rising water level in a well and the equilibrium water table in an aquifer. This relationship can be expressed Equation (103), which was then used to validate the hydraulic conductivities estimated in  $[L T^{-1}]$  via inverse modelling.

$$K = \frac{r_c^2 \ln\left(\frac{R_e}{r_w}\right)}{2L_e} \frac{1}{t} \ln\left(\frac{h_0}{h_t}\right) \quad (103)$$

where,  $r_c$  and  $r_w$  denote the piezometer and perforation radii, respectively,  $R_e$  corresponds to the effective radial distance over which the hydraulic gradient is dissipated,  $L_w$  and  $L_e$  are the saturated thickness and the filter section length of the well, respectively, and the  $h_0$  and  $h_t$  represents the dynamic water level at time 0 and time  $t$ , respectively. For monitoring the water level variation, one fast-response pressure transducer (Diver) was installed in the soil due to the permeable aquifer system.

#### 4.6.3 Validation of the simulated soil moisture profile

HYDRUS-1D model allows for plotting the soil moisture time series at different depths either at a regular time interval (daily in this study) or at every time step of simulation. After the inverse calibration of the soil hydraulic properties using the CRNS data (at site 2), the PR2 profile probe data was used to validate the soil moisture time series simulated by HYDRUS-1D-COSMIC model. For such purpose, six observation points were selected in HYDRUS-1D graphical editor, namely at: -2, -15, -25, -35, -55, and -95 cm; where the first depth was adopted to cope with the high total lattice water equivalent and the air-entry consideration (equal to -2 cm) at soil surface. Moreover, the goodness-of-fit metrics used for assessing the agreement between the predicted and observed time series were the coefficient of determination ( $R^2$ ) and the Kling-Gupta Efficiency coefficient (KGE) (see item 4.4.1). Similarly, the soil moisture time series using TDR data (at site 5) was obtained at three observation points, namely at -5, -20 and -40 cm, and the  $R^2$  and KGE metrics were calculated. Moreover, the linear regressions for both CRNS and TDR datasets at the aforementioned depths were also plotted, for checking their shift in relation to the 1:1 perfect

fit. Thus, the time series and scatter plots for both CRNS and TDR sites were then plotted to allow for an overview of the overall behaviour of peak and recession differences.

#### 4.6.4 Validation of the daily Groundwater Recharge rate

Since the HYDRUS-1D provides daily water flux estimates, the verification of GWR through the WTF graphical method becomes unfeasible. Therefore, a fixed-interval modified WTF method, combining the RISE and Master Recession Curve (MRC) approaches elucidated by Nimmo, Horowitz and Mitchell (2015) (Figure 44), was used as an alternative solution. The RISE procedure was used, which considers that: given a record of water level at equal time intervals, the rise for a given interval is the amount by which the water table at the end of that interval is higher than for the previous interval, namely only positive values are considered. Moreover, this study also considered the MRC approach for determining the contribution of the extrapolated recession curve obtained by a linear regression equation. As such, the MRC was defined along the longer available groundwater recession period, slightly different from Delin et al. (2007), which adopted a nonlinear regression equation. The water level elevation is calculated by the sum of the actual groundwater rise ( $\Delta h_{\text{peak}}$ ) and potential groundwater decline ( $\Delta h_{\text{rec}}$ ) (Jie et al., 2011). Then, the specific yields equal to 0.10, 0.16 and 0.24 were obtained (as explained in item 4.4.5), and they were used together with the water level elevation in the Equation (61) to calculate the GWR on daily fixed-interval. This approach is very simple and objective, as well as involves less subjectivity, once the user does not need to make a judgment based on previous experience to extrapolate the recession curve for each recharge event. Conversely, it is expected that the approach holds a relevant sensitivity to the measurement frequency and probe accuracy.

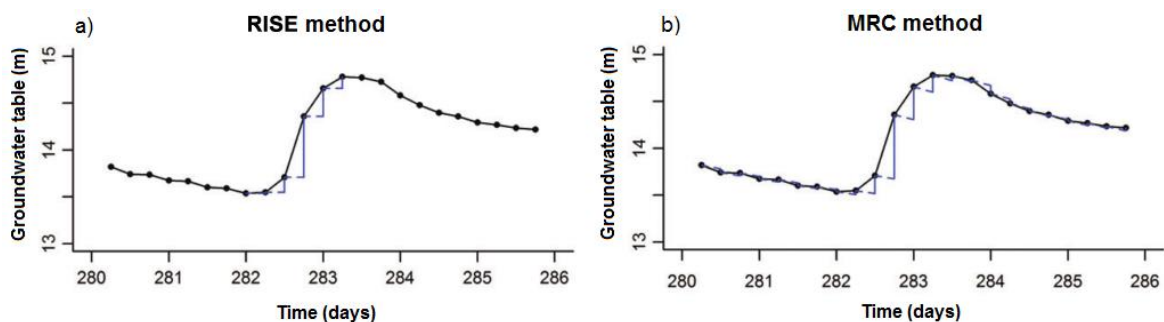


Figure 44 – Two fixed-interval methods based on the WTF method for groundwater recharge estimation, namely: (a) RISE method, and; Master Recession Curve (MRC) method. Source: Nimmo, Horowitz and Mitchell (2015).

## 5 RESULTS

### 5.1 Distributed Groundwater Recharge estimated by an enhanced GIS-based water balance model

The distributed estimates of the water balance components were calculated for 2016 and 2017 on annual and monthly scales and, then, plotted in maps, summarized by histograms and box plots, as well as verified by ground-based data collected over JPA CSA. The results of each water balance component are then presented separately in the following items.

#### 5.1.1 Precipitation analysis

Two precipitation data sources were used in this study: ground-based and satellite-based data; the former interpolated and the latter resampled to 500-m spatial resolution (see item 4.3.1). Comparisons between monthly median estimates revealed the IMERG data underestimation with a reasonable linear association, PBIAS and CC equal to -40% and 90%, respectively, which after the linear scaling bias correction was improved to PBIAS and CC equal to -9% and 99% (Figure 45). The errors were also reduced after the bias correction, once the RRMSE decreased from 59% (70.65 mm) to 15% (18.06 mm). Keeping the original spatial variability data pattern, the satellite-based annual mean values were increased on 43.32% (953.98 to 1367.27 mm) in 2016 and 79.31% (912.17 to 1635.65 mm) in 2017. This underestimation stemmed likely from the inability of the passive microwave sensors in detecting warm-rain processes forced by topography on coastal Northeast of Brazil (Gadelha et al., 2019). Despite that precipitation shift in this coastal area, Figure 45 also showed a decreasing precipitation tendency from shoreline towards inward, which is in agreement, although biased, with the overall behaviour presented by Cabral da Silva et al. (2000b). Moreover, Gadelha et al. (2019) showed that the IMERG data had good performance across most of Brazil, with correlation and root mean square error equal to 99% and 17.6 mm on monthly basis in Northeast region, respectively. Thus, the literature justifies the suitability of using bias-corrected IMERG (henceforth named IMERG\*) in comparison to ground-based data (henceforth named Gauge).

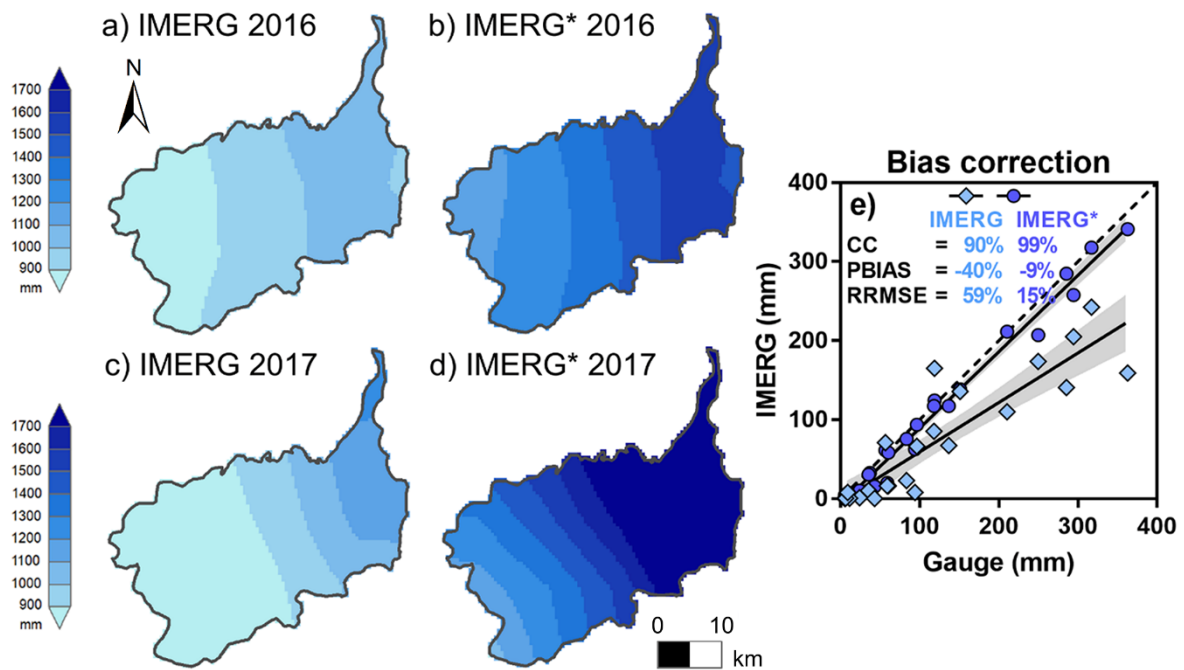


Figure 45 – Bias correction by the linear-scaling method based on monthly mean correction factors applied on IMERG V05B daily precipitation data for correcting the (e) monthly and annual precipitation in (a, c) 2016 and (b, d) 2017 over JPA CSA.

Gauge and IMERG\* data distribution depicted annual decreasing gradients from East to West along the ~46 km from the coastline toward headboard of JPA CSA, averaged on: 1,368.58 (Gauge) and 1,367.27 mm (IMERG\*) in dry year (2016), and; 1,672.06 (Gauge) and 1,635.65 mm (IMERG\*) in average year (2017) (Figure 46). Precipitation range in 2016 varied from 1,001.24 to 1,626.14 mm for Gauge and 1,120.09 to 1,598.53 mm for IMERG\*, while in 2017 it varied from 1,306.89 to 2,072.26 mm for Gauge and 1,049.69 to 2,298.53 mm for IMERG\*. Precipitation occurred mostly within the regular rainy season (refer to Barbosa et al., 2018), mainly from April to June in 2016, summing 769.31 mm (56.21%) for Gauge and 794.39 mm (58.10%) for IMERG\*, and from May to July in 2017, summing 901.8 mm (53.93%) and 898.06 (54.91%). The mean value of the monthly precipitation averages in 2016 and 2017 stood on 114.05 and 139.34 mm for Gauge, and 113.94 and 136.30 mm for IMERG\*, respectively, while the maximum values reached up to 306.22 and 358.32 mm (Gauge) and 325.97 and 389.34 mm (IMERG\*), respectively (see also Supplementary Figure 1 to Supplementary Figure 4). Moreover, in 2016, the scattering of IMERG\* data was slightly smaller than Gauge one, whereas in 2017 the IMERG\* data scattering was greater than Gauge one, once the monthly mean of interquartile ranges differences between IMERG\* and Gauge was -4.09 and 18.03 mm, respectively.



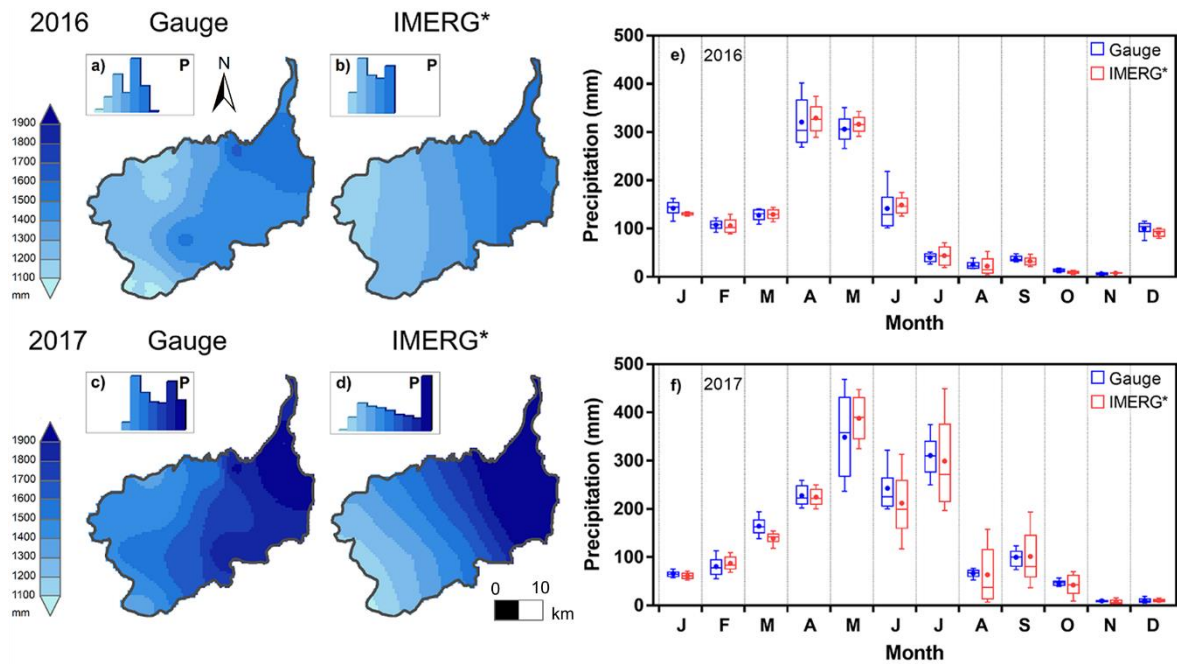


Figure 46 – Annual distributed precipitation obtained by (a, d) Inverse Distance Weighting (IDW) interpolation through the rain gauge network, and by (b, e) bilinear interpolation and bias correction through IMERG imagery, as well as (c, f) monthly percentile (10%, 25%, 50%, 75%, 90%) variability in 2016 and 2017. Points: mean.

### 5.1.2 Evapotranspiration and soil water storage change analyses

For the actual evapotranspiration calculation, the ground-based meteorological data were replaced by reanalysis data assimilated by GLDAS-2.1 Noah (Figure 47). Since four pixels covered mostly JPA CSA and did not meaningfully vary among each other, they were averaged and then inputted in the adapted MODIS algorithm (Gusmão, 2017; Mu et al., 2007; Mu, Zhao and Running, 2011; Teixeira et al., 2014, 2013) (see item 4.3.2). On average, JPA CSA featured a wide oscillation of high relative humidity values varying from 37.74 to 98.01% (mean of 75.29%) and a short oscillation of high air temperature values varying from 19.76 to 33.63°C (mean of 25.95°C). In addition, it held an intense incidence of incoming short-wave radiation reaching up to 982.02 W m<sup>-2</sup> (mean of 390.99 W m<sup>-2</sup>) and is subjected to a mean air pressure condition varying from 100.16 to 101.40 kPa (mean of 100.77 kPa).

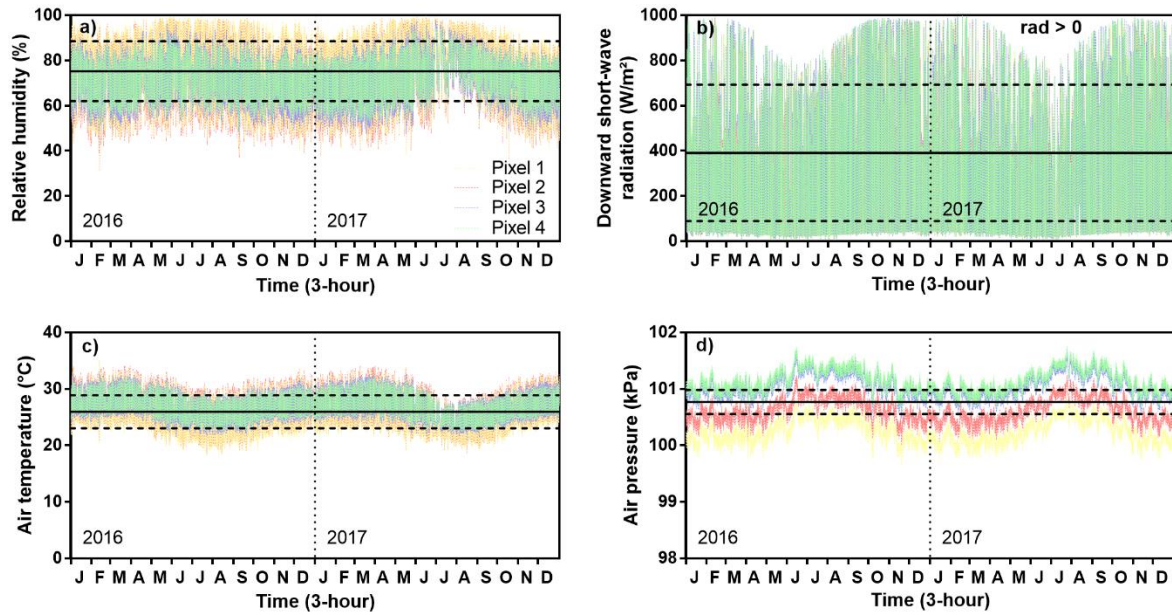


Figure 47 – Meteorological variables obtained by GLDAS-2.1 Noah L4 reanalysis data in 2016 and 2017: (a) relative humidity, (b) incoming short-wave radiation, (c) air temperature, and (d) barometric air pressure. Solid line: mean; Dashed line: mean  $\pm$  standard deviation.

The MODIS-based evapotranspiration also requires the biophysical variables, which depend on the land use/cover spatial distribution over JPA CSA, provided on a high resolution by MapBiomas 3.1 collection. The study area comprehends 14 land uses/covers out of 25 MapBiomas classes listed over Brazil, which were further reduced to 6 classes: bare soil, forest, mosaic of agriculture and pasture, pasture, urban infrastructure and flooded areas (or water) (Figure 48). This procedure was used for simplicity sake on the spatial assignment of phenological parameters (see item 4.3.2.1). A relatively increasing on natural green areas coverage was noticed from 2016 to 2017, so that pasture and forest covers augmented in 6.32% (16.62 km<sup>2</sup>) and 4.76% (13.62 km<sup>2</sup>), respectively, whereas anthropologically-modified coverages decreased, namely bare soil in -15.43% (2.48 km<sup>2</sup>), urban area in -4.63% (4.65 km<sup>2</sup>) and mosaic in -7.16% (23.52 km<sup>2</sup>). Overall, JPA CSA was mainly covered 85.36% on average by all green areas (forest in 292.83 km<sup>2</sup>, mosaic in 316.95 km<sup>2</sup>, and pasture in 271.09 km<sup>2</sup>), while urban infrastructure and bare soil comprehended only 9.50% (98.05 km<sup>2</sup>) and 1.44% (14.83 km<sup>2</sup>). This happened due to recent public policies for conservation and recovery of green permanent areas and for gradual evacuation of irregular human-interfered areas (Crouzeilles et al., 2019; SOSMA and INPE, 2019).

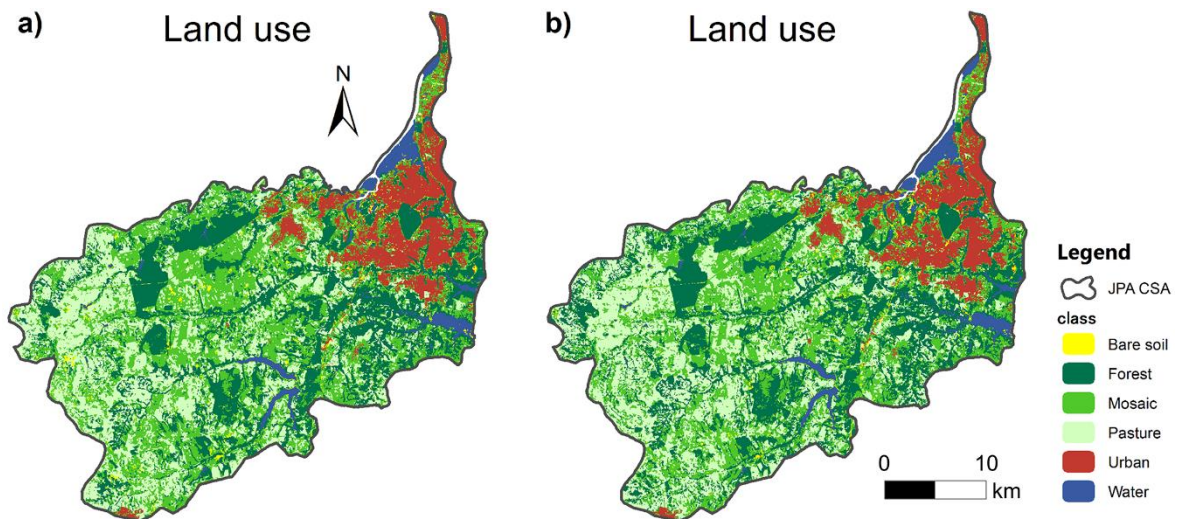


Figure 48 – Land use/cover classification by MapBiomass collection 3.1 over JPA CSA in (a) 2016 and (b) 2017.

The actual evapotranspiration was spatially calculated over JPA CSA in 2016 and 2017 on the daily resolution and then accumulated to a monthly resolution (Figure 49, Supplementary Figure 5 and Supplementary Figure 6). The mean actual evapotranspiration was 1,170.51 (2016) and 1,218.20 mm (2017), corresponding to 85.53% (Gauge) and 85.61% (IMERG\*) of mean precipitation depth in 2016, and 72.86% (Gauge) and 74.48% (IMERG\*) in 2017. The urban area of JPA CSA, mostly located in Northeastern portion, portrayed low evapotranspiration values (less than 850 mm) due to the sizeable less-permeable cover, despite the highest precipitation depths (see Figure 46). On the other hand, the vegetated areas and riparian zones of rural areas, mainly in downstream part of Gramame basin and in Western portion of Paraíba downstream right bank, featured the highest actual evapotranspiration values (higher than 1,450 mm). Regarding the monthly evapotranspiration distribution, it is noticed that the data scattering took the right-skewed leptokurtic histogram shape in rainy season (April to July), which depicted short interquartile ranges of 31.21 (2016) and 28.67 mm (2017). In the other months, the data scattering displayed larger interquartile ranges of 43.14 (2016) and 42.80 mm (2017), among which the drier months (September to October) presented left-skewed (2016) and centre-skewed (2017) histograms shapes with normal kurtosis. These actual evapotranspiration behaviours is likely due to a combination of high incident radiation, water availability, and land use/cover heterogeneity (de Oliveira et al., 2016b), which led to well-distributed histograms throughout the months in JPA CSA with mean of monthly means on 103.27 (2016) and 100.09 mm (2017).

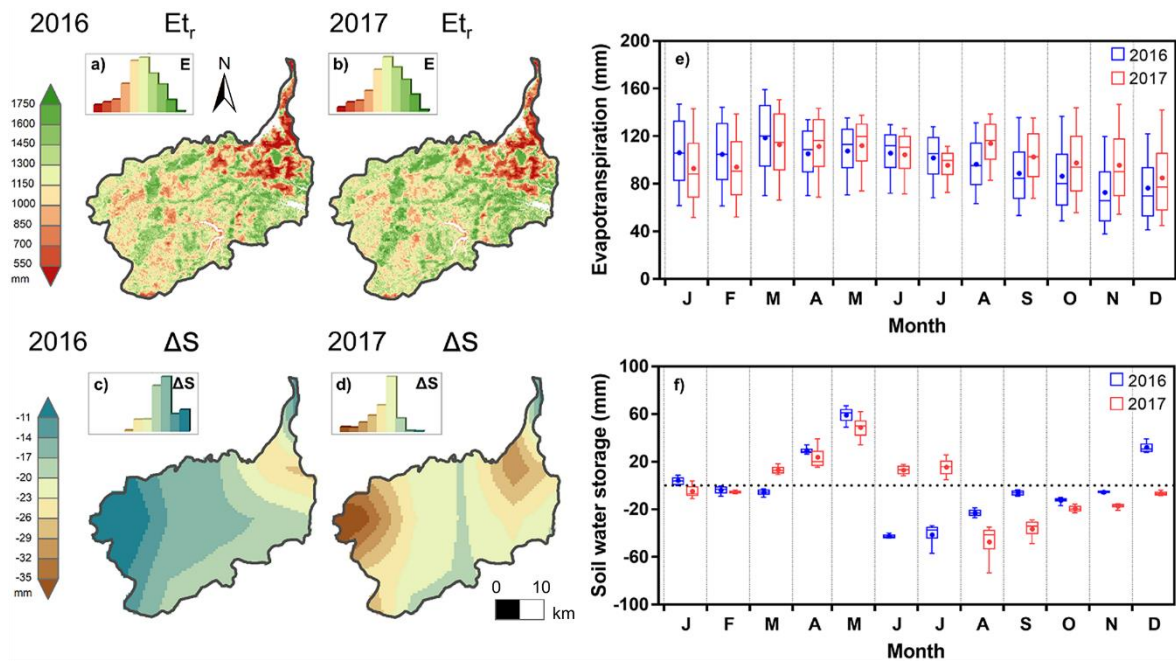


Figure 49 – Annual distributed (a, b) actual evapotranspiration ( $E_{t_r}$ ) obtained by adapted MODIS algorithm (Gusmão, 2017; Mu et al., 2007; Mu, Zhao and Running, 2011; Teixeira et al., 2014, 2013) from MapBiomas land use/cover with map composition for cloud cleaning, and (d, e) soil water storage changes ( $\Delta S$ ) in 1-m root zone obtained by bilinear interpolation, as well as (c, f) monthly percentile (10%, 25%, 50%, 75%, 90%) variability in 2016 and 2017. Points: mean.

The distributed soil water storage changes in the root zone were calculated from SMAP SPL4SMAU soil moisture data and interpolated to 500-m spatial resolution (Figure 49, Supplementary Figure 7 and Supplementary Figure 8). In both dry (2016) and average (2017) years, the soil water storage changes declined throughout the JPA CSA, once they varied from -26.85 to -5.89 mm (2016), and from -40.60 to -11.81 mm (2017). The soil water storage changes in urban area on Northeastern portion featured deep decline in both years, whereas the headboard on Western portion featured a decline deeper in 2017 and shallower in 2016. On monthly scale, the soil water storage changes happened mainly along the rainy seasons (April to May in 2016, and March to July in 2017), and exceptionally on December/2016. This is likely the reason why the decline was deeper in 2017 (mean of -24.04 mm) than 2016 (mean of -16.21 mm). Moreover, the monthly data scattering was averaged on 64.98% higher in 2017 than in 2016, whose interquartile range stood on 4.37 mm and 7.22 mm, respectively. These set of results shows that an above-average rainy condition is required for a positive soil water storage change in JPA CSA, which may impact severely on water shortage over the area.



The precision of actual evapotranspiration estimates was verified against the ground-based reference evapotranspiration, calculated by Penman-Monteith equation (Allen et al., 1998), by averaging on the 500-m footprint of A320 INMET meteorological station (Figure 50). The daily mean actual evapotranspiration on the A320 footprint ranged from 0.98 to 4.60 mm, with the mean and standard deviation of 3.50 and 0.43 mm, respectively, whereas the daily mean reference evapotranspiration calculated from the A320 data varied between 3.01 and 6.95 mm, with mean and standard deviation range of 4.95 and 0.86 mm. Furthermore, the daily mean actual evapotranspiration showed more clearly the annual variation over JPA CSA, which ranged from 1.00 to 4.70 mm d<sup>-1</sup> (Figure 51). Moreover, two relevant behaviours were observed on the previously-mentioned variables, namely: (1) in dry season (September to December of 2016), the actual evapotranspiration decreased while the reference evapotranspiration increased; (2) in rainy season (April to July of 2016 and 2017), the actual evapotranspiration tended to the reference evapotranspiration. The former behaviour is explained by the high incoming radiation along the dry season (see Figure 47) that increases the reference evapotranspiration occurrence, in spite of a low rainwater availability leading to low actual evapotranspiration rates. The latter behaviour occurred, in turn, due to the lower incoming radiation incidence, which decreased the actual evapotranspiration in spite of the high amounts of rainwater available in rainy season. It can be inferred, therefore, that the actual evapotranspiration calculated by the adapted MODIS algorithm was satisfactorily well-estimated over JPA CSA, as it was able to depict trustworthily the meteorological effects over evapotranspiration process.

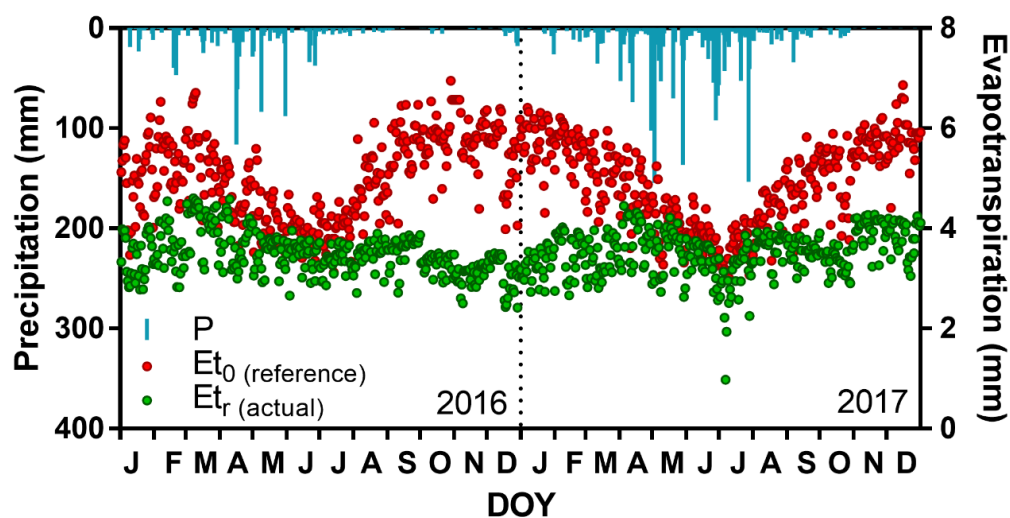


Figure 50 – Verification of daily actual evapotranspiration simulated by adapted MOD16 algorithm (Gusmão, 2017; Mu et al., 2007; Mu, Zhao and Running, 2011; Teixeira et al., 2014, 2013) averaged on 500-m footprint of A320 INMET meteorological station, against the ground-based reference evapotranspiration calculated by Penman-Monteith equation (Allen et al., 1998).

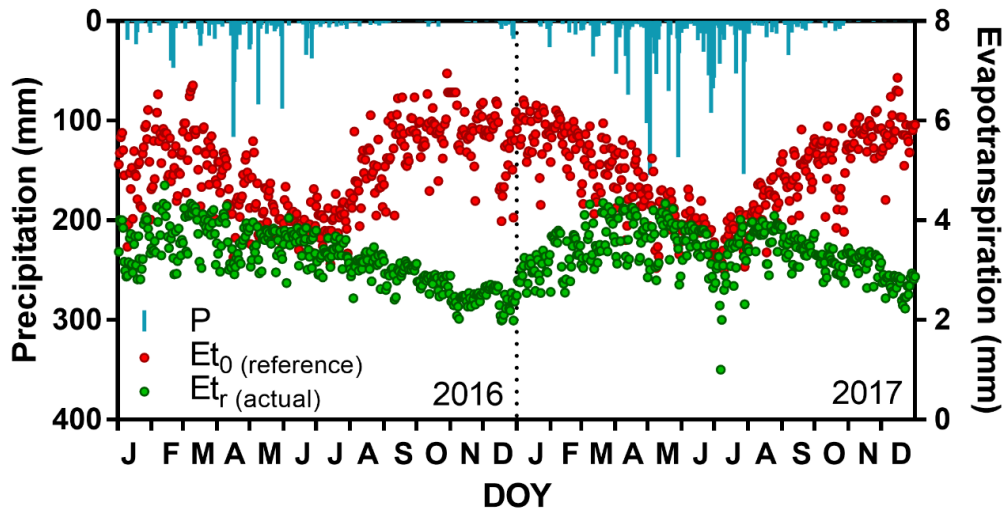


Figure 51 – Comparison between the daily mean actual evapotranspiration over the JPA CSA simulated by the adapted MOD16 algorithm (Gusmão, 2017; Mu et al., 2007; Mu, Zhao and Running, 2011; Teixeira et al., 2014, 2013) with the ground-based reference evapotranspiration calculated by Penman-Monteith equation from A320 INMET meteorological station data (Allen et al., 1998).

For testing the performance of SMAP SPL4SMAU soil moisture product used in the calculation of soil water storage changes, three TDR probes vertically-inserted within the GEB were calibrated by using soil moisture samples collected in five sites (de Lira, 2015). For such purpose, a third-order polynomial function was chosen to associate the dielectric constant measurement to VWC (Figure 52), similarly to da Silva and Coelho (2014).

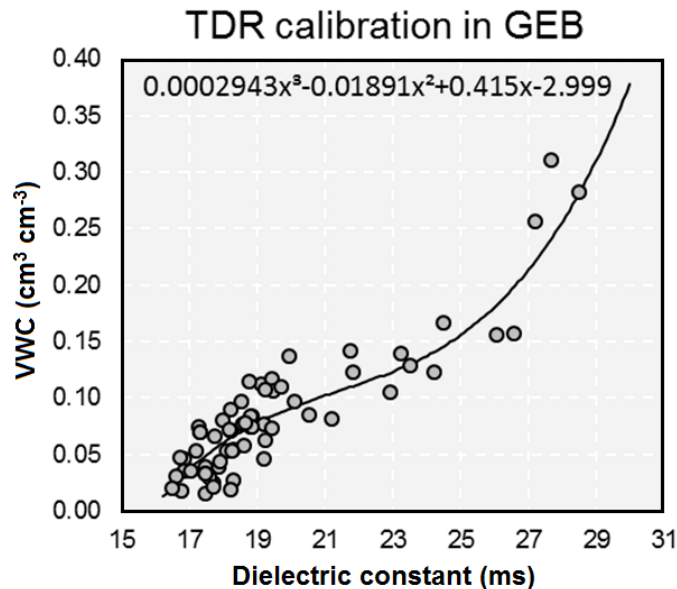


Figure 52 – General soil moisture calibration curve of the TDR probes installed in GEB. Source: data from de Lira (2015).

The soil moisture time series assimilated by SMAP mission was averaged on GEB and plotted against the TDR-based time series (Figure 53). Comparing the daily mean of time series, it is noticed that both satellite- and ground-based datasets respond to the rainfall events similarly along the dry season, but in different magnitudes during the rainy season, with CC equal to 83%. The TDR peaks in rainy season were higher than SMAP standard deviation bounds likely due to original 9-km spatial resolution of the satellite product, which smooth the soil moisture estimates. Moreover, the mean of 100-cm SMAP mean was  $0.104 \text{ cm}^3 \text{ cm}^{-3}$ , relatively close to the mean of 30-cm TDR mean of  $0.087 \text{ cm}^3 \text{ cm}^{-3}$ , showing that SMAP is able to detect the overall soil moisture patterns over GEB, and, by inference, over JPA CSA.

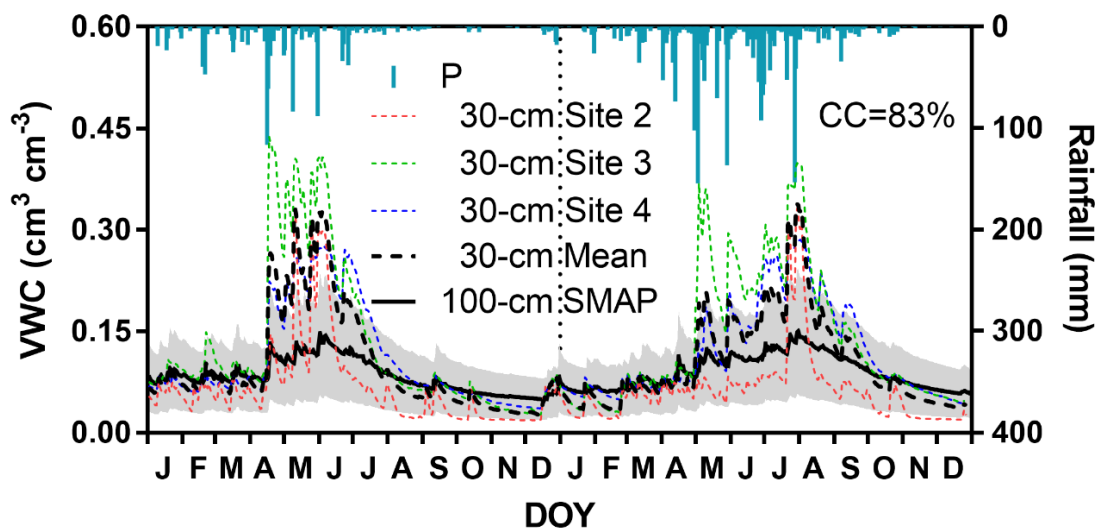


Figure 53 – Comparison between the soil moisture time series assimilated by SMAP mission and ground-based measurements. Shaded interval: mean  $\pm$  standard deviation.

### 5.1.3 Surface runoff analysis

For calculating the surface runoff by NRCS–CN method (Lal et al., 2016; Lal, Mishra and Kumar, 2019), it is essential to calculate the imperviousness of the soil types comprising the JPA CSA. Initially, the ancient soil databases of JPA CSA were retrieved and reclassified according to World Reference Base (WRB) for soil resources (IUSS Working Group WRB, 2015), resulting on 8 distinct soil types with distinct soil characteristics (Figure 54). Acrisols and Lixisols cover 58.69% ( $605.66 \text{ km}^2$ ) and 9.06% ( $93.47 \text{ km}^2$ ) of JPA CSA, respectively, being very important for farming and crop production (see Figure 48), in addition to Acrisol be the largest soil type in JPA CSA, covering all regions of Brazil as well (see Figure 2). Fluvisols, Histosols and Gleysols cover 12.01% ( $123.94 \text{ km}^2$ ), 5.47% ( $56.42 \text{ km}^2$ ) and 0.69%

(7.16 km<sup>2</sup>), respectively, corresponding to the fluvial soils embracing the urban area and the two most important rivers of the coastal area. The Podzols covers 10.72% (110.58 km<sup>2</sup>), being permanent conservation area due to high contamination risk (Linhares et al., 2014). Luvisols and Ferralsols cover 3.16% (32.57 km<sup>2</sup>) and 0.21% (2.2 km<sup>2</sup>), respectively, and are located in the Western portion of JPA CSA, wherein traces of semiarid transition zone are found, such as rock outcrops.

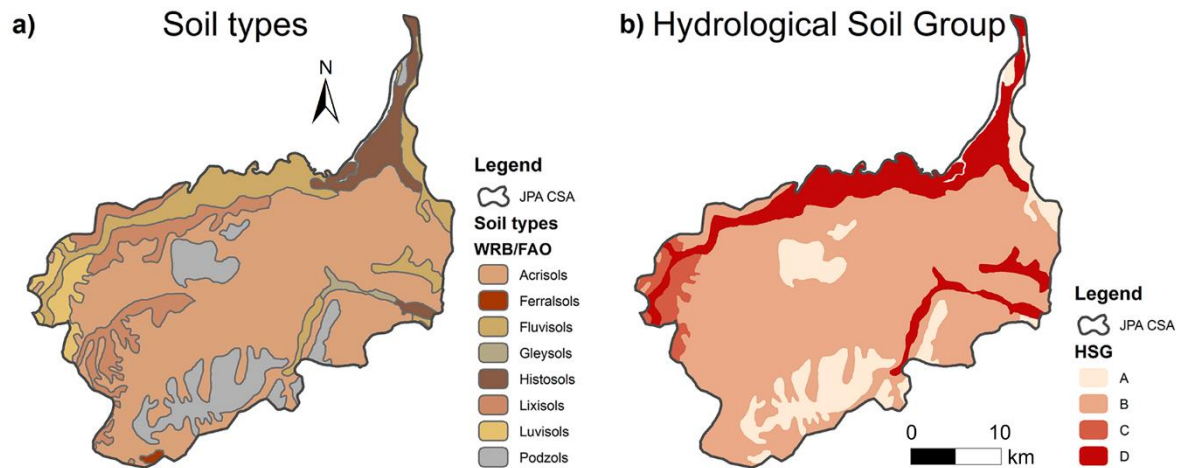


Figure 54 – Soil types and Hydrological Soil Groups (HSG) of JPA CSA. WRB: World Reference Base for soil resources.

The soil types were clustered into 4 Hydrological Soil Groups (HSG, Figure 54), according to Sartori (2010) (see item 4.3.3.1), from their soil characteristics and depth to restrictive layer, for calculating the soil imperviousness. All the main HSGs were found in JPA CSA, namely A, B, C and D, varying from very permeable to very impermeable, respectively. HSG type B and D covered mostly of JPA CSA, totalizing 67.75% (699.13 km<sup>2</sup>) and 15.74% (162.42 km<sup>2</sup>), respectively, followed by A and C encompassing 13.36% (137.88 km<sup>2</sup>) and 3.16% (32.57 km<sup>2</sup>), respectively. It means that 81.11% of JPA CSA is permeable, in opposition to 18.89% being impermeable. Furthermore, the soil imperviousness, so-called Curve Number (CN), were determined using HSG and land use/cover information (see Table 7) in JPA CSA, and calculated under the moderately-wet Antecedent Runoff Condition (ARC-II) by Lal et al. (2016) equation (Figure 55). The CN distribution at ARC-II in 2016 and 2017 exhibited similar histograms, whose CN varied from 30 to 100, with mean values corresponding to 69.08 and 68.44, respectively. The fluvial soil types and urban area held the higher CNs, namely above 80, whereas the Podzol soils and forested areas held the lower CNs, namely below 60. These results were then used to obtain the CN under wet (CN-I) and dry (CN-III) ARCs, depending on 5-days-antecedent Gauge



and IMERG\* cumulative precipitation, by Lal, Mishra and Kumar (2019) equations, for runoff surface estimation (see item 4.3.3.2)

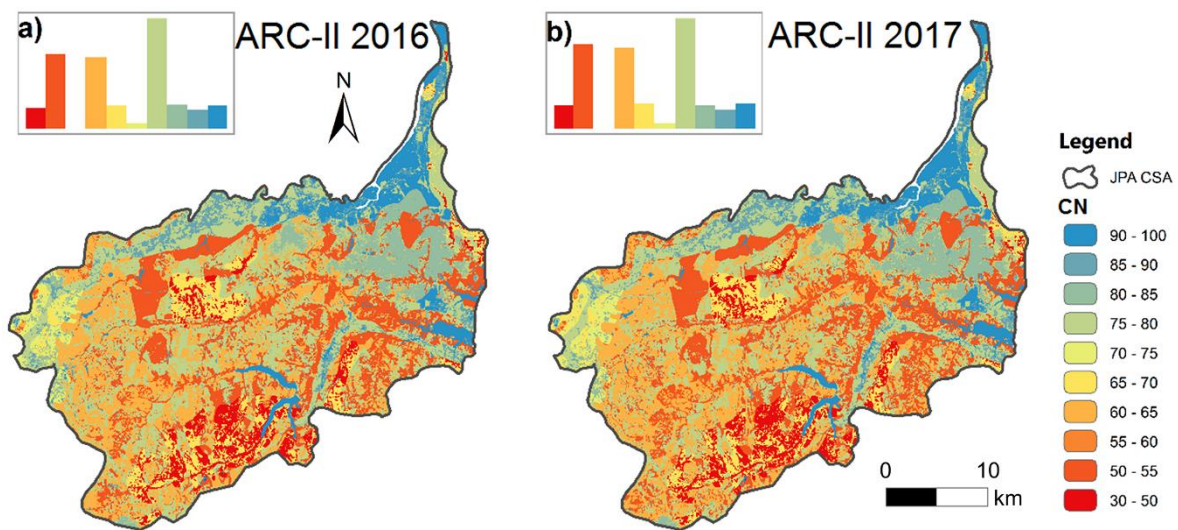


Figure 55 – Distributed Curve Number (CN) estimation under the moderately-wet Antecedent Runoff Condition (ARC) in 2016 and 2017 over JPA CSA.

The distributed surface runoff was estimated from Gauge and IMERG\* precipitation data by NRCS–CN method over JPA CSA in 2016 and 2017 on daily resolution, and then accumulated to a monthly resolution (Figure 56, Supplementary Figure 9 to Supplementary Figure 12). Surface runoff estimates for both Gauge and IMERG\* were higher over the urban areas and fluvial soil types, reaching values greater than 450 mm, whereas the low values occurred on rural areas, reaching values smaller than 225 mm. The high estimates of surface runoff tended to increase even more from 2016 to 2017, due to combination of high precipitation depths and soil imperviousness or shallow groundwater table. The mean surface runoff in 2016 was 174.26 (Gauge) and 224.82 mm (IMERG\*), corresponding, respectively, to 12.73% and 16.44% of the mean precipitation depth, whereas in 2017 it was 176.43 (Gauge) or 301.31 mm (IMERG\*), corresponding to 10.55% and 18.42%, respectively. Averaging the Gauge and IMERG\* mean estimates, the mean annual value of relative surface runoff stood practically unchanged, once it corresponded to 14.59% (199.54 mm) in 2016, and 14.49% (238.87 mm) in 2017. On the other hand, from 2016 to 2017, the mean annual surface runoff of Gauge was nearly unchanged (2.16 mm) compared to IMERG\* (76.49 mm), likely because the short ARC values increased the potential soil water storage, not allowing for precipitation to exceed the initial abstraction to trigger the surface runoff (see item 4.3.3).

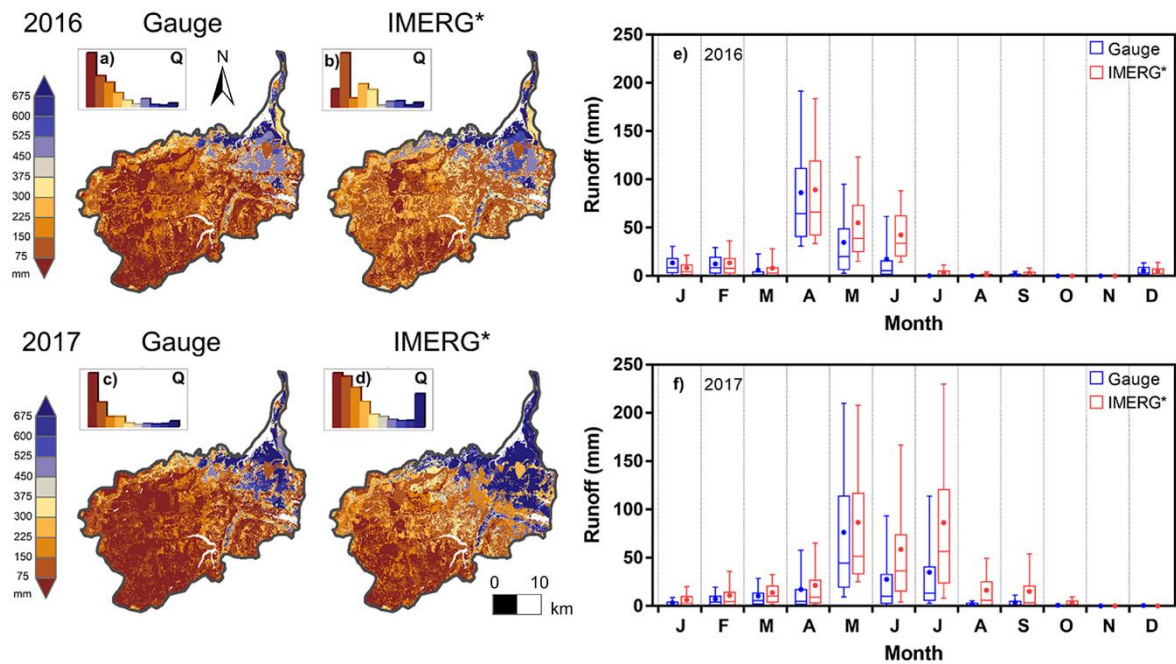


Figure 56 – Annual distributed surface runoff obtained by Natural Resources Conservation Service – Curve Number (NCRS-CN) method from soil type mapping, MapBiomas land use/cover, and (a, c) ground-based precipitation and (b, d) satellite-based IMERG imagery, as well as (e, f) monthly percentile (10%, 25%, 50%, 75%, 90%) variability. Points: mean.

On the monthly scale, the surface runoff estimated by IMERG\* dataset were higher than Gauge in rainy months, due to its more homogeneous distribution of the East-to-West precipitation gradient, which tended to augment the runoff estimates over JPA CSA inland. The sum of the mean surface runoff in the rainy months of 2016 (April to June) corresponded to 77.40% (138.78 mm) for Gauge and 81.25% (187.09 mm) for IMERG\* from the total, whereas in those of 2017 (May to July) corresponded to 75.52% (138.77 mm) for Gauge and 72.57% (231.64 mm) for IMERG\*. Moreover, the monthly surface runoff in 2017 held the higher mean interquartile ranges of 17.21 (Gauge) and 29.19 mm (IMERG\*), in comparison to 14.30 (Gauge) and 18.05 mm (IMERG\*) in 2016 (Figure 56).

To verify the monthly surface runoff, the daily mean Gauge- and IMERG\*-based estimates in 2017, obtained by NRCS-CN method, were averaged on the catchment of stream gauge 503 and summed to monthly scale, so that they could be compared against the monthly sum of daily water level positive differences of the runoff estimates obtained by baseflow separation method at stream gauge 503 (Figure 57). The results showed that Gauge had a reasonable surface runoff estimation in April and May/2017, whereas the IMERG\* had a better performance in June and July/2017. Both scenarios were reasonably well correlated to ground-based estimates, once the CC was equal to 93% for IMERG\* and to 90% for Gauge. Overall, the NRCS-based estimates responded relatively well to the rainfall

events, taking into account that this test was performed around the rural area of JPA CSA, where the lower precipitation incidence implies on a critical condition for NRCS-based surface runoff simulation. In addition, it was noticed that the mean base flow from January to March was lower than from October to December, which occurred due to small natural dams formed from tree branches within the stream channel that came from some fallen trees after the rainy season. Such behaviour, however, does not compromise the identification of daily mean water level positive differences, which were used for the surface runoff verification.

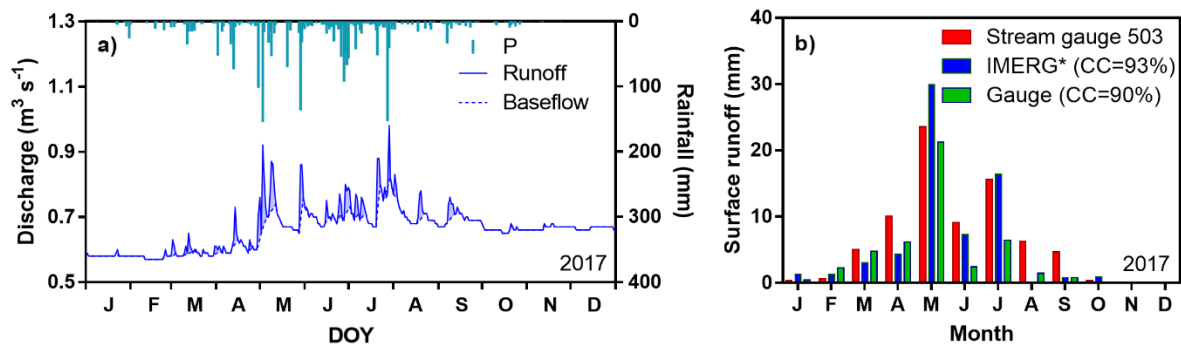


Figure 57 – Verification of the surface runoff in 2017 by comparing the daily water level positive differences of (a) the runoff estimates obtained by baseflow separation method at stream gauge 503 (b), to the daily mean surface runoff estimates obtained by NRCS–CN method from Gauge-based and IMERG\*-based precipitation data, averaged on the gauge 503 catchment.

#### 5.1.4 Groundwater Recharge rate analysis

The GWR was estimated by the water budget equation through satellite products on pixel scale, as well as by WTF method through water table level measurements in unconfined aquifer. The latter was conducted in 23 wells spread over JPA CSA, whose data started to be manually monitored either at the end of 2015 or in 2016 or even in 2017 (Fernandes, 2017). The groundwater level recession was then extrapolated, as required for WTF application, or obtained similarly by the next groundwater recession, due to lack of data, such as in wells W06, W14, W21, W25, W26, W31, W32, W35, W36, W37, W38 and W39 (Figure 58). Due to complex soil underground system, there were shallow and deep wells, whose groundwater levels stood on  $\sim 2$  m in some wells and reached down to  $\sim 30$  m in others. From the 16 monitoring wells in 2016, the potential groundwater level rise ( $\Delta H$ ) varied from 0.83 to 3.69 m (mean of 1.91 m), while from the 23 monitoring wells in 2017, the  $\Delta H$  varied slightly more from 0.85 to 5.30 m (mean of 2.54 m).

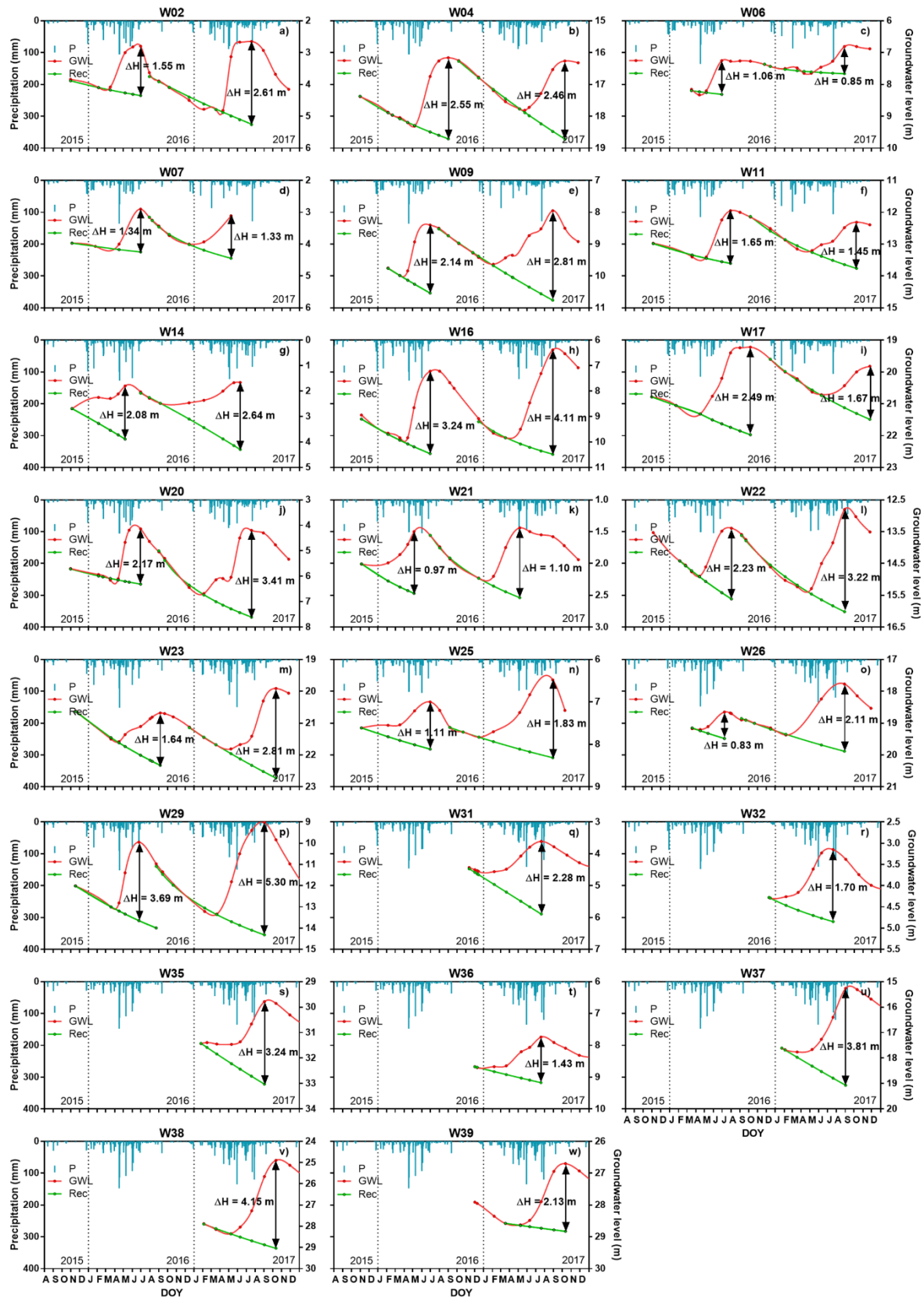
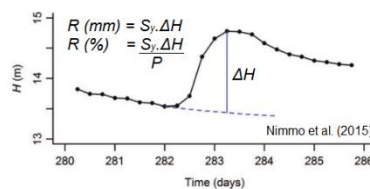


Figure 58 – Potential groundwater level rise ( $\Delta H$ ) obtained in 2016 and 2017 at 23 manually-monitored wells spread over JPA CSA. W: Well identification.

Still for applying the WTF method, the soil specific yield ( $S_y$ ) was calculated from datasets of production tests carried out by LARHENA team in three wells over JPA CSA. The  $S_y$  equal to 0.10 was obtained and initially assigned to mostly wells, similarly to Fernandes (2017), and to the other wells that presented a clear underestimated linear relationship with satellite-based recharge estimates,  $S_y$  was assigned to those as 0.24 (Table 9). The WTF-based recharges in 2016 varied from 106.02 to 396 mm, and from 9.68% to 24.32% of precipitation, whereas in 2017 they varied from 85.15 to 547.83 mm, and from 6.14% to 28.48%. Those results were then confronted with satellite-based estimates.

Table 9 – Groundwater recharge obtained by WTF method in 2016 and 2017 over JPA CSA. id: index of measurement location; lon/lat: longitude/latitude at decimal degree in WGS84 datum;  $S_y$ : soil specific yield;  $\Delta H$ : potential groundwater level rise; P: precipitation averaged around 500 m from the well.

id (-)	lon (°)	lat (°)	$S_y$ (-)	P <sub>2016</sub> (mm)	$\Delta H$ <sub>2016</sub> (m)	R <sub>2016</sub> (mm)	R <sub>2016</sub> (%)	P <sub>2017</sub> (mm)	$\Delta H$ <sub>2017</sub> (m)	R <sub>2017</sub> (mm)	R <sub>2017</sub> (%)
W02	-35.0954	-7.2459	0.10	1244.2	1.55	155.04	12.46	1490.5	2.61	261.08	17.52
W04	-35.1166	-7.2622	0.10	1257.0	2.55	254.68	20.26	1507.5	2.46	246.49	16.35
W06	-35.1335	-7.3752	0.10	1095.6	1.06	106.02	9.68	1387.9	0.85	85.15	6.14
W07	-35.0867	-7.1488	0.10	1175.9	1.34	134.36	11.43	1348.5	1.33	133.49	9.90
W09	-35.0905	-7.3489	0.10	1196.2	2.14	213.69	17.86	1488.9	2.81	281.30	18.89
W11	-35.1279	-7.1830	0.10	1209.1	1.65	165.49	13.69	1431.8	1.45	145.32	10.15
W14	-35.0130	-7.2277	0.10	1368.6	2.08	208.39	15.23	1638.5	2.64	263.56	16.09
W16	-34.9845	-7.2445	0.10	1431.1	3.11	310.73	21.71	1743.2	4.11	410.65	23.56
W17	-35.1145	-7.2019	0.10	1202.8	2.49	249.29	20.73	1441.7	1.67	166.86	11.57
W20	-35.0446	-7.2816	0.10	1462.6	2.17	217.02	14.84	1638.6	3.41	341.13	20.82
W21	-34.9579	-7.3332	0.24	1415.4	0.97	232.72	16.44	1780.1	1.10	263.27	14.79
W22	-34.9587	-7.3242	0.10	1423.7	2.23	222.57	15.63	1803.6	3.22	321.54	17.83
W23	-34.8805	-7.2079	0.10	1483.6	1.64	164.50	11.09	1844.3	2.81	281.45	15.26
W25	-34.9170	-7.2908	0.24	1446.9	1.11	266.64	18.43	1826.5	1.83	440.10	24.10
W26	-34.8004	-7.1646	0.24	1519.8	0.83	199.74	13.14	1949.5	2.11	507.15	26.01
W29	-34.9056	-7.1609	0.10	1517.2	3.69	369.00	24.32	1860.5	5.30	529.96	28.48
W31	-34.8451	-7.0641	0.24					1930.2	2.28	547.83	28.38
W32	-34.8485	-7.0931	0.24					1991.8	1.70	407.28	20.45
W35	-34.8401	-7.1339	0.10					2026.6	3.24	324.35	16.00
W36	-34.8571	-7.1365	0.24					2036.7	1.43	343.97	16.89
W37	-34.8042	-7.1857	0.10					1928.8	3.81	380.76	19.74
W38	-34.8184	-7.1845	0.10					1939.0	4.15	415.01	21.40
W39	-34.8369	-7.1889	0.24					1935.4	2.13	510.35	26.37



The GWR distribution was estimated based on the water budget equation for Gauge and IMERG\* scenarios in 2016 and 2017 (Figure 59); the relative values are shown in Supplementary Figure 17. The GWR rates featured high estimates on Northeastern portion due to combination of decreasing precipitation gradient and permeable soil types, despite the



larger surface runoff values found on urban land use. The mean GWR rates in 2016 was 230.02 (Gauge) and 219.13 mm yr<sup>-1</sup> (IMERG\*), corresponding to 16.81% and 16.03% of the mean precipitation depth, whereas in 2017 it was 364.62 (Gauge) and 301.63 mm yr<sup>-1</sup> (IMERG\*), corresponding to 21.81% and 18.44%, respectively. The mean relative GWR over JPA CSA was then averaged on 18.27% (278.85 mm yr<sup>-1</sup>) for 2016 and 2017. The mean GWR rates in 2017 increased more using Gauge- than IMERG\*-based data due to its great incidence on Western portion, which resulted from the larger precipitation depths and lower surface runoff, mainly in June and July. Conversely, in 2016, the Gauge- and IMERG\*-based data behaved fairly similarly, whose mean of monthly mean recharge stood on 26.11 and 25.95 mm month<sup>-1</sup>, respectively; different from 2017, where they reached 33.69 and 38.53 mm month<sup>-1</sup> (see Supplementary Figure 13 to Supplementary Figure 16). All in all, both data sources were comparatively well-distributed over JPA CSA, since their monthly 90th-percentiles were similar both in 2016, reaching up to 161.1 (Gauge) and 168.85 mm month<sup>-1</sup> (IMERG\*), and in 2017, up to 222.86 (Gauge) and 221.25 mm month<sup>-1</sup> (IMERG\*).

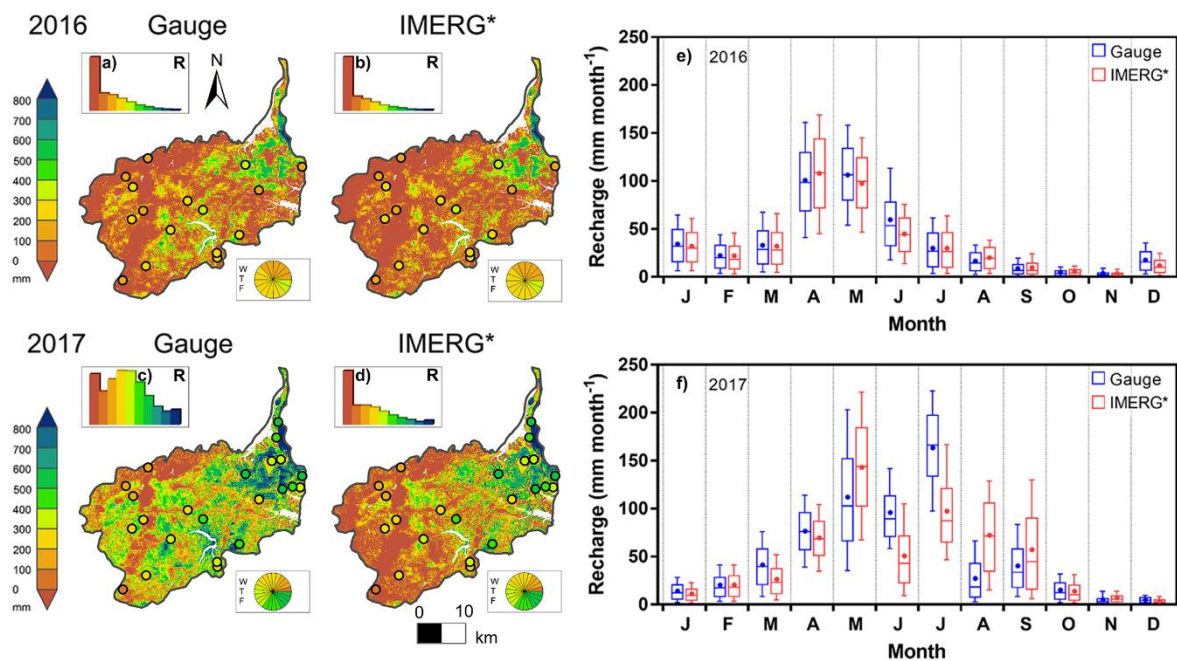


Figure 59 – Annual distributed Groundwater Recharge (R) obtained by water budget equation and WTF method, using (a, b) ground-based, interpolated precipitation and (c, d) bias-corrected IMERG imagery, as well as (e, f) monthly percentile (10%, 25%, 50%, 75%, 90%) variability. Coloured circles: WTF-based recharge; Points: mean.

For validation purposes, the absolute and relative estimates of GWR obtained by WTF method were plotted against the Gauge- and IMERG\*-based outcomes, by averaging the recharge around 1-km of every well (Figure 60). Overall, it was noticed that Gauge and

IMERG\* absolute estimates had relatively high goodness-of-fit, reaching 89% and 83%, respectively, while their relative estimates had satisfactory goodness-of-fit, reaching 73% and 68%; resulting in linear regressions closer to 1:1 perfect fit. Gauge-based data tended to slightly overestimate the WTF data, with a bias of 11% (absolute estimation) and 8% (relative estimation), whereas the IMERG\*-based data tended to slightly underestimate WTF data, with a bias of -9% (absolute estimation) and -13% (relative estimation). In addition, both Gauge and IMERG\* scenarios had similar, satisfactory mean errors either for absolute or relative estimates, with RRMSE equal to 31% and 34%, and to 31 and 30%, respectively. As a result, the mean annual GWR rates for Gauge and IMERG\* data were relatively closer to WTF estimates, whose absolute and relative values stood on 230 (16.2%) and 219 mm yr<sup>-1</sup> (15.3%) compared to 217 mm yr<sup>-1</sup> (16.1%) in 2016, and 365 (21.3%) and 302 mm yr<sup>-1</sup> (16.8%) compared to 331 mm yr<sup>-1</sup> (18.6%) in 2017.

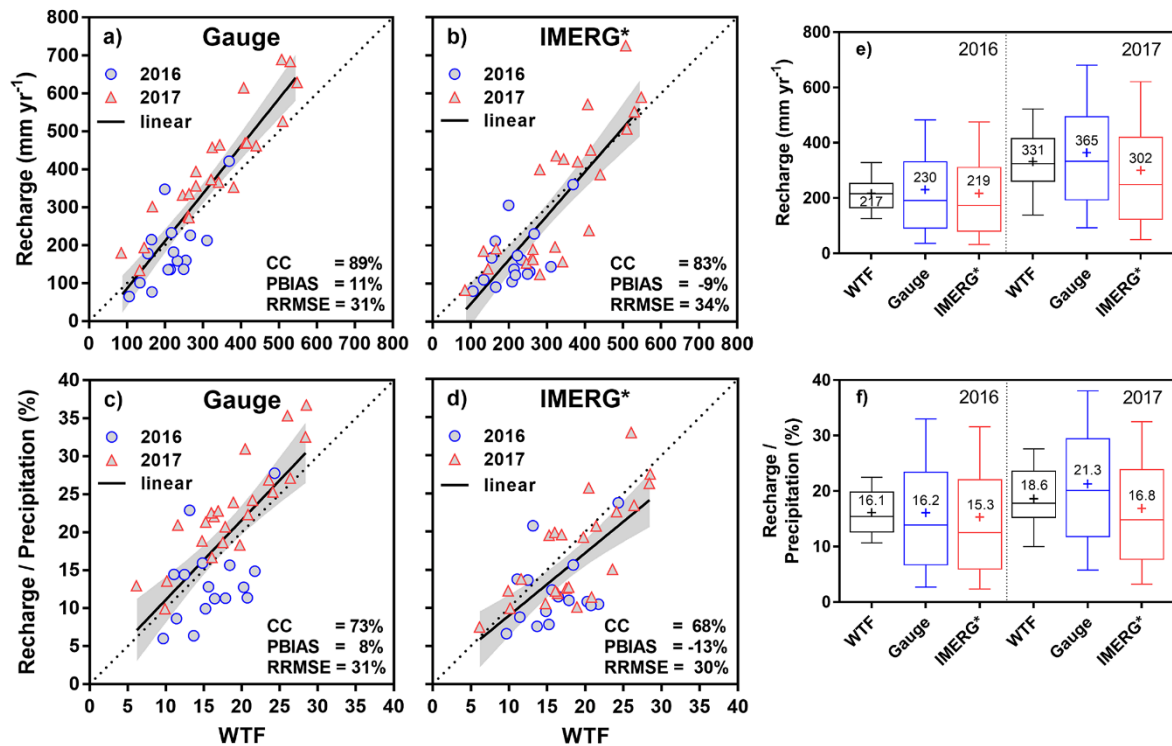


Figure 60 – Validation of annual groundwater recharge rates at (a, b, e) absolute and (c, d, f) relative scales, for ground-based and remotely-sensed precipitation through WTF method, respectively.

The relative estimates of GWR were zonally averaged by land use/cover and soil type over JPA CSA (Figure 61). By land use/cover, the mean plots were relatively well correlated with mean values higher for Gauge than IMERG\*, featuring a shift more pronounced in 2017 than 2016, averaged on 4.88% and 0.89%, respectively. In 2016, the mean relative recharge varied from 13.27% (Mosaic) to 24.75% (Urban) for Gauge, and from 12.40%

(Mosaic) to 23.68% (Urban) for IMERG\*, whereas in 2017, it ranged from 19.62% (Bare soil) to 29.61% (Urban) for Gauge, and from 14.81% (Mosaic) to 22.03% (Urban) for IMERG\* one. It is also worthwhile to mention that Forest held a recharge of 15.56% in 2016 and 18.93% in 2017, on average. Similarly, the mean plots by soil type were higher for Gauge than IMERG\*, and in 2017 than 2016, whose shift was averaged on 4.79% and 1.95%, respectively. In 2016, the mean relative recharge varied from 7.60% (Luvisols) to 22.90% (Fluvisols) for Gauge, and from 4.77% (Luvisols) to 24.22% (Fluvisols) for IMERG\*, whereas in 2017, it ranged from 10.94% (Gleysols) to 28.68% (Ferralsols) for Gauge, and from 8.10% (Luvisols) to 21.81% (Fluvisols) for IMERG\* one. Moreover, it is worthwhile to highlight the relative recharge values of Acrisols and Podzols, which held respectively 15.48% and 15.19% in 2016, and 19.26% and 20.56% in 2017; averaging both values, it results in 17.37% for Acrisols and 17.87% for Podzols. Those previous results show the high GWR potential within the unconfined aquifer of JPA CSA.

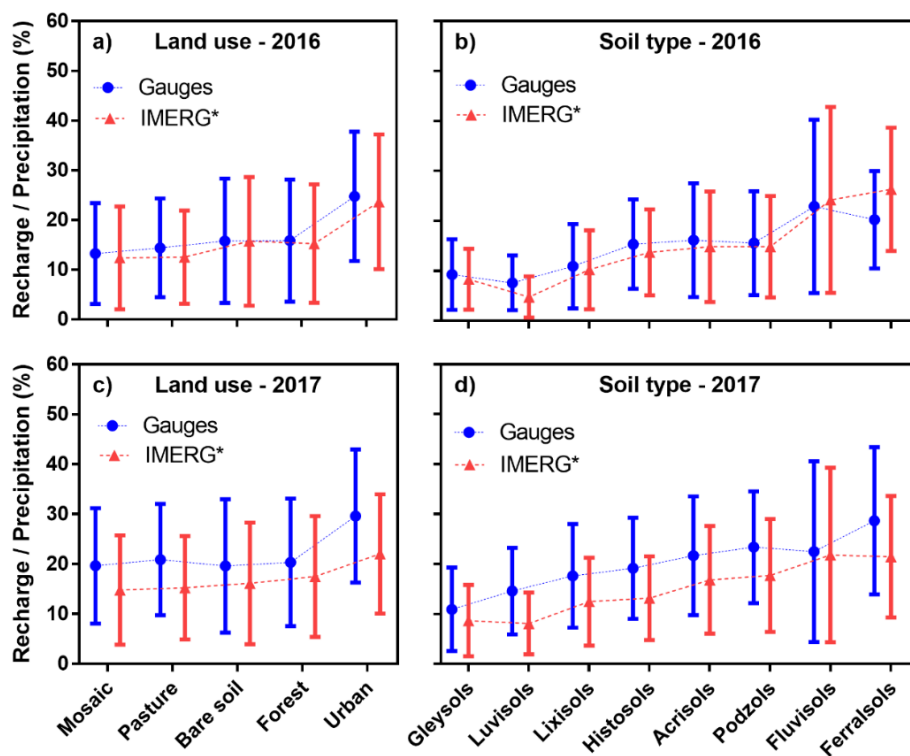


Figure 61 – Relative groundwater recharge rates averaged on JPA CSA in 2016 and 2017 by (a, b, e) land use/cover and (b, d, f) soil type, for Gauge and IMERG\* scenarios. Mean plot: mean  $\pm$  standard deviation.



## **5.2 Intermediary-scale Groundwater Recharge modelling coupled to soil hydraulic property inverse modelling**

The GWR was simulated on daily scale for a proof of two hydrological years, 2017 to 2018 and 2018 to 2019, after the inverse calibration of the soil hydraulic properties using two soil moisture data sources, CRNS data and soil moisture profiles, and was, verified by WTF method over GEB. The results were sub-divided to present understandingly the calibration, parameterization, inverse modelling, validation, and water flux simulation.

### **5.2.1 Cosmic-Ray Neutron Sensing curve calibration**

The CRNS probe operated in the middle of GEB (site 2, see Figure 25) from July 18th, 2018, to June 26th, 2019, to monitor the aboveground neutron flux that can be associated to soil moisture. A fieldwork campaign was undertaken on October 1st, 2018, to collect soil cores according to sampling scheme of Figure 41, for obtaining the Volumetric Water Content (VWC) and bulk density ( $\rho_{bd}$ ) by gravimetric method (Table 10). The mean VWC obtained by the weighting method (see item 4.5.1) at 17 locations spread around the CRNS probe was  $8.8 \text{ cm}^3 \text{ cm}^{-3}$ , while the arithmetic-mean of BD was  $1.11 \text{ g cm}^{-3}$ . The CRNS footprint included flooded and moderately-wet areas due to a shallow groundwater table, by applying the vertical weighting at the calibration time (Figure 62). The dense vegetation cover and soil organic aspect on southwestern portion showed its wet or saturated soil condition, which reached up to  $0.296 \text{ cm}^3 \text{ cm}^{-3}$ , whereas the moderately-sparse vegetation and white soil aspect on centre-eastern portion showed the moderately-wet condition, which reached down to  $0.056 \text{ cm}^3 \text{ cm}^{-3}$ . The addressed condition is a typical scenario of the Podzol soil type in Brazil, whose characteristics can be coped with the CRNS probe, once it has the ability to monitor indirectly the mean soil moisture on intermediary scale.

Table 10 – Soil moisture and bulk density weighting-averaged after the gravimetric experiment at three soil sampling depths carried out on October 1st, 2018.  $\rho_{bd}$ : bulk density; Id: index of measurement location; r: radial distance;  $D_{86}$ : penetration depth;  $W_r$ : horizontal weighs;  $W_d$ : vertical weighs;  $mean_w$ : weighted-mean;  $mean_a$ : arithmetic-mean.

Id (-)	r (m)	$D_{86}$ (cm)	$W_r$	$W_d$ at (cm)			VWC at (cm)				$\rho_{bd}$ at (cm)			
				-2.5 (-)	-7.5 (-)	-17.5 (-)	-2.5 (%)	-7.5 (%)	-17.5 (%)	$mean_w$	-2.5 ( $g\ cm^{-3}$ )	-7.5 ( $g\ cm^{-3}$ )	-17.5 ( $g\ cm^{-3}$ )	$mean_a$
001	10.3	44.9	0.099	0.895	0.716	0.459	9.6	9.7	12.4	10.2	1.21	1.15	1.12	1.16
002	14.9	44.2	0.085	0.893	0.712	0.453	10.7	7.9	4.7	8.4	1.07	1.03	1.25	1.12
003	12.2	44.6	0.090	0.894	0.714	0.456	6.2	7.7	3.9	6.2	1.01	1.24	1.32	1.19
004	13.4	44.4	0.088	0.894	0.713	0.455	11.5	7.1	3.1	8.1	0.81	0.89	1.18	0.96
005	8.1	45.2	0.125	0.895	0.718	0.461	10.1	6.8	6.1	8.1	0.65	1.00	1.03	0.89
006	8.1	45.2	0.125	0.895	0.718	0.461	8.0	5.6	3.7	6.2	0.97	1.18	1.33	1.16
007	65	38.3	0.043	0.878	0.676	0.401	11.5	7.1	6.0	8.9	1.19	1.15	1.31	1.22
008	81.3	36.8	0.038	0.873	0.665	0.386	11.7	14.2	8.3	11.9	1.18	1.21	1.25	1.21
009	71.4	37.7	0.041	0.876	0.672	0.395	11.4	9.2	7.5	9.8	0.73	0.87	1.05	0.89
010	64.5	38.3	0.043	0.878	0.676	0.401	12.3	10.9	9.3	11.2	0.26	0.54	0.60	0.47
011	65	38.3	0.043	0.878	0.676	0.401	7.3	7.7	7.2	7.4	1.25	1.27	1.35	1.29
012	64.1	38.4	0.043	0.878	0.676	0.402	6.5	6.9	4.6	6.3	1.06	1.21	1.27	1.18
013	136	33.1	0.025	0.860	0.636	0.348	7.0	5.5	2.4	5.6	1.22	1.29	1.23	1.25
014	103.9	35.1	0.032	0.867	0.652	0.369	6.7	6.6	6.4	6.6	1.26	1.22	1.36	1.28
015	97.1	35.6	0.033	0.869	0.656	0.374	26.2	31.3	34.8	29.6	0.98	1.44	1.36	1.26
016	124.5	33.8	0.027	0.862	0.641	0.355	7.8	6.2	7.9	7.2	1.06	0.99	1.15	1.07
017	160	32.0	0.021	0.855	0.625	0.335	10.0	8.5	5.4	8.6	1.22	1.37	1.37	1.32
mean										8.8				1.11

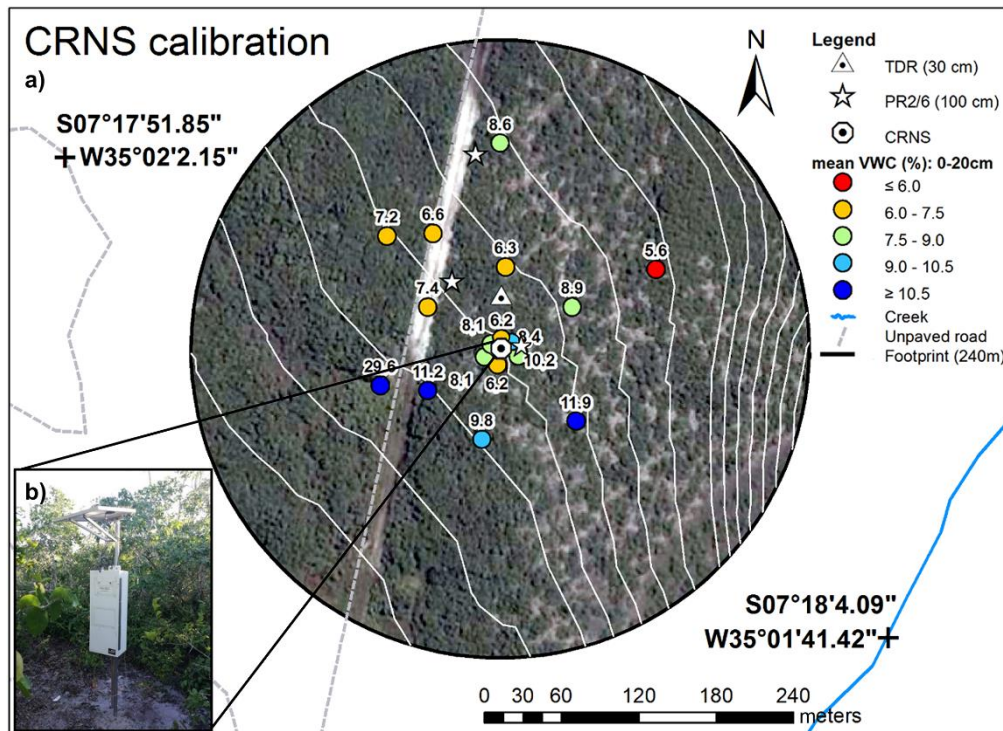


Figure 62 – Distribution of the (a) mean vertically-weighted soil moisture for the (b) CRNS probe calibration through the gravimetric experiment carried out on October 1st, 2018.

The three soil profile probes (PR2 Delta-T model) monitored the soil moisture down to 1 m, during the same time period in which the CRNS probe operated (see Figure 29). After converting the voltage-signal to soil moisture data, the hourly measurements were converted to daily values by calculating the 24-hour moving average and, then, the mean soil moisture per day. The soil moisture profiles were built by connecting the daily soil moisture at depths of -5, -15, -25, -35, -55 and -95 cm (Figure 63). The median soil moisture in DL6-2, DL6-4 and DL6-1 in a distance of 17.5, 65.5 and 153.2 m from the CRNS probe, were 0.097, 0.093 and 0.124  $\text{cm}^3 \text{cm}^{-3}$ , respectively. The DL6-4 probe better detected the wetting and drying fronts than the others, as well as assimilated soil moisture either on saturation or on dry condition. It was noticed that the capacitance sensor at 5-cm depth performed fairly well in all probes, whereas at the other depths the measurements oscillated remarkably, except for the DL6-4 probe (65.5 m from CRNS probe), which performed fairly well after October 15th, 2018. Thereby, the horizontal weighted mean of 5-cm measurements was used to assess the goodness-of-fit of CRNS soil moisture data, while the DL6-4 soil moisture profile was used to assess the goodness-of-fit of the simulated soil moisture profile.

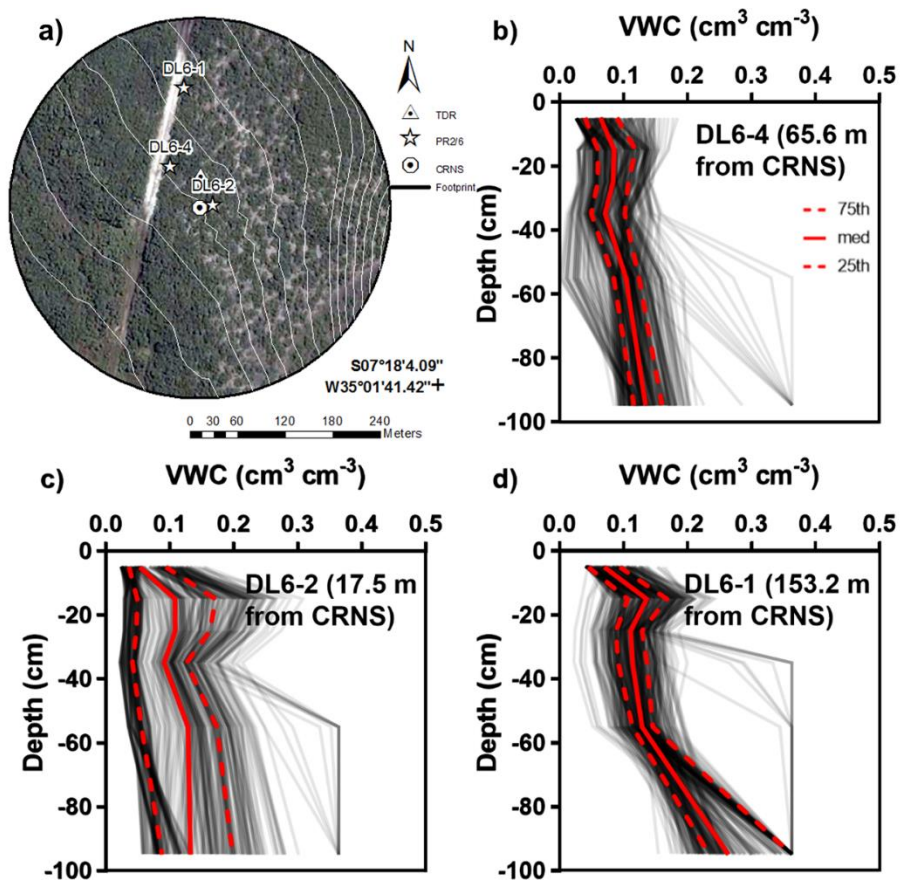


Figure 63 – Soil moisture profiles monitored by the three PR2/6 soil profile probes from July 18th, 2018 to June 06th, 2019.

Another few analysis and experiments were carried out for the parametrization of the CRNS calibration curve and the COSMIC neutron operator (Figure 64). The energy spectra of the detected neutron counts showed that the CRNS probe seemed to reflected correctly the neutrons at the soil surface, as its neutron energy histogram was in accordance with the standard shape reported in the literature (Köhli et al., 2015). The soil organic and lattice water equivalents were determined at the six depths monitored by the profile probes, whose magnitudes were relatively small likely due to the sandy soil texture. The total lattice water equivalent down to -10 cm was summed to the weighted-mean soil moisture, and then considered in the CRNS calibration curve together with arithmetic-mean bulk density, resulting in the determination of  $N_0$  parameter equal to 550 counts. This  $N_0$  value was, in turn, plotted against the  $N_{\text{COSMIC}}$  parameter, the latter obtained by try-and-error through successive simulations in HYDRUS-1D using the mean soil moisture profile, resulting on a reasonable  $N_{\text{COSMIC}}$  value of 90 counts compared to the literature (Baatz et al., 2014). Thus, despite the lower neutron intensity, below 600 counts, the CRNS curve was successively calibrated under unfavourable hydrological and geographic conditions.

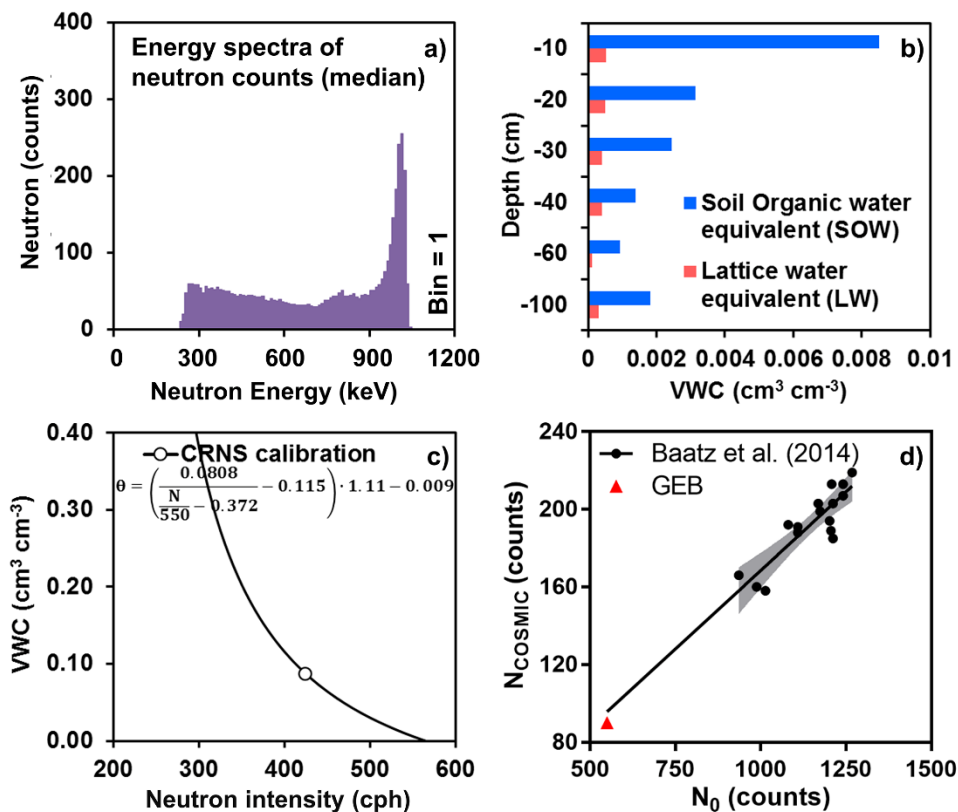


Figure 64 – Data analysis and experiment results about (a) energy spectra of detected neutron counts and (b) soil organic and lattice water equivalent, for the parametrization of the (c) CRNS calibration curve and (d) COSMIC neutron operator.

The calibration curve was then applied to the CRNS neutron intensity to yield the VWC estimates on the hourly scale (Figure 65). Since the neutron intensity range in GEB stood low, the time series were smoothed by 24-hours moving average and, then, compared to 10-cm horizontal-weighted-mean of PR2 soil moisture. Overall, the CRNS time series responded fairly well to the rainfall events, behaving similarly to 10-cm PR2 time series in mostly study period. The mean soil moisture values of CRNS and 10-cm PR2 were 0.074 and 0.068  $\text{cm}^3 \text{cm}^{-3}$ , respectively. The scatter plot showed a relatively high goodness-of-fit between CRNS and PR2 datasets, depicted by KGE and  $R^2$  equal to 80% and 89%, respectively, resulting in a linear regression close to 1:1 perfect fit. A slight influence of groundwater level over CRNS data could be noticed by its time series slope along the recession period from July to August 2018. The groundwater level at CRNS site reached up to 25.36 cm below soil surface. Furthermore, it was noticed a shift during the dry season, likely caused by the shape of the CRNS standard calibration curve, which consider three fixed parameters. Conversely, this behaviour could not be better checked due to data collection failure occurred from September 12th to November 8th, 2018. All in all, the CRNS monitoring period comprised either the dry or the rainy season, encompassing even one of the rainy day of the last decades, June 13th, 2019, reaching 159.26 mm.

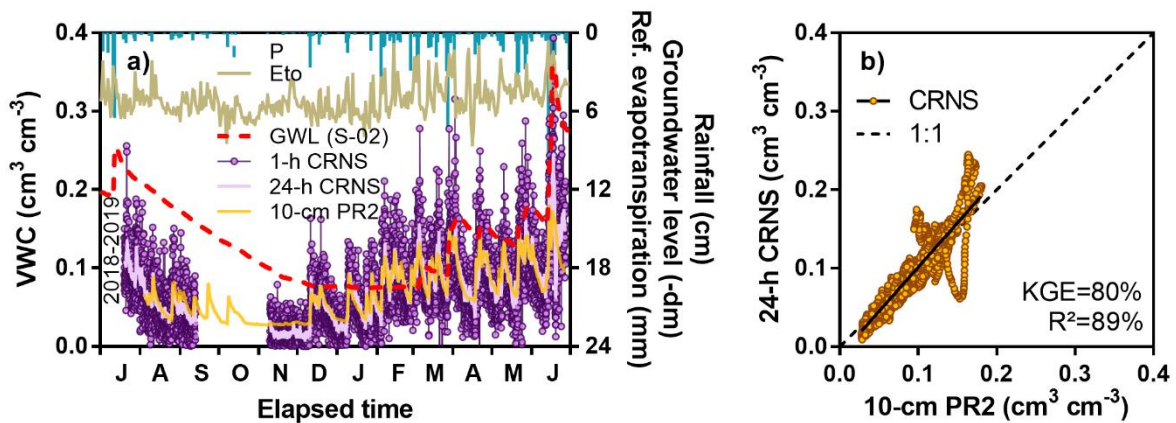


Figure 65 – Soil moisture time series based on (a) 1-h CRNS dataset smoothed by 24-h moving average (b) compared to 10-cm PR2 dataset. P: rainfall;  $E_{to}$ : reference evapotranspiration; GWL: Groundwater Level.

### 5.2.2 Modelling input data and parameters

For setting the model, the initial conditions had to be suitably identified through data analysis and soil experiments, in order to allow for converging correctly the model parameters (Figure 66). The initial soil moisture condition varied from 0.061 to 0.363  $\text{cm}^3 \text{cm}^{-3}$



cm<sup>-3</sup>, which was obtained by averaging the monthly mean soil moisture in the same period of the following hydrological year, as it was unavailable at the beginning of the study period. The root distribution was calculated using the Equation (87) (see item 4.5.3.4) down to 70 cm, after the rooting *in situ* observation of typical tree species by digging a few boreholes, in accordance with the regional literature (Pineiro, Costa and de Araújo, 2013). The normalized water uptake distribution highlighted the maximum value of 0.024 cm<sup>-1</sup> down to 14 cm, following by a linear water uptake decreasing. In addition, the soil particle distribution curves at 6 different depths were built by sieving experiment, finding a remarkable sandy texture along the soil profile. The soil texture consisted of 96.38% by coarse and fine sand contents so that a homogeneous soil discretization was set on the model.

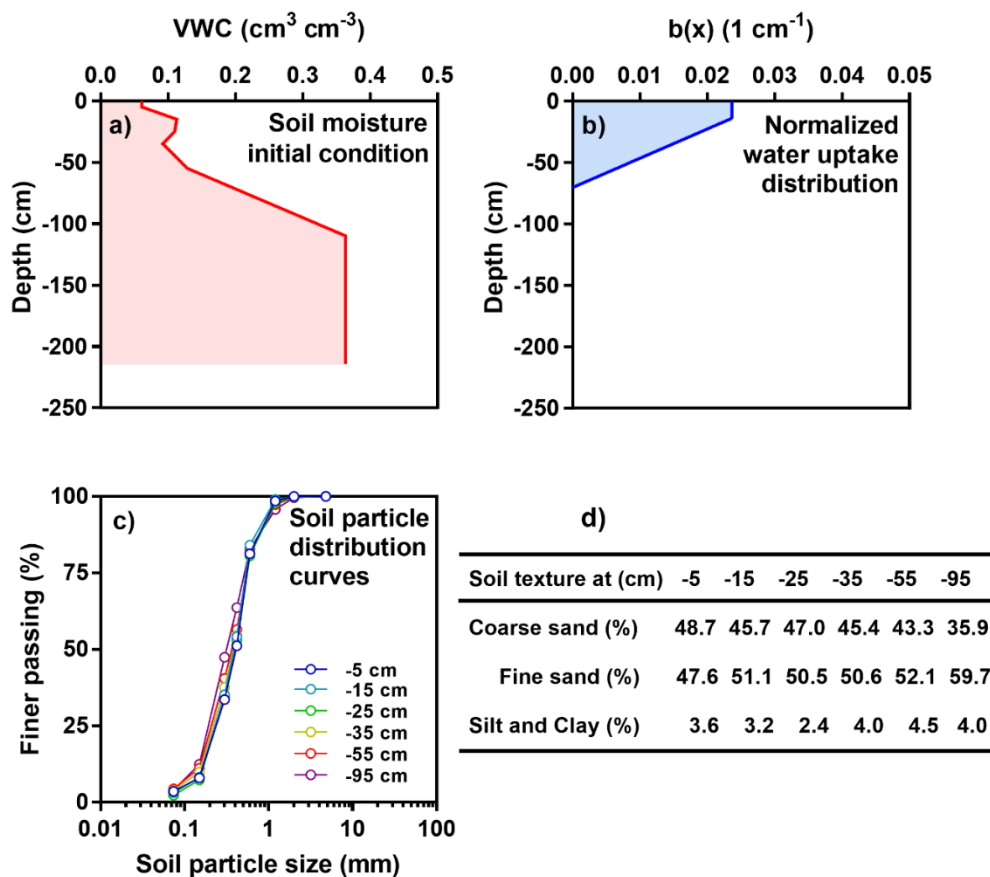


Figure 66 – Data analysis and experiment results of the initial model conditions about (a) soil moisture, (b) normalized water uptake distribution, (c) soil particle distribution curves, and (d) soil textures along the soil profile.  $b(x)$ : normalized water uptake.

The Leaf Area Index (LAI) of GEB vegetation were obtained by geoprocessing the MODIS remotely-sensed reflectance imagery on the monthly scale and, then, averaged on GEB due to its relatively-coarse 250-m spatial resolution (Figure 67). LAI showed a roughly annual sinusoidal pattern, reaching their high values on rainy seasons and low values on dry

seasons. It varied from 2.49 to 5.10  $\text{m}^2 \text{m}^{-2}$  in 2017-2018 hydrological year and 2.16 to 4.87  $\text{m}^2 \text{m}^{-2}$  in 2018-2019 hydrological year, with monthly mean values of 3.95 and 3.71  $\text{m}^2 \text{m}^{-2}$ , respectively. From the LAI and weather (see Supplementary Figure 19) datasets, the potential evaporation and transpiration could be estimated through Penman-Monteith equation for the two hydrological years. Overall, it was found that the potential evaporation reached high values on the dry seasons and that the potential transpiration reached them on the rainy seasons. The potential evaporation varied from 0.11 to 2.00 mm in 2017-2018 and from 0.07 to 2.33 mm in 2018-2019, whereas the potential transpiration ranged from 0.56 to 5.93 mm in 2017-2018 and from 0.61 to 7.49 mm in 2018-2019. The mean values for potential evaporation stood on 0.88 and 1.00 mm, and for potential transpiration stood on 4.08 and 3.94 mm, in 2017-2018 and 2018-2019, respectively.

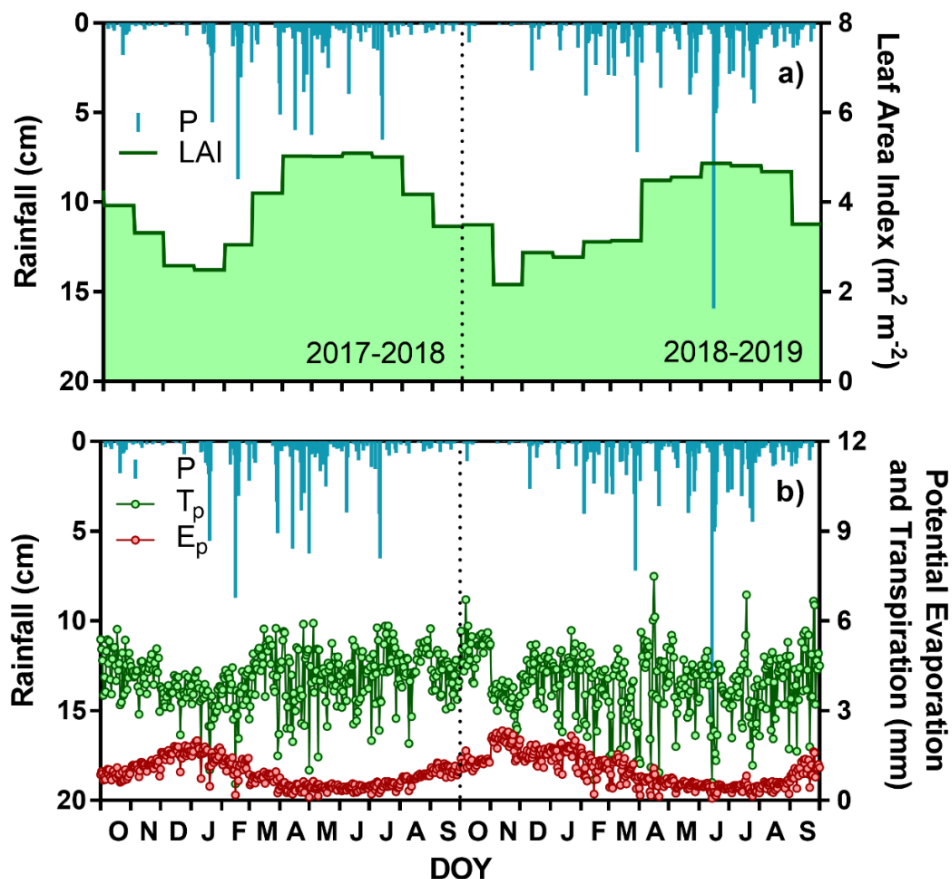


Figure 67 – Time series of the (a) monthly Leaf Area Index (LAI) obtained by geoprocessing the MODIS reflectance imagery over GEB, and the (b) daily potential evaporation ( $E_p$ ) and transpiration ( $T_p$ ) estimated by Penman-Monteith equation.

The 3 Time-Domain Reflectometry (TDR) probes (CS616 model, Campbell Scientific) monitored the soil moisture without flaws at 3 different depths (5, 20 and 40 cm) in a downstream GEB boundary location (site 5) along the two hydrological years (Figure

68). The dielectric signals of such TDR probes were retrieved and converted to soil moisture by the calibration curve shown in Figure 52 (see item 5.1.2). Overall, it is noticed that the 5-cm TDR data responded more sensibly to rainfall events during the rainy seasons, while the 40-cm TDR data dried faster during the dry seasons. The 40-cm TDR data was eventually saturated from June to July 2019, as a result of the capillarity rise stemmed from the groundwater level rise, which reached up to 73.11 cm below surface. Furthermore, the reference evapotranspiration varied from 0.74 to 6.83 mm in 2017-2018 hydrological year and 0.68 to 8.57 mm in 2018-2019 hydrological year, with mean (and standard deviation) of 4.96 (0.99) and 4.94 (1.4) mm. The total rainfall depth in 2017-2018 and 2018-2019 hydrological years stood on 1250.19 and 1616.46 mm, respectively, corresponding to a dry and rainy year in GEB. Thus, the inverse modelling and water flux simulation could be carried out at upstream (site 2) and downstream (site 5) of GEB.

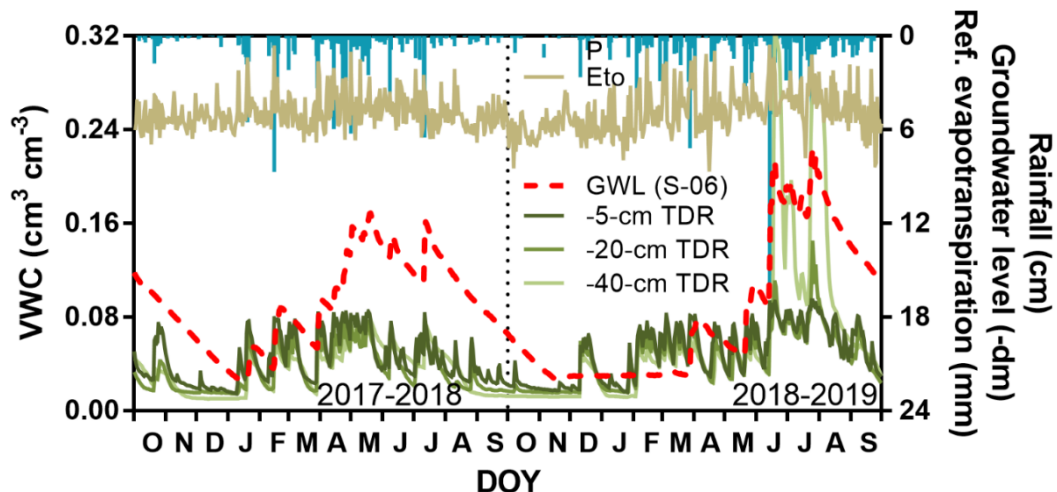


Figure 68 – Soil moisture time series based on 1-h TDR dataset at depth of -5, -20 and -40 cm. Eto: reference evapotranspiration; GWL: Groundwater Level.

### 5.2.3 Inverse modelling of the soil hydraulic properties

The CRNS or TDR datasets were used to calibrate the soil hydraulic properties by inverse modelling through HYDRUS-1D coupled externally with COSMIC neutron operator. The CRNS neutron intensity and the TDR soil moisture profiles were inputted into the model to optimize on the daily scale the objective function in Equation (85) (see item 4.5.3.3). From the CRNS dataset, the model simulated the neutron intensity time series for the two hydrological years with a relatively high goodness-of-fit for KGE and  $R^2$  equal to 89% and 79%, respectively, resulting in a linear regression close to 1:1 perfect fit (Figure 69). The COSMIC time series responded fairly well to the rainfall events, being able to



mirror consistently the variable pattern of neutron intensity along the period with available data. On the other hand, the COSMIC time series tended to underestimate slightly the CRNS neutron intensity particularly during the dry season, the latter, however, likely influenced by the standard parametrisation of the calibration curve in Equation (69) (see item 4.5.2).

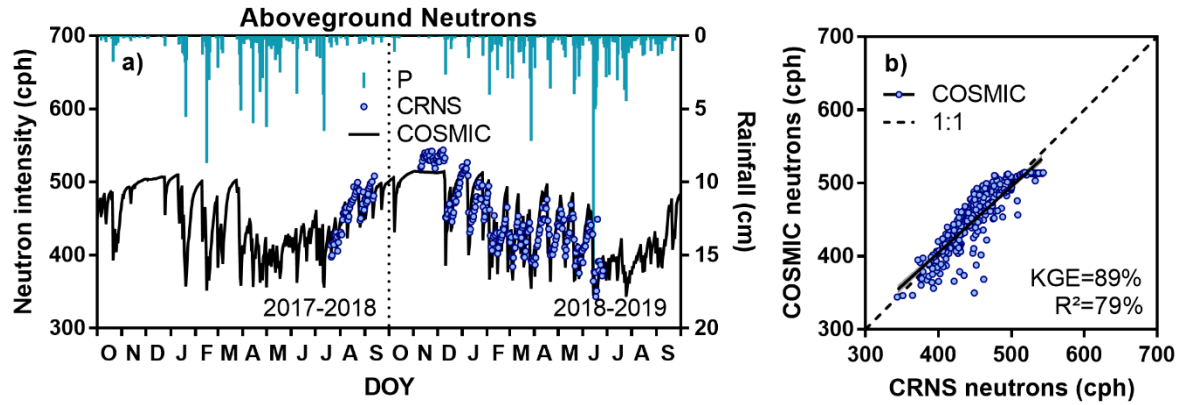


Figure 69 – Neutron intensity simulated by (a) COSMIC neutron operator, after the calibration by using the (b) CRNS dataset through the HYDRUS-1D model.

The curves of the soil hydraulic properties at TDR and CRNS sites were built after the calibration of van Genuchten-Mualem parameters (Table 11 and Figure 70). An air-entry value of -2 cm was considered for CRNS modelling to reduce the non-linearity of hydraulic conductivity function because it was identified by preliminary simulations that parameter  $n$  tended to be around 1.2 (Ries et al., 2015; Šimůnek, 2018), and was at the end calibrated to be 1.2589. Both retention curves obtained by TDR and CRNS datasets were within the interquartile range of the curves obtained by Silva (2009) in GEB, whose difference between curve shapes stemmed mainly from parameter  $\alpha$ , higher at CRNS site ( $0.4431 \text{ cm}^{-1}$ ) than TDR site ( $0.0807 \text{ cm}^{-1}$ ). On the other hand, the hydraulic conductivity curves were relatively more shifted, so that the CRNS curve was closer to the interquartile range (Silva, 2009) than the TDR curve, stemmed mainly from parameter  $K_s$  that was higher at TDR site ( $1.26 \times 10^{-4} \text{ m s}^{-1}$ ) than CRNS site ( $6.47 \times 10^{-4} \text{ m s}^{-1}$ ).

Table 11 – Genuchten-Mualem parameters calibrated at TDR and CRNS sites through inverse modelling from soil moisture datasets. \*Considered air-entry of -2 cm (Ries et al., 2015; Šimůnek, 2018).  $\theta_r$ : residual soil moisture content;  $\theta_s$ : saturated soil moisture content;  $\alpha$ : air-entry pressure factor;  $n$ : pore size distribution measure;  $K_s$ : saturated hydraulic conductivity;  $l$ : pore tortuosity and connectivity parameter.

Sensor	$\theta_r$ ( $\text{cm}^3 \text{cm}^{-3}$ )	$\theta_s$ ( $\text{cm}^3 \text{cm}^{-3}$ )	$\alpha$ ( $\text{cm}^{-1}$ )	$n$ (-)	$K_s$ ( $\text{m s}^{-1}$ )	$l$ (-)
TDRs	0.0192	0.3000	0.0807	1.9156	$6.47 \times 10^{-4}$	0.5
CRNS*	0.0101	0.3031	0.4431	1.2589	$1.26 \times 10^{-4}$	0.5

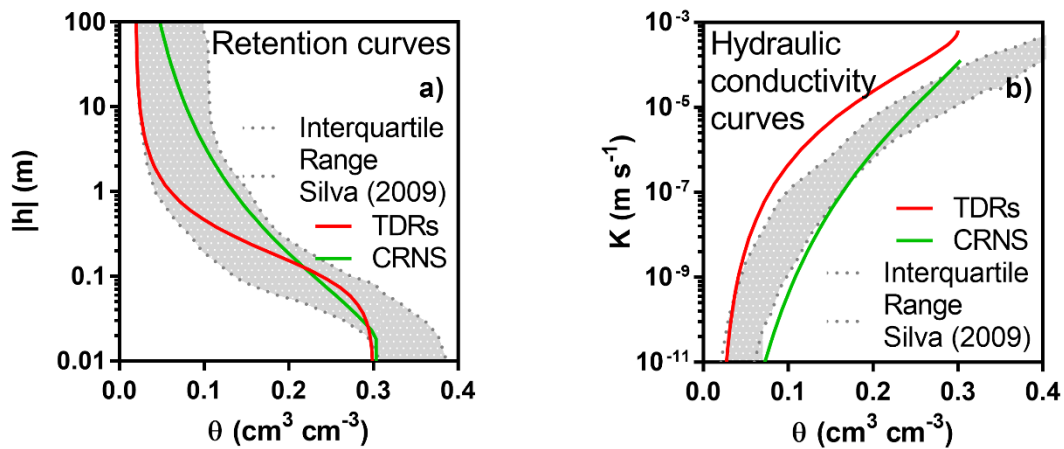


Figure 70 – Soil hydraulic properties obtained through inverse modelling from TDR and CRNS datasets, namely (a) retention curves, and (b) hydraulic conductivity curves, compared to Silva (2009) results over GEB.  $h$ : soil matric potential;  $K$ : hydraulic conductivity.

Since the hydraulic conductivity curves seemed reasonably different over GEB, the slug test was carried out through the Equation (103) (see item 4.6.2), so that the reliability of the  $K_s$  calibrated values could be verified (Figure 71). The experiment was repeated three times, which is subdivided between slug-in and slug-out, every test providing a single value of hydraulic conductivity. The groundwater level ranges from -141.9 cm to -92.5 cm in three slug test attempts. It was noticed an uneven recovering of the groundwater level to the original static level equal to -113 cm, either for the slug insertion or removal in the well. Accordingly, the hydraulic conductivity was differently estimated, overall varying from  $1.18 \times 10^{-4}$  to  $6.96 \times 10^{-4} \text{ m s}^{-1}$ , with mean and standard deviation of  $4.68 \times 10^{-4}$  and  $2.18 \times 10^{-4} \text{ m s}^{-1}$ , respectively. Thereby, since the  $K_s$  parameter values inferred by modelling do fit in the slug test interval, as well as the literature regular range for sand soils (NRCS, 2019), it is assumed that the parameters of the soil hydraulic properties were coherently calibrated from CRNS and TDR datasets.

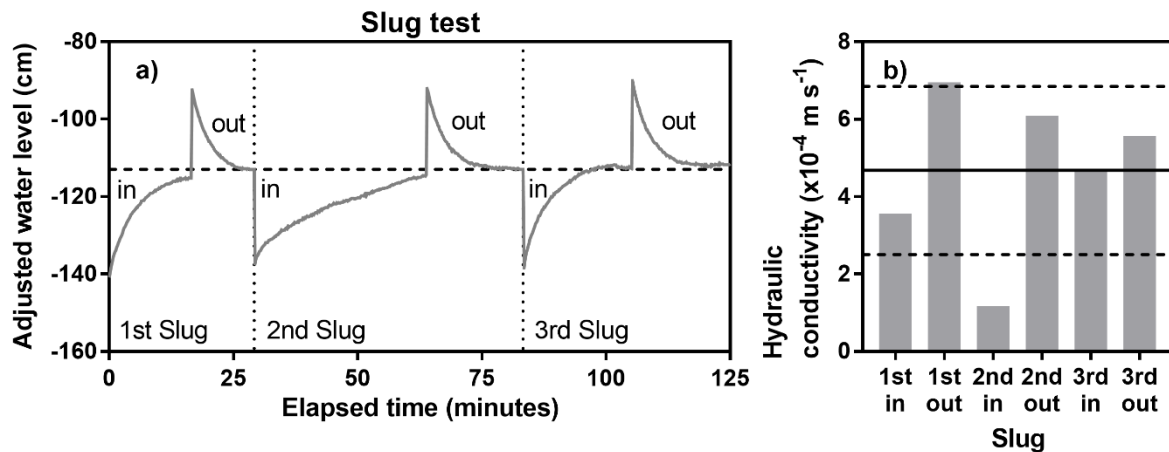


Figure 71 – Slug tests carried out to determine the (a) adjusted water level time series for estimating the (b) hydraulic conductivity over GEB. GEB: Guaraíra experimental basin. Dashed line in (a): static water level; Solid line: mean; Dashed line in (b): mean  $\pm$  standard deviation.

#### 5.2.4 Soil moisture simulation and validation

The soil moisture time series obtained by the curves of the soil hydraulic properties were plotted against the CRNS and TDR datasets, to assess the goodness-of-fit of the calibration. In site 5, the soil moisture was simulated at TDR monitoring depths, namely -5, -20 and -40 cm, for the two hydrological years (Figure 72). Overall, it is noticed that the simulated time series responded fairly well to mostly rainfall events, as well as exhibited a proper recession curve during the dry season. As a result, the scatter plot showed reasonable goodness-of-fit, depicted by KGE and  $R^2$  equal to 75% and 62% at -5 cm, 82% and 69% at -20 cm, and 70% and 64% at -40 cm, considering the daily data resolution. Conversely, by comparing the mean values in 2017-2018 and 2018-2019, the simulated data deviated from the observed ones in -10.88% and -12.25% at -5 cm, 11.36% and -1.00% at -20 cm, and 30.76% and -16.34% at -40 cm, showing that the deeper the more variable the relative mean differences were. Such behaviour stemmed likely from the uncertainty caused by the great sensibility of TDR data to capillarity rise influence (Hird and Bolton, 2017), which resulted on a linear regression deviation from the 1:1 perfect line at -40 cm, differently from the -5 and -20 cm. Nonetheless, those differences did not affect relevantly the aforementioned statistic metrics, suggesting that the soil moisture was realistically well simulated by the model.

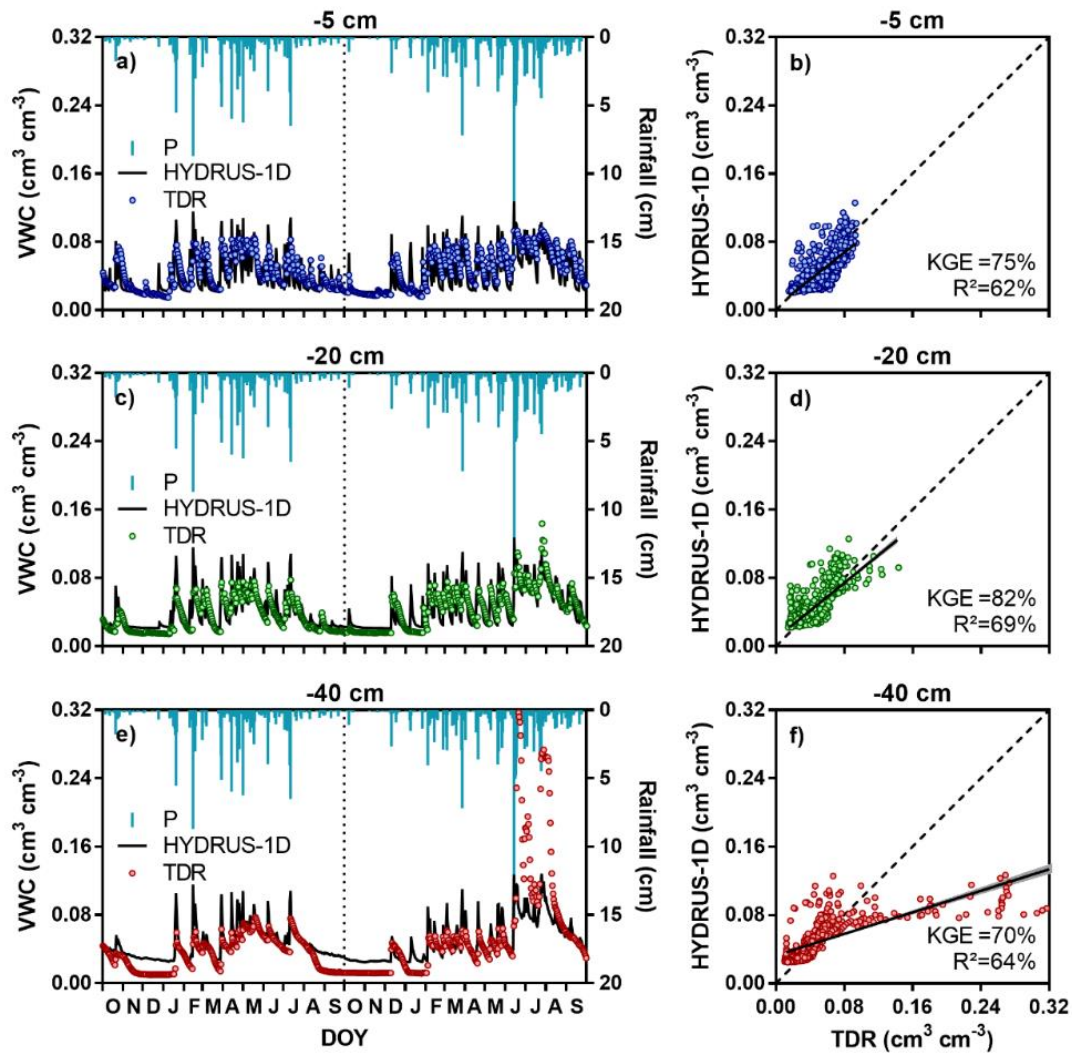
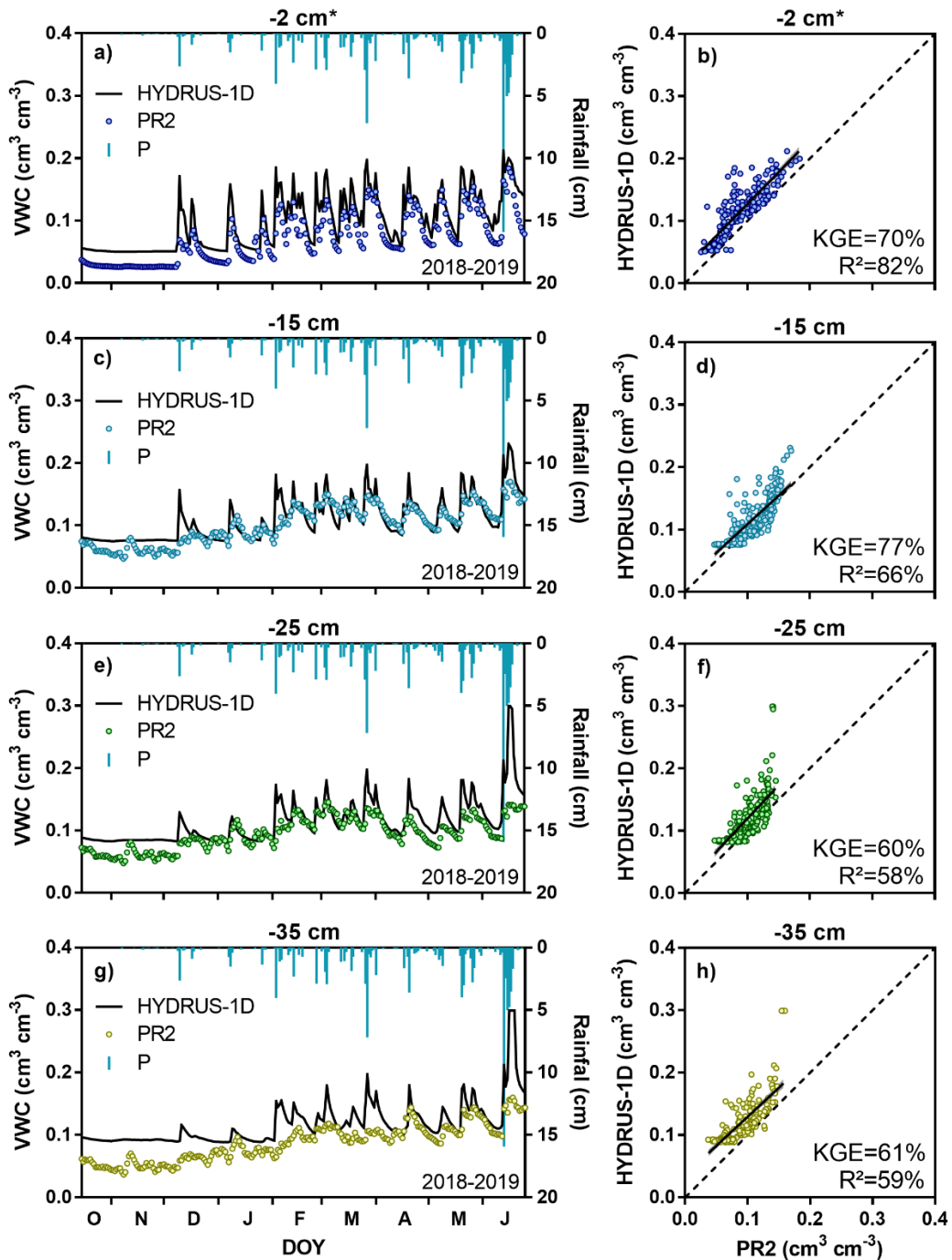


Figure 72 – Soil moisture time series simulated by HYDRUS-1D using the soil hydraulic properties curves plotted against the TDR datasets at the depths of (a, b) -5 cm, (c, d) -20 cm, and (e, f) -40 cm.

In site 2, the soil moisture was simulated at DL6-4 mean monitoring depths, namely -2, -15, -25, -35, -55 and -95 cm, from October 15th, 2018, to June 25th, 2019 (Figure 73). The first depth was adopted as -2 instead of -5 cm to cope with the air-entry account of -2 cm, which seems appropriate due to the higher organic water equivalent immediately below the soil surface. Overall, it is noticed that the simulated time series responded relatively well to rainfall events at the shallow depths, where the CRNS neutron assimilation is higher. Accordingly, the scatter plot pointed out reasonable KGE and  $R^2$  values of 70% and 82% at -2 cm, and 77% and 66% at -15 cm. Furthermore, at the subsequent depths of -25 and -35 cm, the linear regressions stood not far from the 1:1 perfect line, similar to shallow depths, although the KGE and  $R^2$  values stood around 60%. Lastly, at the deeper layers of -55 and -95 cm, the simulated time series tended to be less sensitive to rainfall events, but the mean relative differences deviated in only 8.97% and -1.81%, respectively, a satisfactory result if

compared to 8.02% at -15 cm. It is worthwhile mentioning that the PR2 profile probes showed a high daily sensitivity under the GEB soil condition, which may have been influenced by the installation procedure and hampered by using the standard calibration curve. Nonetheless, despite these uncertainties, the previously-discussed results showed that CRNS-based simulations were able to reflect satisfactorily well the main soil moisture responses to the rainfall events along the soil profile.



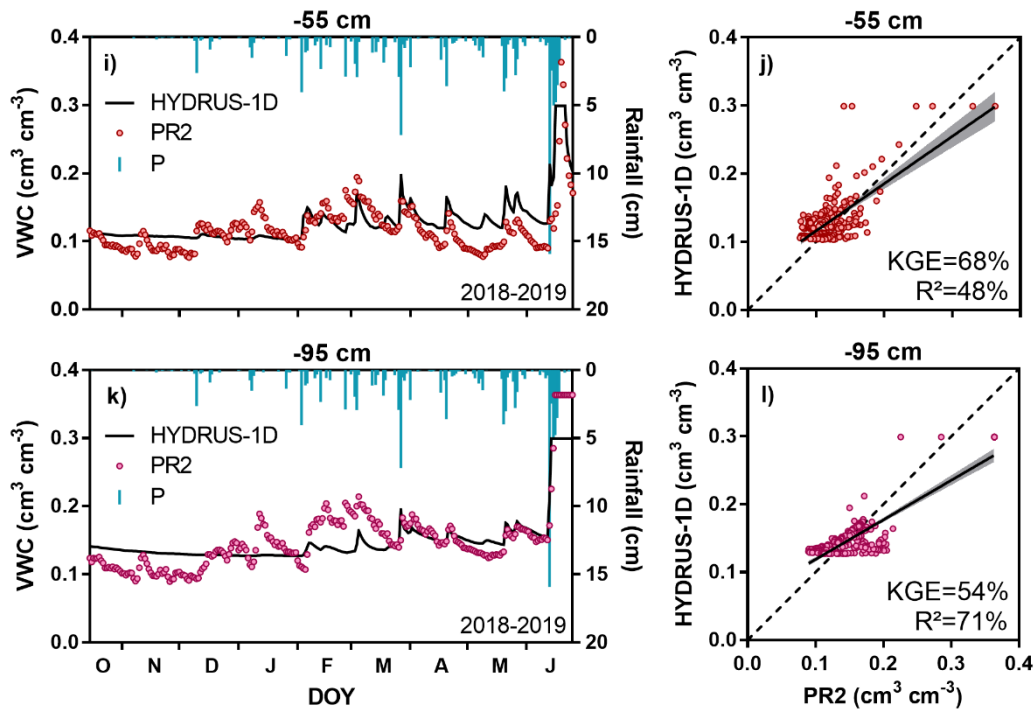


Figure 73 – Soil moisture time series simulated by HYDRUS-1D, by using the soil hydraulic properties curves obtained by CRNS data, plotted against the PR2 profile probe data at the depths of (a, b) -2 cm, (c, d) -15 cm, (e, f) -25 cm, (g, h) -35 cm, (i, j) -55 cm, and (k, l) -95 cm. \*Calculated at -2 cm due to air-entry of -2 cm and soil organic matter.

### 5.2.5 Root Water Uptake and cumulative fluxes

Root water uptake (RWU) was set at the model due to its important role in soil water removal, affecting remarkably the water flux along the soil profile. For GEB, a set of parameters was tested by trial-and-error, and lastly a conservative parameterization was adopted (see item 4.5.3.4). Nevertheless, the Electrical Conductivity (EC) data from two salinity events revealed a very salty aspect of GEB groundwater (Figure 74). In 2018, a prominent peak of EC equal to  $13.84 \text{ dS m}^{-1}$  on May 08th, 2018, was observed at the end of the rainy season, which was lagged from the groundwater peak of -87.22 cm, suggesting the particle travel time towards groundwater table of 24 days. In 2019, however, the salinity event started at the beginning of the rainy season, with no prevailing peak, but with salinity averaging on  $4.93 \text{ dS m}^{-1}$  during the analysis period, practically at the very salty limit of  $5.00 \text{ dS m}^{-1}$  (DPIRD, 2019). It is also noticed that EC was inversely proportional to groundwater level (reaching up to -25.36 cm) but directly proportional to water temperature (reaching down to  $25.47^\circ\text{C}$ ). These saline characteristics resulted from the evapotranspiration and soil podsolization processes, which, respectively, accumulated the salts on the soil surface and, then, leached them towards the groundwater table. This cycle of saline matter subjected the



vegetation under a stress condition, increasing the RWU by osmosis. Despite the saline stress, the sparse distribution and diversity of vegetation species in GEB led to high uncertainties about the proper model parameterization, reason why the RWU was simulated for a more conservative scenario.

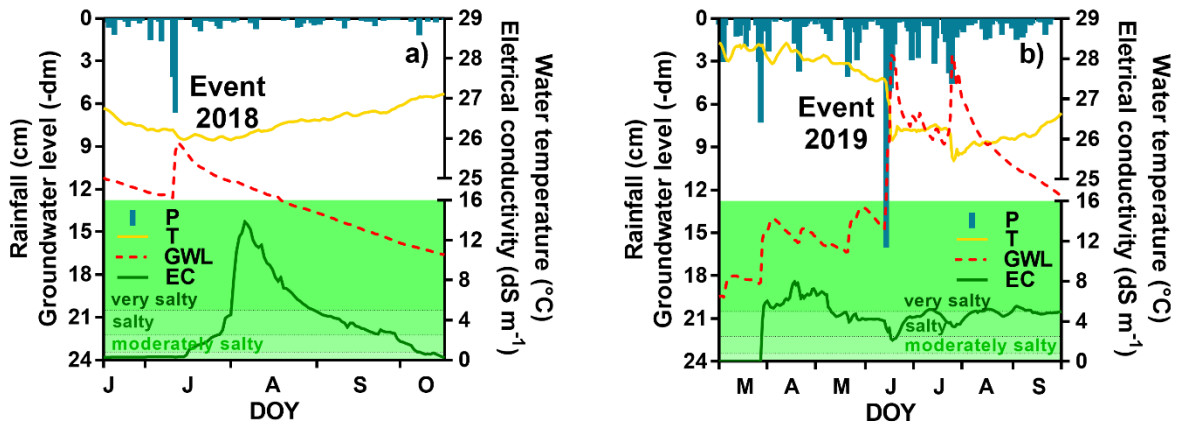


Figure 74 – Two salinity events over GEB occurred in (a) 2018 and (b) 2019, according to DPIRD (2019). P: rainfall; T: water temperature; GWL: Groundwater Level; EC: Electrical Conductivity.

The time series of hydraulic head and actual RWU were calculated along the root zone at TDR and CRNS sites (Figure 75). Overall, it is shown that hydraulic head tends to null values during the rainy season, and to negative values during the dry period. In 2017-2018 hydrological year, it varied from -1,490 to -18.1 cm at CRNS site and from -1,630 to -38.5 cm at TDR site, with monthly mean values of -476.18 and -495.83 cm, respectively. In 2018-2019 hydrological year, in turn, it varied from -1690 to -10.8 cm at CRNS site and from -1,990 to -33.5 cm at TDR site, with monthly mean values of -520.02 and -518.60 cm, respectively. The average hydraulic head was lower in the rainiest hydrological year because it encompassed a dry season with a smaller rainfall depth, along which the TDR site reached lower values than CRNS site. As a result, there was an influence on actual RWU values during dry seasons, in which the TDR site experienced a lower recession than CRNS site, whereas the actual RWU responded similarly to rainfall events at both TDR and CRNS sites during the rainy season. In 2017-2018 hydrological year, it reached up to 0.55 cm d<sup>-1</sup> at CRNS site and up to 0.50 cm d<sup>-1</sup> at TDR site, with monthly mean values of 0.25 and 0.20 cm d<sup>-1</sup>, respectively. In 2018-2019 hydrological year, in turn, it reached up to 0.67 cm d<sup>-1</sup> at CRNS site and up to 0.58 cm d<sup>-1</sup> at TDR site, with monthly mean values of 0.22 and 0.19 cm d<sup>-1</sup>, respectively. The actual RWU was slightly lower in the rainiest hydrological year, which was likely influenced by the shorter inter-event time between rainfall events, leading to an ample RWU oscillation during the rainy season compared to the prior year. These

behaviours may have an important influence on the magnitude and direction of water fluxes at both TDR and CRNS sites along the studied hydrological years.

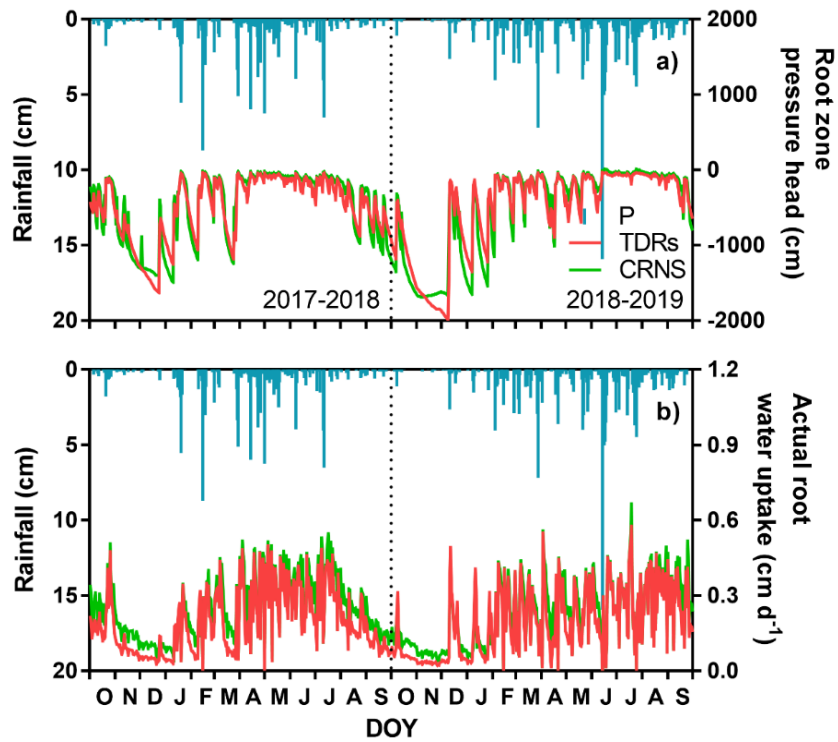


Figure 75 – Time series of (a) root zone pressure head and (b) actual root water uptake ( $RWU_a$ ), at TDR and CRNS sites. P: rainfall.

### 5.2.6 Groundwater Recharge and cumulative water fluxes

The main components of soil water removal were calculated and accumulated for CRNS and TDR sites along the two hydrological years (Figure 76). It is worthwhile to mention that no surface runoff (i.e.  $Q$ ) was obtained by adopting the surface water layer equal to 5 cm after *in situ* observations (see item 4.5.3.6). Actual RWU (i.e.  $RWU_a$ ) represents a percentage of potential RWU (i.e.  $RWU_p$ ), which refers to potential transpiration (i.e.  $T_p$ ) minus interception (i.e.  $I$ ). In addition, actual surface flux (i.e.  $S_a$ ) comes to infiltration (i.e.  $Inf$ ) minus actual evaporation (i.e.  $E_a$ ), which is a percentage of potential surface flux (i.e.  $S_p$ ), referring to infiltration (i.e.  $Inf$ ) minus potential evaporation (i.e.  $E_p$ ).

The actual outward water fluxes represented by  $RWU_a$  and  $E_a$ , and the actual inward water fluxes represented by  $S_a$ , were accumulated to compute the annual absolute and relative values. The relative values refer to actual-potential ratios, calculated for  $E_p$  equal to 32.3 and 36.5  $\text{cm yr}^{-1}$ , and  $T_p$  equal to 148.83 and 143.70  $\text{cm yr}^{-1}$  in 2017-2018 and 2018-2019, respectively, as well as for  $S_p$  equal to -81.1 and -113.0  $\text{cm yr}^{-1}$  obtained from



infiltration equal to  $-113$  and  $-149$   $\text{cm yr}^{-1}$ , respectively. The infiltration corresponded to  $90.7\%$  ( $-113.38$   $\text{cm yr}^{-1}$ ) and  $92.2\%$  ( $-149.02$   $\text{cm yr}^{-1}$ ) of the rainfall depth in 2017-2018 and 2018-2019 years, respectively. Interestingly, the larger rainfall depth in 2018-2019 increased the infiltration in  $36$   $\text{cm yr}^{-1}$  ( $31.9\%$ ), but decreased the  $T_p$  in  $5.13$   $\text{cm yr}^{-1}$  ( $3.4\%$ ), which was likely due to slightly decline on net radiation and relative humidity time series (see Supplementary Figure 19). Furthermore, the  $RWU_a$  held  $90.1$  ( $66\%$ ) and  $81.9$   $\text{cm yr}^{-1}$  ( $62\%$ ) at CRNS site, and  $73.3$  ( $53\%$ ). and  $72.5$   $\text{cm yr}^{-1}$  ( $55\%$ ) at TDR site, whereas the  $E_a$  held  $21.6$  ( $63\%$ ) and  $22.0$   $\text{cm yr}^{-1}$  ( $62\%$ ) at CRNS site, and  $14.4$  ( $44\%$ ) and  $15.9$   $\text{cm yr}^{-1}$  ( $44\%$ ) at TDR site. Overall, the relative values showed negligible percentage differences between the dry and rainy hydrological year, but relevant differences between sites, once the CRNS site stood higher than TDR site for the:  $RWU_a$  on  $13\%$ , and  $E_a$  on  $19\%$  in 2017-2018, and;  $RWU_a$  on  $7\%$ , and  $E_a$  on  $18\%$  in 2018-2019. On the other hand, the  $S_a$  held  $-91.8$  ( $88\%$ ) and  $-127.0$   $\text{cm yr}^{-1}$  ( $89\%$ ) at CRNS site, and  $-99.0$  ( $82\%$ ). and  $-133.0$   $\text{cm yr}^{-1}$  ( $85\%$ ) at TDR site. The actual surface flux results at both locations showed similar water movement on soil surface, likely not affected by the different soil hydraulic properties and groundwater table capillarity rise.

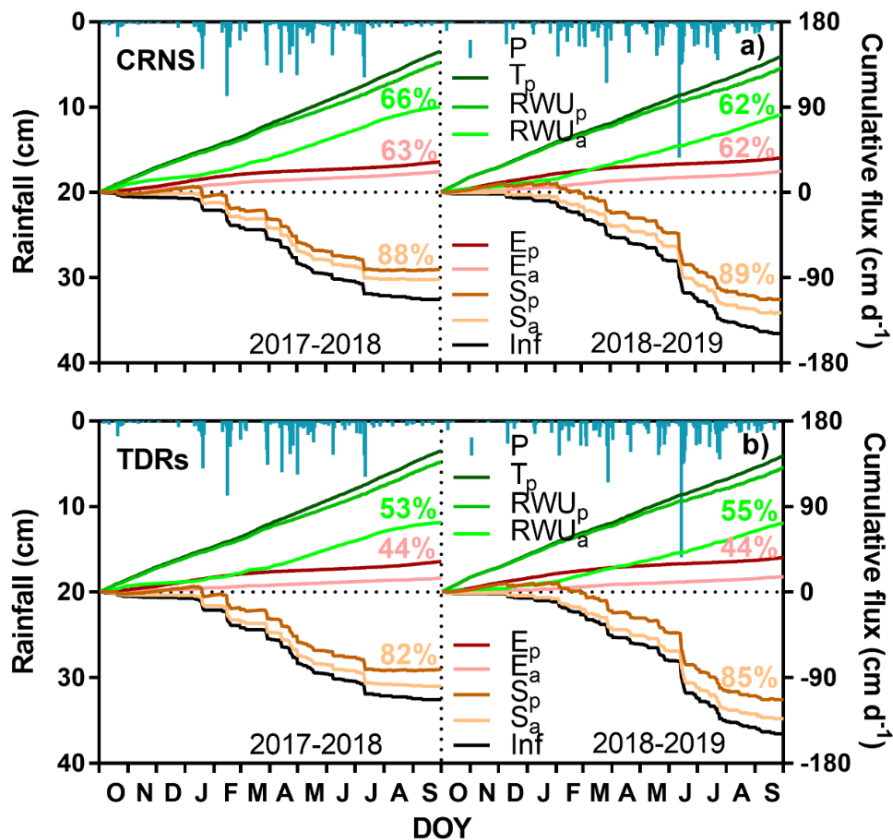


Figure 76 – Cumulative outward (positive) and inward (negative) water fluxes at (a) CRNS and (b) TDR sites in 2017-2018 and 2018-2019 hydrological years. P: rainfall;  $T_p$ : potential transpiration;  $RWU_p$ : Potential Root Water Uptake;  $RWU_a$ : Actual Root Water Uptake;  $E_p$ : potential evaporation;  $E_a$ : actual evaporation;  $S_p$ : potential surface flux;  $S_a$ : actual surface flux; Inf: infiltration.

Finally, the GWR (or simply R) at the variable bottom boundary, as well as the percolation water flux at -20, -30, -40, -60 and -100 cm soil depths, were calculated and accumulated along the two hydrological years (Figure 77). By analysing the vertical water percolation fluxes, it is possible to notice the influence of RWU along the root zone, which reduced the water flux down to -60 cm depth to -26.46 (21% of rainfall) and -61.07 cm yr<sup>-1</sup> (38%) at CRNS site, and to -47.09 (38%) and -77.93 cm yr<sup>-1</sup> (48%) at TDR sites in 2017-2018 and 2018-2019, respectively. In relation to infiltration, the water percolation corresponded to 23% and 41% at CRNS site, and to 42% and 52% at TDRs, in 2017-2018 and 2018-2019, respectively.

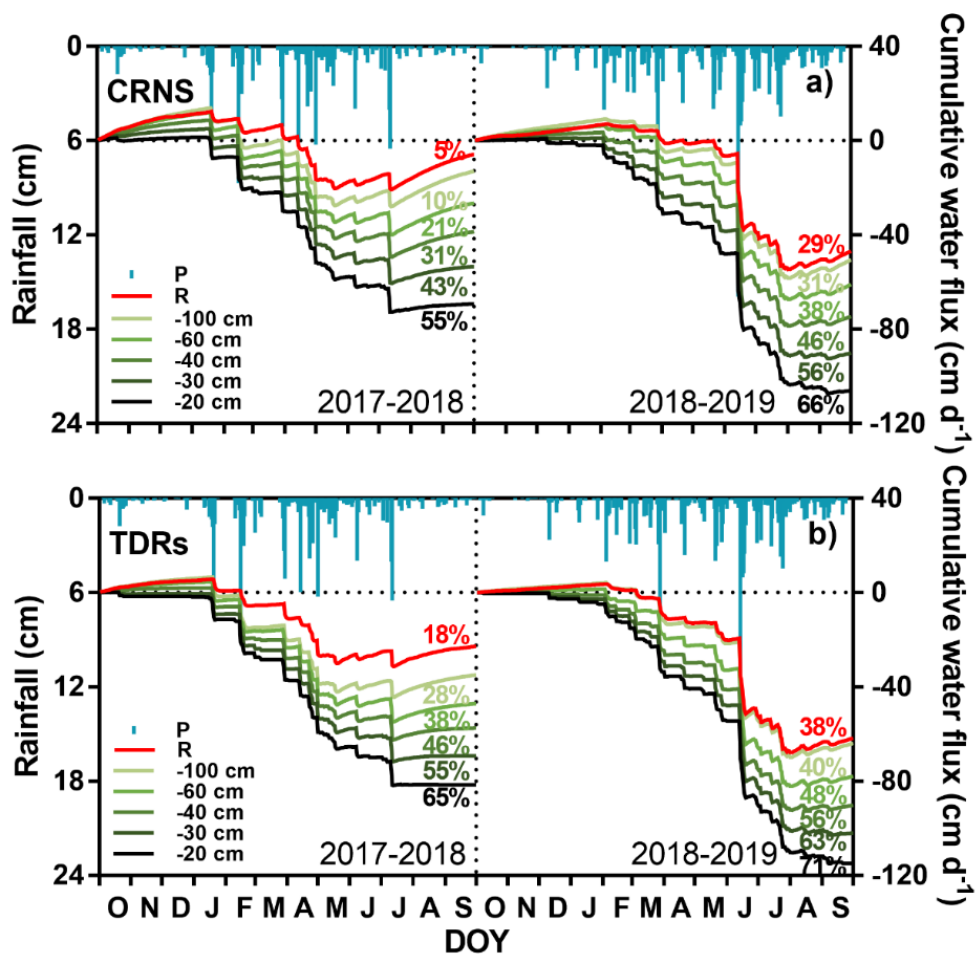


Figure 77 – Cumulative groundwater recharge (R) and percolation water flux and at -20, -30, -40, -60 and -100 cm soil depths at (a) CRNS and (b) TDR sites in 2017-2018 and 2018-2019 hydrological years. P: Rainfall.

Concerning the GWR rates, the downward water fluxes were overall greater in 2017-2018 than in 2018-2019, and at TDR site than at CRNS site. The CRNS site held -5.87 (5%) and -46.9 cm yr<sup>-1</sup> (29%) in 2017-2018 and 2018-2019, respectively, whereas the TDR site held -22.80 (18%) and -61.81 cm yr<sup>-1</sup> (38%), respectively. In relation to infiltration, the

recharge corresponded to 5% and 31% at CRNS site, and to 20% and 41% at TDR site, in 2017-2018 and 2018-2019, respectively. On average, the recharge stood on  $-26.39 \text{ cm yr}^{-1}$  (17% of the rainfall) at CRNS site, and  $-46.31 \text{ cm yr}^{-1}$  (28% of the mean rainfall) at TDR site, showing that at downstream of GEB the recharge rate stood 75.48% higher than at upstream portion. This difference stemmed likely from the changing on soil hydraulic properties at the vicinity of the Podzol-Acrisol soil type transition, wherein the groundwater level is deeper. On the other hand, the relative recharge at CRNS site (17%), the most representative site on GEB (Barbosa et al., 2019), was close to remote sensing estimation over Podzol soil type averaged on 17.87% (see item 5.1.4).

The GWR estimates were verified using the WTF-MRC-RISE approach, which applies a fixed time interval (daily in this study) on the WTF method to estimate episodic recharge (see item 4.6.4). In this study, one Master Recession Curve (MRC) for each sites was obtained by a linear regression equation along the longer available groundwater recession period (Figure 78). The master recession curves were fairly similar between the study sites, holding the slope of  $-0.6704$  at CRNS site and the slope of  $-0.7018$  at TDR site. Such difference is likely due to different depths to groundwater table, as well as to different values of the soil hydraulic properties.

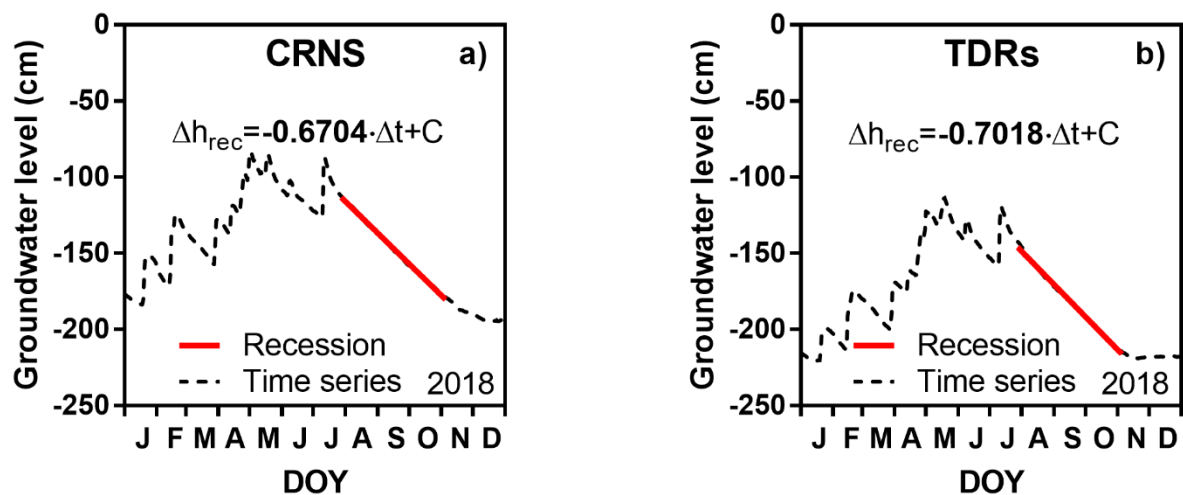


Figure 78 – Master Recession Curves (MRC) obtained by linear regression equation along the longer available groundwater recession period at (a) CRNS and (b) TDR sites.  $\Delta h_{rec}$ : potential groundwater decline;  $\Delta t$ : daily time interval; C: constant relative to the time of recharge event occurrence.

The GWR events expressed by the daily negative water flux were obtained by HYDRUS-1D and WTF simulations and accumulated along the two hydrological years for validation purposes (Figure 79). The WTF-MRC-RISE approach calculated the downward water fluxes using the specific yield (i.e.  $S_y$ ) equal to 0.10, 0.16 and 0.24, obtained by

production tests in surrounding areas (see item 5.1.4). At CRNS site, the estimations held a reasonable goodness-of-fit for both 2017-2018 and 2018-2019 years, as KGE was equal to 83% and 79%, respectively, by using only one value of  $S_y$  equal to 0.16. On the other hand, by using the same  $S_y$  value, the estimations at TDR site held a reasonable goodness-of-fit in 2017-2018 but not in 2018-2019, once the KGE was equal to 78% and 36%. Conversely, for  $S_y$  equal to 0.24 the TDR site found a high goodness-of-fit of KGE equal to 84%. These results showed a more reliable performance at CRNS site than at TDR site for estimating the GWR in the shallow groundwater system of GEB. Nevertheless, it is worthwhile to mention that the specific yield may vary significantly along the soil profile influenced by the depth to groundwater table (Dettmann and Bechtold, 2016). Lastly, the results demonstrate the reliability and suitability of using the CRNS dataset for modelling inversely the soil hydraulic properties and, in turn, simulating the unidimensional groundwater flux.

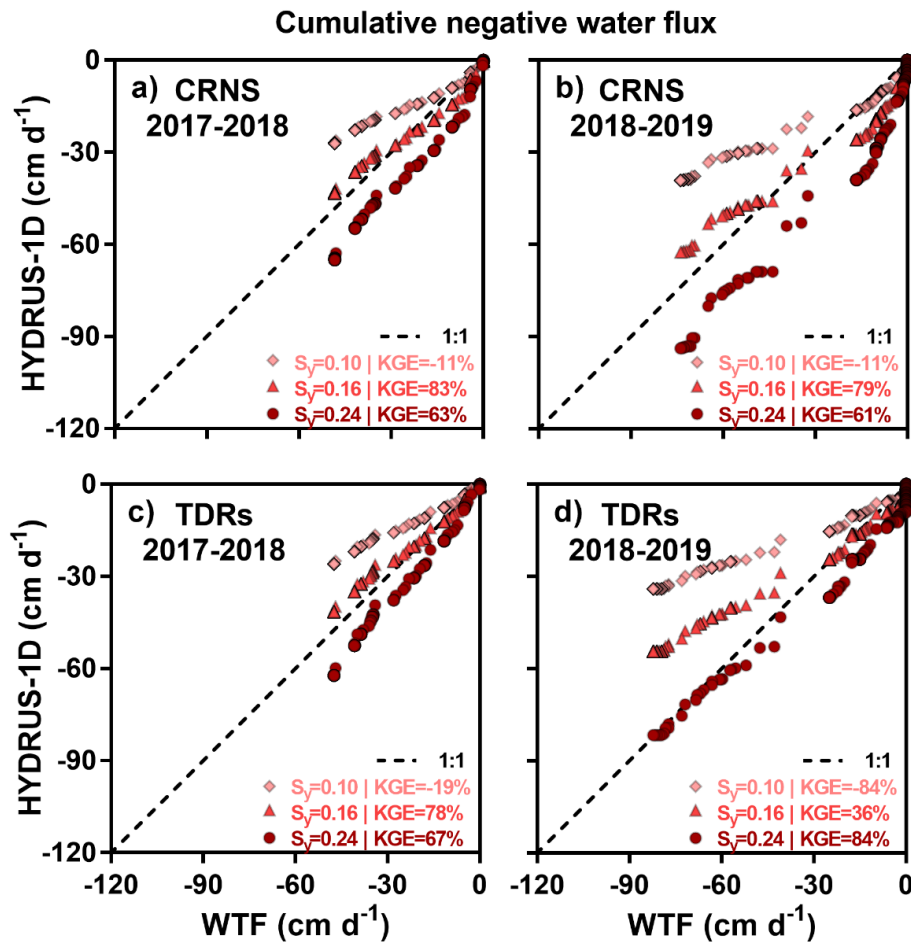


Figure 79 – Validation of groundwater recharge rates simulated by HYDRUS-1D through the comparison between the cumulative negative water fluxes obtained by WTF method, for specific yield ( $S_y$ ) equal to 0.10, 0.16 and 0.24, at (a, b) CRNS and (c, d) TDR sites in 2017-2018 and 2018-2019 years, respectively.

## 6 DISCUSSION

### 6.1 Distributed Groundwater Recharge estimated by an enhanced GIS-based water balance model

In this study, the satellite-based data inputted into the water budget equation for estimating the hydro(geo)logical responses was the precipitation based on a GPM IMERG V05B satellite product. This product was selected due to its very good performance over most of Brazil, in spite of its considerable bias on coastal area (Gadelha et al., 2019), which required a data correction for GWR estimation. For such a purpose, some studies have at least recommended performing the bias correction on IMERG products (Salles et al., 2019; Turini, Thies and Bendix, 2019; Yuan et al., 2018) and others have successfully applied it already to improve the IMERG data quality (Sun et al., 2018; Wang et al., 2019a). After the grid-box correction and resampling of IMERG data, the so-called IMERG\* displayed an acceptable monthly performance according to Salles et al. (2019), once the CC, PBIAS and RRMSE were equal to 99%, -9% and 15%, respectively. In other words, IMERG\* slightly underestimates the ground-based mean interpolated results, so-called Gauge, similar to literature results (Sateg  et al., 2017; Sharifi, Steinacker and Saghafian, 2016; Yuan et al., 2017), with a good monthly correlation in JPA CSA, also found in the literature (Tan and Duan, 2017; Wang et al., 2019c; Xu, Shen and Niu, 2019; Yang et al., 2019a). According to Tang et al. (2016), this behaviour may occur due to the better performance of IMERG over sub-regions with mild/wet climate and mid-/low-latitudes.

The IMERG\* yielded mean error values within the reviewed range either before or after the bias correction (Sharifi, Steinacker and Saghafian, 2016; Yuan et al., 2017). The high errors before the data correction (RRMSE equal to 59%) were likely due to poor sensitivity of IMERG to light precipitation events, similar to the RRMSE of 58% obtained by Wei et al. (2018). On the other hand, the high underestimation before the data correction (PBIAS equal to -40%), also found by Yuan et al. (2017), was likely caused by warm-rain process-dominated systems forced by topography, which is not well-detected by the passive microwave sensors (Gadelha et al., 2019; Palharini and Vila, 2017; Rozante et al., 2018). Nevertheless, both Gauge- and IMERG\*-based data were able to depict the annual decreasing precipitation gradients from East to West toward the basin headboard, which is the prevailing behaviour reported over JPA CSA (Cabral da Silva et al., 2000a). Thereby, after the pixel resampling and bias correction, the IMERG\* product better depicted the

spatial distribution of precipitation over JPA CSA, allowing for use it as input data in the water budget equation for simulating the hydro(geo)logical responses.

The actual evapotranspiration was the first water-loss component analysed in JPA CSA. It was estimated on a distributed scale through an adapted MOD16 algorithm (Gusmão, 2017; Mu et al., 2007; Mu, Zhao and Running, 2011; Teixeira et al., 2014, 2013) based on the Penman-Monteith equation (Allen et al., 1998), using GLDAS reanalysis data rather than point-based meteorological data. Its spatiotemporal variability pattern was assessed over distinct land uses/covers under different temporal resolutions. The results highlighted a large difference in the evapotranspiration estimates between urban and rural areas because of the anthropologic pressure causing soil sealing. The daily actual evapotranspiration varied from 1.00 to 4.70 mm d<sup>-1</sup> over JPA CSA (in Atlantic Forest biome), within the range of Brazilian biomes: 1.00-5.80 in Pampas Lowlands; 1.63-6.22 mm d<sup>-1</sup> in Xeric Shrubland, 2.28-5.67 mm d<sup>-1</sup> in Atlantic Forest, 2.50-6.6 mm d<sup>-1</sup> in Neotropical Savannah; 3.30-10.00 mm d<sup>-1</sup> in Amazon; 4.00-5.50 mm d<sup>-1</sup> in Pantanal Wetland (Andrade et al., 2012; Mendonça et al., 2012; de Oliveira et al., 2018a; Paca et al., 2019; Silva; Silva; Santos, 2019; Souza et al., 2019). In Atlantic Forest, the mean annual and monthly actual evapotranspiration over JPA CSA stood on 1,207.65 mm yr<sup>-1</sup> (79.93% of precipitation) and ranged from 72.81 to 118.64 mm month<sup>-1</sup>, respectively.

The evapotranspiration results were relatively similar to ones found in São Paulo state, covered mostly by Atlantic Forest, whose annual mean value stood on 1,248 mm yr<sup>-1</sup> and the monthly results ranged from 26.1 to 116.8 mm month<sup>-1</sup> (de Oliveira et al., 2016b). In addition, another study nearby the Brazil-Argentina-Paraguay triple border, also covered by Atlantic Forest, found the MOD16 evapotranspiration ranging from 1,161 to 1,389 mm yr<sup>-1</sup> across native Atlantic Forest and tree plantations from remote sensing data (Cristiano et al., 2015). The monthly evapotranspiration estimates in Atlantic Forest were less variable than in Neotropical Savannah and Amazon biomes, which ranged roughly from 19 to 140 mm month<sup>-1</sup>, and from 50 to 140 mm month<sup>-1</sup>, respectively (de Oliveira et al., 2018a; Ruhoff et al., 2013). In this sense, Templeton et al. (2014) found that distributed input measurements (such as reanalysis data) led to an improvement in estimating evapotranspiration (~7% reduction in error), compared to the single station data (~40% reduction in error). Although no straightforward validation of this evapotranspiration estimates could have been performed in this study, its performance was verified against the ground-based reference evapotranspiration. Overall, the difference between potential and actual evapotranspiration was higher in dry season than in rainy season, similarly to Coelho et al. (2017) and Oliveira

et al. (2018), due to high net radiation at the expenses of low rainwater availability along the dry season, and the opposite during the rainy season. It can be inferred, therefore, that the actual evapotranspiration calculated by the adapted MOD16 algorithm was well-estimated over JPA CSA, as it was able to depict the meteorological effects over evapotranspiration.

The soil water storage changes were calculated from soil moisture data assimilated by SPL4SMAU satellite product down to the 1-m root zone. The SMAP was selected due to its better performance compared to other satellites, as validated by CRNS networks (Duygu and Akyürek, 2019; Montzka et al., 2017). Moreover, SPL4SMAU root-zone product was validated in 17 watersheds, meeting the accuracy requirements such as unbiased RMSE lower than  $0.04 \text{ m}^3 \text{ m}^{-3}$ , under a greater variety of climate and land cover conditions (Reichle et al., 2017). Applying the SMAP to calculate in root zone, annual declines of soil water storage changes were obtained both in dry (2016) and moderately-rainy (2017) years, showing the high susceptibility of JPA CSA to water shortage. Similarly, Zhang (2018) found that the surface soil water storage changes decreased constantly by an average rate of  $-4 \text{ mm yr}^{-1}$  from 2009 to 2017 in four regions of the semiarid of the Northeast of Brazil. The urbanization process and precipitation deficit are likely the more important factors impacting the decline of the soil water storage changes, whose tendency may alter between positive and negative along the decades (Chen et al., 2018). This represents a critical scenario due to the recent intensification of drought events not seen in several decades in the Northeast of Brazil, which affects mainly the rural areas for not being yet adapted for mitigating such hazards (Marengo, Alves and Alvala, 2018; Marengo, Torres and Alves, 2016). Using SMAP to assess the soil water storage changes was similarly performed by Bai et al. (2018), who proposed a Soil Water Deficit Index (SWDI) derived from SMAP dataset for monitoring the agricultural drought, showing a relatively good performance over a transition zone between humid and semiarid climates, similarly to JPA CSA condition.

The surface runoff was the water-loss component that yielded the lowest hydrological output in JPA CSA. It was estimated on a distributed scale through the adapted NRCS–CN method on a daily basis for initial abstraction ratio equal to 0.03 and for recalculated Curve Numbers (Lal et al., 2016; Lal, Mishra and Kumar, 2019). The mean annual surface runoff over JPA CSA along the study period was roughly 14.54% (219.21 mm) of precipitation, close to mean value of 11.85% (141.86 mm) from the plot-scale runoff compiled data over Brazil (Anache et al., 2017). In Atlantic Forest biome of Brazil, the hydrological response was simulated by applying AnnAGNPS model, which use the NRCS–CN method for runoff calculations, reporting similarly a mean value of 14.82% for a sample of 11 erosive events



along three years (Zema et al., 2018). In Pernambuco, neighbour state to Paraíba, a mean surface runoff of ~15% over the bare soil coverage was found by plot-scale studies (Montenegro et al., 2019). On the other hand, still in the Northeast of Brazil, Coelho et al. (2017) found a surface runoff equal to 28.62% of the precipitation depth over a alluvial basin, nearly 2 times the estimation over JPA CSA, likely because the former area was encompassed mostly by HSG type C, and the latter by HSG type B, according to Sartori et al. (2005) and NRCS (1986). Thereby, using globally-gridded HSG, such as HYSOGs250m (Ross et al., 2018), for CN-based runoff modelling, may not suit to regional soil characteristics. Furthermore, IMERG\* provided higher and more plausible runoff estimates than Gauge, similarly to Gilewski and Nawalany (2018), who claimed that the high degree of uncertainty stemmed from Gauge interpolated data may be higher than that caused by the low spatial resolution of IMERG. Similarly to Li et al. (2019), it may also be inferred that the soil imperviousness, together with the precipitation spatial distribution, are likely the more important conditions for runoff generation over JPA CSA, highlighted by the high estimates on urban area compared to other land uses/covers.

The GWR was the target water balance component investigated in this study in JPA CSA. Since it comes to a hard-working, directly-measured variable, the water budget equation was chosen because of its simplicity and widely-used indirect approach for estimating the distributed GWR compared to other techniques and methods (Ali and Mubarak, 2017; Martos-Rosillo et al., 2015; Ni et al., 2018; Singh et al., 2019; Thakur, Singh and Ekanthalu, 2016; Xu and Beekman, 2018). Overall, the proposed GIS-based model showed reasonable GWR rates in JPA CSA, whose estimates in the average rainy year (2017) ranged from 301.63 to 364.62 mm yr<sup>-1</sup>, similar to the 360 mm yr<sup>-1</sup> averaged on by semi-distributed hydrogeological modelling (Tsuyuguchi et al., 2018). Such results also showed a reasonable goodness-of-fit, namely CC and RRMSE ranging from 68% to 89%, and from 30% to 34%, respectively, and slight overestimation for Gauge (PBIAS varying from 8% to 11%) and slight underestimation for IMERG\* (PBIAS varying from -13% to -9%). The results showed a decreasing East-to-West recharge tendency mainly due to precipitation gradient, with the mean value of 18.27% (278.85 mm yr<sup>-1</sup>) of precipitation, which was 1.27 times higher than surface runoff and 0.23 times lower than evapotranspiration. Borges et al. (2017) found a similar mean annual value of 19.5% (333.83 mm yr<sup>-1</sup>) averaged on an Atlantic Forest study area composed of 6 out of 8 JPA CSA soil types. Rabelo and Wendland (2009) also found a mean annual value of 21.71% (297.6 mm yr<sup>-1</sup>) in a transition zone between Neotropical Savannah and Atlantic Forest biomes.

The annual relative recharge was also calculated by soil type and land use/cover in JPA CSA, obtaining similar mean values for the classes of the latter analysis (except for urban use) than those of the former, which displayed either high or low mean values. Regarding the land uses/covers, the mean annual relative recharge in JPA CSA was relatively close to global estimates reviewed by Mohan et al. (2018), showing very close mean values for bare soil, cropland (mosaic) and forest, whose difference was equal to 2.76%, -0.64% and -0.95%, respectively, and slightly higher differences of -6.74% and -7.18% for pasture and urban covers, respectively. Regarding the soil types, the Acrisols and Fluvisols encompass together 70.7% of JPA CSA, similarly to Cinzas and Laranjinhas river basins (Borges et al., 2017), whose mean annual recharges differed satisfactorily by only -5.70%. Comparing the relative recharge of Acrisol to another Atlantic Forest location (de Souza et al., 2019), a higher difference between the mean annual estimates of 9.63% was found, which, however, stemmed likely from the fairly higher evapotranspiration in JPA CSA. Finally, It can be then inferred that GWR was realistically well-estimated by the proposed GIS-based model, whose results backed up the considerable potential of GWR in the unconfined aquifer of JPA CSA.

## **6.2 Intermediary-scale Groundwater Recharge modelling coupled to soil hydraulic property inverse modelling**

The hourly neutron intensity measured by the CRNS probe was initially converted to volumetric water content through the standard calibration curve based on the  $N_0$  site-specific parameter (Desilets, Zreda and Ferré, 2010), equal to 550 neutron counts when using the weighting function (Köhli et al., 2015; Schrön et al., 2017), which included other hydrogen pools as well. Earlier, Baroni et al. (2018) had shown that CRNS performed well when lattice water and organic carbon water equivalents are added to soil moisture. Notably, GEB gathers most of unfavourable environmental conditions for CRNS operation, namely low altitude, low latitude, high air humidity, and high soil moisture conditions; the two latter reducing the penetration depth and horizontal footprint of neutron sensing (Köhli et al., 2015).

The CRNS time series smoothed by moving average to 24-hours showed a relatively high goodness-of-fit compared to weighted-mean soil moisture in 10-cm depth obtained from three soil profile probes, as the KGE and  $R^2$  were equal to 80% and 89%, respectively. Similar to GEB, Schrön et al. (2017) found that CRNS better performed in areas under the influence of shallow groundwater level rise when the weighting function was used, reaching

high values of KGE and CC metrics. Furthermore, such results showed that CRNS also can hold a good performance in tropical Podzol soil type, featured by sandy texture with sand content averaged on 96.38%, which are found in Amazon and Atlantic Forest biomes. Such Podzol soil types encompass the intermediate secondary-growth vegetation, which together with small fragments (lower than 100 ha), comprehend from 32% to 40% of the original cover of Atlantic Forest, remaining only from 11.4% to 16% (Ribeiro et al., 2009). Despite the high importance of Podzol for native vegetation conservation and water resource regulation and preservation, still little information about the soil hydraulic properties of this soil type is available in tropical regions (Cooper et al., 2017).

Despite the CRNS broad applicability on soil sciences, only few studies so far have employed its data in inverse modelling to improve the accuracy of the calibration of the soil hydraulic properties (Batz et al., 2017; Brunetti et al., 2019; Rivera Villarreyes, Baroni and Oswald, 2014). Brunetti et al. (2019) coupled externally the neutron operator COSMIC (Shuttleworth et al., 2013) with the HYDRUS-1D model, allowing for a confident estimation of the shape parameters  $\alpha$  and  $n$  from van Genuchten-Maulem model, in spite of certain uncertainty found on saturated hydraulic conductivity  $K_s$ . In the present study, the HYDRUS-1D-COSMIC coupled model was run with soil moisture time series of CRNS and TDR datasets to calibrate the curves of soil hydraulic properties at upstream and downstream of GEB. By using the CRNS data, the model was able to simulate the neutron intensity with a relatively high goodness-of-fit (KGE and  $R^2$  were equal to 89% and 79%, respectively), as well as to simulate satisfactorily well the soil moisture profiles. Similarly, Batz et al. (2017) and Shuttleworth et al. (2013) coupled COSMIC with land models for updating the estimates of the soil hydraulic properties and recalibrating the model, respectively, reducing the errors between the simulated and observed estimates of soil moisture and neutron intensity.

The aspect of both hydraulic conductivity and retention curves agreed reasonably with the results found in GEB through the Beerkan method (Santos, Silva and Silva, 2012; Silva, 2009). The Podzol soil types of GEB was susceptible to successive periods of water stress and flooding, as a consequence of high levels of hydraulic conductivity with low water retention. Thereby, the estimates of saturated hydraulic conductivity varied over GEB, holding  $1.26 \times 10^{-4} \text{ m s}^{-1}$  at upstream and  $6.47 \times 10^{-4} \text{ m s}^{-1}$  at downstream locations. Such results were likely due to combination of sandy texture and shallow groundwater table at the CRNS site, leading to higher estimates than the range obtained by Podzol in Ilha do Cardoso state park, which varied from  $10^{-5}$  to  $10^{-7}$  (Ribeiro et al., 2009), and the mean value of  $2.15 \times 10^{-5} \text{ m s}^{-1}$  obtained by Rosetta Lite software from Podzol hydrophysical data provided

by HYBRAS (Hydrophysical Database for Brazilian Soils) database (Ottoni et al., 2018). Nonetheless, the estimates of soil hydraulic properties based on inverse modelling were within the range determined by slug tests in GEB, which varied from  $1.18 \times 10^{-4}$  to  $6.96 \times 10^{-4}$   $\text{m s}^{-1}$ , being within the range for porous media with high permeability, varying from  $10^{-4}$  to  $10^{-5}$  (Reynolds and Canada, 1986).

The HYDRUS-1D model was also used to simulate the root water uptake and percolation water flux along the root zone as well as the GWR rate obtained at the variable bottom boundary, both on daily scale, to avoid the bias caused by temporal averaging of meteorological data on higher temporal resolutions (Batalha et al., 2018). Thereby, the main cumulative water fluxes were simulated to assess the root distribution effects on the hydrogeological processes of GEB. On average, the vertical water percolation reduction due to root water uptake ranged from ~32% (CRNS) to ~47% (TDRs) of infiltration, in agreement with recent findings claiming that uniformly-distributed rooting in the unsaturated zone may halve the GWR rates (Grimaldi, Orellana and Daly, 2015). Moreover, the relative recharge upstream of GEB ranged from 5% to 29%, whereas at downstream of GEB the recharge ranged from 18% to 38%, for the dry and average hydrological years, respectively, showing the influence of the curves of the soil hydraulic properties and the groundwater depth on the predictions. The relative recharge on the average rainy year was within the range of a typical Podzol reported from Belgium, which spatially varied from 27% ( $226 \text{ mm yr}^{-1}$ ) to 47% ( $392 \text{ mm yr}^{-1}$ ) of precipitation, with mean value of 29% ( $242 \text{ mm yr}^{-1}$ ) (Dams et al., 2009; Leterme, Gedeon and Jacques, 2013). Šimůnek (2015) found GWR rates equal to ~39.5% ( $\sim 350 \text{ mm yr}^{-1}$ ) in a dry Podzol simulated by HYDRUS-1D.

The GWR estimates were then validated by WTF-MRC-RISE approach, showing a reasonable goodness-of-fit at both CRNS and TDR datasets. The latter, however, showed different specific yield values between the dry and rainy years. This likely occurred because of the remarkable variability of the apparent specific yield in shallow groundwater systems, whose dependence on the depth to groundwater makes its measurement difficult or even impossible (Crosbie et al., 2019; Dettmann and Bechtold, 2016). Conversely, the specific yield of 0.16 found at the CRNS site was similar to mean estimate of ~0.15 found in a hydrogeological management zone at downstream of Paraíba river basin (Braga, Rêgo and Galvão, 2015). Lastly, the results of such studies are valuable for decision-makers in water resources, in view of the worldwide effects of climate changes on GWR, which may face a decrease of up to 72% in areas comprehended by Podzol soil type, according to a study carried out in four different analogue locations (Leterme, Mallants and Jacques, 2012).

## 7 CONCLUSION AND OUTLOOK

Recent advances in remote sensing have launched new techniques and methods for estimating the water balance components with better spatiotemporal resolutions, which have allowed for a more accurate indirect simulation of GWR through the water budget equation over either large- and intermediary-scale areas. Accordingly, this study targeted on providing alternative means of GWR estimation by merging well-established hydrogeological models and state-of-the-art monitoring data sources. Such datasets comprehended: satellite products, reanalysis data, land use/cover mapping, hydrogeological models, Cosmic-Ray Neutron Sensing/Operators, *in situ* and laboratory experiments (gravimetric method, slug test, pumping test, and soil sieving), and various ground-based data sources (rain gauges, meteorological stations, stream gauges, soil moisture profile probes, and monitoring wells). The methodologies herein investigated were assessed in two tropical wet basins located in a complex sedimentary aquifer, in the coastal Northeast of Brazil. From the accomplished results, the following conclusions can be addressed:

1. GPM IMERG V05B satellite product, after the bias correction and pixel resampling, estimated more comprehensively the spatially-distributed precipitation patterns, depicting an East-to-West precipitation gradient;
2. Adapted MOD16 algorithm estimated coherently the actual evapotranspiration by applying the reanalysis data and the monthly cloud-cleaning map composition on biophysical parameters, accounting for the land use/cover particularities;
3. SMAP SPL4SMAU product allowed for averaging the soil water storage changes down to 1-m root zone, revealing the likely susceptibility of the study area to water shortage, in spite of the relatively coarse resolution even after pixel resampling;
4. Updated NRCS–CN method, after the Curve Number recalculation and the Antecedent Runoff Condition reformulation, provided satisfactory surface runoff estimates, accounting for the soil type and land use/cover particularities;
5. GIS-based model coupling showed that GWR estimates had a slight underestimation for Gauge scenario and slight overestimation for IMERG\* one, and mean relative rates generally more variable when averaged by soil types than by land use/cover;
6. CRNS-based soil moisture behaved convincingly with high goodness-of-fit in a region with a shallow groundwater system under tropical wet conditions, despite the unfavourable operational conditions including the low incoming neutron intensity;

7. COSMIC operator coupled with HYDRUS-1D model allowed for calibrating successfully via inverse modelling the parameters of the soil hydraulic properties, and for simulating the aboveground neutron intensity, in a sandy Podzol soil type;
8. HYDRUS-1D was able to simulate on daily scale the vertical water percolation along the root zone and the GWR at the variable bottom boundary, the latter matching the WTF-MRC-RISE-based estimates in the CRNS location;
9. The curves of the soil hydraulic properties and the groundwater depth were likely the most important environmental factors that differentiated the upstream and downstream GWR rates in the small-scale tropical wet basin;
10. GWR estimates were realistically well estimated over the study areas through both the GIS-based methods and the HYDRUS-1D-COSMIC model based on CRNS data, as shown by the similar results found in the Podzol soil type.

This study revealed the progressive improvement on the quality of satellite products as new sensor advancements and algorithm refinements have been released. Accordingly, enhancements on spatiotemporal resolution and goodness-of-fit in the sources of monitoring data shall cope with burdensome and time-consuming maintaining of extensive monitoring networks. Those advances shall boost increasingly more the hydrogeological applications, so that the hard-tasking measurement of relevant variables, such as GWR, can be promptly undertaken to afford a diligent water resource management. Conversely, the current technology limitations and the increasingly stringent environmental requirements have compelled immediate solutions for measuring the soil moisture at field scale. The present study then demonstrated the effective performance of CRNS probes under unfavourable operating conditions, thus encouraging the adoption of such technology in emerging countries, such as Brazil. Nevertheless, studies on the CRNS application for soil water and matter transport simulation have been underexplored in the literature yet. Thus, this study pioneering in South America showed the high potential of CRNS for further hydrogeological uses, representing a first step on the feasible employment of such state-of-the-art technology on the continent. Technical improvements are being made, e.g. in the *Cosmic Sense* research project, to enhance the CRNS sensitivity, modifying its ground penetration depth and horizontal footprint of measurement. Ultimately, further studies are firmly recommended to better assess the sources of uncertainty in water budget approaches, namely: (1) lack of water demand, interception and irrigation; (2) satellite-based precipitation and soil moisture spatial resolutions; (3) runoff potential and phenological regional parameters; (4) soil hydraulic property inverse modelling, and; (5) CRNS performance under tropical semiarid condition.

## REFERENCES

- Abdulkareem, J. H. et al. Long-term runoff dynamics assessment measured through land use/cover (LULC) changes in a tropical complex catchment. **Environment Systems and Decisions**, v. 39, n. 1, p. 16–33, 2019.
- AESA – Agência Executiva de Gestão das Águas do Estado da Paraíba. **SIGAESA-WEB: Geo Portal**. Disponível em: <<http://geo.aesa.pb.gov.br/>>. Access in: May, 2018.
- Aeschbach-Hertig, W.; Gleeson, T. Regional strategies for the accelerating global problem of groundwater depletion. **Nature Geoscience**, v. 5, n. 12, p. 853–861, 2012.
- Agarwal, R.; Garg, P. K. Remote sensing and GIS based groundwater potential and recharge zones mapping using multi-criteria decision making technique. **Water Resources Management**, v. 30, n. 1, p. 243–260, 2016.
- Aggarwal, S. Principles of remote sensing. **Satellite Remote Sensing and GIS Applications in Agricultural Meteorology**. p. 23–38, 2004.
- Ajmal, M. et al. Investigation of SCS-CN and its inspired modified models for runoff estimation in South Korean watersheds. **Journal of Hydro-Environment Research**, v. 9, n. 4, p. 592–603, 2015.
- Ajmal, M.; Kim, T.-W. Quantifying excess stormwater using SCS-CN-based rainfall runoff models and different Curve Number determination methods. **Journal of Irrigation and Drainage Engineering**, v. 141, n. 3, p. 1–12, 2015.
- Ali, M. H.; Mubarak, S. Approaches and methods of quantifying natural groundwater recharge – a review. **Asian Journal of Environment & Ecology**, v. 5, n. 1, p. 1–27, 2017.
- Allen, R. G. et al. Crop evapotranspiration – Guidelines for computing crop water requirements. In: **FAO Irrigation and drainage**. Rome, Italy: FAO – Food and Agriculture Organization of the United Nations, 56p. 1–15, 1998.
- Allen, R. G.; Tasumi, M.; Trezza, R. Satellite-based energy balance for mapping evapotranspiration with Internalized Calibration (METRIC)-Model. **Journal of Irrigation and Drainage Engineering**, v. 133, p. 380–394, 2007.
- Almeida, C. das N. et al. **BRAMAR - Situação do estudo de caso de João Pessoa**. XX Simpósio Brasileiro de Recursos Hídricos. **Annals...** Florianópolis: 2017
- Alvares, C. A. et al. Köppen's climate classification map for Brazil. **Meteorologische Zeitschrift**, v. 22, n. 6, p. 711–728, 2013.
- Anache, J. A. A. et al. Runoff and soil erosion plot-scale studies under natural rainfall: a meta-analysis of the Brazilian experience. **Catena**, v. 152, p. 29–39, 2017.
- Anderson, L. O. et al. **Sensor MODIS: uma abordagem geral**. São José dos Campos/SP: INPE, 2003.
- Andrade, R. G. et al. Geotecnologias aplicadas à avaliação de parâmetros biofísicos do Pantanal. **Pesquisa Agropecuária Brasileira**, v. 47, n. 9, p. 1227–1234, 2012.
- Andrades Filho, C. de O. **Evolução tectono-sedimentar da porção central emersa da bacia Paraíba, Nordeste do Brasil**. PhD thesis. University of São Paulo, 2014.
- Andreasen, M. et al. Modeling cosmic ray neutron field measurements. **Water Resources Research**, v. 52, p. 6451–6471, 2016.
- Andreasen, M. et al. Status and perspectives on the cosmic-ray neutron method for soil moisture estimation and other environmental science applications. **Vadose Zone Journal**, v. 16, n. 8, p. 11, 2017a.



- Andreasen, M. et al. Cosmic-ray neutron transport at a forest field site: the sensitivity to various environmental conditions with focus on biomass and canopy interception. **Hydrology and Earth System Sciences**, v. 21, p. 1875–1894, 2017b.
- Anjum, M. N. et al. Assessment of IMERG-V06 precipitation product over different hydro-climatic regimes in the Tianshan Mountains, North-western China. **Remote Sensing**, v. 11, n. 2314, p. 1–23, 2019.
- Arai, E.; Freitas, R. Pré-processamento MODIS. In: Rudorff, B. F. T.; Shimabukuro, Y. E.; Ceballos, J. C. (Eds.). **O sensor MODIS e suas aplicações ambientais no Brasil**. São José dos Campos/SP: Editora Parêntese, p. 71–82, 2007.
- Araújo, D. et al. Fácies e Sistemas Depositionais da Formação Barreiras na Região da Barreira do Inferno, Litoral Oriental do Rio Grande do Norte. **Geologia USP (Série Científica)**, v. 6, n. 2, p. 43–50, 2006.
- Araújo Filho, J. C. et al. **Levantamento de reconhecimento de baixa e média intensidade dos solos do Estado de Pernambuco Boletim de Pesquisa n. 11**. Rio de Janeiro/RJ: Embrapa Solos, 2000.
- Arnold, J. G. et al. **SWRRB: a basin scale simulation model for soil and water resources management**. College Station: Texas A&M University Press, 1990.
- ASTM. G173-03: standard tables for reference solar spectral irradiances - direct normal and hemispherical on 37° tilted surface. **American Society for Testing and Materials (ASTM)**, 2003.
- Awadallah, A. G.; Farahat, M. S.; Haggag, M. Discussion of "Interfacing the geographic information system, remote sensing, and the soil conservation service-curve number method to estimate curve number and runoff volume in the ASIR region of Saudi Arabia" by Fawzi S . Mohammad , Jan Adamowski. **Arabian Journal of Geosciences**, 2017.
- Baatz, R. et al. Calibration of a catchment scale cosmic-ray probe network : A comparison of three parameterization methods. **Journal of Hydrology**, v. 516, p. 231–244, 2014.
- Baatz, R. et al. Evaluation of a cosmic-ray neutron sensor network for improved land surface model prediction. **Hydrology and Earth System Sciences**, v. 21, p. 2509–2530, 2017.
- Badgley, G. et al. On uncertainty in global terrestrial evapotranspiration estimates from choice of input forcing datasets. **Journal of Hydrometeorology**, v. 16, p. 1449–1455, 2015.
- Bai, J. et al. Assessment of the SMAP-Derived Soil Water Deficit Index (SWDI-SMAP) as an agricultural drought index in China. **Remote Sensing**, v. 10, n. 1302, p. 1–21, 2018.
- Baik, J.; Liaqat, U. W.; Choi, M. Assessment of satellite- and reanalysis-based evapotranspiration products with two blending approaches over the complex landscapes and climates of Australia. **Agricultural and Forest Meteorology**, v. 263, p. 388–398, 2018.
- Barbosa, L. R. **Relações precipitação-umidade do solo-vazão de eventos subdiários em bacias experimentais do NE brasileiro**. Master dissertation. Federal University of Paraíba, 2015.
- Barbosa, L. R. et al. Sub-hourly rainfall patterns by hyetograph type under distinct climate conditions in Northeast of Brazil: a comparative inference of their key properties. **Revista Brasileira de Recursos Hídricos**, v. 23, n. 46, p. 1–14, 2018.
- Barbosa, L. R. et al. Stability of soil moisture patterns retrieved at different temporal resolutions in a tropical watershed. **Revista Brasileira de Ciência do Solo**, v. 43, p. 1–21, 2019.
- Barbosa, J. A. et al. A estratigrafia da bacia Paraíba: uma reconsideração. **Estudos Geológicos**, v. 13, n. 1, p. 89–108, 2003.
- Baroni, G. et al. Uncertainty, sensitivity and improvements in soil moisture estimation with cosmic-ray neutron sensing. **Journal of Hydrology**, v. 564, p. 873–887, 2018.

- Baroni, G.; Oswald, S. E. A scaling approach for the assessment of biomass changes and rainfall interception using cosmic-ray neutron sensing. **Journal of Hydrology**, v. 525, p. 264–276, 2015.
- Bastiaanssen, W. G. M. et al. A remote sensing surface energy balance algorithm for land (SEBAL), Part 1: Formulation. **Journal of Hydrology**, v. 212–213, p. 213–229, 1998.
- Batalha, M. S. et al. Effect of temporal averaging of meteorological data on predictions of groundwater recharge. **Journal of Hydrology and Hydromechanics**, v. 66, n. 2, p. 143–152, 2018.
- Berhanu, B.; Melesse, A. M.; Seleshi, Y. Gis-based hydrological zones and soil geo-database of Ethiopia. **Catena**, v. 104, p. 21–31, 2013.
- Beurlen, K. Estratigrafia da faixa sedimentar costeira Recife – João Pessoa. **Boletim da Sociedade Brasileira de Geologia**, v. 16, n. 1, p. 43–53, 1967.
- Bi, H. et al. Comparison of soil moisture in GLDAS model simulations and in situ observations over the Tibetan Plateau. **Journal of Geophysical Research: Atmospheres**, v. 121, p. 2658–2678, 2016.
- Blasi, P. Recent results in cosmic ray physics and their interpretation. **Brazilian Journal of Physics**, v. 44, n. 5, p. 426–440, 2014.
- Blandford, R. D.; Ostriker, J. P. Particle acceleration by astrophysical shocks. **The Astrophysical Journal**, v. 221, p. L29–L32, 1978.
- Bogena, H. R. et al. Accuracy of the cosmic-ray soil water content probe in humid forest ecosystems: The worst case scenario. **Water Resources Research**, v. 49, p. 5778–5791, 2013.
- Bogena, H. R. et al. Emerging methods for noninvasive sensing of soil moisture dynamics from field to catchment scale: a review. **Wiley Interdisciplinary Reviews: Water**, v. 2, n. 6, p. 635–647, 2015.
- Bolton, D. K.; Friedl, M. A. Forecasting crop yield using remotely sensed vegetation indices and crop phenology metrics. **Agricultural and Forest Meteorology**, v. 173, p. 74–84, 2013.
- Borges, V. M. et al. Groundwater recharge estimating in the Serra Geral aquifer system outcrop area – Paraná state, Brazil. **Águas Subterrâneas**, v. 31, n. 4, p. 338–346, 2017.
- Børgesen, C. D. et al. Soil hydraulic properties near saturation, an improved conductivity model. **Journal of Hydrology**, v. 324, p. 40–50, 2006.
- Boscha, D. D. et al. Temporal variations in baseflow for the Little River experimental watershed in South Georgia, USA. **Journal of Hydrology: Regional Studies**, v. 10, p. 110–121, 2017.
- Bouwer, H.; Rice, R. C. A slug test for determining hydraulic conductivity of unconfined aquifers with completely or partially penetrating wells. **Water Resources Research**, v. 12, n. 3, p. 423–428, 1976.
- Bowen, I. S. The ratio of heat losses by conduction and by evaporation from any water surface. **Physical review**, v. 27, p. 779–787, 1926.
- Braga, A. C. **Evapotranspiração e Produtividade Primária Bruta em áreas agrícolas utilizando técnicas de sensoriamento remoto**. PhD thesis. Federal University of Campina Grande, 2014.
- Braga, A. C. R.; Rêgo, J. C.; Galvão, C. de O. Variação intra-sazonal da potencialidade hídrica subterrânea e sua influência na outorga. **Revista Brasileira de Recursos Hídricos**, v. 20, n. 3, p. 647–656, 2015.
- Brocca, L. et al. Soil moisture for hydrological applications: open questions and new opportunities. **Water**, v. 9, n. 140, p. 1–20, 2017.
- Brodzik, M. J. et al. EASE-Grid 2.0: incremental but significant improvements for Earth-Gridded

- Data Sets. **ISPRS International Journal of Geo-Information**, v. 1, p. 32–45, 2012.
- Brunetti, G. et al. On the information content of cosmic-ray neutron data in the inverse estimation of soil hydraulic properties. **Vadose Zone Journal**, v. 18:180123, p. 1–24, 2019.
- Brunner, P. et al. How can remote sensing contribute in groundwater modeling? **Hydrogeology Journal**, v. 15, n. 1, p. 5–18, 2007.
- Caballero, L. A. **Hydrology, hydrochemistry and implications for water supply of a cloud forest in Central America**. PhD thesis. Faculty of the Graduate School of Cornell University, 2012.
- Cabral da Silva, T. et al. Geologia, recursos minerais e atividade minerária, geomorfologia e estudo de erosão, pedologia, aptidão agrícola, classes de terra para irrigação e zoneamento edafoclimático para culturas. In: Governo da Paraíba; SEMARH; SCIENTEC (Eds.). **Plano Diretor de Recursos Hídricos da Bacia do Rio Gramame**. João Pessoa/PB: Governo do Estado da Paraíba, p. 1–57, 2000a.
- Cabral da Silva, T. et al. Climatologia. In: Governo da PARAÍBA; SEMARH; SCIENTEC (Eds.). **Plano Diretor de Recursos Hídricos da Bacia do Rio Gramame**. João Pessoa/PB: Governo do Estado da Paraíba, p. 1–48, 2000b.
- Cai, Z.; Ofterdinger, U. Analysis of groundwater-level response to rainfall and estimation of annual recharge in fractured hard rock aquifers, NW Ireland. **Journal of Hydrology**, v. 535, p. 71–84, 2016.
- Camillo, P. J.; Gurney, R. J. A resistance parameter for bare-soil evaporation models. **Soil Science**, v. 141, n. 2, p. 95–105, 1986.
- Cary, L. et al. Origins and processes of groundwater salinization in the urban coastal aquifers of Recife (Pernambuco, Brazil): A multi-isotope approach. **Science of The Total Environment**, v. 530, p. 411–429, 2015.
- Cavalcante, R. B. L. et al. Opposite effects of climate and land use changes on the annual water balance in the Amazon arc of deforestation. **Water Resources Research**, v. 55, p. 1–15, 2019.
- Chatton, E. et al. Glacial recharge, salinisation and anthropogenic contamination in the coastal aquifers of Recife (Brazil). **Science of The Total Environment**, v. 569, p. 1114–1125, 2016.
- Chaudhuri, S.; Ale, S. Long-term (1930–2010) trends in groundwater levels in Texas: influences of soils, landcover and water use. **Science of The Total Environment**, v. 490, p. 379–390, 2014.
- Chen, F. et al. Modeling of land surface evaporation by four schemes and comparison with FIFE observations. **Journal of Geophysical Research**, v. 101, n. D3, p. 7251–7268, 1996.
- Chen, Z. et al. The impact of precipitation deficit and urbanization on variations in water storage in the Beijing-Tianjin-Hebei urban agglomeration. **Remote Sensing**, v. 10, n. 4, p. 1–12, 2018.
- Cho, Y.; Engel, B. A. Spatially distributed long-term hydrologic simulation using a continuous SCS CN method-based hybrid hydrologic model. **Hydrological Processes**, v. 32, n. 7, p. 904–922, 2018.
- Chow, V.; Maidment, D.; Mays, L. **Applied hydrology**. New York/NY: McGraw-Hill, 1988.
- Chrisman, B.; Zreda, M. Quantifying mesoscale soil moisture with the cosmic-ray rover. **Hydrology and Earth System Sciences**, v. 17, p. 5097–5108, 2013.
- Chung, I. et al. Estimating groundwater recharge in the humid and semi-arid African regions: review. **Geosciences Journal**, v. 20, n. 5, p. 731–744, 2016.
- Chung, S.; Horton, R. Soil heat and water flow with a partial surface mulch. **Water Resources Research**, v. 23, n. 12, p. 2175–2186, 1987.

- Cleugh, H. A. et al. Regional evaporation estimates from flux tower and MODIS satellite data. **Remote Sensing of Environment**, v. 106, n. 3, p. 285–304, 2007.
- Clothier, B. E.; Green, S. **Leaching processes**. Elsevier, 2005.
- Coelho, V. H. R. et al. Dinâmica do uso e ocupação do solo em uma bacia hidrográfica do semiárido brasileiro. **Revista Brasileira de Engenharia Agrícola e Ambiental**, v. 18, n. 1, p. 64–72, 2014.
- Coelho, V. H. R. et al. Alluvial groundwater recharge estimation in semi-arid environment using remotely sensed data. **Journal of Hydrology**, v. 548, p. 1–15, 2017.
- Colliander, A. et al. Validation of SMAP surface soil moisture products with core validation sites. **Remote Sensing of Environment**, v. 191, p. 215–231, 2017.
- Cooper, M. et al. Hydro-physical characterization of soils under the Restinga Forest. **Scientia Agrícola**, v. 74, n. 5, p. 393–400, 2017.
- Cordeiro, M. R. C. et al. Deriving a dataset for agriculturally relevant soils from the Soil Landscapes of Canada (SLC) database for use in Soil and Water Assessment Tool (SWAT) simulations. **Earth System Science Data**, v. 10, n. 3, p. 1673–1686, 2018.
- Cronin, J. W.; Gaisser, T. K.; Swordy, S. P. Cosmic rays at the energy frontier. **Scientific American**, v. 276, n. 1, p. 44–49, 1997.
- Crosbie, R. S. et al. Ground truthing groundwater-recharge estimates derived from remotely sensed evapotranspiration: a case in South Australia. **Hydrogeology Journal**, v. 23, p. 335–350, 2015.
- Crosbie, R. S. et al. Estimating groundwater recharge and its associated uncertainty: Use of regression kriging and the chloride mass balance method. **Journal of Hydrology**, v. 561, p. 1063–1080, 2018.
- Crosbie, R. S. et al. Constraining the magnitude and uncertainty of specific yield for use in the water table fluctuation method of estimating recharge. **Water Resources Research**, v. 55, n. 8, p. 7343–7361, 2019.
- Crouzeilles, R. et al. There is hope for achieving ambitious Atlantic Forest restoration commitments. **Perspectives in Ecology and Conservation**, v. 17, n. 2, p. 80–83, 2019.
- da Costa, A. M. et al. Groundwater recharge potential for sustainable water use in urban areas of the Jequitiba river. **Sustainability**, v. 11, n. 2955, p. 1–20, 2019.
- da Silva, A. F.; Almeida, C. das N. Utilização do método Bávaro para avaliação das condições hidromorfológicas de uma bacia experimental no Nordeste Brasileiro. **Revista Brasileira de Recursos Hídricos**, v. 20, p. 106–118, 2017.
- da Silva, A. J. P.; Coelho, E. F. Estimation of water percolation by different methods using TDR. **Revista Brasileira de Ciência do Solo**, v. 38, p. 73–81, 2014.
- Dai, Y. et al. The common land model. **Bulletin of the American Meteorological Society**, v. 84, n. 8, p. 1013–1023, 2003.
- Dams, J. et al. **Case Kleine Nete: hydrologie, wetenschappelijk rapport - NARA 2009**. Brussels: 2009.
- Das, K.; Singh, J.; Hazra, J. Comparison of SMAP, GLDAS and simulated soil moisture datasets over a Malaysian region. **IEEE International Geoscience and Remote Sensing Symposium (IGARSS)**, p. 6298–6301, 2019.
- de Bruin, H. From Penman to Makkink. In: HOOGHART, J. C. (Ed.). **Evaporation and Weather: Technical Meeting 44**. Proceedings and Information/TNO Committee on Hydrological Research, p. 5–30, 1987.
- de Lira, N. B. **Análise da variabilidade espaço-temporal da umidade do solo na bacia**

- experimental do riacho Guaraíra.** Master thesis. Federal University of Paraíba, 2015.
- de Oliveira, L. F. C. et al. Comparação de metodologias de preenchimento de falhas de séries históricas de precipitação pluvial anual. **Revista Brasileira de Engenharia Agrícola e Ambiental**, v. 14, n. 11, p. 1186–1192, 2010.
- de Oliveira, G. et al. Use of MODIS sensor images combined with reanalysis products to retrieve net radiation in Amazonia. **Sensors**, v. 16, n. 956, p. 1–28, 2016a.
- de Oliveira, G. et al. Analysis of precipitation and evapotranspiration in Atlantic Rainforest remnants in Southeastern Brazil from remote sensing data. In: **Tropical Forests - The Challenges of Maintaining Ecosystem Services while Managing the Landscape**. INTECH, p. 93–112, 2016b.
- de Oliveira, J. V. et al. Differences in precipitation and evapotranspiration between forested and deforested areas in the Amazon rainforest using remote sensing data. **Environmental Earth Sciences**, v. 77, n. 239, p. 1–14, 2018b.
- de Souza, E. et al. Spatial and temporal potential groundwater recharge: the case of the Doce River basin, Brazil. **Revista Brasileira de Ciência do Solo**, v. 43, n. e0180010, p. 1–27, 2019.
- Delin, G. N. et al. Comparison of local- to regional-scale estimates of ground-water recharge in Minnesota, USA. **Journal of Hydrology**, v. 334, p. 231–249, 2007.
- DELTA-T. **User manual for the Profile Probe, type PR2**. Cambridge/UK: Delta-T Devices Ltd., 2016.
- Deshmukh, D. S. et al. Estimation and comparison of curve numbers based on dynamic land use land cover change, observed rainfall-runoff data and land slope. **Journal of Hydrology**, v. 492, p. 89–101, 2013.
- Desilets, D.; Zreda, M. On scaling cosmogenic nuclide production rates for altitude and latitude using cosmic-ray measurements. **Earth and Planetary Science Letters**. v. 193, n. 1–2, p. 213–225, 2001.
- Desilets, D.; Zreda, M. Footprint diameter for a cosmic-ray soil moisture probe: theory and Monte Carlo simulations. **Water Resources Research**, v. 49, p. 3566–3575, 2013.
- Desilets, D.; Zreda, M.; Ferré, T. P. A. Nature's neutron probe: land surface hydrology at an elusive scale with cosmic rays. **Water Resources Research**, v. 46, n. W11505, p. 1–7, 2010.
- Desilets, D.; Zreda, M.; Prabu, T. Extended scaling factors for in situ cosmogenic nuclides: new measurements at low latitude. **Earth and Planetary Science Letters**, v. 246, p. 265–276, 2006.
- Dettmann, U.; Bechtold, M. One-dimensional expression to calculate specific yield for shallow groundwater systems with microrelief. **Hydrological Processes**, v. 340, p. 334–340, 2016.
- Dias, L. C. P. et al. Patterns of land use, extensification, and intensification of Brazilian agriculture. **Gloval Change Biology**, v. 22, n. 8, p. 2887–2903, 2016.
- Diniz, C. et al. Brazilian mangrove status: three decades of satellite data analysis. **Remote Sensing**, v. 11, n. 808, p. 1–19, 2019.
- Doble, R. C.; Crosbie, R. S. Review: current and emerging methods for catchment-scale modelling of recharge and evapotranspiration from shallow groundwater. **Hydrogeology Journal**, v. 25, n. 1, p. 3–23, 2016.
- Doherty, J. **PEST: Model-Independent Parameter Estimation User Manual**. 5th. ed. Brisbane/AU: Watermark Numerical Computing, 2004.
- Dong, J. et al. Calibration and validation of the COSMOS rover for surface soil moisture measurement. **Vadose Zone Journal**, v. 13, n. 4, p. 1–8, 2014.
- Dorfi, E. A.; Breitschwerdt, D. Time-dependent galactic winds. **Astronomy & Astrophysics**, v. 540,

- n. A77, p. 1–15, 2012.
- dos Santos, C. A. C. et al. Spatio-temporal patterns of energy exchange and evapotranspiration during an intense drought for drylands in Brazil. **International Journal of Applied Earth Observation and Geoinformation**, v. 85, n. 101982, p. 1–11, 2020.
- dos Santos, H. et al. **SiBCS – Sistema Brasileiro de Classificação de Solos**. 5. ed. Brasília/DF: Embrapa Amazônia Ocidental; Embrapa Solos, 2018.
- DPIRD. **Water salinity and plant irrigation**. DPIRD – Department of Primary Industries and Regional Development. Disponível em: <<https://www.agric.wa.gov.au/water-management/water-salinity-and-plant-irrigation>>, Access in: September, 2019.
- Duffield, G. M. **AQTESOLV for windows version 4.5 user's guide**. Reston/VA: HydroSOLVE, Inc., 2007.
- Duncan, H. P. Base flow separation – a practical approach. **Journal of Hydrology**, v. 575, p. 308–313, 2019.
- Durner, W.; Iden, S. C. Extended multistep outflow method for the accurate determination of soil hydraulic properties near water saturation. **Water Resources Research**, v. 47, n. W08526, p. 1–13, 2011.
- Duygu, M. B.; Akyürek, Z. Using cosmic-ray neutron probes in validating satellite soil moisture products and land surface models. **Water**, v. 11, n. 1362, p. 1–29, 2019.
- Efstratiadis, A. et al. Flood design recipes vs . reality: can predictions for ungauged basins be trusted? **Natural Hazards Earth System Sciences**, v. 14, p. 1417–1428, 2014.
- Entekhabi, D. et al. The Soil Moisture Active Passive (SMAP) mission. **Proceedings of the IEEE**, v. 98, n. 5, p. 704–716, 2010.
- Entekhabi, D. et al. **SMAP handbook – Soil Moisture Active Passive: mapping soil moisture and freeze/thaw from Space**. Pasadena/CA: JPL Publisher, 2014.
- Ertürk, A. et al. Model-based assessment of groundwater vulnerability for the Dalyan region of southwestern Mediterranean Turkey. **Regional Environmental Change**, p. 1193–1203, 2017.
- Escarabajal-Henarejos, D. et al. Selection of device to determine temperature gradients for estimating evapotranspiration using energy balance method. **Agricultural Water Management**, v. 151, p. 136–147, 2015.
- Evans, J. G. et al. Soil water content in southern England derived from a cosmic-ray soil moisture observing system – COSMOS-UK. **Hydrological Processes**, v. 30, n. 26, p. 4987–4999, 2016.
- Feddes, R. A.; Kowalik, P. J.; Zaradny, H. **Simulation of field water use and crop yield**. New York/NY: John Wiley & Sons, 1978.
- Fernandes, L. A. **Aplicação do método WTF para estimativa da recarga do aquífero livre da região da bacia do rio Gramame e do baixo curso do rio Paraíba/PB**. Master thesis. Federal University of Paraíba, 2017.
- Ferreira, V. et al. Uncertainties of the Gravity Recovery and Climate Experiment time-variable gravity-field solutions based on three-cornered hat method. **Journal of Applied Remote Sensing**, v. 10, n. 1, 2016.
- Filoso, S. et al. Reassessing the environmental impacts of sugarcane ethanol production in Brazil to help meet sustainability goals. **Renewable and Sustainable Energy Reviews**, v. 52, p. 1847–1856, 2015.
- Florenzano, T. G. **Iniciação ao sensoriamento remoto**. São Paulo: 2007.
- Forbush, S. E. World-wide cosmic-ray variations, 1937-1952. **Journal of Geophysical Research**,

- v. 59, n. 4, p. 525–542, 1954.
- Foster, S. et al. Groundwater – a global focus on the “local resource”. **Current Opinion in Environmental Sustainability**, v. 5, n. 6, p. 685–695, 2013.
- Franz, T. E. et al. Field validation of a cosmic-ray neutron sensor using a distributed sensor network. **Vadose Zone Journal**, v. 11, n. 4, p. 1–10, 2012a.
- Franz, T. E. et al. Measurement depth of the cosmic ray soil moisture probe affected by hydrogen from various sources. **Water Resources Research**, v. 48, n. W08515, p. 1–9, 2012b.
- Franz, T. E. et al. Ecosystem-scale measurements of biomass water using cosmic ray neutrons. **Geophysical Research Letters**, v. 40, n. 1936, p. 3929–3933, 2013a.
- Franz, T. E. et al. An assessment of the effect of horizontal soil moisture heterogeneity on the area-average measurement of cosmic-ray neutrons. **Water Resources Research**, v. 49, p. 6450–6458, 2013b.
- Freitas, L. et al. Assessment of sustainability of groundwater in urban areas (Porto, NW Portugal): a GIS mapping approach to evaluate vulnerability, infiltration and recharge. **Environmental Earth Sciences**, v. 78, n. 140, p. 1–17, 2019.
- Furrier, M.; de Araújo, M. E.; de Meneses, L. F. Geomorfologia e tectônica da formação barreiras no estado da Paraíba. **Geologia USP – Serie Científica**, v. 6, n. 2, p. 61–70, 2006.
- Gadelha, A. N. et al. Grid box-level evaluation of IMERG over Brazil at various space and time scales. **Atmospheric Research**, v. 218, p. 231–244, 2019.
- Garrett, R. D. et al. Intensification in agriculture-forest frontiers: land use responses to development and conservation policies in Brazil. **Global Environmental Change**, v. 53, p. 233–243, 2018.
- Gilewski, P.; Nawalany, M. Inter-comparison of rain-gauge, radar, and satellite (IMERG GPM) precipitation estimates performance for rainfall-runoff modeling in a mountainous catchment in Poland. **Water**, v. 10, n. 1665, p. 1–23, 2018.
- Gleeson, T. et al. Water balance of global aquifers revealed by groundwater footprint. **Nature**, v. 488, n. 7410, p. 197–200, 2012.
- Gokmen, M. et al. Assessing groundwater storage changes using remote sensing-based evapotranspiration and precipitation at a large semiarid basin scale. **Journal of Hydrometeorology**, v. 14, n. 6, p. 1733–1753, 2013.
- Goldhagen, P. et al. Measurement of the energy spectrum of cosmic-ray induced neutrons aboard an ER-2 high-altitude airplane. **Nuclear Instruments and Methods in Physics Research A**, v. 476, p. 42–51, 2002.
- Graeff, T. et al. A quality assessment of spatial TDR soil moisture measurements in homogenous and heterogeneous media with laboratory experiments. **Hydrology and Earth System Sciences**, v. 14, n. 6, p. 1007–1020, 2010.
- Graham, S. L. et al. Soil hydraulic modeling outcomes with four parameterization methods: comparing soil description and inverse estimation approaches. **Vadose Zone Journal**, v. 17, n. 170002, p. 1–10, 2018.
- Grimaldi, S.; Orellana, F.; Daly, E. Modelling the effects of soil type and root distribution on shallow groundwater resources. **Hydrological Processes**, v. 29, p. 4457–4469, 2015.
- Gusev, Y. et al. The uncertainty of assessments of the water balance components of river basins due to the climate noise. **Geophysical Research Abstracts**, v. 18, p. 2016, 2016.
- Gusmão, A. C. V. e L. **Mapeamento da evapotranspiração real por imagens orbitais em bacia representativa no estado de Pernambuco**. PhD thesis. Rural Federal University of Pernambuco, 2017.



- Han, M. et al. Evaluating the impact of groundwater on cotton growth and root zone water balance using HYDRUS-1D coupled with a crop growth model. **Agricultural Water Management**, v. 160, p. 64–75, 2015.
- Hansen, N.; Müller, S. D.; Koumoutsakos, P. Reducing the time complexity of the derandomized evolution strategy with Covariance Matrix Adaptation (CMA-ES). **Evolutionary Computation**, v. 11, n. 1, p. 1–18, 2003.
- Hawdon, A.; Mcjannet, D.; Wallace, J. Calibration and correction procedures for cosmic-ray neutron soil moisture probes located across Australia. **Water Resources Research**, v. 50, n. 6, p. 5029–5043, 2014.
- Hawkins, R. H. Et Al. **Curve number hydrology**. Reston/VA: American Society of Civil Engineers (ASCE), 2009.
- Hawkins, R. H. et al. **Continuing evolution of rainfall-runoff and the curve number precedent**. 2nd Joint Federal Interagency Conference. **Annals...** Las Vegas/NV: 2010
- Hawkins, R. H.; Hjelmfelt, A. T.; Zevenbergen, A. W. Runoff probability, storm depth, and curve numbers. **Journal of Irrigation and Drainage Engineering**, v. 111, n. 4, p. 330–340, 1985.
- Healy, R. W.; Cook, P. G. Using groundwater levels to estimate recharge. **Hydrogeology Journal**, v. 10, n. 1, p. 91–109, 2002.
- Heidbüchel, I.; Güntner, A.; Blume, T. Use of cosmic-ray neutron sensors for soil moisture monitoring in forests. **Hydrology and Earth System Sciences**, v. 20, p. 1269–1288, 2016.
- Hendrick, L. D.; Edge, R. D. Cosmic-ray neutrons near the Earth. **Physical review**, v. 145, n. 4, p. 1023–1025, 1966.
- Hiez, G. L'homogénéité des données pluviométriques. **Cahiers ORSTOM. Série Hydrologie**. Paris: v. 14, n. 2, p.129–172, 1977.
- Hillas, A. M. Can diffusive shock acceleration in supernova remnants account for high-energy galactic cosmic rays? **Journal of Physics G: Nuclear and Particle Physics**, v. 31, n. 5, p. R95–R131, 2005.
- Hird, R.; Bolton, M. D. Clarification of capillary rise in dry sand. **Engineering Geology**, v. 230, p. 77–83, 2017.
- Hoffman, G. J.; Van Genuchten, M. T. Soil properties and efficient water use: Water management for salinity control. In: Taylor, H. M.; Jordan, W. R.; Sinclair, T. R. (Eds.). **Limitations and Efficient Water Use in Crop Production**. Madison/WI: American Society of Agronomy, p. 73–85, 1983.
- Hong, Y. et al. A first approach to global runoff simulation using satellite rainfall estimation. **Water Resources Research**, v. 43, n. 8, p. 1–8, 2007.
- Hornero, J. et al. Integrating soil water and tracer balances, numerical modelling and GIS tools to estimate regional groundwater recharge: application to the Alcadozo Aquifer System (SE Spain). **Science of the Total Environment**, v. 568, p. 415–432, 2016.
- Hou, A. Y. et al. The global precipitation measurement mission. **American Meteorological Society**, p. 701–722, 2014.
- Huete, A. R. A soil-adjusted vegetation index (SAVI). **Remote Sensing of Environment**, v. 25, n. 3, p. 295–209, 1988.
- Huffman, G. J. et al. **Algorithm Theoretical Basis Document (ATBD) NASA Global Precipitation Measurement (GPM) Integrated Multi-satellitE Retrievals for GPM (IMERG)**. Greenbelt/MD: NASA/GSFC, 2015.
- Huffman, G. J.; Bolvin, D. T.; Nelkin, E. J. **Integrated Multi-satellitE Retrievals for GPM (IMERG) Technical Documentation**. 2017.

- IAEA. **Cosmic ray neutron sensing: use, calibration and validation for soil moisture estimation**. IAEA-TECDOC-1809. *Annals...* Vienna: International Atomic Energy Agency (IAEA), 2017
- IBESA. Relatório final da caracterização das bacias experimentais do Semiárido Brasileiro. In: UFRN-UFC-UFPB-UFCG-UFRPE-UFPE-UFBA (Ed.). **IBESA – Implantação de bacias experimental do semiárido para o desenvolvimento de metodologias de avaliação dos balanços hídricos e energéticos em diferentes escalas temporais e espaciais**. João Pessoa/PB: 2004.
- Iden, S. C. et al. Numerical test of the laboratory evaporation method using coupled water, vapor and heat flow modelling. **Journal of Hydrology**, v. 570, p. 574–583, 2019.
- Indarto; Novita, E.; Wahyuningsih, S. **Preliminary study on baseflow separation at watersheds in East Java regions**. Agriculture and Agricultural Science Procedia. *Annals...* Elsevier. 2016.
- IUSS Working Group WRB. **World Reference Base for Soil Resources 2014, update 2015, International soil classification system for naming soils and creating legends for soil maps**. Rome: Food and Agriculture Organization (FAO) of the United Nations (UN), 2015.
- Iwema, J. et al. Investigating temporal field sampling strategies for site-specific calibration of three soil moisture–neutron intensity parameterisation methods. **Hydrology and Earth System Sciences**, v. 19, p. 3203–3216, 2015.
- Jackson, T. J. III. Measuring surface soil moisture using passive microwave remote sensing. **Hydrological Processes**, v. 7, p. 139–152, 1993.
- Jakobi, J. et al. Cosmic ray neutron sensing for simultaneous soil water content and biomass quantification in drought conditions. **Water Resources Research**, v. 54, p. 7383–7402, 2018.
- Jensen, J. R. **Sensoriamento remoto do ambiente: uma perspectiva em recursos terrestres**. São José dos Campos/SP: Editora Parênteses, 2009.
- Ji, L.; Senay, G. B.; Verdin, J. P. Evaluation of the Global Land Data Assimilation System (GLDAS) air temperature data products. **Journal of Hydrometeorology**, p. 2463–2480, 2015.
- Jia, S. et al. Estimating live fuel moisture using SMAP L-band radiometer soil moisture for southern California, USA. **Remote Sensing**, v. 11, n. 1575, p. 1–20, 2019.
- Jiang, Z. et al. Development of a two-band enhanced vegetation index without a blue band. **Remote Sensing of Environment**, v. 112, p. 3833–3845, 2008.
- Jie, Z. et al. Combination of soil-water balance models and water-table fluctuation methods for evaluation and improvement of groundwater recharge calculations. **Hydrogeology Journal**, v. 19, n. 8, p. 1487–1502, 2011.
- Justice, C. O. et al. An overview of MODIS Land data processing and product status. **Remote Sensing of Environment**, v. 83, p. 3–15, 2002.
- Kahsay, G. H. et al. Spatial groundwater recharge estimation in Raya basin, Northern Ethiopia: an approach using GIS based water balance model. **Sustainable Water Resources Management**, v. 5, p. 961–975, 2019.
- Kayet, N. et al. Evaluation of soil loss estimation using the RUSLE model and SCS-CN method in hillslope mining areas. **International Soil and Water Conservation Research**, v. 6, n. 1, p. 31–42, 2018.
- Khalaf, A.; Donoghue, D. Estimating recharge distribution using remote sensing: A case study from the West Bank. **Journal of Hydrology**, v. 414–415, p. 354–363, 2012.
- Kodama, M.; Kudo, S.; Kosuge, T. Application of atmospheric neutrons to soil moisture measurement. **Soil Science**, v. 140, n. 4, p. 237–242, 1985.

- Köhli, M. et al. Footprint characteristics revised for field-scale soil moisture monitoring with cosmic-ray neutrons. **Water Resources Research**, v. 51, n. 7, p. 5772–5790, 2015.
- Köppen, W. Das geographische System der Klimate. In: KÖPPEN, W. AND GEIGER, G. (Ed.). **Handbuch der Klimatologie**. Berlin: Gebrüder Borntraeger, p. 1–44, 1936
- Koster, R. D.; Suarez, M. J. **Technical report series on global modeling and data assimilation: Energy and water balance calculations in the mosaic LSM**. Greenbelt/MD: 1996.
- Kubicz, J. et al. Groundwater recharge assessment in dry years. **Environmental Earth Sciences**, v. 78, n. 555, p. 1–9, 2019.
- Kwoczyńska, B. et al. Analysis of land development conformity obtained using photogrammetric and remote sensing methods with Geographic Information System (GIS) technology. **International Journal of Physical Sciences**, v. 9, n. 7, p. 123–139, 2014.
- Lal, D.; Peters, B. **Cosmic ray produced radioactivity on the Earth**. Berlin, Heidelberg: Springer, 1967.
- Lal, M. et al. Evaluation of the Soil Conservation Service curve number methodology using data from agricultural plots. **Hydrogeology Journal**, v. 25, n. 1, p. 151–167, 2016.
- Lal, M.; Mishra, S. K.; Kumar, M. Reverification of antecedent moisture condition dependent runoff curve number formulae using experimental data of Indian watersheds. **Catena**, v. 173, p. 48–58, 2019.
- Landsberg, J. J.; Gower, S. T. **Applications of physiological ecology to forest management**. San Diego/CA: Academic Press, 1997.
- Langan, L. N.; Lammers, D. A. Definitive criteria for hydrologic soil groups. **Soil survey horizons**, v. 32, n. 3, p. 69–77, 1991.
- Latorre, M. L. et al. Integração de dados de sensoriamento remoto multi resoluções para a representação da cobertura da terra utilizando campos contínuos de vegetação e classificação por árvores de decisão. **Revista Brasileira de Geofísica**, v. 25, p. 63–74, 2007.
- Leão, T. P.; Gentry, R. Numerical modeling of the effect of variation of boundary conditions on vadose zone hydraulic properties. **Revista Brasileira de Ciência do Solo**, v. 35, n. 1, p. 263–272, 2011.
- Leon, A.; Khalsa, S. J. S.; Leslie, S. **SMAP data and services at the NASA DAACS**. IEEE International Geoscience and Remote Sensing Symposium (IGARSS). **Annals...** 2015
- Letaw, J. R.; Normand, E. Guidelines for predicting single-event upsets in neutron environments. **IEEE Transactions on Nuclear Science**, v. 38, n. 6, p. 1500–1506, 1991.
- Leterme, B.; Gedeon, M.; Jacques, D. **Groundwater recharge modeling of the Nete catchment (Belgium) using the HYDRUS-1D – MODFLOW package**. Proceedings of 4th International Conference: HYDRUS software applications to subsurface flow and contaminant transport problems. **Annals...** Prague: Czech University of Life Sciences and PC-Progress, 2013
- Leterme, B.; Mallants, D.; Jacques, D. Sensitivity of groundwater recharge using climatic analogues and HYDRUS-1D. **Hydrology and Earth System Sciences**, v. 16, p. 2485–2497, 2012.
- Li, C. et al. Characteristics of impervious surface and its effect on direct runoff: a case study in a rapidly urbanized area. **Water Supply**, v. 19, n. 7, p. 1885–1891, 2019.
- Li, Z. et al. Multiscale hydrologic applications of the latest satellite precipitation products in the Yangtze river basin using a distributed hydrologic model. **Journal of Hydrometeorology**, v. 16, n. 1, p. 407–426, 2015.
- Liang, X. et al. A simple hydrologically based model of land surface water and energy fluxes for general circulation models. **Journal of Geophysical Research**, v. 99, n. D7, p. 14415–

14428, 1994.

- Lillesand, T. M.; Kiefer, R. W.; Chipman, J. W. **Remote sensing and image interpretation**. New York/NY: John Wiley & Sons, Inc., 2004.
- Lima, R. N. de S.; Ribeiro, C. B. de M. Spatial variability of daily evapotranspiration in a mountainous watershed by coupling surface energy balance and solar radiation model with gridded weather dataset. **Proceedings**, v. 2, n. 342, p. 1–6, 2018.
- Linhares, F. M. et al. Avaliação da vulnerabilidade e do risco à contaminação das águas subterrâneas da bacia hidrográfica do rio Gramame (PB). **Sociedade & Natureza**, v. 26, n. 1, p. 139–157, 2014.
- Liu, Q. et al. The contributions of precipitation and soil moisture observations to the skill of soil moisture estimates in a land data assimilation system. **Journal of Hydrometeorology**, v. 12, p. 750–765, 2011.
- Liu, S. M. et al. Measurements of evapotranspiration from eddy-covariance systems and large aperture scintillometers in the Hai river basin, China. **Journal of Hydrologic**, v. 487, p. 24–38, 2013.
- Liu, W. et al. A worldwide evaluation of basin-scale evapotranspiration estimates against the water balance method. **Journal of Hydrology**, v. 538, p. 82–95, 2016.
- Liu, Z. et al. Global precipitation measurement mission products and services at the nasa ges disc. **Bulletin of the American Meteorological Society**, v. 98, n. 3, p. 437–444, 2017.
- Loarie, S. R. et al. Direct impacts on local climate of sugar-cane expansion in Brazil. **Nature Climate Change**, v. 1, n. 5, p. 105–109, 2011.
- Lombardi Neto, F. et al. **Nova abordagem para calculo de espaçamento entre terracos**. Simpósio sobre terraceamento agrícola. **Annals...** Campinas/SP: Fundação Cargill, 1989
- Long, D. et al. Deriving scaling factors using a global hydrological model to restore GRACE total water storage changes for China's Yangtze river basin. **Remote Sensing of Environment**, v. 168, p. 177–193, 2015.
- Long, D.; Longuevergne, L.; Scanlon, B. R. Uncertainty in evapotranspiration from land surface modeling, remote sensing, and GRACE satellites. **Water Resources Research**, v. 50, n. 2, p. 1131–1151, 2014.
- López López, P. et al. Improved large-scale hydrological modelling through the assimilation of streamflow and downscaled satellite soil moisture observations. **Hydrology and Earth System Sciences**, v. 20, n. 7, p. 3059–3076, 2016.
- Lu, D. et al. Land use/cover classification in the Brazilian Amazon using satellite images. **Pesquisa Agropecuária Brasileira**, v. 47, n. 9, p. 1185–1208, 2012.
- Lu, X. et al. Groundwater recharge at five representative sites in the Hebei Plain, China. **Groundwater**, v. 49, n. 2, p. 286–294, 2011.
- Lucas, M. et al. Evaluation of remotely sensed data for estimating recharge to an outcrop zone of the Guarani Aquifer System (South America). **Hydrogeology Journal**, p. 961–969, 2015.
- Lunetta, R. S. et al. Land-cover change detection using multi-temporal MODIS NDVI data. **Remote Sensing of Environment**, v. 105, p. 142–154, 2006.
- Luo, T.; Jutla, A.; Islam, S. Evapotranspiration estimation over agricultural plains using MODIS data for all sky conditions. **International Journal of Remote Sensing**, v. 36, n. 5, p. 1235–1252, 2015.
- Lv, M. et al. Water budget closure based on GRACE measurements and reconstructed evapotranspiration using GLDAS and water use data for two large densely-populated mid-latitude basins. **Journal of Hydrology**, v. 547, p. 585–599, 2017.

- Lv, M. et al. Assessment of runoff components simulated by GLDAS against UNH–GRDC dataset at global and hemispheric scales. **Water**, v. 10, n. 969, p. 1–17, 2018.
- Ly, S.; Charles, C.; Degré, A. Geostatistical interpolation of daily rainfall at catchment scale : the use of several variogram models in the Ourthe and Ambleve catchments, Belgium. **Hydrology and Earth System Sciences**, v. 15, p. 2259–2274, 2011.
- MA; SUDENE. **Levantamento exploratório-reconhecimento de solos do estado da Paraíba**. Technical Bulletin No. 15. Rio de Janeiro/RJ: Ministério da Agricultura (MA), Superintendência do Desenvolvimento do Nordeste (SUDENE), 1972.
- MABC. **Soil water storage capacity and available soil moisture**. Ministry Of Agriculture of British Columbia (MABC), 2015.
- Mabesoone, J. M. **Sedimentary basins of Northeast Brazil**. Recife. Editora Universitária, Federal University of Pernambuco (UFPE), p. 1–308, 1994.
- Maclaren, O. J.; Nicholson, R. **What can be estimated? Identifiability, estimability, causal inference and ill-posed inverse problems**. Technical course. Auckland/NZ: Cornell University, 2019.
- Mahmoud, S. H. Investigation of rainfall–runoff modeling for Egypt by using remote sensing and GIS integration. **Catena**, v. 120, p. 111–121, 2014.
- Mahmoud, S. H.; Alazba, A. A. A coupled remote sensing and the Surface Energy Balance based algorithms to estimate actual evapotranspiration over the western and southern regions of Saudi Arabia. **Journal of Asian Earth Sciences**, v. 124, p. 269–283, 2016.
- Maliva, R. G. Economics of managed aquifer recharge. **Water**, v. 6, n. 5, p. 1257–1279, 2014.
- Malkov, M. A.; Drury, L. O. Nonlinear theory of diffusive acceleration of particles by shock waves. **Reports on Progress in Physics**, v. 64, n. 4, p. 429–481, 2001.
- Marengo, J. A.; Alves, L. M.; Alvala, R. C. S. Climatic characteristics of the 2010–2016 drought in the semiarid Northeast Brazil region. **Anais da Academia Brasileira de Ciências**, v. 90, p. 1973–1985, 2018.
- Marengo, J. A.; Torres, R. R.; Alves, L. M. Drought in Northeast Brazil – past, present, and future. **Theoretical and Applied Climatology**, 2016.
- Mariano, D. A. et al. Use of remote sensing indicators to assess effects of drought and human-induced land degradation on ecosystem health in Northeastern Brazil. **Remote Sensing of Environment**, v. 213, p. 129–143, 2018.
- Martos-Rosillo, S. et al. Review on groundwater recharge in carbonate aquifers from SW Mediterranean (Betic Cordillera, S Spain). **Environmental Earth Sciences**, v. 74, n. 12, p. 7571–7581, 2015.
- Matei, D. **Runoff modeling using GIS: Application in torrential basins in the Apuseni Mountains**. PhD thesis. Vrije Universiteit Brussel, 2012.
- Mateo-Sagasta, J.; Zadeh, S. M.; Turrall, H. **Water pollution from agriculture: a global review**. Rome: Food and Agriculture Organization of the United Nations & International Water Management Institute. Available on: <<http://www.fao.org/3/a-i7754e.pdf>>. Access in: May, 2018. 2017.
- Mathias, S. A.; Sorensen, J. P. R.; Butler, A. P. Soil moisture data as a constraint for groundwater recharge estimation. **Journal of Hydrology**, v. 552, p. 258–266, 2017.
- Matos, R. M. D. The northeastern Brazilian Rift System. **Tectonics**, v. 11, n. 4, p. 766–791, 1992.
- Mccord, P.; Tonini, F.; Liu, J. The telecoupling GeoApp : a Web-GIS application to systematically analyze telecouplings and sustainable development. **Applied Geography**, v. 96, p. 16–28, 2018.

- Melo, D. C. D.; Wendland, E. Shallow aquifer response to climate change scenarios in a small catchment in the Guarani Aquifer outcrop zone. **Annals of the Brazilian Academy of Sciences**, v. 89, p. 391–406, 2017.
- Mendonça, J. C. et al. Assessment of evapotranspiration in North Fluminense region, Brazil, using MOIS products and SEBAL algorithm. In: IRMAK, A. (Ed.). **Evapotranspiration - Remote Sensing and Modeling**. 1 ed. Rijeka: INTECH. p. 1–18, 2012.
- Meresa, H. Modelling of river flow in ungauged catchment using remote sensing data: application of the empirical (SCS-CN), Artificial Neural Network (ANN) and Hydrological Model (HEC-HMS). **Modeling Earth Systems and Environment**, v. 5, n. 1, p. 257–273, 2019.
- Miranda, R. D. Q. et al. Reliability of MODIS evapotranspiration products for heterogeneous dry forest: a study case of Caatinga. **Advances in Meteorology**, v. 2017, n. 9314801, p. 1–15, 2017.
- Mishra, S. K. et al. Comparison of AMC-dependent CN-conversion Formulae. **Water Resources Management**, v. 22, p. 1409–1420, 2008.
- Mls, J. Formulation and solution of fundamental problems of vertical infiltration. **Vodohosp. Čas.**, v. 30, p. 304–313, 1982.
- Mohan, C. et al. Predicting groundwater recharge for varying land cover and climate conditions – a global meta-study. **Hydrology and Earth System Sciences**, v. 22, p. 2689–2703, 2018.
- Montenegro, A. A. A. et al. Spatio temporal soil moisture dynamics and runoff under different soil cover conditions in a semiarid representative basin in Brazil. **Advances in Geosciences**, v. 48, p. 19–30, 2019.
- Montenegro, A. A. A.; Ragab, R. Hydrological response of a Brazilian semi-arid catchment to different land use and climate change scenarios: A modelling study. **Hydrological Processes**, v. 24, n. 19, p. 2705–2723, 2010.
- Montzka, C. et al. Validation of spaceborne and modelled surface soil moisture products with Cosmic-Ray Neutron Probes. **Remote Sensing**, v. 9, n. 2, p. 1–30, 2017.
- Morais, R. M. O. et al. Fácies sedimentares e ambientes deposicionais associados aos depósitos da Formação Barreiras no Estado do Rio de Janeiro. **Geologia USP (Série Científica)**, v. 6, n. 2, p. 19–30, 2006.
- Mu, Q. et al. Development of a global evapotranspiration algorithm based on MODIS and global meteorology data on MODIS and global meteorology data. **Remote Sensing of Environment**, v. 111, p. 519–536, 2007.
- Mu, Q.; Zhao, M.; Running, S. W. Improvements to a MODIS global terrestrial evapotranspiration algorithm improvements to a MODIS global terrestrial evapotranspiration algorithm. **Remote Sensing of Environment**, v. 115, n. 8, p. 1781–1800, 2011.
- Mualem, Y. A new model for predicting the hydraulic conductivity of unsaturated porous media. **Water Resources Research**, v. 12, n. 3, p. 513–522, 1976.
- Münch, Z. et al. Satellite earth observation as a tool to conceptualize hydrogeological fluxes in the Sandveld, South Africa. **Hydrogeology Journal**, v. 21, p. 1053–1070, 2013.
- Mushtaha, A.; van Camp, M.; Walraevens, K. Quantification of recharge and runoff from rainfall using new GIS tool: example of the Gaza Strip Aquifer. **Water**, v. 11, n. 84, p. 1–14, 2019.
- Muthu, A. C. L.; Santhi, M. H. Estimation of surface runoff potential using SCS-CN method integrated with GIS. **Indian Journal of Science and Technology**, v. 8, p. 1–5, 2015.
- Nagarajan, M.; Basil, G. Remote sensing- and GIS-based runoff modeling with the effect of land-use changes (a case study of Cochin corporation). **Natural Hazards**, v. 73, n. 3, p. 2023–2039, 2014.

- Nagarajan, N.; Poongothai, S. Spatial mapping of runoff from a watershed using SCS-CN method with remote sensing and GIS. **Journal of Hydrologic Engineering**, v. 17, n. 11, p. 1268–1277, 2012.
- Narasimhan, T. N. **Hydrological cycle and water budgets**. Elsevier Inc., 2009.
- Naylor, S. et al. A hydrogeological approach to quantifying groundwater recharge in various glacial settings of the mid-continental USA. **Hydrological Processes**, v. 30, p. 1594–1608, 2016.
- Nesterenok, A. Numerical calculations of cosmic ray cascade in the Earth's atmosphere – results for nucleon spectra. **Nuclear Instruments and Methods in Physics Research B**, v. 295, p. 99–106, 2013.
- Neto, D. C.; Chang, H. K.; van Genuchten, M. T. A mathematical view of water table fluctuations in a shallow aquifer in Brazil. **Groundwater**, v. 54, p. 82–91, 2013.
- Nemes, A. et al. Description of the unsaturated soil hydraulic database UNSODA version 2.0. **Journal of Hydrology**, v. 251, n. 3–4, p. 151–162, 2001.
- Neuman, S. P.; Feddes, R. A.; Bresler, E. **Finite element simulation of flow in saturated-unsaturated soils considering water uptake by plants, third annual report** **Third Annual Report, Project No. A10- SWC-77**. Haifa, Israel: Technion, Israel Institute of Technology, 1974.
- Ni, B. et al. **Review on the groundwater potential evaluation based on remote sensing technology**. IOP Conf. Series: Materials Science and Engineering. **Annals...** 2018
- Nimmo, J. R.; Horowitz, C.; Mitchell, L. Discrete-storm water-table fluctuation method to estimate episodic recharge. **Groundwater**, v. 53, n. 2, p. 282–292, 2015.
- Noojipady, P. et al. Forest carbon emissions from cropland expansion in the Brazilian Cerrado biome. **Environmental Research Letters**, v. 12, n. 2, p. 1–11, 2017.
- NRCS. **Urban hydrology for small watersheds**. Natural Resources Conservation Service (NRCS), United States Department of Agriculture (USDA), 1986.
- NRCS. Land use and treatment. In: VICTOR MOCKUS; NRCS (Eds.). **Part 630 Hydrology, National Engineering Handbook**. Washington/DC: Natural Resources Conservation Service (NRCS), United States Department of Agriculture (USDA). p. 1–11, 2002.
- NRCS. Hydrologic soil-cover complexes. In: MOCKUS, V.; MOODY, H. F.; NRCS (Eds.). **Part 630 Hydrology, National Engineering Handbook**. Washington/DC: Natural Resources Conservation Service (NRCS), United States Department of Agriculture (USDA), p. 1–20, 2004.
- NRCS. **Saturated hydraulic conductivity in relation to soil texture**. Natural Resources Conservation Service (NRCS), United States Department of Agriculture (USDA). 2019.
- Oliveira, B. S. et al. Improved albedo estimates implemented in the METRIC model for modeling energy balance fluxes and evapotranspiration over agricultural and natural areas in the Brazilian Cerrado. **Remote Sensing**, v. 10, n. 1181, p. 1–27, 2018a.
- Oliveira, P. T. S. et al. Trends in water balance components across the Brazilian Cerrado. **Water Resources Research**, v. 50, n. 9, p. 7100–7114, set. 2014.
- Oren, R. et al. Survey and synthesis of intra- and interspecific variation in stomatal sensitivity to vapour pressure deficit. **Plant, Cell & Environment**, v. 22, n. 12, p. 1515–1526, 1999.
- Otoni, M. V. et al. Hydrophysical Database for Brazilian Soils (HYBRAS) and pedotransfer functions for water retention. **Vadose Zone Journal**, v. 17, n. 1, p. 1–17, 2018.
- Paca, V. H. Da M. et al. The spatial variability of actual evapotranspiration across the Amazon River Basin based on remote sensing products validated with flux towers. **Ecological Processes**, v. 8, n. 6, p. 1–20, 2019.



- Palharini, R. S. A.; Vila, D. A. Climatological behavior of precipitating clouds in the northeast region of Brazil. **Advances in Meteorology**, p. 17–21, 2017.
- Pardo, J. M. et al. Instrumental monitoring of the subsidence due to groundwater withdrawal in the city of Murcia (Spain). **Environmental Earth Sciences**, v. 70, n. 5, p. 1957–1963, 2013.
- Penman, H. L. Natural evaporation from open water, bare soil and grass. **Proceedings of the Royal Society of London**, v. 193, p. 120–145, 1948.
- Phillips, F. M.; Stone, W. D.; Fabryka-Martin, J. T. An improved approach to calculating low-energy cosmic-ray neutron fluxes near the land/atmosphere interface. **Chemical Geology**, v. 175, n. 2001, p. 689–701, 2001.
- Pinheiro, E. A. R.; Costa, C. A. G.; de Araújo, J. C. Effective root depth of the Caatinga biome. **Journal of Arid Environments**, v. 89, p. 1–4, 2013.
- Ponce, V. M.; Hawkins, R. H. Runoff curve number: has it reached maturity? **Journal of Hydrologic Engineering**, v. 1, n. 1, p. 11–19, 1996.
- Prakash, S. et al. From TRMM to GPM: How well can heavy rainfall be detected from space? **Advances in Water Resources**, v. 88, p. 1–7, 2016.
- Rabelo, J. L.; Wendland, E. Assessment of groundwater recharge and water fluxes of the Guarani Aquifer System, Brazil. **Hydrogeology Journal**, v. 17, p. 1733–1748, 2009.
- Rahman, M. A. et al. An integrated study of spatial multicriteria analysis and mathematical modelling for managed aquifer recharge site suitability mapping and site ranking at Northern Gaza coastal aquifer. **Journal of Environmental Management**, v. 124, p. 25–39, 2013.
- Rahmati, M. et al. Development and analysis of the Soil Water Infiltration Global database. **Earth System Science Data**, p. 1237–1263, 2018.
- Raoufi, R.; Beighley, E. Estimating daily global evapotranspiration using Penman–Monteith equation and remotely sensed land surface temperature. **Remote Sensing**, v. 9, n. 1138, 2017.
- Refsgaard, J. C. et al. Uncertainty in the environmental modelling process – a framework and guidance. **Environmental Modelling & Software**, v. 22, p. 1543–1556, 2007.
- Regan, H. M.; Colyvan, M.; Burgman, M. A. A taxonomy and treatment of uncertainty for ecology and conservation biology. **Ecological Applications**, v. 12, n. 2, p. 618–628, 2002.
- Reichle, R. H. et al. Assessment of the SMAP Level-4 Surface and root-zone soil moisture product using in situ measurements. **Journal of Hydrometeorology**, v. 18, p. 2621–2645, 2017.
- Reichle, R. H. et al. **Soil Moisture Active Passive (SMAP) project assessment report for version 4 of the L4\_SM sata product**. Technical Report Series on Global Modeling and Data Assimilation, volume 52. Greenbelt/MD: NASA Goddard Space Flight Center, 2018.
- Reynolds, D.; Canada, A. A method for simultaneous in situ measurement in the vadose zone of field-saturated hydraulic conductivity, sorptivity and the conductivity-pressure head relationship. **Groundwater Monitoring & Remediation**, v. 6, n. 1, p. 84–95, 1986.
- Ribeiro, M. C. et al. The Brazilian Atlantic Forest: how much is left, and how is the remaining forest distributed? Implications for conservation. **Biological Conservation**, v. 142, n. 6, p. 1141–1153, 2009.
- Ries, F. et al. Recharge estimation and soil moisture dynamics in a Mediterranean, semi-arid karst region. **Hydrology and Earth System Sciences**, v. 19, n. 3, p. 1439–1456, 2015.
- Rivera Villarreyes, C. A.; Baroni, G.; Oswald, S. E. Integral quantification of seasonal soil moisture changes in farmland by cosmic-ray neutrons. **Hydrology and Earth System Sciences**, v. 15, n. 12, p. 3843–3859, 2011.
- Rivera Villarreyes, C. A. **Cosmic-ray neutron sensing for soil moisture measurements in cropped**

- fields**. PhD thesis. Potsdam: University of Potsdam, 2013.
- Rivera Villarreyes, C. A.; Baroni, G.; Oswald, S. E. Calibration approaches of cosmic-rayneutron sensing for soil moisture measurement in cropped fields. **Hydrology and Earth System Sciences Discussions**, v. 10, p. 4237–4274, 2013.
- Rivera Villarreyes, C. A.; Baroni, G.; Oswald, S. E. Inverse modelling of cosmic-ray soil moisture for field-scale soil hydraulic parameters. **European Journal of Soil Science**, v. 65, n. 6, p. 876–886, 2014.
- Robinson, D. A. et al. Soil moisture measurement for ecological and hydrological watershed-scale observatories: a review. **Vadose Zone Journal**, v. 7, n. 1, 2008.
- Rocha, A. V.; Shaver, G. R. Advantages of a two band EVI calculated from solar and photosynthetically active radiation fluxes. **Agricultural and Forest Meteorology**, v. 149, n. 9, p. 1560–1563, 2009.
- Rodell, M. et al. **NASA/NOAA’s Global Land Data Assimilation System (GLDAS): recent results and future plans**. Proceedings of ECMWF/ELDAS Workshop on Land Surface Assimilation. **Annals...** 2004
- Rosolem, R. et al. The effect of atmospheric water vapor on neutron count in the cosmic-ray soil moisture observing system. **Journal of Hydrometeorology**, v. 14, p. 1659–1672, 2013.
- Ross, C. W. et al. Data Descriptor: HYSOGs250m, global gridded hydrologic soil groups for curve-number-based runoff modeling. **Nature: Scientific Data**, v. 5, p. 1–8, 2018.
- Rossetti, D. F. et al. Contribution to the stratigraphy of the onshore Paraíba Basin, Brazil. **Anais da Academia Brasileira de Ciência**, v. 84, n. 2, p. 313–334, 2012.
- Rossetti, D. F. et al. Late Quaternary sedimentation in the Paraíba Basin, Northeastern Brazil: implications for the interplay among landform, sea level and tectonics in Eastern South America passive margin. **Palaeogeography, Palaeoclimatology, Palaeoecology**, v. 300, n. 1–4, p. 191–204, 2011.
- Rozante, J. R. et al. Evaluation of TRMM/GPM blended daily products over Brazil. **Remote Sensing**, v. 10, n. 882, p. 1–17, 2018.
- Ruhoff, A. L. et al. Assessment of the MODIS global evapotranspiration algorithm using eddy covariance measurements and hydrological modelling in the Rio Grande basin Assessment of the MODIS global evapotranspiration algorithm using eddy covariance measurements and hydrologic. **Hydrological Sciences Journal**, v. 58, n. 8, p. 1658–1676, 2013.
- Running, S. W. et al. **NASA Earth Observing System MODIS land algorithm user’s guide: MODIS global terrestrial evapotranspiration (ET) Product (NASA MOD16A2/A3)**. National Aeronautics and Space Administration (NASA), 2017.
- Sadeghi, M. et al. An analytical model for estimation of land surface net water flux from near-surface soil moisture observations. **Journal of Hydrology**, v. 570, p. 26–37, 2018.
- Salles, L. et al. Seasonal effect on spatial and temporal consistency of the new GPM-based IMERG-V5 and GSMaP-V7 satellite precipitation estimates in Brazil’s Central Plateau region. **Water**, v. 11, n. 668, p. 1–18, 2019.
- Santos, C. A. G.; Silva, J. F. C. B. C.; da Silva, R. M. Caracterização hidrodinâmica dos solos da bacia experimental do riacho Guaraira utilizando o Método Beerkan. **Revista Brasileira de Recursos Hídricos**, v. 17, p. 149–160, 2012.
- Santos, F. A. C. et al. Desempenho de metodologias para estimativa do saldo de radiação a partir de imagens MODIS. **Revista Brasileira de Meteorologia**, v. 3, p. 295–306, 2015.
- Sartori, A. et al. Classificação hidrológica de solos brasileiros para a estimativa da chuva excedente com o Método do Serviço de Conservação do Solo dos Estados Unidos Parte 2: Aplicação. **Revista Brasileira de Recursos Hídricos**, v. 10, p. 19–29, 2005.

- Sartori, A. **Desenvolvimento de critérios para classificação hidrológica do solos e determinação de valores de referência para o parâmetro CN**. PhD thesis. Campina State University, 2010.
- Satgé, F. et al. Comparative assessments of the latest GPM Mission's spatially enhanced satellite rainfall products over the main Bolivian watersheds. **Remote Sensing**, v. 9, n. 369, p. 1–16, 2017.
- Sato, T.; Niita, K. Analytical functions to predict cosmic-ray neutron spectra in the atmosphere. **Radiation Research**, v. 166, n. 3, p. 544–555, 2006.
- Saxton, K. E.; Rawls, W. J. Soil water characteristic estimates by texture and organic matter for hydrologic solutions. **Soil Science Society of America Journal**, v. 70, p. 1569–1578, 2006.
- Scanlon, B. R.; Healy, R. W.; Cook, P. G. Choosing appropriate techniques for quantifying groundwater recharge. **Hydrogeology Journal**, v. 10, n. 1, p. 18–39, 2002.
- Scarinci, A. L.; Marineli, F. The wave model of light as a tool to explain the causes of color. **Revista Brasileira de Ensino de Física**, v. 36, n. 1, p. 1-14, 2014.
- Schaap, M. G.; Leij, F. J.; van Genuchten, M. T.. Rosetta: a computer program for estimating soil hydraulic parameters with hierarchical pedotransfer functions. **Journal of Hydrology**, v. 251, p. 163–176, 2001.
- Schattan, P. et al. Continuous monitoring of snowpack dynamics in alpine terrain by aboveground neutron sensing, **Water Resources Research**, v. 53, p. 3615–3634, 2017.
- Scheiffele, L. M. **Assessment of soil moisture dynamics on an irrigated maize field using cosmic ray neutron sensing**. Master thesis. Potsdam: University of Potsdam, 2015.
- Schlickeiser, R. **Cosmic Ray Astrophysics**. Heidelberg: Springer, 2002.
- Schrön, M. Cosmic-ray neutron sensing and its applications to soil and land surface hydrology. **PhD thesis**. Potsdam: University of Potsdam, 2016.
- Schrön, M. et al. Improving calibration and validation of cosmic-ray neutron sensors in the light of spatial sensitivity – theory and evidence. **Hydrology and Earth System Sciences**, v. 21, p. 5009–5030, 2017.
- Schrön, M. et al. Intercomparison of cosmic-ray neutron sensors and water balance monitoring in an urban environment. **Geoscientific Instrumentation Methods and Data Systems**, v. 7, p. 83–99, 2018.
- SCS. Section 4: Hydrology. In: **National engineering hand-book**. Washington/DC: Soil Conservation Service (SCS), United States Department of Agriculture (USDA), 1972.
- Sears, V. F. Neutron scattering lengths and cross sections. **Neutron News**, v. 3, n. 3, p. 26–37, 1992.
- Sharifi, E.; Steinacker, R.; Saghafian, B. Assessment of GPM-IMERG and other precipitation products against gauge data under different topographic and climatic conditions in Iran: preliminary results. **Remote Sensing**, v. 8, n. 135, p. 1–24, 2016.
- Shaw, G.A.; Burke, H. K. Spectral imaging for remote sensing. **Lincoln Laboratory Journal**, v. 14, n. 1, p. 1–28, 2003.
- Sheffield, J. et al. Closing the terrestrial water budget from satellite remote sensing. **Geophysical Research Letters**, v. 36, n. 7, p. 1–5, 2009.
- Sheffield, J.; Wood, E. F.; Roderick, M. L. Little change in global drought over the past 60 years. **Nature**, v. 491, n. 7424, p. 435–438, 2012.
- Shuttleworth, J. et al. The COsmic-ray Soil Moisture Interaction Code (COSMIC) for use in data assimilation. **Hydrology and Earth System Sciences**, v. 17, p. 3205–3217, 2013.
- Shuttleworth, W. J. Evaporation. In: MAIDMENT, D. R. (Ed.). **Handbook of Hydrology**. New

- York/NY: McGraw Hill, p. 4.1-4.53, 1993.
- Siejka, M. et al. Algorithm of land cover spatial data processing for the local flood risk mapping. **Survey Review**, v. 50, n. 362, p. 1–7, 2017.
- Silva, A. M.; Silva, R. M.; Santos, C. A. G. Automated surface energy balance algorithm for land (ASEBAL) based on automating endmember pixel selection for evapotranspiration calculation in MODIS orbital images. **International Journal of Applied Earth Observation and Geoinformation**, v. 79, p. 1–11, 2019.
- Silva, B. B. et al. Changes to the energy budget and evapotranspiration following conversion of tropical savannas to agricultural lands in São Paulo State, Brazil. **Ecohydrology**, v. 8, n. 7, p. 1272–1283, 2015.
- Silva, C. O. F.; Manzione, R. L.; Teixeira, A. H. C. Spatial modeling of evapotranspiration and water productivity in the outcrop area of the Guarani Aquifer in São Paulo state between 2013 and 2015. **Holos Environment**, v. 18, p. 126–140, 2018.
- Silva, J. F. C. B. C. **Análise espacial das características hidrodinâmicas e do uso e ocupação do solo da bacia experimental do riacho Guaraíra mediante uso de geotecnologias**. Master thesis. Federal University of Paraíba, 2009.
- Šimůnek, J. et al. Numerical modeling of contaminant transport using HYDRUS and its specialized modules. **Journal of the Indian Institute of Science**, v. 93, n. 2, p. 265–284, 2013a.
- Šimůnek, J. et al. **The HYDRUS-1D software package for simulating the one-dimensional movement of water, heat, and multiple solutes in variably-saturated media 1.0**. Riverside/CA: University of California, Department of Environmental Sciences, 2013b.
- Šimůnek, J. Estimating groundwater recharge using HYDRUS-1D. **Engineering Geology and Hydrogeology**, v. 29, p. 25–36, 2015.
- Šimůnek, J. **Convergence issue with sand and clay combination**. PC-PROGRESS: Available on: <https://www.pc-progress.com/forum/viewtopic.php?f=4&t=3241>, 2018.
- Šimůnek, J.; van Genuchten, M. T. Modeling nonequilibrium flow and transport processes using HYDRUS. **Vadose Zone Journal**, v. 7, n. 2, p. 782–797, 2008.
- Šimůnek, J.; van Genuchten, M. T.; Šejna, M. Development and applications of the HYDRUS and STANMOD software packages and related codes. **Vadose Zone Journal**, v. 7, n. 2, p. 587–600, 2008.
- Šimůnek, J.; van Genuchten, M. T.; Šejna, M. Recent developments and applications of the HYDRUS computer software packages. **Vadose Zone Journal**, v. 15, n. 7, p. 1–25, 2016.
- Singh, A. et al. An assessment of groundwater recharge estimation techniques for sustainable resource management. **Groundwater for Sustainable Development**, v. 9, n. 100218, 2019.
- Sinha, M. K. et al. Impact of urbanization on surface runoff characteristics at catchment scale. **Water Resources and Environmental Engineering I**, p. 31–42, 2019.
- Skofronick-Jackson, G. et al. The global precipitation measurement (GPM) mission for science and society. **Bulletin of the American Meteorological Society**, v. 98, n. 8, p. 1679–1695, 2017.
- Sobhani, G. **A review of selected small watershed design methods for possible adoption to Iranian conditions**. Master thesis. Logan/UT: Utah State University, 1975.
- SOSMA; INPE. **Atlas dos remanescentes florestais da Mata Atlântica**. Technical report. São Paulo/SP: SOS Mata Atlântica (SOSMA) and Instituto Nacional de Pesquisas Espaciais (INPE), 2019.
- Souza, A. G. S. S.; Neto, A. R.; Souza, L. L. Use of SMOS L3 soil moisture data : validation and drought assessment for Pernambuco state, Northeast Brazil. **Remote Sensing**, v. 10, n. 1314, p. 1–19, 2018.

- Souza, V. De A. et al. Evaluation of MOD16 algorithm over irrigated rice paddy using flux tower measurements in Southern Brazil. **Water**, v. 11, n. 1911, p. 1–23, 2019.
- Subramanian, T. S.; Abraham, M. Assessment of natural groundwater recharge: a case study of North Chennai Aquifer. **Environmental Geosciences**, v. 26, n. 2, 41–50, 2019.
- Sun, W. et al. Evaluation and correction of GPM IMERG precipitation products over the capital circle in Northeast China at multiple spatiotemporal scales. **Advances in Meteorology**, v. 2018, p. 1–14, 2018.
- Sun, Y. et al. Inverse modeling of hydrologic parameters using surface flux and runoff observations in the Community Land Model. **Hydrology and Earth System Sciences**, v. 17, p. 4995–5011, 2013.
- Sutanto, S. J. et al. Partitioning of evaporation into transpiration, soil evaporation and interception: a comparison between isotope measurements and a HYDRUS-1D model. **Hydrology and Earth System Sciences**, v. 16, n. 8, p. 2605–2616, 2012.
- Szilágyi, J. et al. Mapping mean annual groundwater recharge in the Nebraska Sand Hills, USA. **Hydrogeology Journal**, v. 19, n. 8, p. 1503–1513, 2011.
- Szilágyi, J.; Kovács, Á.; Józsa, J. Remote-sensing based groundwater recharge estimates in the Danube-Tisza sand plateau region of Hungary. **Journal of Hydrology and Hydromechanics**, v. 60, n. 1, p. 64–72, 2012.
- Tan, M. L.; Duan, Z. Assessment of GPM and TRMM precipitation products over Singapore. **Remote Sensing**, v. 9, n. 720, p. 1–16, 2017.
- Tang, G. et al. Statistical and hydrological comparisons between TRMM and GPM Level-3 products over a midlatitude basin: is day-1 IMERG a good successor for TMPA 3B42V7? **Journal of Hydrometeorology**, v. 17, n. 1, p. 121–137, 2016.
- Tarantola, A. **Inverse Problem Theory and Methods for Model Parameter Estimation**. Philadelphia/PA: Society for Industrial and Applied Mathematics, 2005.
- Tapley, B. D. et al. The gravity recovery and climate experiment: Mission overview and early results. **Geophysical Research Letters**, v. 31, n. 9, p. 1–4, 2004.
- Teixeira, A. H. D. C. et al. Coupling MODIS images and agrometeorological data for agricultural water productivity analyses in the Mato Grosso state, Brazil. **Remote Sensing for Agriculture, Ecosystems, and Hydrology**, v. 9239, n. 92390W, p. 1–14, 2014.
- Teixeira, A. H. de C. et al. Large-scale water productivity assessments with MODIS images in a changing semi-arid environment: a Brazilian case study. **Remote Sensing**, v. 5, p. 5783–5804, 2013.
- Templeton, R. C. et al. High-resolution characterization of a semiarid watershed: Implications on evapotranspiration estimates. **Journal of Hydrology**, v. 509, p. 306–319, 2014.
- Teutschbein, C.; Seibert, J. Bias correction of regional climate model simulations for hydrological climate-change impact studies: review and evaluation of different methods. **Journal of Hydrology**, v. 456–457, p. 12–29, 2012.
- Thakur, J. K.; Singh, S. K.; Ekanthalu, V. S. Integrating remote sensing, geographic information systems and global positioning system techniques with hydrological modeling. **Applied Water Science**, v. 7, n. 4, p. 1595–1608, 2016.
- Thornton, P. E. **Regional ecosystem simulation: combining surface- and satellite- based observations to study linkages between terrestrial energy and mass budgets**. PhD thesis. Missoula/MT: University of Montana, 1998.
- Tong, K. et al. Evaluation of satellite precipitation retrievals and their potential utilities in hydrologic modeling over the Tibetan Plateau. **Journal of Hydrology**, v. 519, p. 423–437, 2014.

- Tsuyuguchi, B. B. et al. Modelagem Hidro(geo)lógica (Resultados do WP 2). In: ABELS, A. et al. (Eds.). **PROJETO BRAMAR - Mitigação da Escassez de Água no Nordeste do Brasil**. 1. ed. Frankfurt: p. 38–57, 2018.
- Turini, N.; Thies, B.; Bendix, J. Estimating high spatio-temporal resolution rainfall from MSG1 and GPM IMERG based on machine learning: case study of Iran. **Remote Sensing**, v. 11, n. 2307, p. 1–27, 2019.
- Tyukavina, A. et al. Types and rates of forest disturbance in Brazilian Legal Amazon, 2000 – 2013. **Science Advances**, v. 2005, p. 1–16, 2017.
- Ulloa, J. et al. Two-step downscaling of TRMM 3b43 V7 precipitation in contrasting climatic regions with sparse monitoring: the case of Ecuador in tropical South America. **Remote Sensing**, v. 9, n. 758, p. 1–23, 2017.
- Usman, M.; Liedl, R.; Kavousi, A. Estimation of distributed seasonal net recharge by modern satellite data in irrigated agricultural regions of Pakistan. **Environmental Earth Sciences**, v. 74, p. 1463–1486, 2015.
- Uusitalo, L. et al. An overview of methods to evaluate uncertainty of deterministic models in decision support. **Environmental Modelling and Software**, v. 63, p. 24–31, 2015.
- Valle Junior, R. F. et al. Multi criteria analysis for the monitoring of aquifer vulnerability: a scientific tool in environmental policy. **Environmental Science & Policy**, v. 48, p. 250–264, 2015.
- van de Griend, A. A.; Owe, M. Bare soil surface resistance to evaporation by vapor diffusion under semiarid conditions. **Water Resources Research**, v. 30, n. 2, p. 181–188, 1994.
- van Genuchten, M. T. A closed-form equation for predicting the hydraulic conductivity of unsaturated soils. **Soil Science Society of America Journal**, v. 44, p. 892–898, 1980.
- van Genuchten, M. T. **A numerical model for water and solute movement in and below the root zone**. Research Report No 121. Riverside/CA: 1987.
- van Genuchten, M. T.; Gupta, S. K. A reassessment of the crop tolerance response function. **Journal of the Indian Society of Soil Science**, v. 41, n. 4, p. 730–737, 1993.
- van Steenbergen, N.; Ronsyn, J.; Willems, P. A non-parametric data-based approach for probabilistic flood forecasting in support of uncertainty communication. **Environmental Modelling and Software**, v. 33, n. 2012, p. 92–105, 2012.
- Vasconcelos, S. M. S.; Teixeira, Z. A.; Neto, J. A. Caracterização do Aquífero Jandaíra, porção situada no Estado do Ceará, Brasil. **Revista de Geologia**, v. 23, n. 1, p. 50–60, 2010.
- Velpuri, N. M. et al. A comprehensive evaluation of two MODIS evapotranspiration products over the conterminous United States: using point and gridded FLUXNET and water balance ET. **Remote Sensing of Environment**, v. 139, p. 35–49, 2013.
- Ventrella, D. et al. Assessment of the physically-based HYDRUS-1D model for simulating the water fluxes of a Mediterranean cropping system. **Water**, v. 11, n. 1657, p. 1–19, 2019.
- Vereecken, H. et al. Modeling soil processes: review, key challenges, and new perspectives. **Vadose Zone Journal**, v. 15, n. 5, 2016.
- Vink, J. et al. The X-ray synchrotron emission of RCW 86 and the implications for its age. **The Astrophysical Journal**. v. 648, n. 1, p 33–37, 2006.
- Vogel, T.; van Genuchten, M. T.; Cislérova, M. Effect of the shape of the soil hydraulic functions near saturation on variably-saturated flow predictions. **Advances in Water Resources**, v. 24, n. 2, p. 133–144, 2001.
- Vogeler, I. et al. Estimation of soil subsurface hydraulic conductivity based on inverse modelling and soil morphology. **Journal of Hydrology**, v. 574, p. 373–382, 2019.
- Voss, K. A. et al. Groundwater depletion in the Middle East from GRACE with implications for

- transboundary water management in the Tigris-Euphrates-Western Iran region. **Water Resources Research**, v. 49, p. 904–914, 2013.
- Walega, A.; Salata, T. Influence of land cover data sources on estimation of direct runoff according to SCS-CN and modified SME methods. **Catena**, v. 172, p. 232–242, 2019.
- Walker, D. et al. Insights from a multi-method recharge estimation comparison study. **Groundwater**, v. 57, n. 2, p. 245–258, 2019.
- Wan, Z. et al. Water balance-based actual evapotranspiration reconstruction from ground and satellite observations over the conterminous United States. **Water Resources Research**, v. 51, p. 6485–6499, 2015.
- Wang, C. et al. Global intercomparison and regional evaluation of GPM IMERG version-03, version-04 and its latest version-05 precipitation products: similarity, difference and improvements. **Journal of Hydrology**, v. 564, n. February, p. 342–356, 2018.
- Wang, D. et al. Evaluation of TMPA 3B42V7, GPM IMERG and CMAP precipitation estimates in Guangdong Province, China. **International Journal of Climatology**, v. 39, p. 738–755, 2019a.
- Wang, Q. et al. Application and accuracy of cosmic-ray neutron probes in three soil textures on the Loess Plateau, China. **Journal of Hydrology**, v. 569, p. 449–461, 2019b.
- Wang, S. et al. Evaluation of GPM IMERG V05B and TRMM 3B42V7 precipitation products over high mountainous tributaries in Lhasa with dense rain gauges. **Remote Sensing**, v. 11, n. 2080, p. 1–20, 2019c.
- Wang, T. et al. Using pedotransfer functions in vadose zone models for estimating groundwater recharge in semiarid regions. **Water Resources Research**, v. 45, p. 1–12, 2009.
- Wang, W. et al. Evaluation of GLDAS-1 and GLDAS-2 forcing data and Noah model simulations over China at the monthly scale. **Journal of Hydrometeorology**, v. 17, p. 2815–2833, 2016.
- Wang, Y. et al. Mapping tropical disturbed forests using multi-decadal 30 m optical satellite imagery. **Remote Sensing of Environment**, v. 221, p. 474–488, 2019d.
- Wei, G. et al. Evaluation of satellite-based precipitation products from IMERG V04A and V03D, CMORPH and TMPA with gauged rainfall in three climatologic zones in China. **Remote Sensing**, v. 10, n. 30, p. 1–22, 2018.
- Wendland, E.; Barreto, C.; Gomes, L. H. Water balance in the Guarani Aquifer outcrop zone based on hydrogeologic monitoring. **Journal of Hydrology**, v. 342, n. 3, p. 261–269, 2007.
- Weng, Q. **Remote sensing and GIS integration: theories, methods and applications**. New York/NY: McGraw-Hill, 2010.
- Wessolek, G.; Duijnsveld, W. H. M.; Trinks, S. Hydro-pedotransfer functions (HPTFs) for predicting annual percolation rate on a regional scale. **Journal of Hydrology**, v. 356, p. 17–27.
- Weynants, M. et al. **European HYdropedological Data Inventory (EU-HYDI)**. Luxembourg, GD Luxembourg: Publications Office of the European Union, 2013.
- Wolski, P.; Savenije, H. H. G. Dynamics of floodplain-island groundwater flow in the Okavango delta, Botswana. **Journal of Hydrology**, v. 320, p. 283–301, 2006.
- Woodward, D. E. et al. **Runoff curve number method: Examination of the initial abstraction ratio**. World Water and Environmental Resources Congress. **Annals...** 2003
- Wosten, J. H. M. et al. Development and use of a database of hydraulic properties of European soils. **Geoderma**, v. 90, p. 169–185, 1999.
- Wu, W.; Dickinson, R. E. Time scales of layered soil moisture memory in the context of land-atmosphere interaction. **Journal of Climate**, v. 17, n. 14, p. 2752–2764, 2004.

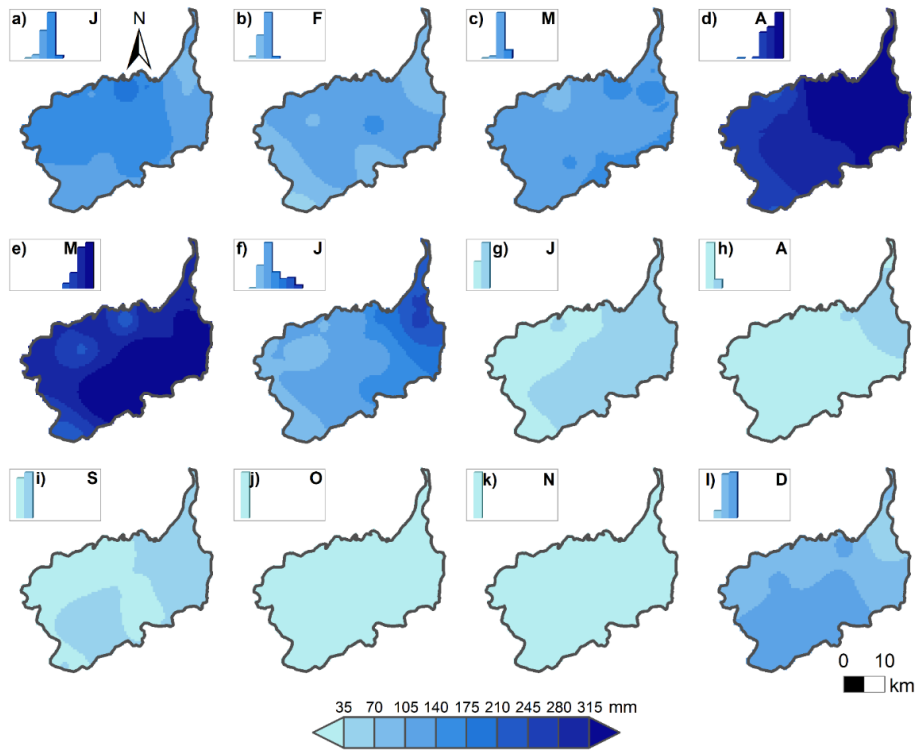
- Xavier, A. C.; King, C. W.; Scanlon, B. R. Daily gridded meteorological variables in Brazil (1980-2013). **International Journal of Climatology**, v. 36, n. 6, p. 2644–2659, maio 2016.
- Xu, L.; Baldocchi, D. D. Seasonal trends in photosynthetic parameters and stomatal conductance of blue oak (*Quercus douglasii*) under prolonged summer drought and high temperature. **Tree Physiology**, v. 23, n. 13, p. 865–877, 2003.
- Xu, S.; Shen, Y.; Niu, Z. Evaluation of the IMERG version 05B precipitation product and comparison with IMERG Version 04A over mainland China at hourly and daily scales. **Advances in Space Research**, v. 63, n. 8, p. 2387–2398, 2019.
- Xu, Y.; Beekman, H. E. Review : Groundwater recharge estimation in arid and semi-arid southern Africa. **Hydrogeology Journal**, v. 27, n. 3, p. 929–943, 2018.
- Yang, H.; Choi, H. T.; Lim, H. Applicability assessment of estimation methods for baseflow recession constants in small. **Water**, v. 10, n. 1074, p. 1–15, 2018.
- Yang, L. et al. A modified water-table fluctuation method to characterize regional groundwater discharge. **Water**, v. 10, n. 503, p. 1–16, 2018.
- Yang, M. **Benchmarking rainfall interpolation over the Netherlands**. Master thesis. Enschede: University of Twente, 2015.
- Yang, M. et al. Integrated multi-satellite retrievals for Global Precipitation Measurement (IMERG) over the Tianshan mountains of China. **Water**, v. 11, n. 1139, p. 1–20, 2019a.
- Yang, W. et al. Two base flow separation methods based on daily average gage height and discharge. **Water Supply**, v. 19, n. 7, p. 1978–1985, 2019b.
- Yee, M. S. et al. On the identification of representative in situ soil moisture monitoring stations for the validation of SMAP soil moisture products in Australia. **Journal of Hydrology**, v. 537, p. 367–381, 2016.
- Yin, L. et al. Groundwater-recharge estimation in the Ordos Plateau, China: comparison of methods. **Hydrogeology Journal**, v. 19, n. 8, p. 1563–1575, 2011.
- Yu, G. et al. Root water uptake and profile soil water as affected by vertical root distribution. **Plant Ecology**, v. 189, n. 1, p. 15–30, 2016.
- Yuan, F. et al. Assessment of GPM and TRMM multi-satellite precipitation products in streamflow simulations in a data-sparse mountainous watershed in Myanmar. **Remote Sensing**, v. 9, n. 302, p. 1–23, 2017.
- Yuan, F. et al. Evaluation of hydrological utility of IMERG Final run V05 and TMPA 3B42V7 satellite precipitation products in the Yellow River source region, China. **Journal of Hydrology**, v. 567, p. 696–711, 2018.
- Zema, D. A. et al. Simulating the hydrological response of a small tropical forest watershed (Mata Atlantica, Brazil) by the ANNAGNPS model. **Science of the Total Environment**, v. 636, p. 737–750, 2018.
- Zeng, H. et al. Accuracy validation of TRMM multisatellite precipitation analysis daily precipitation products in the Lancang River Basin of China. **Theoretical Applied Climatology**, v. 112, p. 389–401, 2013.
- Zeng, J. et al. A preliminary evaluation of the SMAP radiometer soil moisture product over United States and Europe using ground-based measurements. **IEEE International Geoscience and Remote Sensing Symposium (IGARSS)**, v. 54, n. 8, p. 4929–4940, 2016.
- Zhang, J. et al. Evaluating relative merits of four baseflow separation methods in Eastern Australia. **Journal of Hydrology**, v. 549, p. 252–263, 2017.
- Zhang, S. **Mapping the surface water storage variation in densely impounded semi-arid NE Brazil with satellite remote sensing approach**. PhD thesis. Berlin: Freie Universität Berlin,



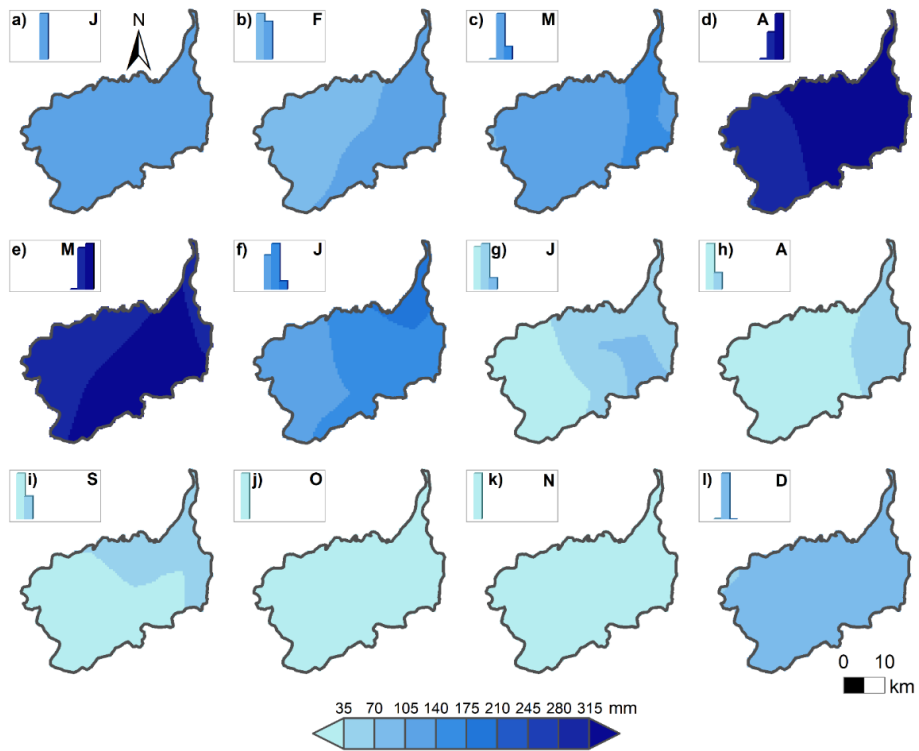
2018.

- Zhang, Y. et al. Multi-decadal trends in global terrestrial evapotranspiration and its components. **Scientific Reports**, v. 6, n. 19124, p. 1–12, 2016.
- Zhang, Y. et al. Coupled estimation of 500 m and 8-day resolution global evapotranspiration and gross primary production in 2002–2017. **Remote Sensing of Environment**, v. 222, p. 165–182, 2019.
- Zou, J. et al. Effects of anthropogenic groundwater exploitation on land surface processes: a case study of the Haihe river basin, Northern China. **Journal of Hydrology**, v. 524, p. 625–641, 2015.
- Zreda, M. et al. Measuring soil moisture content non-invasively at intermediate spatial scale using cosmic-ray neutrons. **Geophysical Research Letters**, v. 35, n. 21, p. 1–5, 2008.
- Zreda, M. et al. COSMOS: The COsmic-ray Soil Moisture Observing System. **Hydrology and Earth System Sciences**, v. 16, n. 11, p. 4079–4099, 2012.

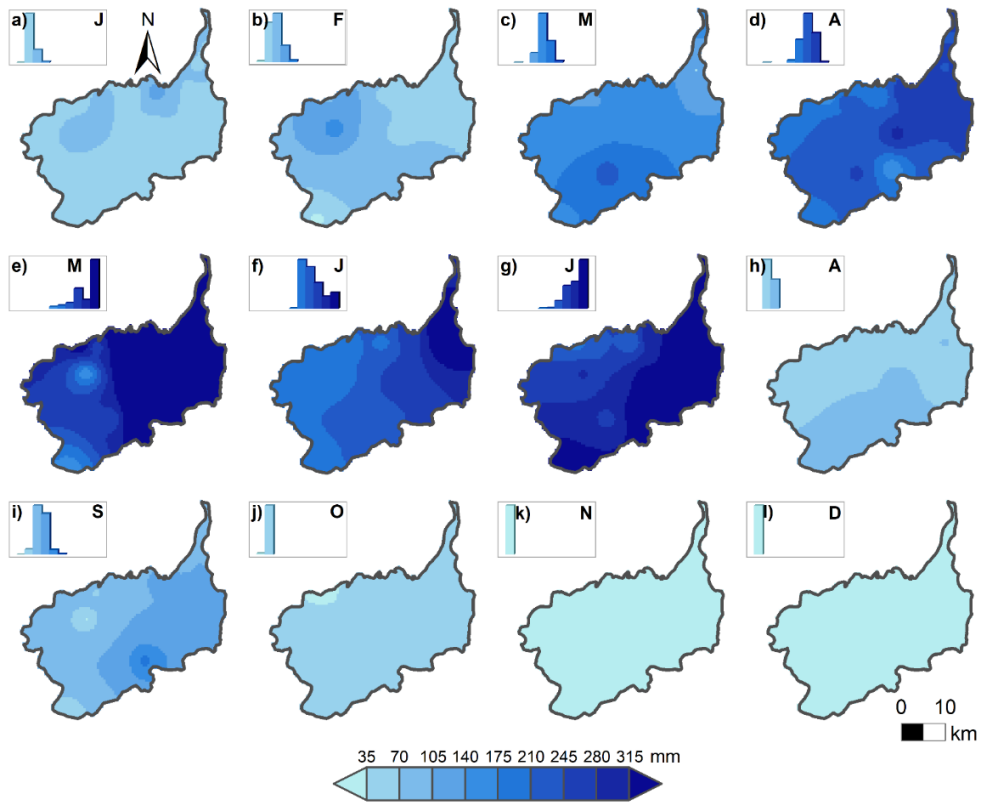
## APPENDIXES



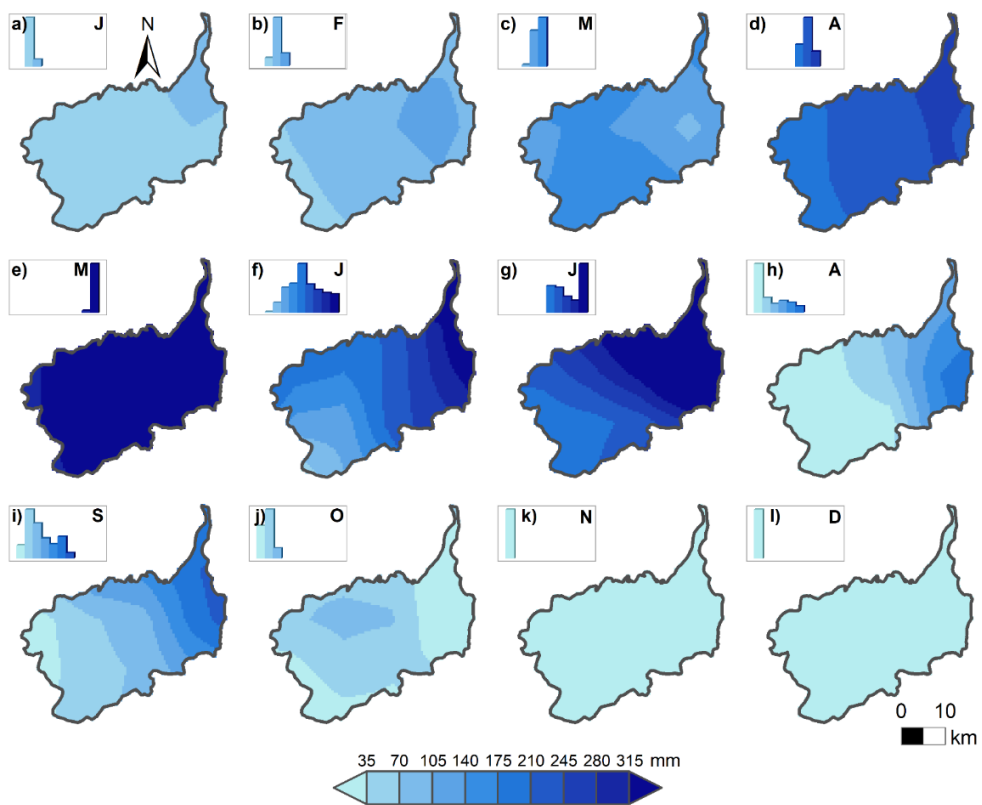
Supplementary Figure 1 – Monthly distributed precipitation obtained by Inverse Distance Weighting interpolation through the rain gauge network in 2016.



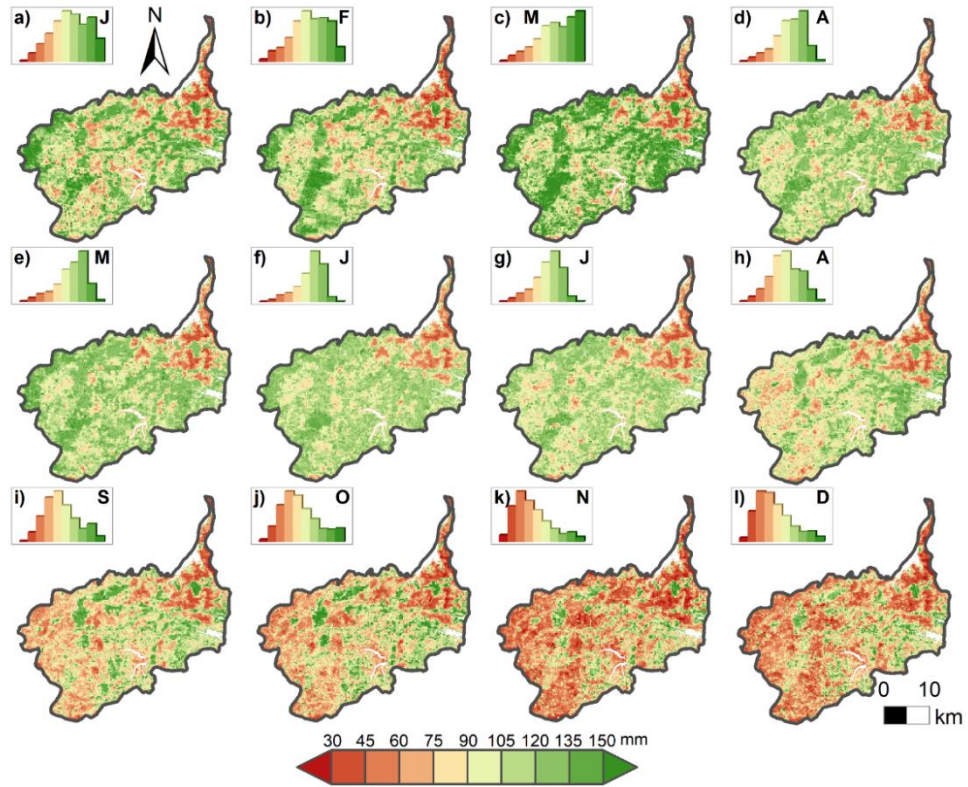
Supplementary Figure 2 – Monthly distributed precipitation obtained by bilinear interpolation and bias correction through IMERG imagery in 2016.



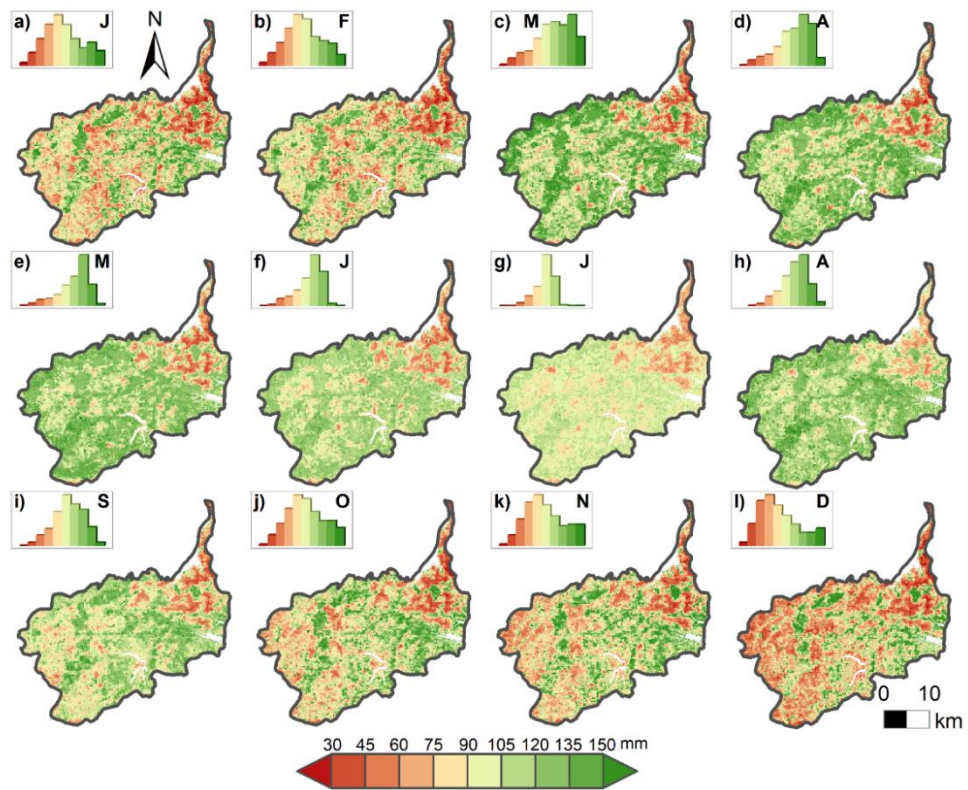
Supplementary Figure 3 – Monthly distributed precipitation obtained by Inverse Distance Weighting interpolation through the rain gauge network in 2017.



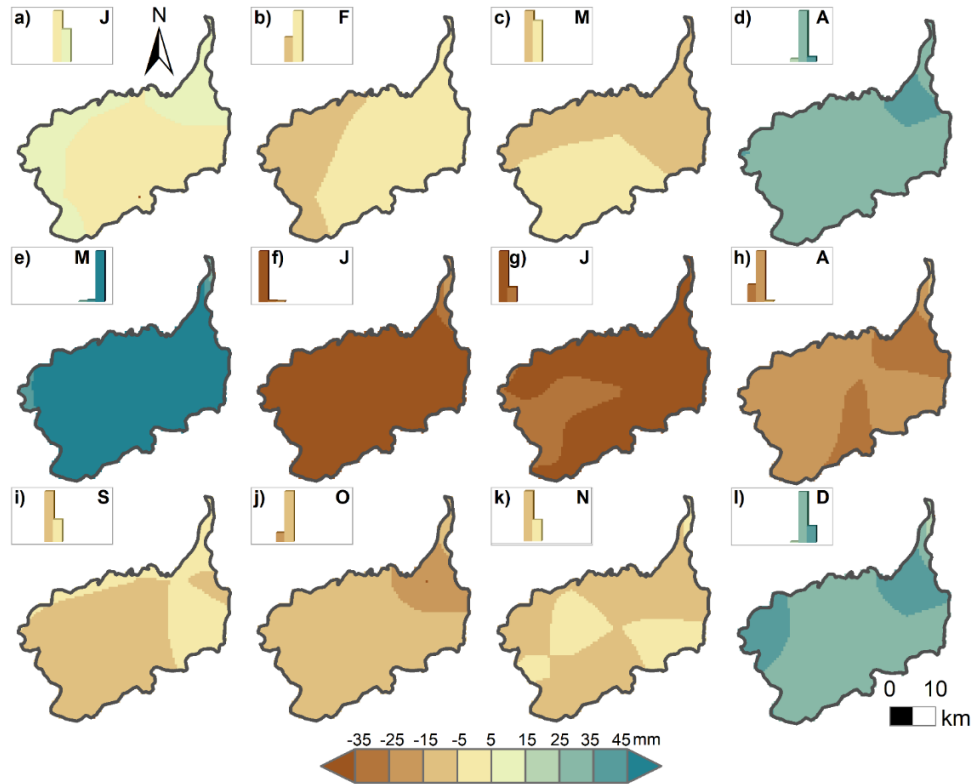
Supplementary Figure 4 – Monthly distributed precipitation obtained by bilinear interpolation and bias correction through IMERG imagery in 2017.



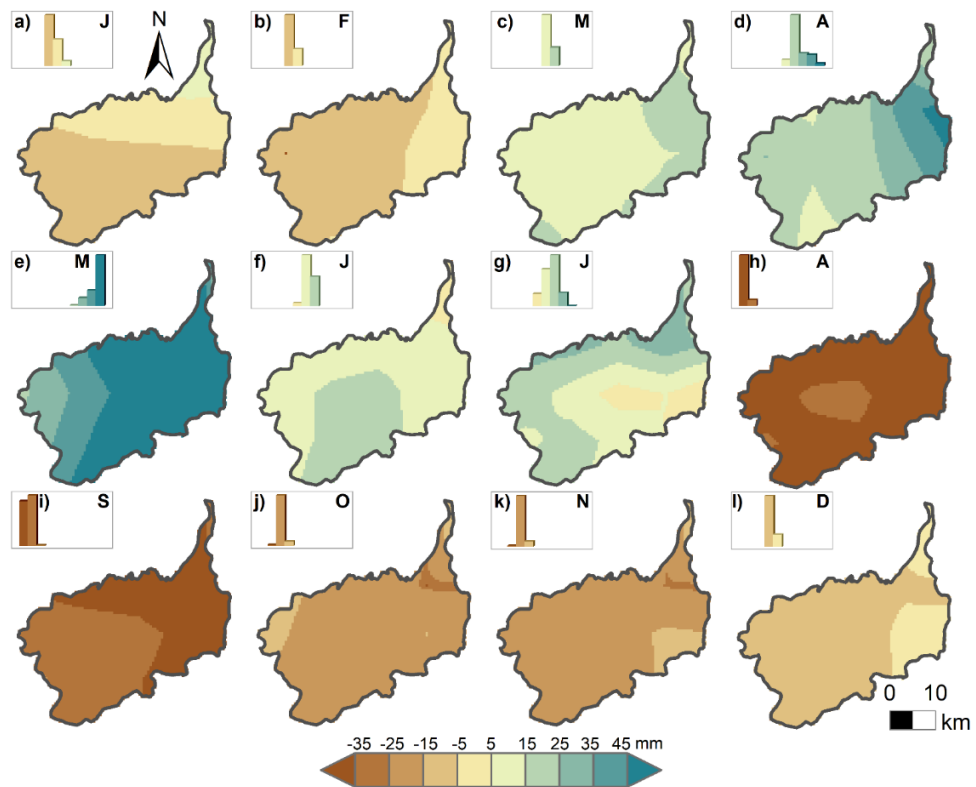
Supplementary Figure 5 – Monthly distributed evapotranspiration obtained by MODIS algorithm from MapBiomas land use/cover with cloud cleaning map composition in 2016.



Supplementary Figure 6 – Monthly distributed evapotranspiration obtained by MODIS algorithm from MapBiomas land use/cover with cloud cleaning map composition in 2017.

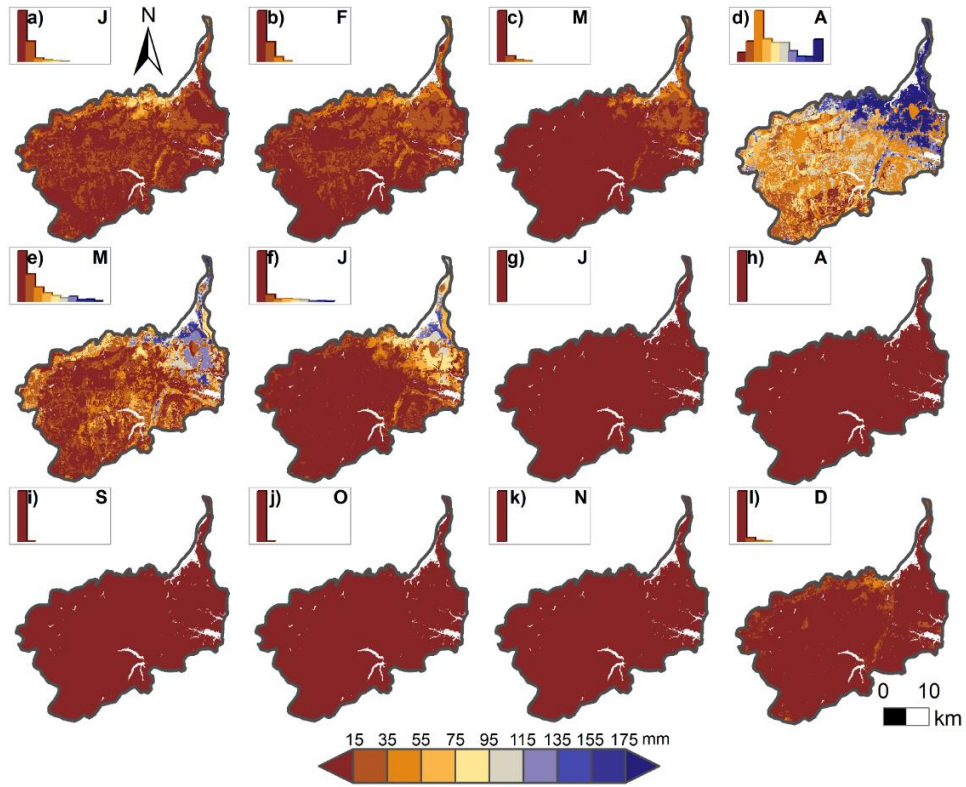


Supplementary Figure 7 – Monthly distributed soil water storage changes in 1-m root zone obtained by bilinear interpolation in 2016.

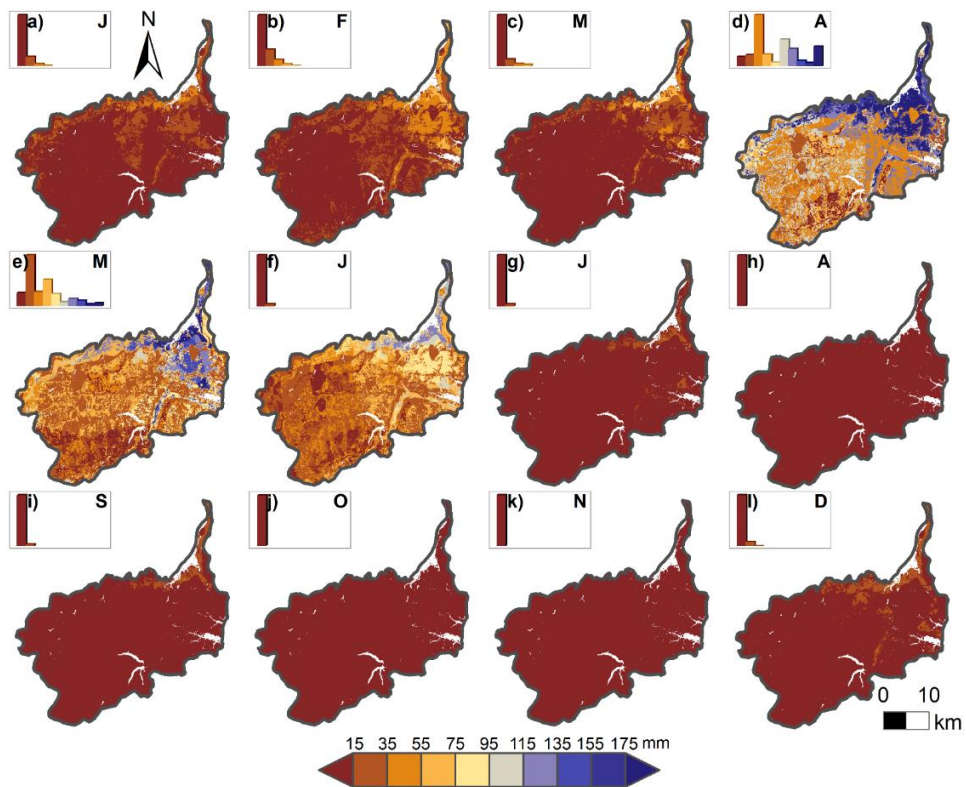


Supplementary Figure 8 – Monthly distributed soil water storage changes in 1-m root zone obtained by bilinear interpolation in 2017.

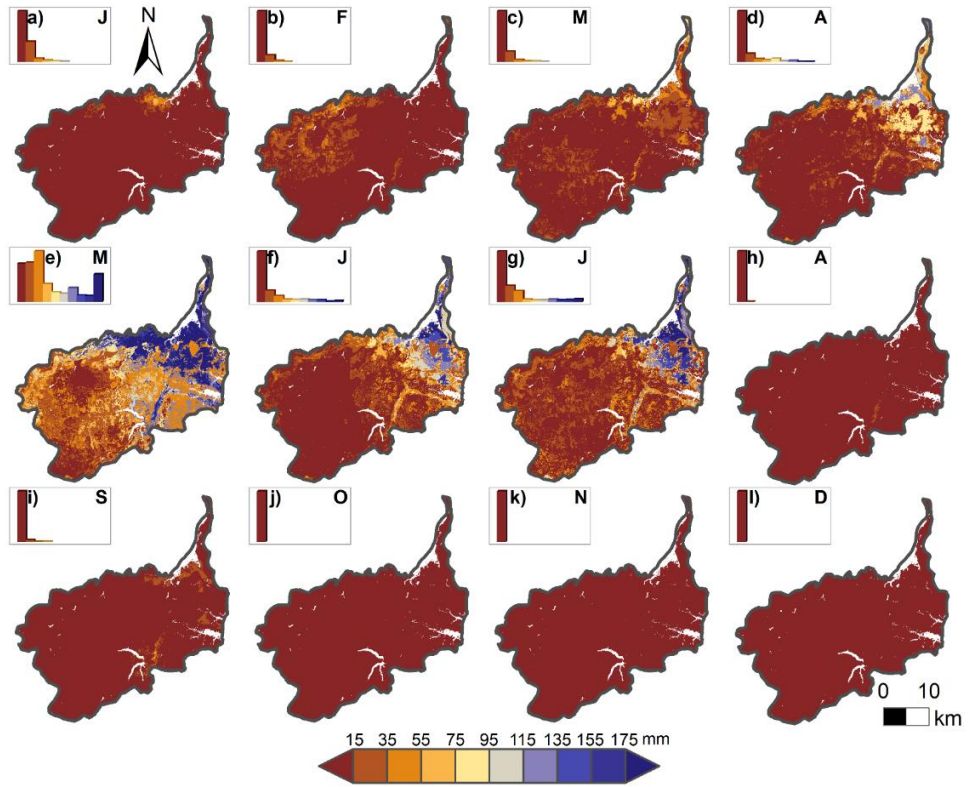




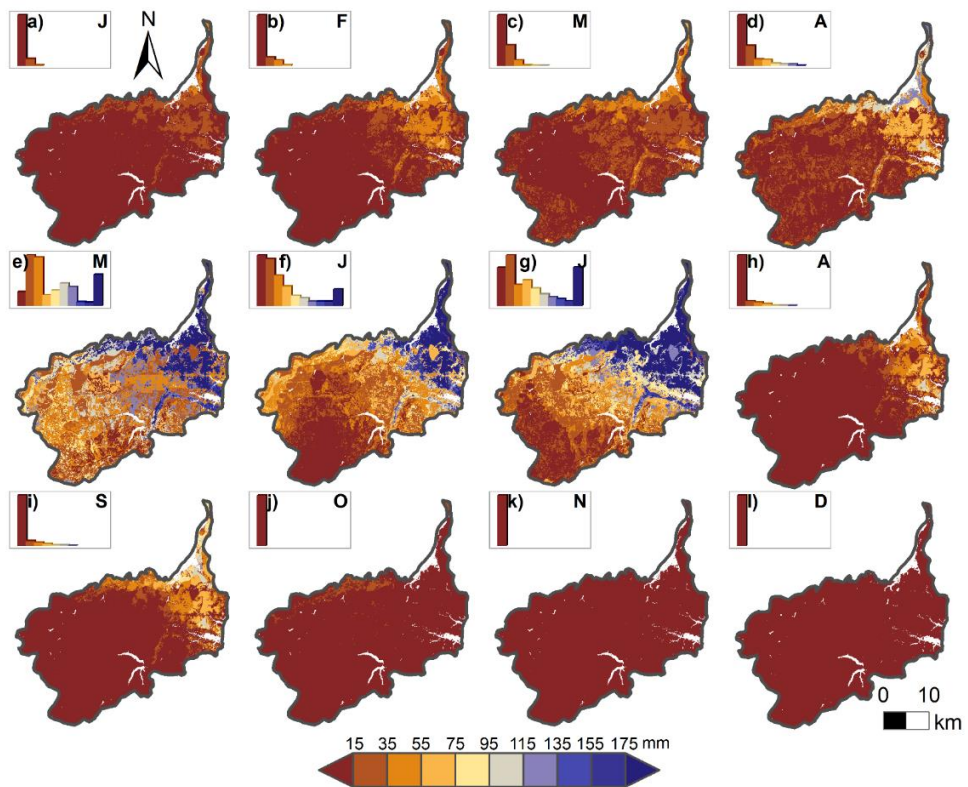
Supplementary Figure 9 – Monthly distributed surface runoff obtained by NCRS-CN method from ground-based, interpolated precipitation in 2016.



Supplementary Figure 10 – Monthly distributed surface runoff obtained by NCRS-CN method from bias-corrected IMERG imagery in 2016.

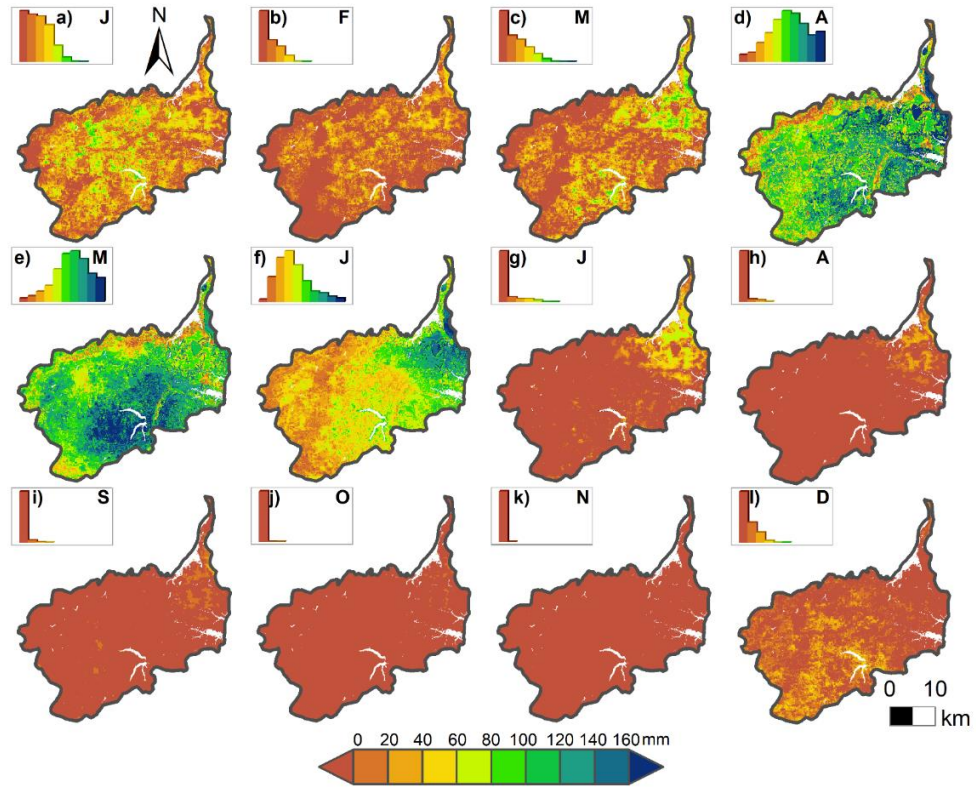


Supplementary Figure 11 – Monthly distributed surface runoff obtained by NCRS-CN method from ground-based, interpolated precipitation in 2017.

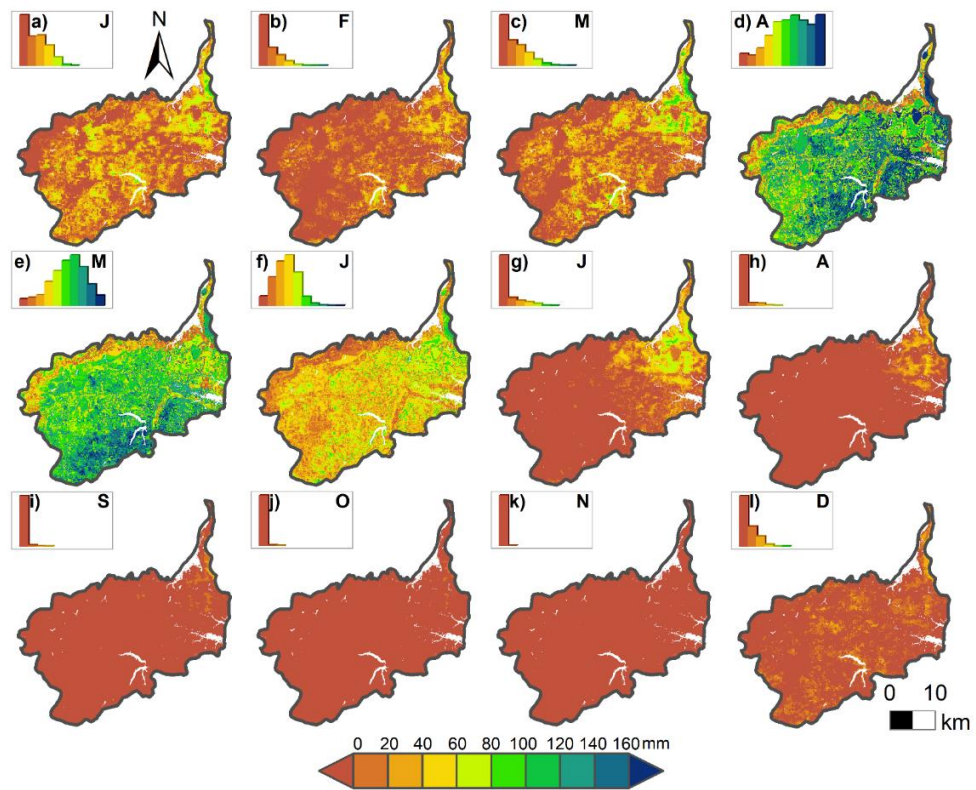


Supplementary Figure 12 – Monthly distributed surface runoff obtained by NCRS-CN method from bias-corrected IMERG imagery in 2017.



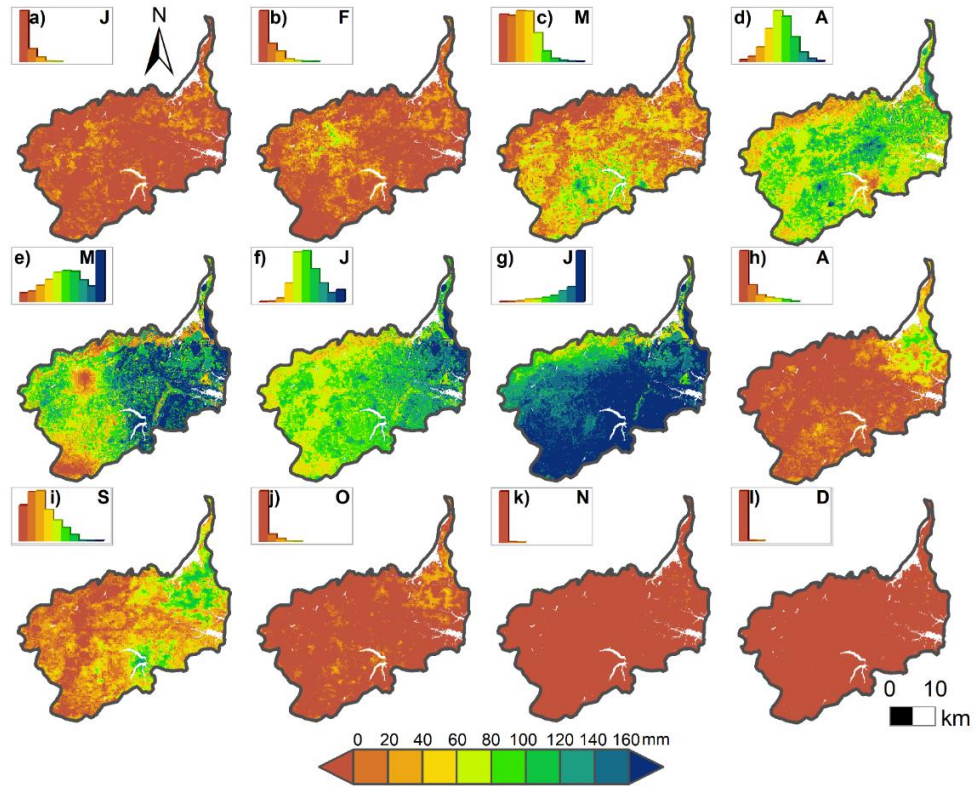


Supplementary Figure 13 – Monthly distributed groundwater recharge rates obtained by water budget equation from ground-based, interpolated precipitation in 2016.

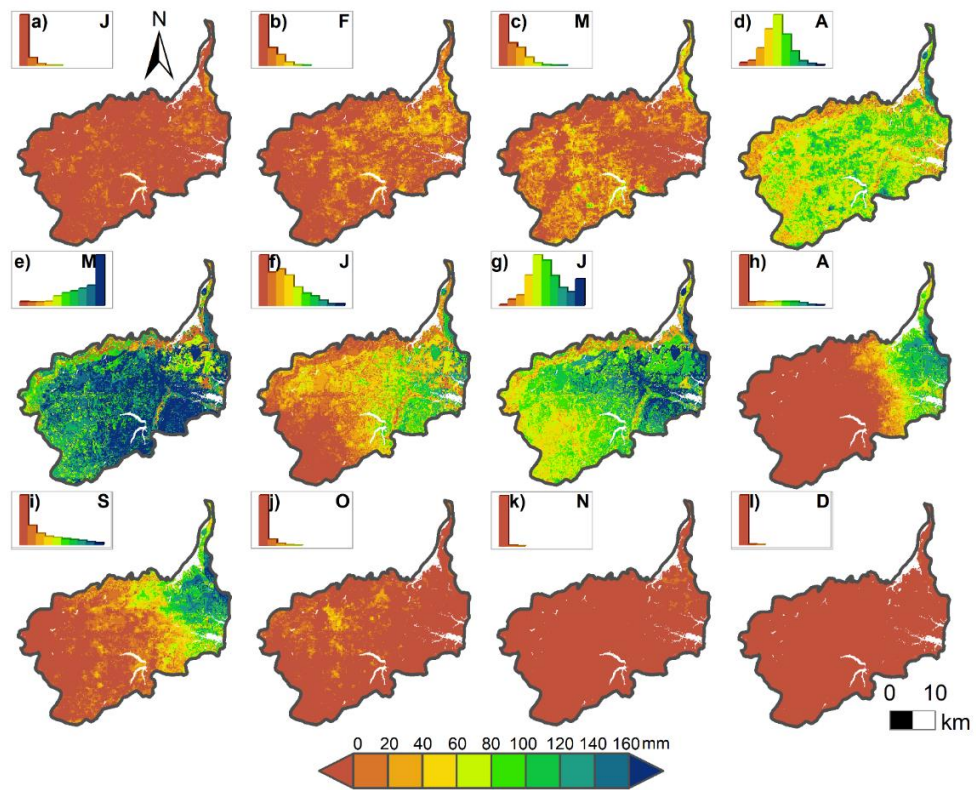


Supplementary Figure 14 – Monthly distributed groundwater recharge rates obtained by water budget equation from bias-corrected IMERG imagery in 2016.

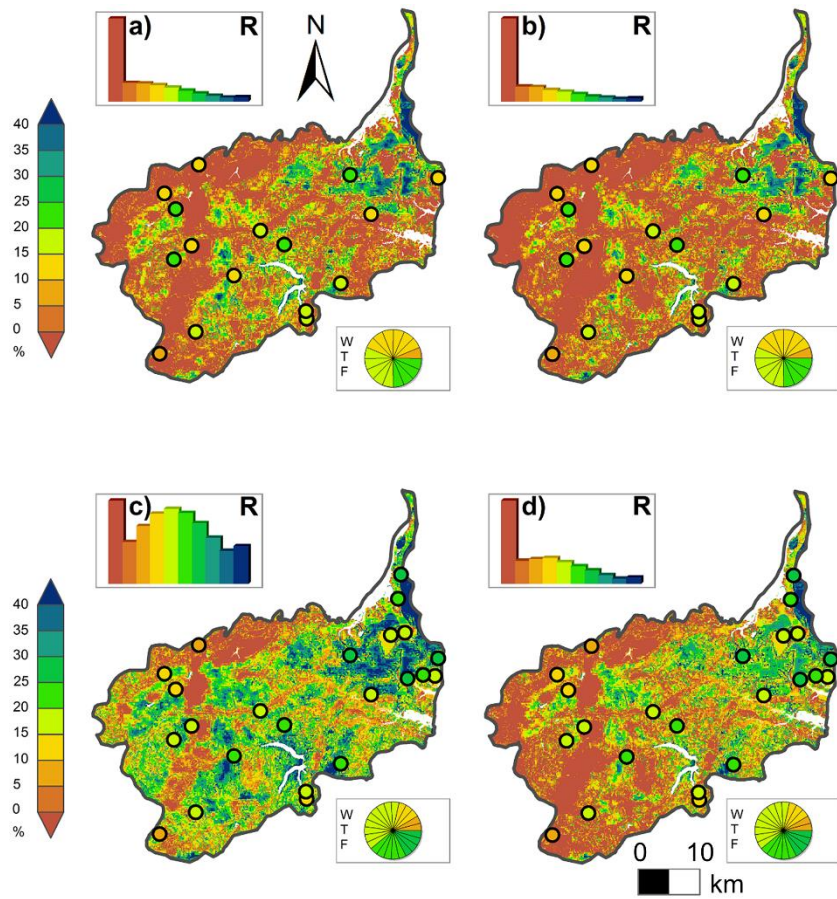




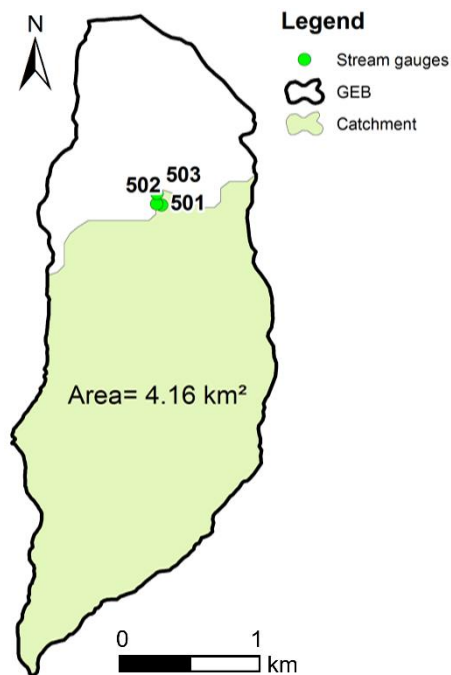
Supplementary Figure 15 – Monthly distributed groundwater recharge rates obtained by water budget equation from ground-based, interpolated precipitation in 2017.



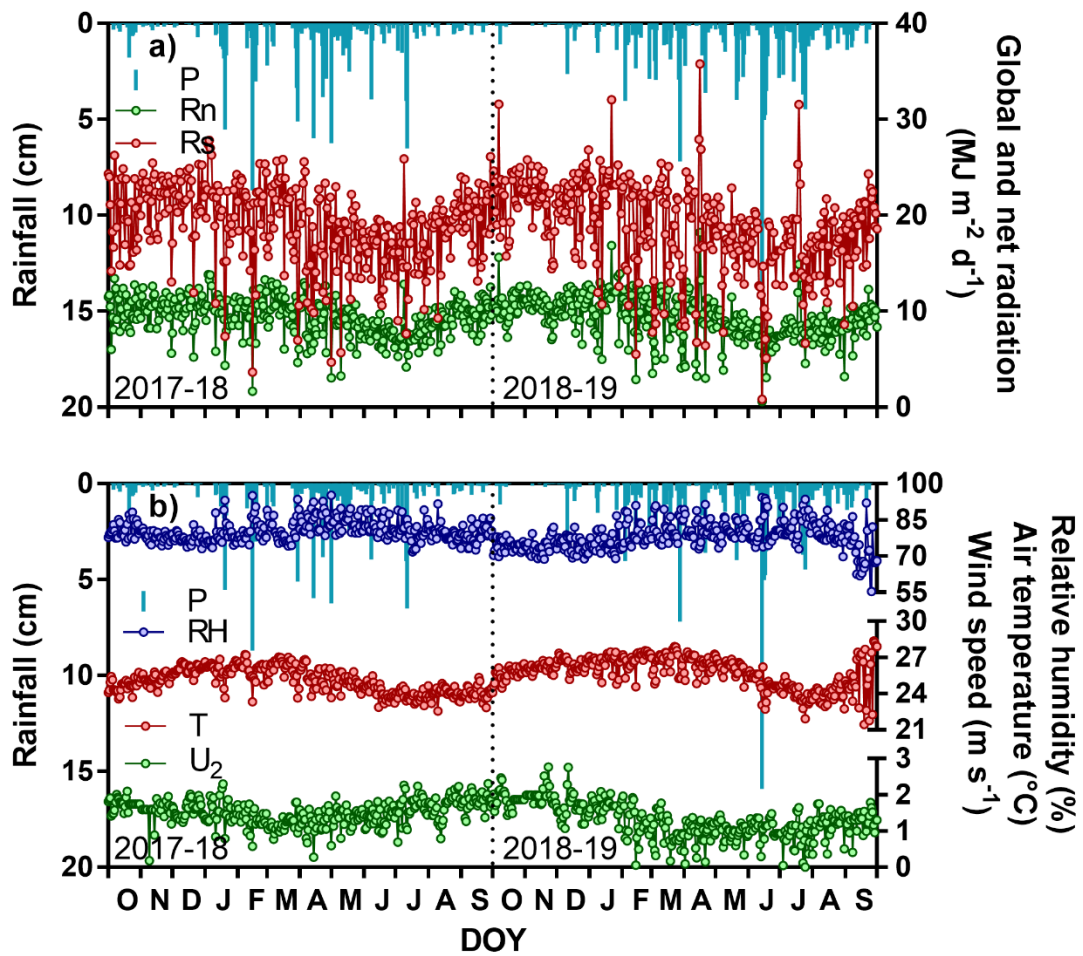
Supplementary Figure 16 – Monthly distributed groundwater recharge rates obtained by water budget equation from bias-corrected IMERG imagery in 2017.



Supplementary Figure 17 – Annual distributed relative groundwater recharge rates obtained by water budget equation and WTF method, using ground-based, interpolated precipitation in (a) 2016 and (c) 2017, and using the bias-corrected IMERG imagery in (b) 2016 and (d) 2017.



Supplementary Figure 18 – Delimitation of the 503 stream gauge catchment within the Guaraíra Experimental Basin (GEB).



Supplementary Figure 19 – Time series of the weather variables used for hydrogeological modelling in HYDRUS-1D, namely (a) daily mean global ( $R_s$ ) and net radiation ( $R_n$ ), and (b) relative humidity (RH), air temperature (T) and wind speed ( $U_2$ ).